STUDIES IN PARTIAL SLIP CONTACTS APPLIED TO FRETTING FATIGUE

Thesis submitted to the Department of Engineering Science of Oxford University in partial fulfilment of the requirements for the degree of Doctor in Philosophy

by

Anothai Thaitirarot

JESUS COLLEGE

OXFORD

Hilary Term, 2013

Abstract

Detailed analysis of all the fretting fatigue test results available in the literature is carried out by employing refined asymptotic solutions. Several different criteria are used and it is shown that two give an improvement over stress-based criteria. These procedures provide a practical method for both designing against fretting fatigue failure and quantifying the nucleation time when fretting is unavoidable.

The reduced stiffness method is developed together with the evolutionary algorithm which is the direct implementation of the Signorini and Coulomb friction contact inequalities. This method is capable of solving two dimensional frictional contact problems in significantly less time and is more accurately than a traditional FE approach. In addition, algorithms for determining shakedown limit of coupled contacts have also been developed.

A problem of a plane receding contact was considered where a strip is pressed against an elastically similar half-plane by normal pressure extending along the strip surface but stopping short of the end. These phenomena are analysed, together with the behaviour of the system when the pressure is removed.

Interfacial characteristics of a lap joint formed using friction grip bolts is also considered as these produce a receding contact. The joints consist of two elastically similar laps pressed in contact by a constant normal force and subject to oscillatory bulk load at the free end of the laps. Bulk load applied at the free ends causes a smooth change in the size of contact and the development of the slip zones. The trend of energy dissipation with the extent of contact and magnitude of remote tension, at various friction coefficients, has been found.

Lastly, axisymmetric receding contact between a circular elastic disc pressed against a half-space has been studied. The disc is first subjected to normal pressure followed by torsion. Normal pressure alone causes a contact interface to separate, if the loaded area is sufficiently small. Torsion is subsequently applied which causes a change in the size of contact and has a significant effect on the direction of the resultant slip displacement and the stick/slip boundaries.

Preface

This thesis is a collection of research work carried out by the author in the Department of Engineering Science, University of Oxford, under the supervision of Professor David Hills and Doctor Daniele Dini. The research work is original and no part has been submitted for a degree at this university or elsewhere.

The following publications or submission for publications have been based on work in this thesis.

1) A. Thaitirarot, R. Flicek, D.A. Hills and J.R. Barber, The Use of Static Reduction in Finite Element Solution of Two-Dimensional Frictional Contact Problems, *International Journal of Mechanical Science, under review.*
2) D.A. Hills, A. Thaitirarot, J.R. Barber and D. Dini, Correlation of Experimental Fretting Fatigue, *International Journal of Fatigue*, Volume 43, October 2012, page 62-75.
3) A. Thaitirarot, D.A. Hills and D. Dini, Contact mechanics of frictional lap joint, *Journal of Strain Analysis for Engineering Design*, *in press.*
4) A. Thaitirarot, D.A. Hills and D. Dini, Plane receding contact, *Proceeding of the 9th Tribo UK Conference in Tribology,* March 2012, p.69-70, National Centre for Advanced Tribology, UK.
5) A. Thaitirarot, D. A. Hills and D.Dini, Behaviour of frictional lap joint under tangential forces, *5th World Tribology Congress*, September 2013, Torino, Italy, *accepted for oral presentation*.
6) A. Thaitirarot, D.A. Hills and D. Dini, Axisymmetric Receding Contact, *Journal of Strain analysis for Engineering Design, to be submitted.*

Dedication

To my parents, my brother and my sister.

None of this would have been possible without their love and encouragement.

ACKNOWLEDGEMENTS

First and foremost, I would like to thank my supervisors Professor David A. Hills and Doctor Daniele Dini for their guidance and insightful suggestions. It has been a great honour and pleasure working with them.

I wish to express my gratitude to Professor James R. Barber from Michigan University and Assistant Professor Macro Paggi from Polytechnic University of Turin whom I have had the privilege of working with. I would like to thank all members of Solid Mechanics Group at Oxford for their friendship and support.

I acknowledge Jesus College for their scholarship and financial support.

Contents

1 Introduction and literature reviews

1.1 Introduction

The motivation for the work in this thesis was the need to better our understanding of the response of incomplete, complete and receding contacts to fretting conditions. The ultimate goal is to provide design criteria in order to avoid the premature failure of the mechanical assemblies or bolted joint structures.

Many engineering assemblies or structures consist of different elastic components usually connected by a rigid connection and they rely on frictional force to inhibit the relative motion along the contact interface. Examples of this are the bolted joints and the firtree contact between the turbine blades and disc in an aero-plane engine as shown Figure 1.1.

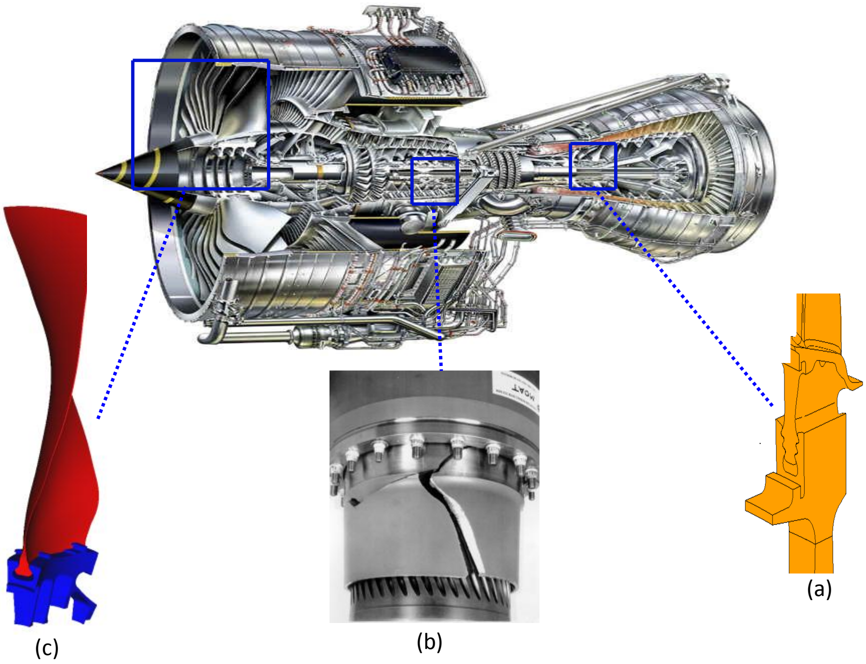

Figure 1.1: Locations of the incomplete and complete contacts in the aeroplane engine (a) Turbine Blade to Disc Joint (b) Shaft Drive Splines and (c) Fan Blade to Disc Joint.

These frictional contacts are often subjected to both constant normal loads and time-varying tangential loads that depend on the operating conditions of the engineering assemblies or other environmental factors. This typically causes zones of microslip to develop between two contacting surfaces. This microslip causes energy dissipation and may lead to two significant effects. The first effect is fretting wear which is the wear of the surfaces and this usually occurs at low normal loads and at high displacement amplitude. The second effect is fretting fatigue which could result in a life reduction of the component if the stress concentration is sufficiently high to encourage crack nucleation and growth. Fretting fatigue has been the cause of premature failure or damage of many engineering components especially in aerospace and nuclear industries. Hence, fretting fatigue has significant industrial and economic relevance as it is a major safety issue in engineering design.

Figure 1.1(a) shows a turbine blade which is connected to the disc joint and this can be idealised as an incomplete contact. An incomplete contact, Figure 1.2(a), is when the extent of the contact between the two bodies is not fixed geometrically but increases with load. If the size of the contact half-width is small in comparison to the radius of curvature then contacting bodies may be represented using half-plane formulations. The contact pressure falls smoothly to zero at the extreme edges of the contact area and a relatively small magnitude of shearing force can generate microslip. A region suffers microslip where there exists local relative tangential motion of the particles along the contact interface, even though a larger part of the contact remains stuck. This is known as the stick zone. Figure 1.1(b) shows a spline connection, used to couple the shafts, which has failed due to fretting fatigue. It can be represented by a complete contact because the edges of the contact between inner and outer shafts are abrupt. A complete contact is when the extent of contact is independent of the magnitude of the load. Since the contact-defining body has sharp corners the contact pressure will tend to infinity in the proximity of the contact edge. Figure 1.1(c) shows the fan blade which is connected to a disc joint. The edge of this type of contact is slightly rounded and it may be idealised as a flat and rounded contact where there is a flat region in the middle of the contact. This is also regarded as an incomplete contact.

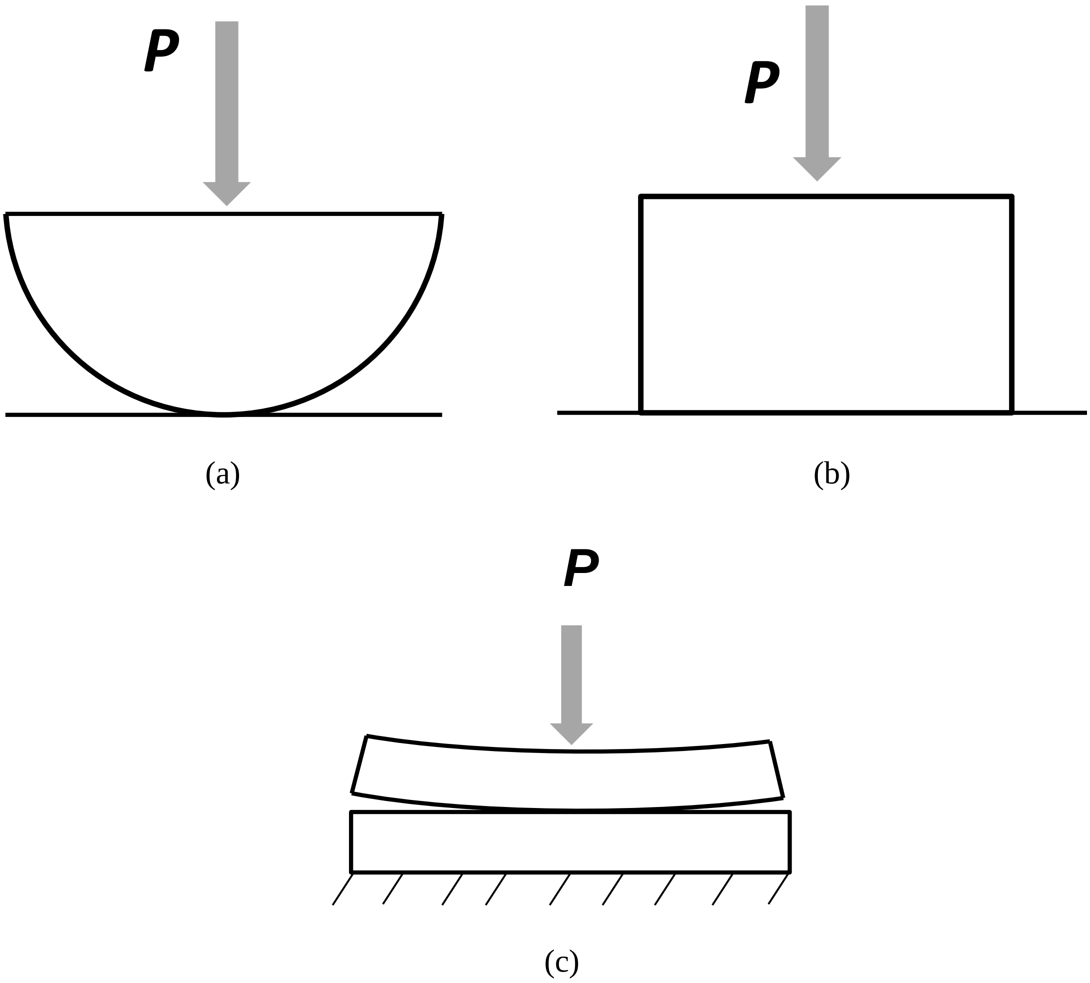

Figure 1.2: Different types of contact; a) incomplete b) complete c) receding contacts

Another type of contact is a receding contact, Figure 1.2(c), which can be used to model the contact in the bolted joint assemblies or structures. An example of this is the contact of bolted flange joints in aircraft engine casings.

1.2 Literature reviews

1.2.1 Analytical solutions for elastic contacts

Some of the earliest studies of contact mechanics focussed on friction. When the surfaces of two solid bodies are pressed into contact, a frictional force may be formed which tends to oppose any relative tangential motion along the contact interface. In 1785, Coulomb's friction law [1] was discovered which is still widely used today. Contact problems can be considered as static or quasi-static and dynamic. The former is when inertial effects can be neglected which will be focussed on in this thesis, whereas in the latter inertial effects become significant.

In 1882 Hertz [2] published important results which are the stress distributions for the frictionless contact of two bodies of ellipsoidal profile. The bodies were idealised as semi-infinite half-spaces and their surface are described by second order polynomials. The solution was developed as a result of his work on how the normal load affects the properties of the glass lenses. Hertz analysis is still widely used in the design procedure involving elastic contacts. Since then there has been a considerable development in the field of contact mechanics with an emphasis on extending Hertz solutions to other geometries and constitutive laws. Boussinesq [3] and Cerruti [4] found a solution for the stress and displacement in elastic half-space subjected to surface tractions by using the theory of potential. A problem of a normal line force acting upon the sharp corner of a semi-infinite elastic plane was analysed by Flamant [5] and later by Timoshenko and Goodier [6]. This provides a basis of determining the solution of a punch with arbitrary profile pressed against a half space. Gladwell [7] and Johnson [8] provide an overview of all the various contact geometries that have come into consideration. A partial slip problem of a Hertzian contact subjected to constant normal force and a monotonically increasing shear force was first analysed by Cataneo [9]. The results were then re-discovered by Mindlin [10] and extended by Mindling and Deresiewics [11] to other loading conditions particularly when the normal and shearing forces are proportional. Recently, Jager [12] and Ciavarell [13] provide a significant generalisation of this solution. A partial slip problem of Hertzian contact where oscillating shear and bulk tension are in phase at constant normal load has been studied by Nowell and Hills [14]. They showed that the addition of remote bulk tension to the specimen has a significant effect on stick and slip zones as well as interfacial shearing traction.

In 1952, Williams [15] published an important solution for the stress field and the order of stress' singularity at the apex of a semi-infinite two-dimensional wedge under general remote loading. Later, Bogy [16] found the solution for the stress state of two elastically dissimilar wedges which are bonded together along a common edge. In 1969, Dundurs [17] published a discussion of Bogy's paper [16] and showed that three parameters $(\mu_1 / \mu_2, \upsilon_1, \upsilon_2)$ used by Bogy [16] for the problem can be fully accounted for with two composite material parameters (α, β). Based on Dundurs finding, Body [18] published a refined form of the solution which is more concise. In 1975, Gdoutos and Theocaris [19] and Comninou [20] independently found the solution for a sliding frictional contact between an elastic wedge and elastically dissimilar half-plane and the characteristic equations were found in terms of two Dundurs constants and coefficient of friction.

In 1973, another important result was made by Spencer [21] who showed that a rigid punch with a power law profile pressed against an elastic half-space in the presence of friction is self-similar. This means the ratio of the central stick zone to the extent of contact area remain the same under monotonic loading. Later it was proved that the result is also applicable to the punch with flat profile and this solution enabled him to analyse the axi-symmetric Hertzian contact [22].

1.2.2 Fretting fatigue

The first paper on fretting fatigue was published by Eden *et al.* in 1911 [23]. He reported that there was iron oxide debris on the contacting surface between a fatigue specimen and its test rig clamp. The first methodical study of the subject was carried out by Tomlinson in the 1930's [24] and he suggested that tangential displacement may be one of the possible parameters affecting fretting fatigue. Further systematic studies on fretting fatigue in 1941 by Warlow-Davies [25] showed a reduction in fatigue strength of fretted steel specimens. In the early 1950's, McDowell [26] found that the combined effects of fretting and fatigue on the fatigue strength are even more significant, reducing it by a factor of 5 compared to the 18% reduction in life in the study carried out by Warlow-Davies [25]. In the late 1950s, Fenner and Field [27, 28] conducted fretting experiments using bridge type of fretting pads with two flat surfaces and demonstrated that the fretting highly accelerated crack initiation.

In the 1960's, Nishioka *et al.* [29 – 34] carried out fretting experiments using cylindrical pads and investigated possible parameters that could be involved in controlling fretting fatigue. The pads used were convex and hence gave rise to incomplete contact and therefore can be represented by the half-plane formulation. The other advantage of using these cylindrical pads was that the tests are less sensitive to the minor misalignments, unlike the bridge type pads. A number of interesting findings were published by Nishioka and colleagues. They reported the existence of non-propagating fretting fatigue cracks which suggested that the cracks can arrest under certain conditions. They also demonstrated the effect of different relative tangential displacement between the surfaces on fatigue life. Another finding was the increase in friction coefficient during the experiments and this effect was later confirmed [35, 36]. Further study from the same authors showed the small effect of mean stress on crack initiation and and also the small effect of hardness on the fretting fatigue life. In 1974, Hoeppner and Goss [37] introduced the concept of fretting damage threshold in which the fatigue strength was reduced when the damage reached a certain amount. These concepts of fretting damage were also developed by Endo and Goto [38]. In an effort to predict fatigue life due to fretting they also found that the initial propagation of fretting fatigue cracks was faster than plain fatigue cracks. In the late 1970's, Alice and Kantimathi [39] investigated the effect of periodic high loads on fretting fatigue of an aluminium alloy and also stated that fretting must be responsible only for the initial stage of the crack development and play no further role in the propagation phase. Bramhall [40] carried out experiments to investigate the effects of different contact sizes while the peak pressure is held constant, by using the classical Hertzian contacts. The results suggest the existence of a critical contact size and an infinite life was found for contact dimensions less than this critical value. This effect was later confirmed by Nowell [41]. Over the past thirty years, a number of books on fretting fatigue have been published such as those by Waterhouse [42], Bannantine [43] and more recently by Hills [44].

1.2.3 Receding contact

Most contacts fall into two classes; incomplete and complete. The size of the contact increases as the load is applied in an incomplete contact, but is independent of the applied load in a complete contact. However, receding contacts do not come into either category. An example of receding contact is two elastic strips sitting on top of one another with an applied load P. As the load is applied the contact 'snaps' to a finite size. Filon [45] predicted the result based on the fact that a single rectangular block loaded by two equal and opposite forces experiences a tensile stress near the edges. As a result, the strip separated at both edges. In

1957, the semi-contact width was shown to be 1.35 times the block thickness [46] and the technique used was photoelasticity. This phenomenon was then described in [47] as a "Receding contact". *If the contact area in a frictionless elastic system under the load is equal or smaller than the contact area in the unloaded state*. This class of problem was further studied in [48, 49]. Due to the lack of computational power in the 1970's, the receding contact was analytically studied by many researchers. Recently, Ju Ahn [50] analysed the two-dimensional problem where the elastic block is pressed against a rigid plane surface.

1.2.4 Shakedown of frictional contacts

When elastic bodies under contact with a frictional interface are subjected to cyclic loading, the steady state behaviour of the system may lead to three different scenarios. These could be rachetting, cyclic slip or frictional shakedown.

Rachetting is defined as the accumulation of strain deformation in mechanical assemblies under cyclic loading. It occurs when micro-slip arises in a region of the contact for each loading cycle and accumulates over many cycles, eventually showing a rigid body motion. Cyclic slip, sometimes called plastic shakedown, is when a micro-slip shows no net accumulation but just repeatedly varies between two limiting values in a loading cycle. Frictional shakedown occurs when a micro-slip zone is only present for the first few loading cycles, and then a fully adhered state applies throughout the contact area as a result of beneficial residual stresses that prevent the development of slip. This is practically very useful in engineering design against fretting fatigue. If we know the conditions which can lead to full adhesion of the contact then we can minimise the possibility of the premature failure of mechanical assemblies through fretting fatigue. Comminou and Barber [51] analysed the shakedown limits of a frictional contact of an elastic layer pressed against an elastic half-plane and subjected to a cyclically varying tangential force. Bree [52] investigated the elastic-plastic behaviour of thin tubes in the design of nuclear reactor fuel elements which are subjected to internal pressure. The temperature gradients occur across the tube wall cycles because of start-up or shutdown of the reactor and it was shown that the plastic strains produced may cause rachetting or plastic cycling. Churchman [53] studied a simple contact problem which is the frictional equivalent of the Bree analysis. Different responses of the system are classified when it is subject to periodic loading in the form of Bree diagram.

A number of authors [53, 54] considered whether Melan's theorem [55] for plasticity may be applicable to a frictional contact problem. As the Melan for classical plasticity is associative this may not be applicable to frictional systems. This is because the friction law is non-associative which means that the slip will be in the same direction as the shear force. However, shakedown theorem in plasticity requires the flow rule to be associative and an incremental plastic strain occurs in the direction of the outward normal of the yield surface. This suggests that Melan's theorem [55] would not necessarily be applicable to coupled problems. Klabring *et al.*[56] shows that Melan's theorem [55] can be applied to discrete uncoupled systems. It was also shown to be applicable to the continuous uncoupled systems by Barber and co-workers [57]. Recently, Ahn [58] investigated the shakedown limits of a discrete coupled system in which a coupling is present and found that the Melan's theorem [55] does not hold. However, it is unclear whether the results found for the coupled discrete systems would equally apply to a continuous system when coupling is present: this will be investigated in this thesis.

1.3 Summary

Since the first report on fretting fatigue in 1911 [23] there has been considerable progress made in this field. However, a thorough understanding of fretting fatigue under all conditions and all geometries is yet to be accomplished. The study of fretting fatigue can be categorised into crack initiation and propagation phases. Many questions remain unanswered about the former and a number of approaches have been developed to better an understanding of the crack initiation mechanisms. However, further systematic study is required to improve the predictive lifting methods.

In this thesis, the focus of the work will be on the areas in which there has been less research work. For instance, it was noticed from the literature review that there has been little focus on frictional receding contacts as it has only been investigated in recent years. The study of complete contacts has only been carried out extensively over the last decade or so.

The main aim is to analyse incomplete, complete and receding contacts which are subject to fretting loads. The types of incomplete contacts which will be analysed are ones where cylindrical pads are employed, and also flat and rounded pads. The experimental results of fretting fatigue tests available in the literature and those readily available will be analysed accurately with the tools developed. An attempt will be made to provide a practical method for designing against fretting fatigue and to quantify the nucleation time of cracks when fretting fatigue failure takes place.

The development of the reduced stiffness method capable of solving two dimension frictional contact problems including incomplete contacts will be carried out as well as the evolutionary algorithm using Guass-Seidel principle. Different types of example problems will be considered to illustrate the implementation of the method developed. The comparison with ABAQUS will also be made to investigate if there are any differences.

The shakedown analysis of elastic systems, where the degree of coupling is present, will be carried out. Three different algorithms for the shakedown calculation will be developed. The results will then be tested using the evolutionary algorithm. The effect of different initial conditions on steady-state response of the systems will also be investigated.

The remainder of the thesis will be focussed on the investigation of receding contacts. The first is the plane receding contact subjected to a constant normal load. Secondly, mechanical lap joints which are pressed by a constant normal force in the presence of friction and subjected to oscillatory remote loadings at the free end of the laps under partial slip conditions will be treated. Lastly, an axi-symmetric receding contact between a circular disc and elastically half-space is first subjected to pressure and subsequently to torsion.

2 Correlation of Experimental Fretting Fatigue

2.1 Introduction

When two contacting bodies are subjected to oscillatory loadings they experience small scale reciprocating motion. This causes a zone (or zones) of microslip to develop along the contact interface and it may be associated with a reduction in fatigue life when compared to a plain fatigue. This phenomenon is known as 'fretting fatigue'. It has been the cause for many premature failures of several engineering components, for example, that of dovetail joint in the aeroplane engine [59]. The failure is due to the initiation and subsequent propagation of a crack in the joint and this can be very costly to both industry and the general public. Therefore, a better understanding of this failure mechanism is vitally important to safety-critical industries such as the aerospace and nuclear sectors.

The first quantitative studies of fretting fatigue were conducted by [40, 60-62] with a series of researchers in the late 1960s and early 1970s. One of the most far-reaching was a set of tests conducted by Bramhall [40] in which very carefully controlled fatigue tests were carried out with cylindrical pads pressed onto the surface. These were also subjected to a shearing force which varies harmonically and synchronously with the tension in the specimen. These tests exploit the well-known Cattaneo-Mindlin [10, 63] solution for partial slip to give a well-defined slip regime where the shearing tractions and magnitude of the relative slip displacement are known explicitly at all points. One finding from those tests was a pronounced 'size effect'. It was noted that if a small contact were subjected to a particular contact traction regime, and then a second experiment conducted with the *same* tractions and slip, but extending over a larger region, the latter would invariably give a shorter life. These tests were repeated and extended by Nowell [41] and the same property of ‘size effect’ was reported.

There have been several possible explanations for this effect put forward (see e.g. [64]) but it can be argued that none has been demonstrated to be totally convincing. The intention of this chapter is not to provide a further candidate but to describe the environment in which the crack nucleates by an asymptotic form [65 – 67] and then to display this as a suitable correlator of fatigue life. Concepts of threshold stress intensity are well known in plain fatigue and one question which is explicitly addressed here is whether the same, or a modified value, is appropriate for fretting nucleated fatigue. If the threshold for plain and fretting fatigue is the same, this provides evidence that fretting causes no additional damage to the material through the action of rubbing. However, if this assumption cannot be sustained then it would follow that there would be no alternative, if threshold conditions were to be found, to carrying out laboratory experiments in the presence of slip.

2.2 Adhered asymptotes and their calibration

Asymptotic approaches were developed by Dini et al. [67] as a way of correlating different contacts under fretting conditions. The key concept of the asymptotic procedure is to specify the complete local state of stress and interfacial tangential (slip) displacement present at the edge of a contact by two asymptotic forms; one for interfacial contact pressure distribution $p(t)$ and another for corresponding interfacial shear traction, $q(t)$. This is a very useful procedure because it reduces a number of independent variables needed to quantify the local state of stress and slip displacement. In this chapter only incomplete contacts will be considered where the interfacial normal tractions at the extreme contact edges are equal to zero. Additionally, I will restrict ourselves to those which are sufficiently non-conformal for each body to be capable of idealisation by a half-plane.

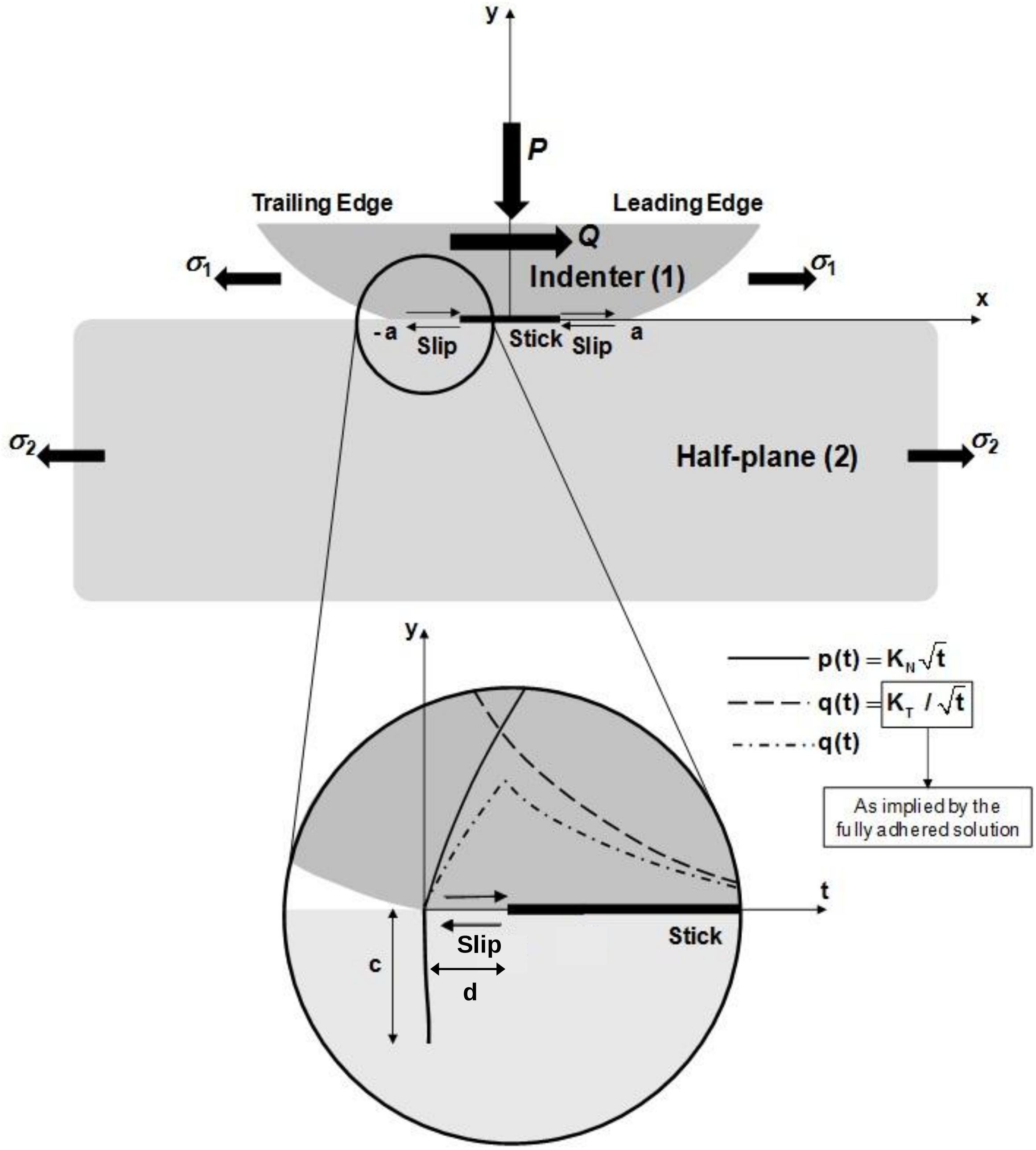

Figure 2.1: Schematic of the fretting fatigue related contact problem and asymptotic characterisation (zoomed-in view of the trailing edge of the contact).

The bodies are also assumed to be elastically similar so that the effects of normal and shear loading are uncoupled. This means a normal load induces only contact pressure and a shearing force or the application of bulk tension, Figure 2.1, induces only shearing tractions. I now 'zoom in' our field of view so that only the very edge of the contact, in the neighbourhood where cracks nucleate, is within view. The local interfacial contact pressure distribution at the contact edge, $p(t)$, can be written in the form [65]

$$p(t) = K_N \sqrt{t}, \tag{2.1}$$

where t is measured inwards from the contact edge, zoomed-in inset to Figure 2.1, and the constant K_N is a geometry-dependent quantity which may be found from the solution to the whole contact problem, Figure 2.1, by shifting the origin and taking the lead term in an expansion. For example, for a Hertzian contact of half width a, and having a peak pressure p_o the contact pressure is semi-elliptical in form

$$p(x) = p_o \sqrt{1 - \left(\frac{x}{a}\right)^2}, \tag{2.2}$$

and the corresponding value of K_N [65] is

$$K_N = p_o \sqrt{\frac{2}{a}}. \tag{2.3}$$

Suppose, for the time being, that the coefficient of friction, f, between the contacting bodies is sufficiently high to inhibit all tangential movement of the particles along the contact interface so that the contacting bodies can be regarded as a monolith or bilateral. It follows that, at the edge of contact the shearing traction, $q(t)$, must be square root singular, and can therefore be represented in the form

$$q(t) = \frac{K_T}{\sqrt{t}}. \tag{2.4}$$

The calibration for the multiplicative constant does not, here, depend on the contact geometry. If the half-width is a the application of a shearing force, Q , generates a shearing traction, $q(x)$, of the form

$$q(x) = \frac{Q}{\pi\sqrt{a^2 - x^2}}. \tag{2.5}$$

By shifting the origin to trailing edge of the contact by the change of coordinate $x = (t - a)$ in equation 2.5 and expanding the expression as a polynomial series, this gives

$$q(t) = \frac{Q}{\pi\sqrt{2at}} \qquad t << a$$

and

$$K_T^Q = \frac{Q}{\pi\sqrt{2a}}. \tag{2.6}$$

If, instead, each body is subject to a bulk tension acting parallel with the free surface, and the difference between the tensions is $\sigma_o = \sigma_2 - \sigma_1$, then the integral equation ensuring that the surface strains are matched within the contact is

$$\int_{-a}^{a} \frac{q(\xi)}{x - \xi} d\xi = \frac{\pi\sigma_0}{4}, \tag{2.7}$$

and this can be inverted to give

$$q(x) = \frac{\sigma_o x}{4\sqrt{a^2 - x^2}}. \tag{2.8}$$

Similarly, if the origin is shifted to the trailing edge of the contact and using a series expansion so that

$$q(t) = \frac{\sigma_o\sqrt{a}}{4\sqrt{2t}} \qquad t << a$$

and

$$K_T^\sigma = \frac{\sigma_o}{4}\sqrt{\frac{a}{2}}. \tag{2.9}$$

This calibration term is also independent of the profile of the contact. It is worth mentioning the sign of these quantities at the contact edges. At the trailing edge of the contact the shearing force acts to the right in body 1 producing a positive contribution to K_T, and so does the tension in body 2. However, at the leading edge of the contact the same shearing force produces a negative contribution to K_T whilst the tension still produces a positive contribution. Very close to the ends of the contact, both forms of loading (shear force and a difference in bulk tension) excite the same response in terms of the local traction distribution. This is also applicable to the field over a length scale within which the tractions are appropriately represented by the asymptotic forms.

2.3 Effect of finite friction

Suppose that the friction coefficient is no longer artificially large, so that a small region of slip is allowed to develop at the contact edge. Providing that the coefficient of friction is not too small such that the inequality of equation 2.10 is satisfied.

$$\frac{K_T}{fK_N} \ll a, \tag{2.10}$$

This ensures that the slip zone is very small compared with the overall size of the contact. Therefore the asymptotic representations of the tractions remain valid, and the slip zone size, *d*, is given by [66].

$$\frac{K_T}{fK_N} = \frac{d}{2}, \tag{2.11}$$

whilst the shearing traction, $q(t)$, is now

$$\frac{q(t)}{\sqrt{fK_N K_T}} = 2\left[\sqrt{\hat{t}} - \sqrt{\hat{t} - 1}\right], \tag{2.12}$$

where $\hat{t} = \frac{t}{d}$, and this shear traction distribution is also included in the zoomed-in view of the trailing edge in Figure 2.1, shown by the chain line.

2.4 Process zone size

The 'process zone' is defined as the region in which non-linear behaviour of the material occurs, leading to plastic exhaustion, material damage and, eventually, the nucleation of a crack. Precise details of the irreversibilities are unknown and, at this scale, there is likely to be significant localisation of stress by anisotropy of the grains. As a first approximation, I take the process zone to be the region in which a classical bulk yield criterion is violated. It will clearly be helpful to quantify the range of loads where the process zone falls well within the slip region, and when it envelops it. The Muskhelishvili [68] potentials for the problem are known [65] and the contact normal pressure gives rise to a stress field whose Muskhelishvili potential [65] is

$$\Phi_N(\hat{w}) = \frac{K_N\sqrt{d}}{2}\sqrt{\hat{w}}, \tag{2.13}$$

where $\hat{w} = \left(\frac{t}{d} + i\frac{y}{d}\right)$. I turn, now, to the shear traction, and note that, for a shearing traction distribution given by equation 2.12, the Muskhelishvili potential [65] is given by

$$\Phi_T(\hat{w}) = i \times \sqrt{fK_N K_T}\left[\sqrt{\hat{w}} - \sqrt{\hat{w}-1}\right]. \tag{2.14}$$

Using these definitions, I can develop an expression for the state of stress in the following form:

$$\sigma_{ij}\left(\hat{t},\hat{y}\right) = K_N\sqrt{\hat{r}}\,g_{ij}(\theta) + \sqrt{fK_N K_T}\,h_{ij}(\hat{t},\hat{y}), \tag{2.15}$$

where $g_{ij}(\theta)$, $h_{ij}(\hat{t},\hat{y})$ are found from the Muskhelishvili potentials and $\hat{r}^2 = \hat{t}^2 + \hat{y}^2$. I may write this in a dimensionless form as

$$\frac{\sigma_{ij}(\hat{t},\hat{y})}{K_N\sqrt{d}} = \sqrt{\hat{r}}\, g_{ij}(\theta) + \frac{f}{\sqrt{2}} h_{ij}(\hat{t},\hat{y}). \tag{2.16}$$

It is possible to re-write the normalising magnitude $K_N\sqrt{d}$ in any number of different ways by using the identity for d. The second deviatoric invariant for a plane problem may be written down as

$$J_2 = \sigma_{xx}^2 + \sigma_{yy}^2 + \sigma_{zz}^2 - (\sigma_{xx}\sigma_{yy} + \sigma_{yy}\sigma_{zz} + \sigma_{zz}\sigma_{xx}) + 3\tau_{xy}^2, \tag{2.17}$$

and, with this scaling, von Mises' yield condition arises when

$$3k^2 = J_2, \tag{2.18}$$

where k is the yield stress in pure shear. I will assume that a state of plane strain exists and that Poisson's ratio is 0.3. Level lines of the normalised deviatoric invariant $\frac{\sqrt{J_2}}{K_N\sqrt{d}}$ may easily be found in the $(\hat{t},\hat{y})$ plane, and the only independent parameter is the coefficient of friction, f. Figures 2.2(a-b) gives contours of $\frac{\sqrt{J_2}}{K_N\sqrt{d}}$ for $f = 0.8$ and 0.6.

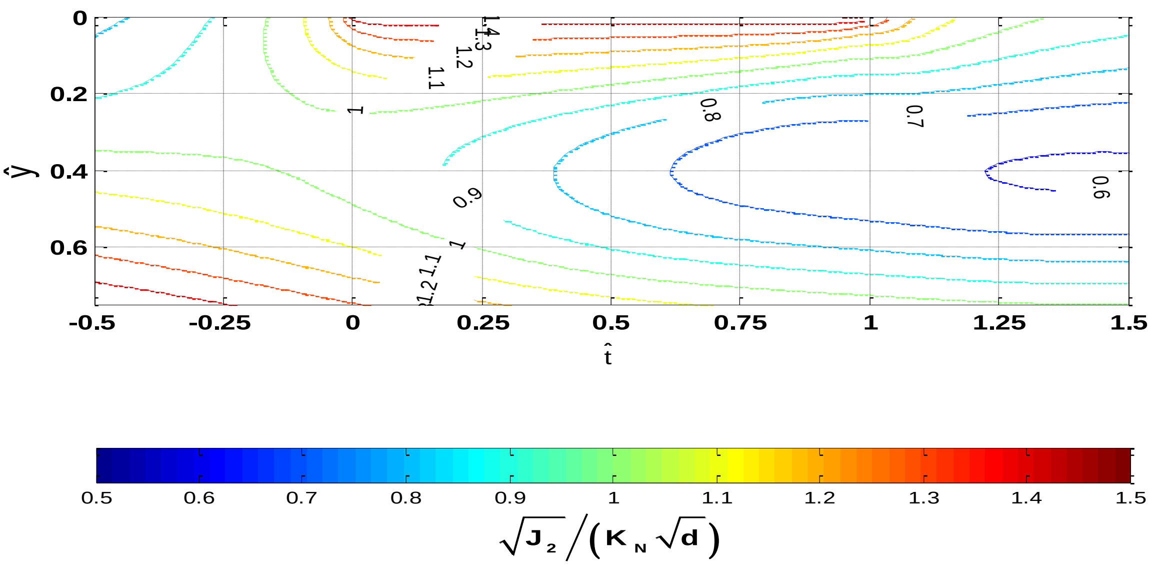

Figure 2.2(a): Contours of the normalised deviatoric invariant, $\left(\frac{\sqrt{J_2}}{K_N\sqrt{d}}\right)$, for f = 0.8.

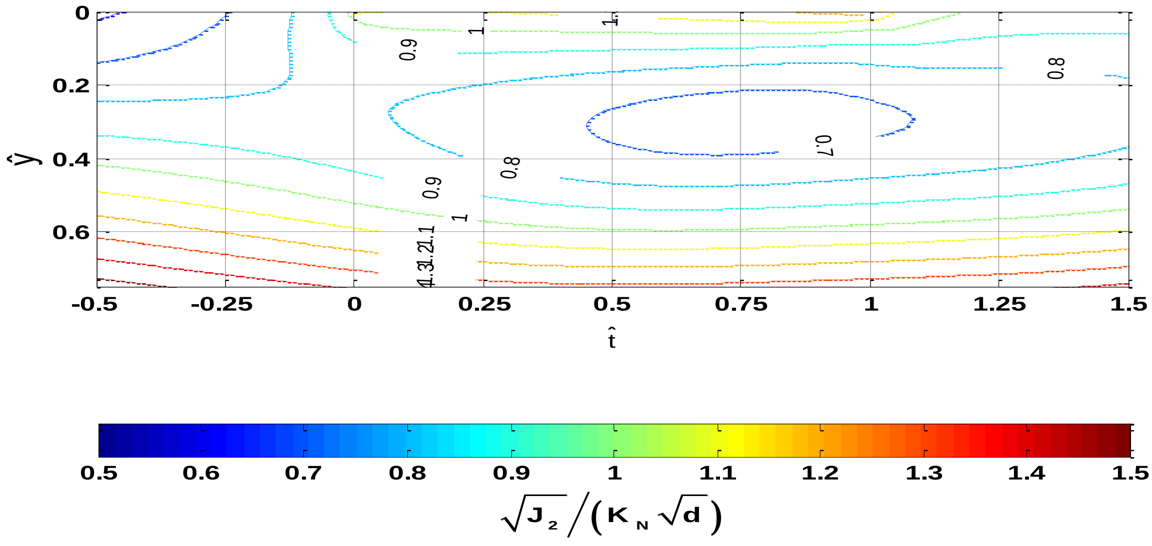

Figure 2.2(b): Contours of the normalised deviatoric invariant, $\left(\dfrac{\sqrt{J_2}}{K_N\sqrt{d}}\right)$, for f = 0.6.

One particular noteworthy result is that the normalised deviatoric invariant (and therefore yield parameter) at the surface is very nearly constant across the slip region, as shown in more detail in Figure 2.3, for a sensible range of coefficients of friction. By replacing $\sqrt{J_2}$ by $\sqrt{3k}$ and inverting, these contours represent an estimate of the location of the plastic front, for particular values of $\dfrac{K_N\sqrt{d}}{k}$, again for various values of the coefficient of friction. Note that it is expected the severest state of stress to lie at the contact trailing edge only if the coefficient of friction exceeds a certain critical value. For a Hertzian contact this is about 0.26. In most fretting fatigue experiments, although the initial coefficient of friction may be relatively low, at about this threshold value, it invariably quickly rises and is usually about 0.5-0.7, (well above the value where the severest state of stress migrates to the surface), in the steady state.

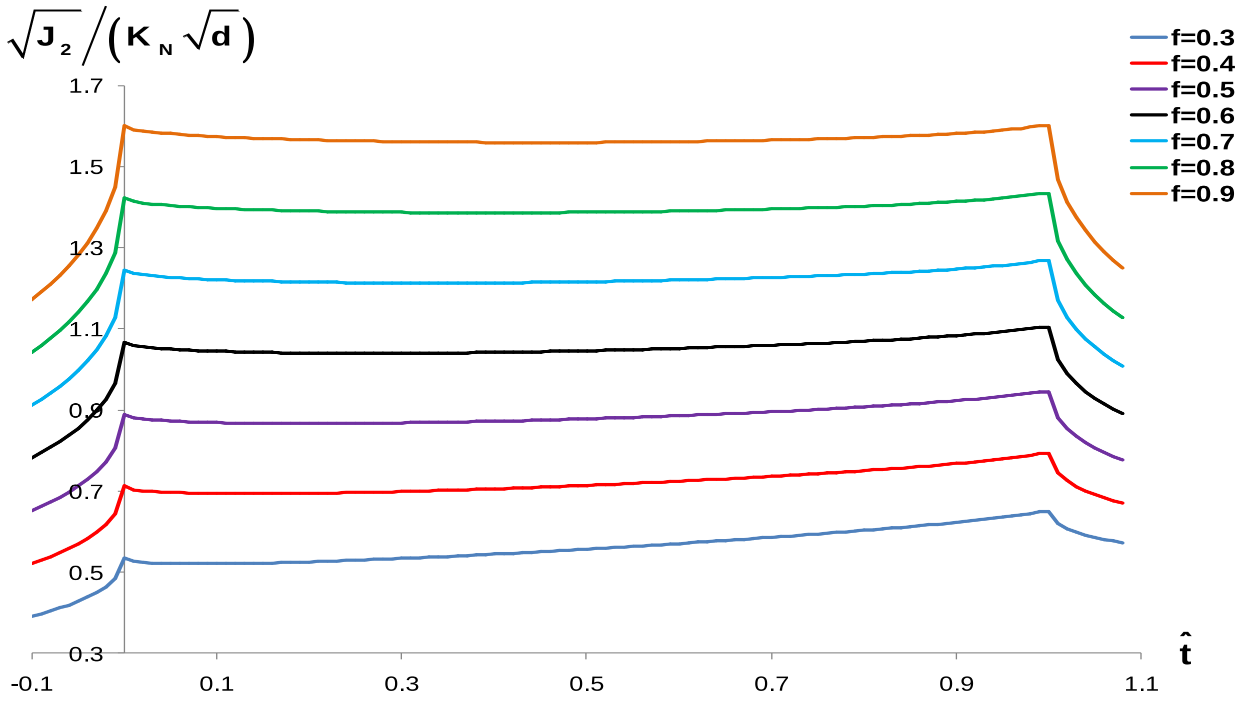

Figure 2.3: Normalised deviatoric invariant, $\left(\dfrac{\sqrt{J_2}}{K_N\sqrt{d}}\right)$, at the contact surface for a range of coefficients of friction.

This means that the value of the load at which the contact starts to go plastic(elastic limit) is only very slightly less than that at which the whole slip region yields. This would be the case at least for moderate and large values of the coefficient of friction as shown in Figure 2.4. It would follow that, if the load was sufficiently severe to cause local yielding the plastic region would almost certainly envelop the slipping region. The contact edge would then experience a strain field controlled by a square root singular mode II asymptote. Hence it would be quite similar to a mode II loaded crack in nature. Figure 2.4 includes 'spots' which show where various sets of experiments conducted lie with respect to the yielding condition, and these will be discussed in detail in section 2.5.

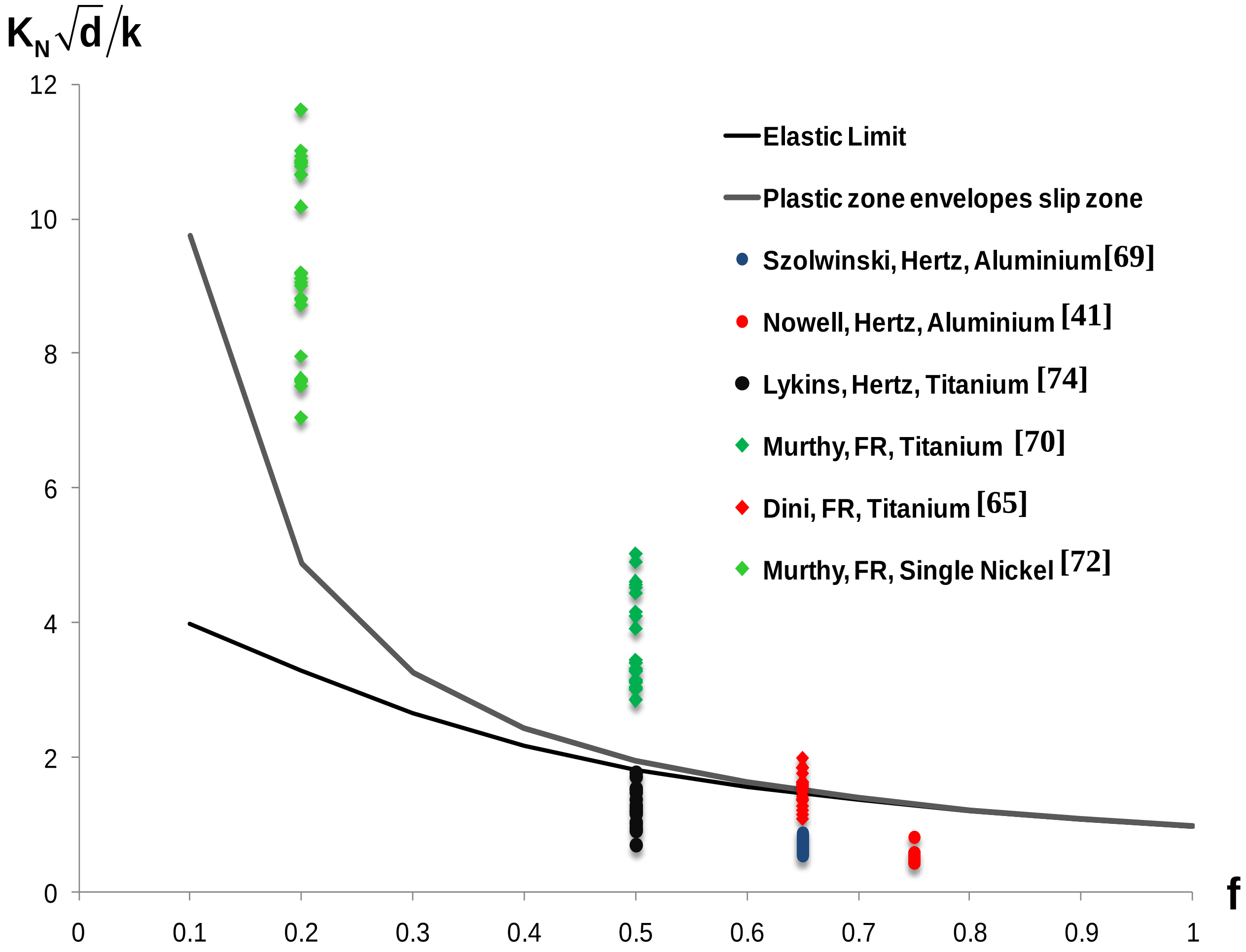

Figure 2.4: $\frac{K_N\sqrt{d}}{k}$ **vs. f map showing the elastic limit and the threshold at which the whole slip region yields. Data points represent the experimental tests in [41, 65, 69 , 70, 72, 74].**

I turn now to the fitting of the asymptotic (near-edge) solutions described to particular example geometries. For the shear traction this is geometry independent, and can be written as

$$\frac{K_T^Q}{k} = \frac{Q}{2ak}\frac{\sqrt{2a}}{\pi} + \frac{\sigma_o}{k}\sqrt{\frac{a}{32}}, \tag{2.19}$$

and, for the particular case of a Hertzian contact, the calibration for the contact pressure solution is given by

$$\frac{K_N}{k} = \frac{p_o}{k}\sqrt{\frac{2}{a}} = \frac{P}{\pi\, a\, k}\sqrt{\frac{8}{a}}\,. \tag{2.20}$$

These values were employed in determining the locations of the ‘spots’ included in Figure 2.4, together with a calibration for a ‘flat and rounded edge contact’ (denoted FR in the figure), which is rather more complicated in form and described in Appendix A. I now set out the three candidate quantities for correlating fatigue crack nucleation under incomplete contacts. However, before doing that the sources of the experimental data analysed in this chapter will be listed.

2.5 Experimental data

The correlations to be presented have used all the known publicly available experimental results for fretting fatigue strength. These available data are the fretting fatigue strength of an aluminium and titanium alloy [69, 70] and single crystals of nickel [72]. This supplements data from Oxford Solid Mechanics Laboratory on aluminium alloy HE15TF found by Nowell [41] and Titanium-6Al-4V [65], and some data obtained by the U.S. Air Force Research Laboratory at Wright Patterson [73, 74]. Although many data sets are obtained using the classical Hertzian configuration, part of the database comprises data from experiments performed using 'flat and rounded' pads. Independently measured material properties such as stiffness, plain fatigue strength and thresholds will be assumed for these materials and those used in the subsequent analysis are reported in Table 2.1, where ΔK_{th} is the threshold stress intensity factor and σ_{fl} is the fatigue limit.

Material	**Young's Modulus E [GPa]**	**Poisson's ratio, v**	**ΔK_{th} [MPa.m$^{1/2}$]**	**σ_{fl} [MPa]**	**k [MPa]**	**f**	**Refs.**
Al alloys	74	0.3	2.1	124	270	0.65-0.75	[41, 69]
Ti6Al4V	115	0.3	4.5	500	550-650	0.5-0.65	[65, 70, 71, 73 74]
Nickel	200	0.31	7.9	450-500	600	0.2	[72, 75, 76]

Table 2.1: Material properties obtained from [41, 65, 69, 70, 71, 72, 73, 74, 75, 76] for the analysed database of fretting fatigue experiments.

Figure 2.4 displays the normalised magnitude of the load employed in the sets of tests just cited. The plot includes two contours derived from the calculation described earlier to find the load at the onset of plasticity which is the elastic limit. The other contour is the load at which the plastic region envelops the slip zone. As stated, the difference between these loads is significant only at small values of the coefficient of friction. One of the features of many tests which surprised us is that, in many cases, the loads employed were relatively high. In particular, many of Murthy's tests were conducted at loads well above those where some plasticity might be anticipated. This implies any process zone involved in these experiments is likely to be large. I have therefore not included Murthy's results (and some other highly loaded cases) in our subsequent analysis. This is because it would not be reasonable to expect that a solution procedure which hinges on the process zone being small compared with the domain of validity of the asymptote to display the sequence of nesting required in these cases. I now describe three possible quantities each of which may be a candidate for controlling the nucleation of fretting fatigue cracks.

2.5.1 Classical stress-controlled fatigue

Let consider the first correlator which is the simplest way to portray fatigue data by using the classical 'S-N' approach first developed by Wöhler [77] about 130 years ago. This works well in plain fatigue and has been successfully applied as a design tool in its original form by many engineers to solve problems characterised by weak or no size effects and in the absence of large stress gradients. Here, I interpret 'S' as the stress at the trailing edge of the contact, and, within the context of the asymptote, note that $\sigma_{xx}(0,0) = \sqrt{2\, fK_N K_T}$. Figures 2.5(a-c) show plots of the fatigue life correlated in this way. It can be seen that there is a very considerable spread of results, because all size information is absent from this analysis, and this is known to be of great importance. A more detailed commentary on the quality of correlation will be provided later.

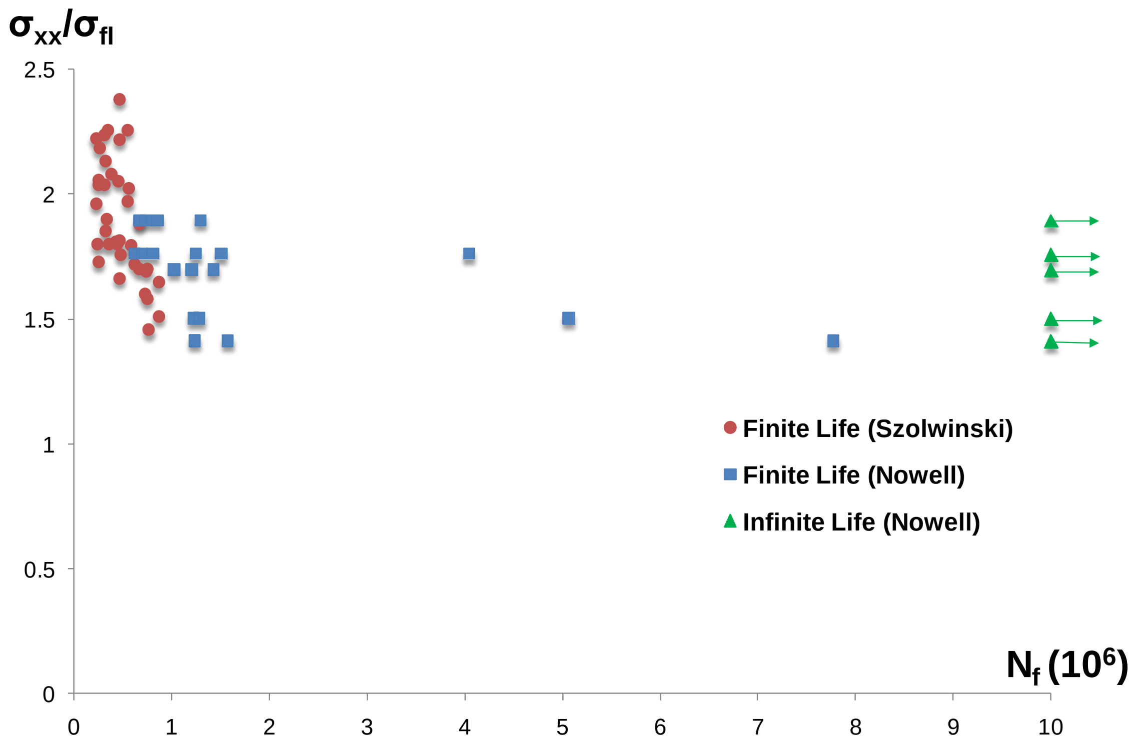

Figure 2.5(a): S-N approach for the experimental results from Nowell [41] and Szolwinski [69].

Figure 2.5(b): S-N approach for the experimental results from Lykins [74].

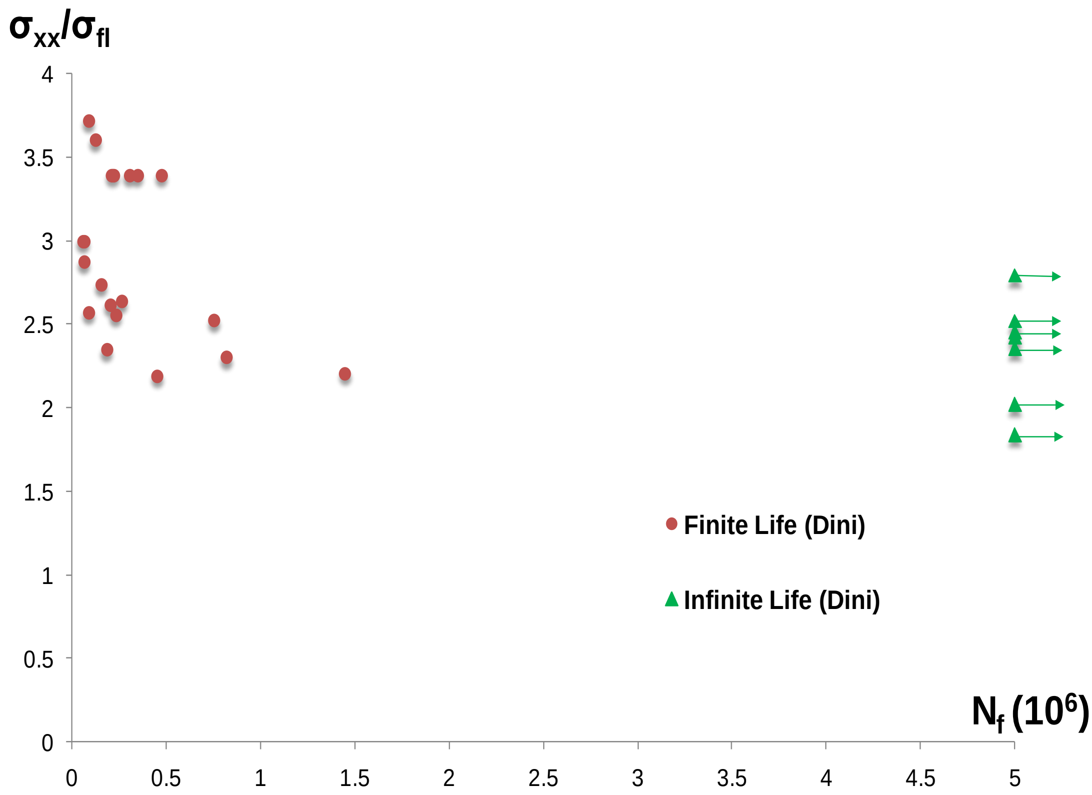

Figure 2.5(c): S-N approach for the experimental results from Dini [65].

One simple way of using essentially the same information but incorporating a simple length scale is to use the 'go-no-go' criterion for crack nucleation developed by Kitagawa and Takahashi [78]. This length scale is derived from intrinsic material properties which are the threshold stress intensity and fatigue limit. It provides a means of predicting whether a very short crack will develop and eventually propagate (see red curve in Figure 2.6). The original paper should be consulted for details, but the essential idea is that nucleation is assumed to end when the embryonic 'crack' reaches a critical length a_o and, therefore, short crack arrest takes place if ΔK_I trajectory as a function of the crack length falls below the threshold (see shaded area in Figure 2.6). It has been applied to fretting fatigue problems by others working in the field [79 - 81] but principally in the context of a Cattaneo-Mindlin contact. The first step in implementing within the asymptote is to determine the crack-tip stress intensity factor for a crack, of depth c, normal to the surface, and which I will assume is initiated at the contact edge, Figure 2.1. Most cracks are observed to start either precisely at the edge of the contact, or slightly within the slip zone. Also, cracks may start in 'Stage I', and therefore be angled [44].

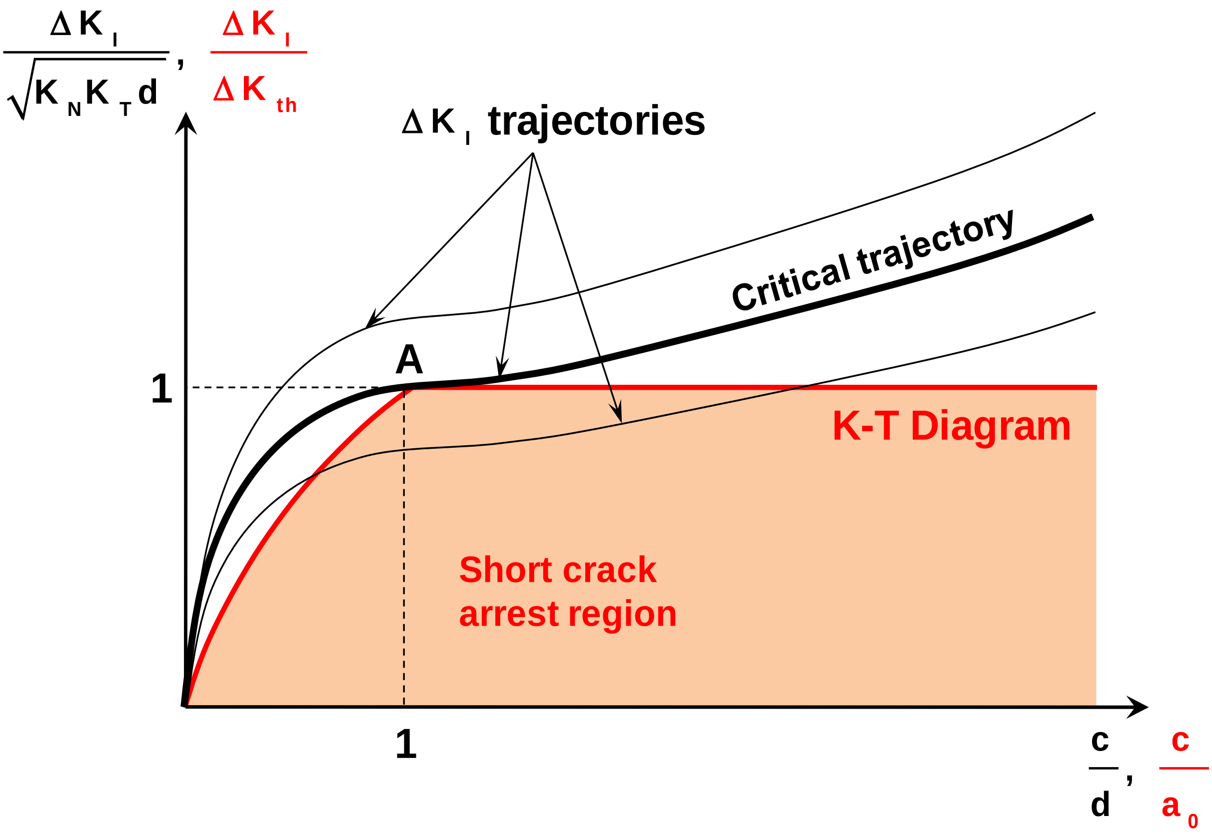

Figure 2.6: Schematic of the K-T diagram and description of the normalised ΔK_I trajectories as a function of the normalised crack length.

However, in order to reduce the number of independent variables, I will assume that the crack grows normal to the free surface. The crack tip stress intensity factor may be found using the distributed dislocation method [82, 83]. Note that, instead of using a description of the stress field appropriate to finite contacts, I shall assume that the critical distance is comparable with the slip region length, ($d \sim a_0$). Therefore the surface tractions driving nucleation are adequately described by the asymptotic form. This restricts the cases which may be covered. However, it also means that the results obtained are universal in nature which may then be applied to any incomplete contact. It also means that the solution is dependent on the coefficient of friction, f and the ratio $\frac{c}{d}$ only. Typical results of the trajectories describing the evolution of $\frac{\Delta K_I}{\sqrt{K_N K_T d}}$ with normalised crack length are displayed in Figure 2.6 (black curves). Note that the K_T corresponds to the equivalent stress intensity in shear calculated at the end of the loading cycle, and therefore, $\Delta K_T = 2K_T$ for fully reversing loading cycle $\left(R = \frac{K_T^{\min}}{K_T^{\max}} = -1 \right)$. Things would be different if the load ratio were less than $R = -1$ and an extra variable would need to be considered to account for the lack of symmetry of the loading history. However, detailed calculations show that there is only weak dependence on the evolution of the threshold trajectories with R .

I am now in a position to determine the boundary between long crack propagation and short crack arrest (which is considered to be safe in terms of design against fretting failures). In the K-T procedure, the critical length a_o is the point at which the threshold stress intensity, ΔK_{th}, is achieved when the driving stress is given by the fatigue limit, σ_{fl}, i.e.

$$\Delta K_{th} = \sigma_{fl} \sqrt{\pi a_o}. \tag{2.21}$$

Looking at the critical trajectory in Figure 2.6, the boundary between long crack propagation and crack self-arrest is achieved when the trajectory passes through point A. I therefore set $\Delta K_I = \Delta K_{th}$, and $c = a_o$ and, after some manipulation, I obtain the fatigue threshold implied by the application of the K-T procedure using the asymptotic description. This is shown in Figure 2.7 for different values of the coefficient of friction, which becomes the only variable governing the curves in $\frac{\Delta K_T}{\Delta K_{th}}$ vs $\frac{\Delta K_{th} K_N}{\pi \sigma_{fl}^2}$ space. These are valid for *any* incomplete contact whose stress and displacement fields can be captured by the asymptotic description proposed.

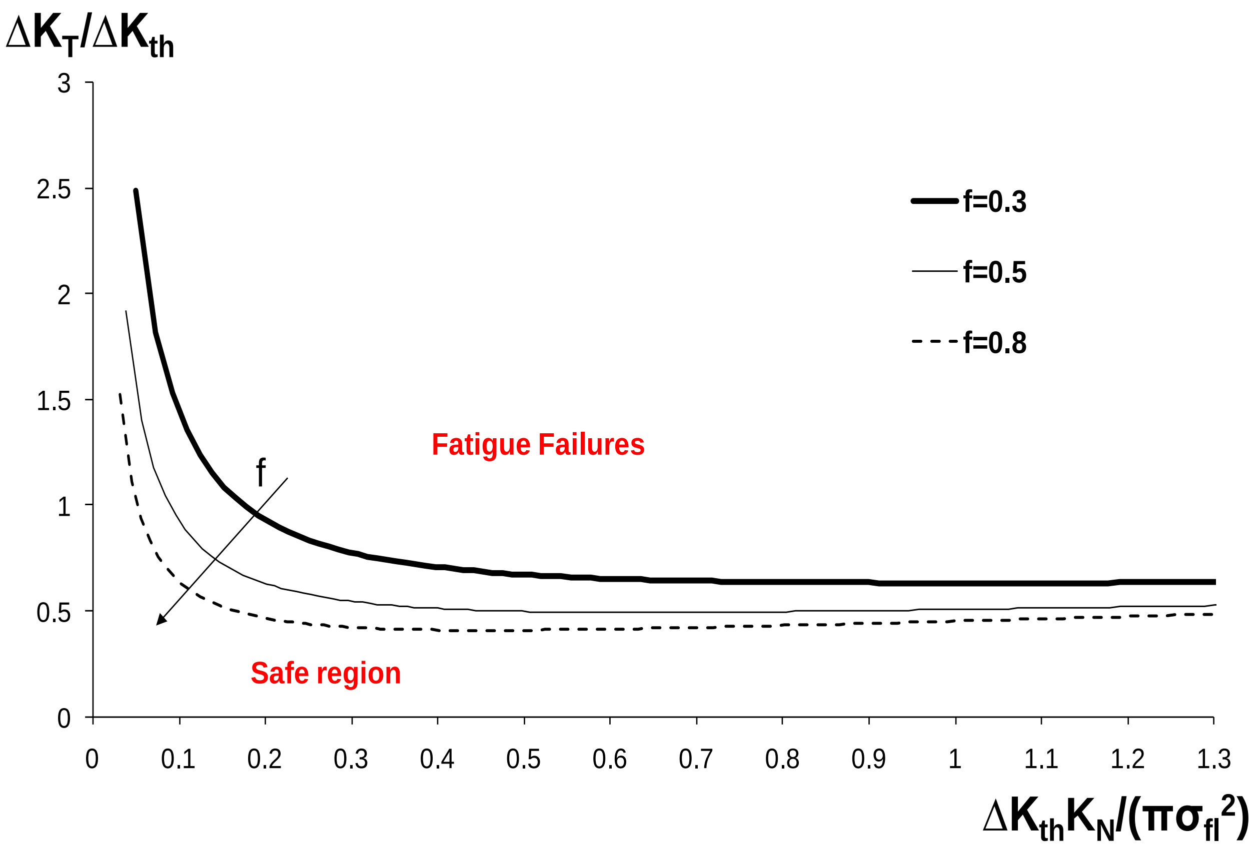

Figure 2.7: Fretting fatigue threshold implied by the application of the K-T procedure using the asymptotic description for three example values of coefficient of friction, *f* = 0.3, 0.5, 0.8

The thresholds have been re-plotted in Figures 2.8(a-c) using the friction values for the experimental data reported in Table 2.1. The graphs now include 'spots' which show the condition present in the various experiments being used. Note that a triangle is used when the specimen did not fail and circle and squares when failure occurred before 10^6 cycles. It may be seen that the short crack growth procedure satisfactorily predicts this boundary, but this is not surprising as the same result was found for the Cattaneo-Mindlin problem for both fully reversing loads [79] and arbitrary load ratios [65]. The advantage of the current form of the solution is that Figure 2.7 is completely general and may be applied to any geometry. In fact, some of the experiments here employed the 'flat and rounded' type of pad, and these have been satisfactorily correlated with the Hertz case.

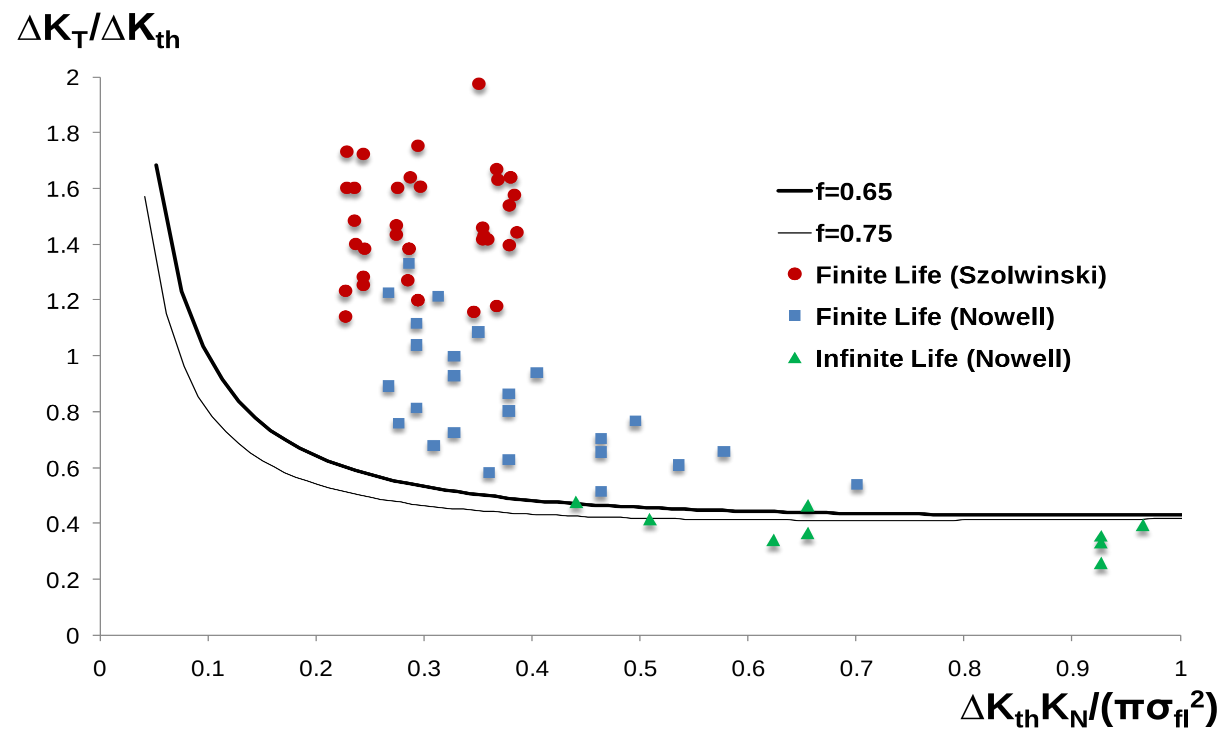

Figure 2.8(a): Fretting fatigue thresholds implied by the application of the K-T for the aluminium alloys used in [41], [69] and the friction coefficients measured by Szolwinski and Nowell. Data points represent the experimental tests in [41], [69].

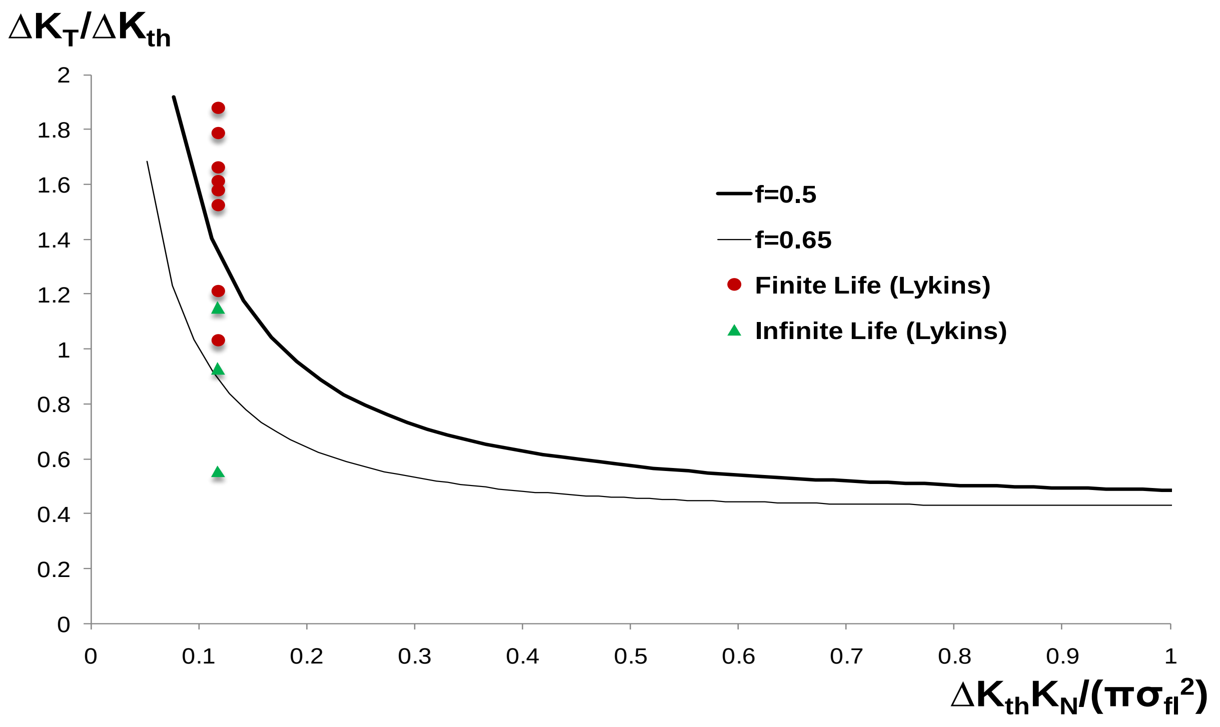

Figure 2.8(b): Fretting fatigue thresholds implied by the application of the K-T for Ti6Al4V and the friction coefficients measured by Lykins [74]. Data points represent the experimental tests in [74].

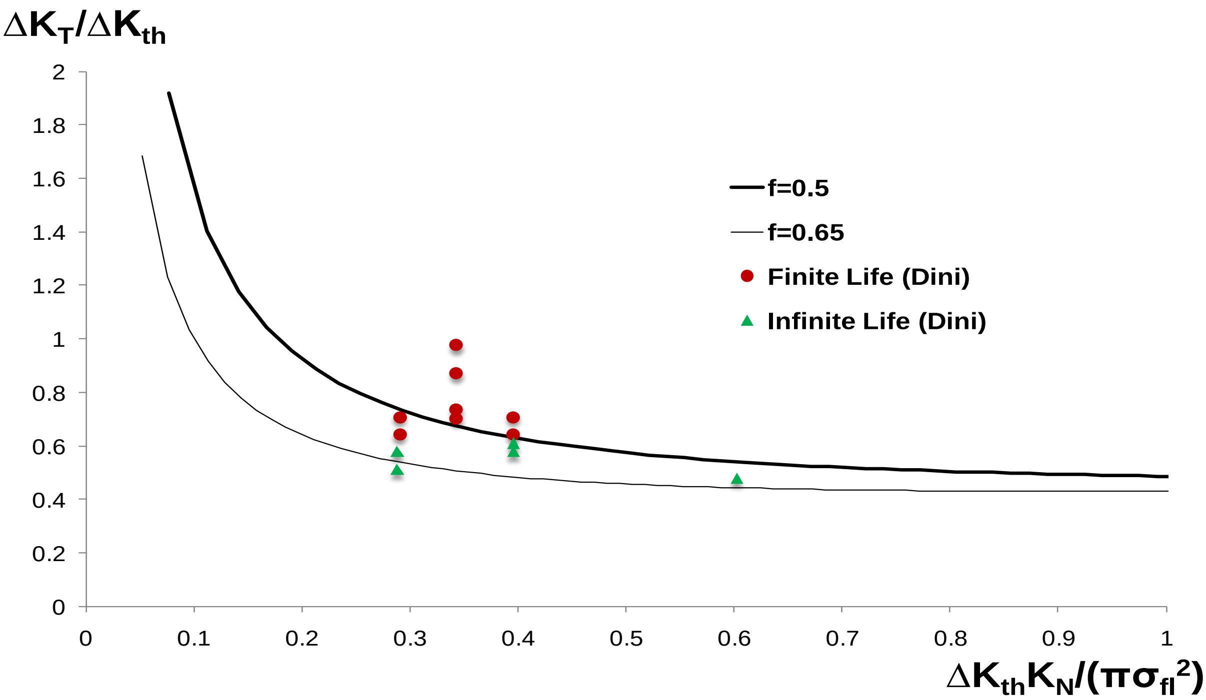

Figure 2.8(c): Fretting fatigue thresholds implied by the application of the K-T for Ti6Al4V and the friction coefficients measured by Dini [65] . Data points represent the experimental tests in [65].

2.5.2 Threshold based on a mode II crack-tip field

The form of the results displayed above clearly shows the inadequacy of the state of stress alone as a predictor of the fretting fatigue performance. The hybrid K-T method satisfactorily gives the finite/infinite life boundary. However, it does not allow us to predict accurately the component life when it is finite (unless something is assumed about finite thresholds or they are experimentally determined). This observation was one of the principal prompts for developing the asymptotic forms, which include size (or equivalently, stress-gradient) information. Both the normal and shear tractions have an influence on the local state of stress, but the contact pressure contribution is (a) constant in time and (b) has a negligible influence at the contact edge itself. The shear traction, on the other hand, reverses in sign and has an influence even at the contact edge. The form of the traction distribution depends also on both f and K_N, unless the process zone is so large that it envelops the entire slip region, and I know that this is not, in some of the experiments conducted, so. It is therefore an approximation to suggest that the range of stresses experienced at the contact edge is controlled by the range of K_T. However, it is worthwhile at least to consider ΔK_T as a possible correlator of fatigue lives, and it is expected this approximation to be best when the process zone is relatively large. This is because the process zone will exceed the slip region in extent but not excessively large so that small scale yielding conditions are not satisfied. Figures 2.9 (a-c) life correlations based on ΔK_T are shown, for different materials and with all the data I have available. The characteristic curves clearly shows a lot less spread than using the stress range and the runout condition is also properly portrayed. The original definition of K_T was for an adhered contact, so that the contact edge displays an implied square root singularity in stress. This is of the same orders as the crack tip stress field, and with a similar local field. It follows that the stress field at the contact edge, under conditions of near adhesion, are very similar to those at the tip of a crack subjected to mode II loading. It follows that threshold for growth of a mode II crack might actually apply to nucleation conditions at the contact edge, and this is now explored. In Figures 2.9(a-c), I have also included a line showing the mode II crack threshold, estimated as $\Delta K_{II}^{th} = 0.8 \times \Delta K_{I}^{th}$ [84, 85]. Note that this value is not universal but it helps by providing direct comparison between the threshold identified using ΔK_T as a correlator for fretting fatigue lives and more conventional mode II crack thresholds for plain fatigue. The aim of this comparison is to check if ΔK_{th} can be used as a threshold for ΔK_T and this would enable design against fretting to be obtained using only plain fatigue data. One of the difficulties I have had in carrying out these correlations is in ensuring that the basic materials data I have used is correct. In many cases I could not find the precise values I needed for a particular material in the open literature. One of the biggest problems is in obtaining a threshold (plain) fatigue crack stress intensity which has been measured at the same R-ratio as that present in the fretting test.

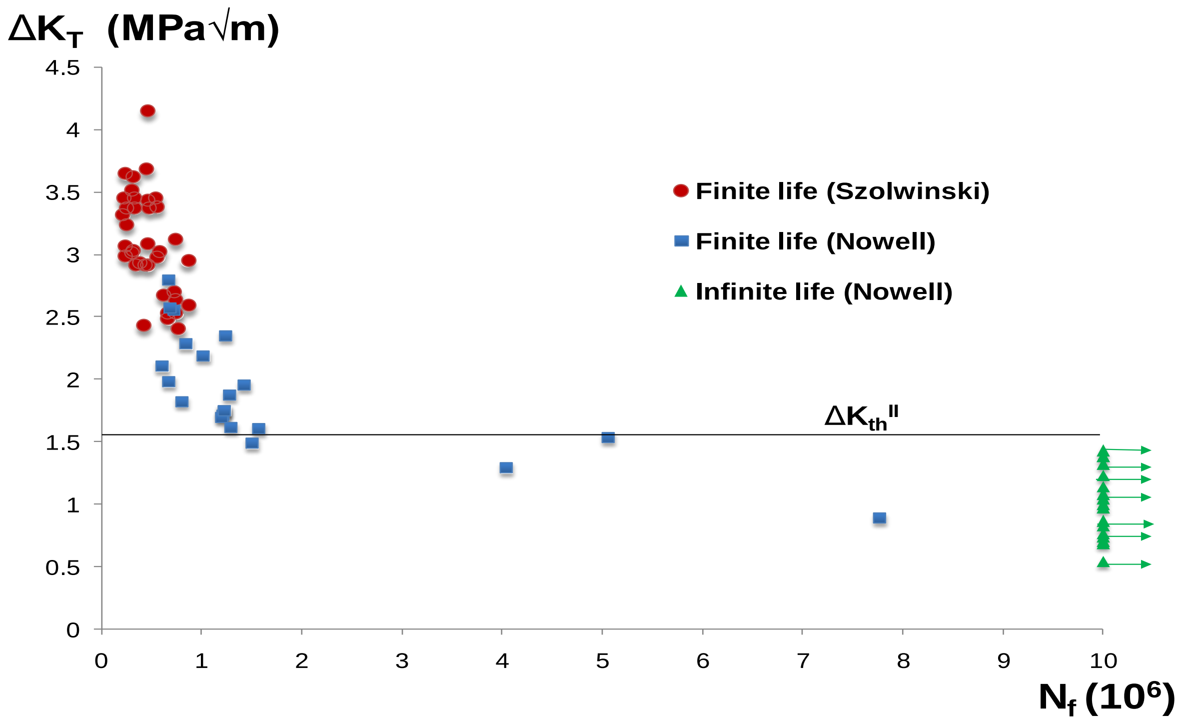

Figure 2.9(a): Life correlation based on ΔK_T for the tests reported in [41, 69].

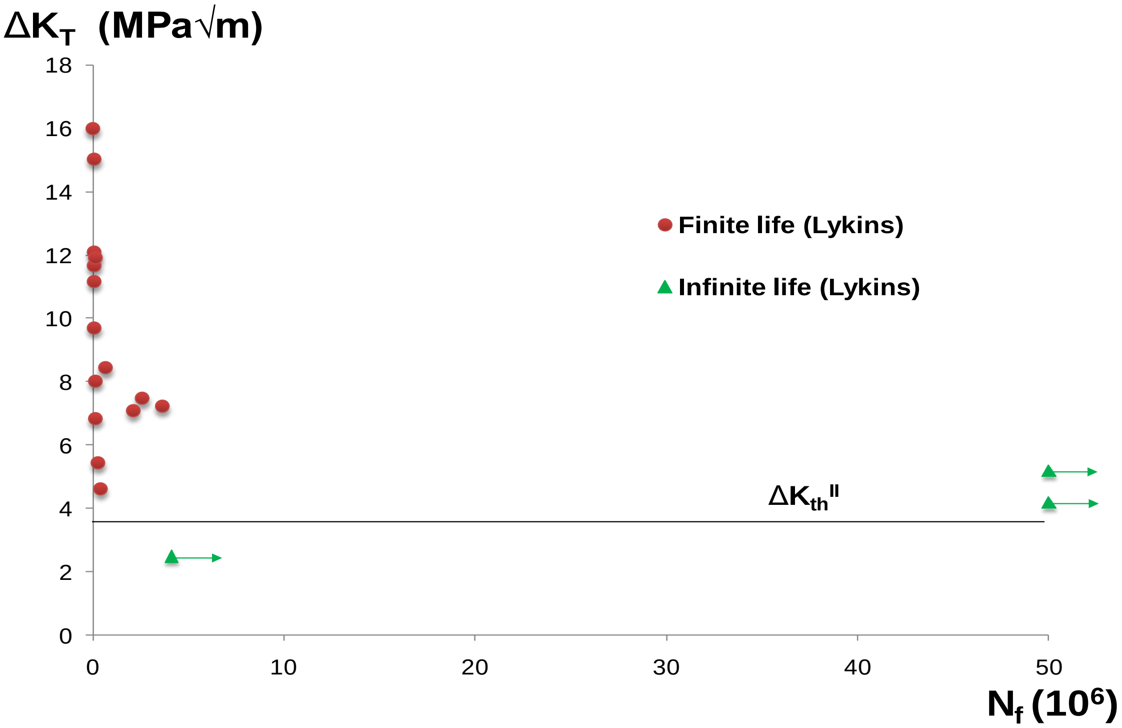

Figure 2.9(b): Life correlation based on ΔK_T for the tests reported in [74].

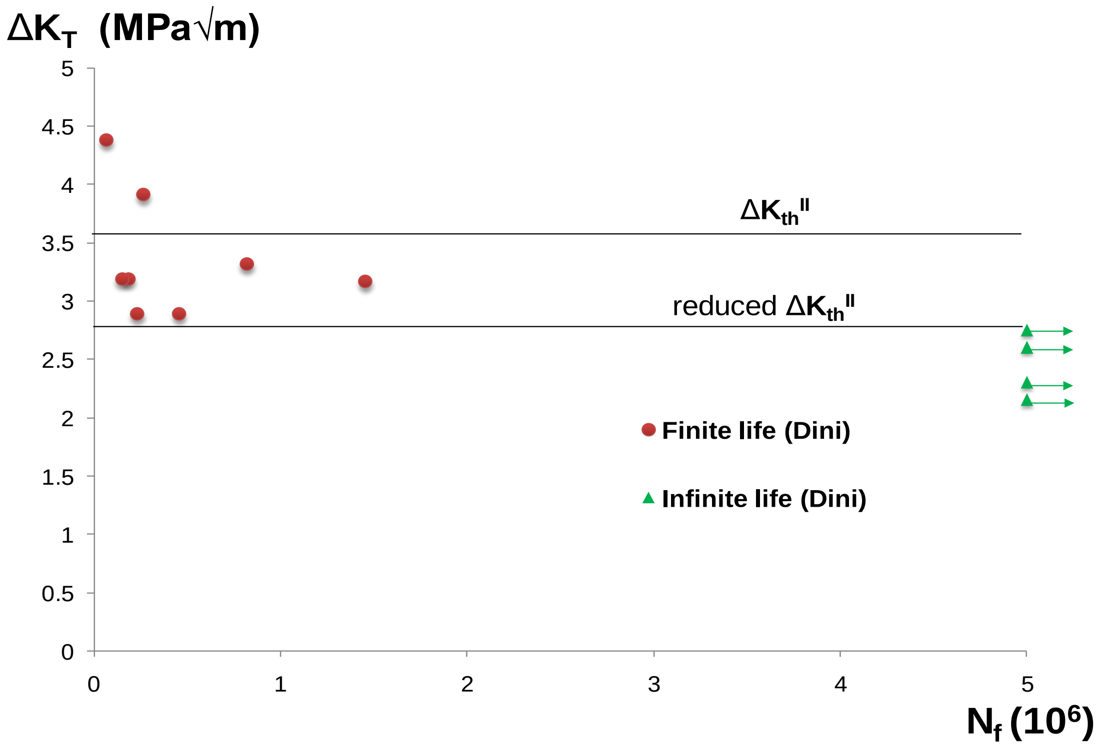

Figure 2.9(c): Life correlation based on ΔK_T for the tests reported in [65].

For example, the experimental results reported in Dini [65] have been performed using an initial tensile bulk stress that offsets the equivalent load ratio to R=0.5-0.6. The R-ratio at which the threshold was measured quoted in the Table 2.1 was -1, and this suggests that a reduced $\Delta K_{\mathrm{II}}^{th}$ should be applied to Dini's results. This is displayed in Figure 2.9(c) as a 'reduced ΔK_{II}^{th}'.

2.5.3 *Frictional energy expenditure density*

The imperfection of the above correlation is that the influence of both f and K_N were ignored. In the experiments the contact pressure, and hence K_N were kept constant, so that they relate to a static stress field, and hence one which does not, in itself, produce damage. This is because the asymptote was developed under conditions of, as a first estimate, full adhesion. This is a necessary step so that the effects of a shearing force and bulk tension can be consistently treated. Therefore the coefficient of friction might be regarded as a further parameter unless the process zone bridged the slip region. Note that a process zone in a monolithic material and an equivalent zone bridging a slipping interface differ in that there is a line (the interface) along which frictional as well as plastic slip may occur. An alternative quantity which might sensibly be used to correlate nucleation life is the magnitude of the density of irreversible frictional energy expended within the slip region. Note that this is a pointwise quantity and has a maximum value towards the centre of the slip region [86]. For a monotonically increasing shearing force (and hence K_T), the maximum frictional energy expended per unit area at steady-state can be expressed as

$$W = c\frac{K_T^{\max 2}}{K_N\sqrt{d}} = c\frac{K_T^{\max 2}}{K_N}\sqrt{\frac{2K_T}{fK_N}} = c'\frac{K_T^{\max\frac{5}{2}}}{fK_N^{\frac{3}{2}}}, \quad (2.22)$$

and c' can be found by performing the following integration $W = \int_{cycle} q(s, t_{cycle}) d\delta(s, t_{cycle})$

where δ is the slip displacement at every point in space, s, and time, t_{cycle}, during the loading cycle. Analytical or numerical integration can also be performed to obtain the evolution of the slip displacements during the entire cycle for different loading scenarios. This allows closed form analytical or equivalent numerical solutions to be determined for all experimental cases. Therefore I have extended the range of the previous solution, and now give the calibration constant, c', for all conditions. Plots of correlated lives using this quantity are shown in Figures 2.10(a-c).

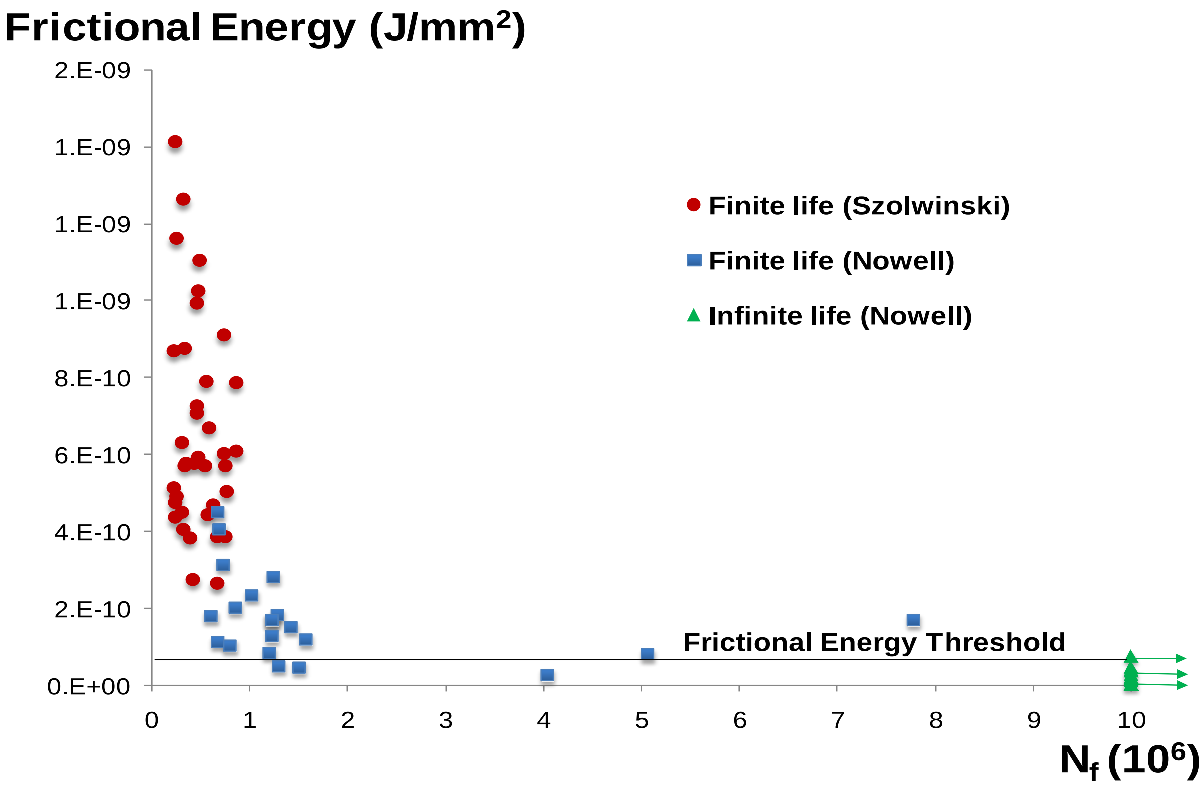

Figure 2.10(a): Life correlation based on frictional energy expenditure for the tests in [41] ,[69].

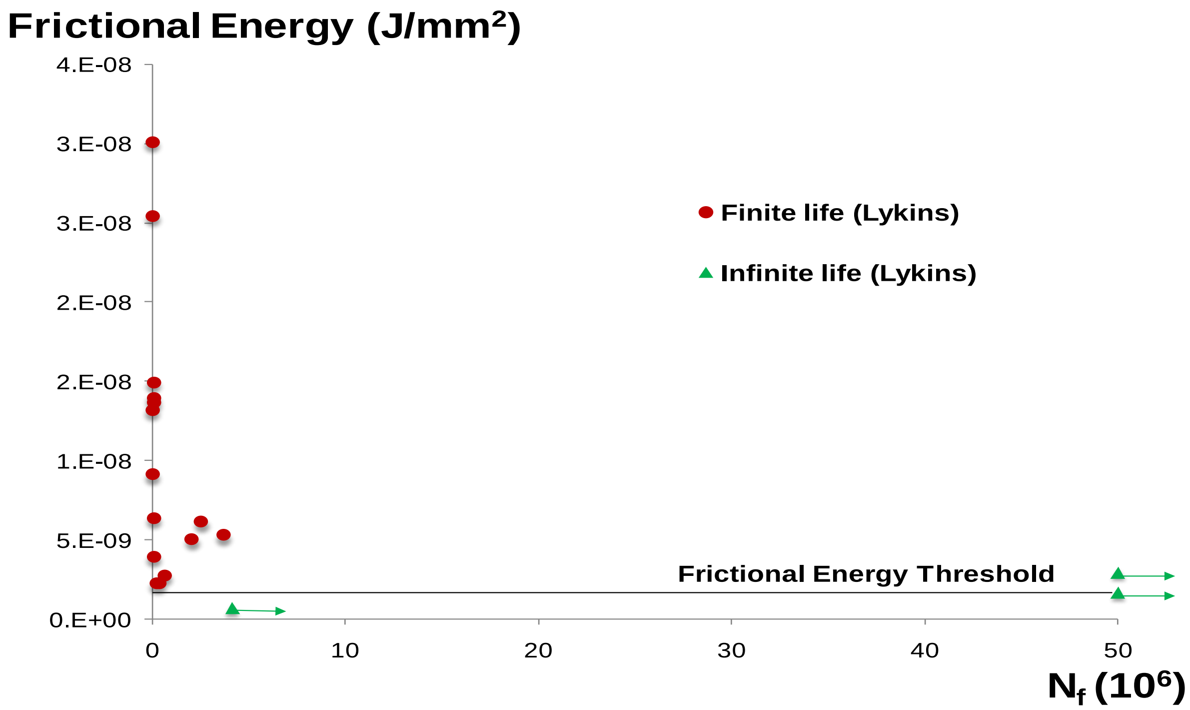

Figure 2.10(b): Life correlation based on frictional energy expenditure for the tests reported in [74].

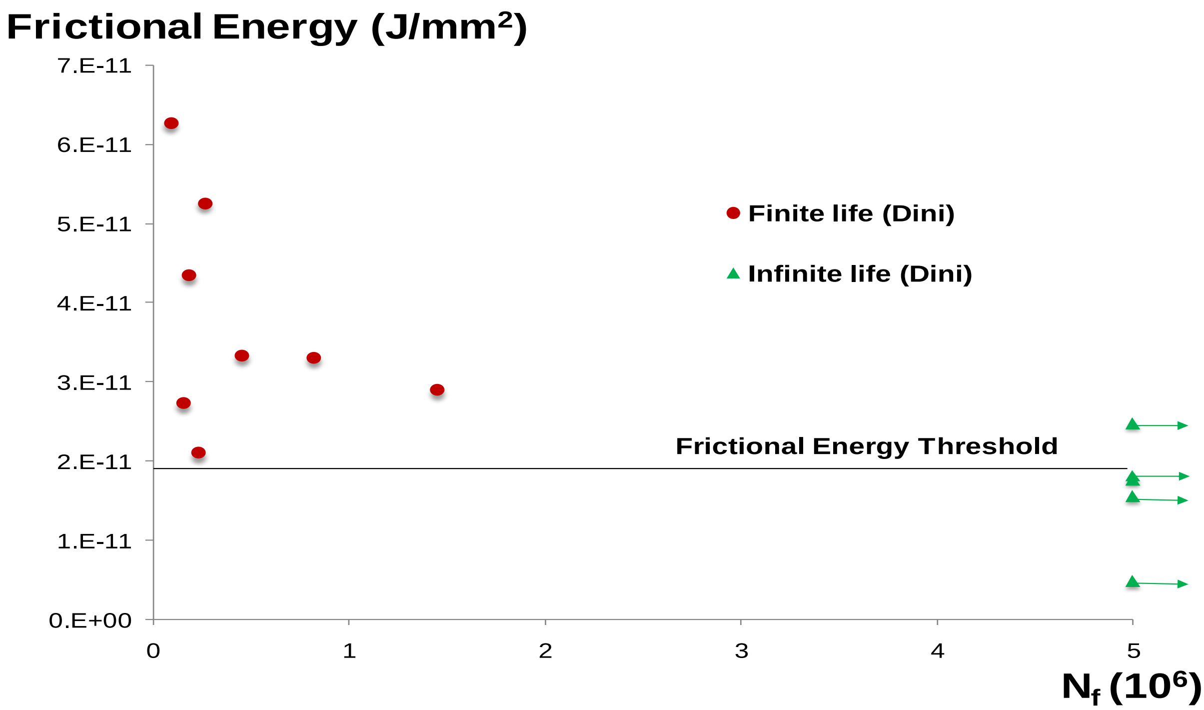

Figure 2.10(c): Life correlation based on frictional energy expenditure for the tests reported in [65].

The results of this correlation differ in character from those earlier. This is because in each of the other possible criteria there is some threshold information obtained by *independent* experiment - σ_{fl} for the S-N curve, σ_{fl} and ΔK_{th} for the K-T procedure, and ΔK_{th} alone for the 'mode II crack' method. However, I have no pre-existing materials data available in this correlation. I am therefore free to choose the threshold condition for infinite life, and, have inserted what seems to be the best choice in Figure 2.10 (a) for the aluminium alloy, (b) for the titanium alloy cylindrical pads and (c) for the titanium alloy flat and rounded ends pads. In each case, the tests are correctly ranked with little spread and few outliers; and, the cut-off threshold is very distinct. However, it is unexpected that the two sets of tests on titanium seem to give different thresholds. One possible explanation for this is that the length scale inherent in the asymptote does not, here, figure in the final quantity being employed which is the maximum frictional energy expenditure per unit area as it arises only at a spot. All information concerning size effects is, in this sense, lost again here. However, if the calculation is extended to find the total frictional energy dissipated per loading cycle which contains information about the extent of slip and therefore includes the asymptotic length scale, the results show the same trends seen in Figure 2.10. It is argued that, although larger values of energy dissipation at the contact interface might help promote crack nucleation [59], the frictional energy expenditure is in reality more directly linked to the tendency of the surfaces to wear [87] rather than to initiation of the fatigue process. For the cases analysed here, which are characterised by very low fretting wear, seem to be controlled by the stress and strain fields in the proximity of the contact edge where the tractions are appropriately represented by the asymptotic forms. It is envisaged that the frictional energy dissipation density will provide a good correlator for fretting wear tests as already suggested by others working in the field (see e.g. [87]). The asymptotic approach proposed in this chapter provides a rapid tool to characterise this in closed form.

2.6 Conclusion

The detailed nature of the local stress field of the contact edge for incomplete contacts which can be described by half-plane theory has been considered, together with its influence on crack nucleation life under fretting conditions. I have taken as our starting point the work on asymptotic representations of the local field already discovered, and added further properties relevant to the nucleation process. These results have been used to form four potential correlators of fretting fatigue crack nucleation lives: the first is the one of stress range at the critical point. This is probably the most common choice based on classical S-N (Wöhler) principles. It is unsuitable because all size effect information is neglected. The K-T approach to determining the threshold for crack nucleation, and which bridges classical fatigue and fracture mechanics principles was also used, and this was shown satisfactorily to predict the boundary between finite and infinite life. This result is a generalisation of that already found for a Hertz contact, and provides, in the form displayed in Figure 2.7, a usable design tool for the avoidance of fretting failures.

Two further correlators of nucleation lives were then introduced, based solely on the multipliers of the asymptotic solutions. The first is simply an approximate correlation of the reversing stress field due to shear loading, and seems very satisfactorily to collapse the experimental data. It also captures size information inherent in the experimental contact very well. The second is based on the quantity controlling nucleation being the maximum density of irreversible frictional energy expenditure.

It is worth emphasizing that the procedures described involve no ‘fitting parameters’ or volume averages. In all cases, the possible controlling variable correlates at least reasonably well with the number of cycles to failure and provides some trend of varying quality. In the case of all but the energy correlation, there is also some pre-existing materials data with which the quantity may be compared and obtained from plain fatigue theory. This prompts the question ‘Does fretting exacerbate or ameliorate nucleation conditions compared with a plain problem?’ At first sight, it would seem that both the K-T and ΔK_T methods suggest that the effect is quite neutral. This might be due to the fact that most of the experimental results collated and used in the present contribution were designed to study partial slip fretting configurations. In partial slip, only a very limited amount of wear takes place and the fatigue phenomenon is almost entirely controlled by the stress concentration and the stress and strain gradients at the contact edges [88]. It also explains the partial success that conventional multiaxial fatigue approaches have met in predicting fretting lives in most of the work carried out by different groups around the world (see e.g. [72, 89-90]). A further characteristic of the asymptotic correlators used here is that, whereas the asymptotes used in the K-T and ΔK_T methods incorporate stress gradient or size information (particularly in the latter approach), they do not function in this way in the energy density approach. It should also be highlighted that since the accumulated frictional energy dissipated at the contact interface plays a fundamental role in assessing fretting wear damage, the closed form solutions developed in this chapter can be implemented to study the interplay between wear and fatigue damage. Therefore it can be used to develop predictive tools for scenarios where these two mechanisms cannot be decoupled and only semi-empirical parameters are available to provide an estimate of damage [59, 91] .

Finally, it should be pointed out that the asymptotic descriptions formulated can also potentially be incorporated in numerical tools (as super-elements in FEM or BEM formulations) and/or be used for fast assessment of fretting fatigue life using conventional multiaxial criteria. Furthermore, the asymptotic formulation could also be used as a starting point to incorporate other properties relevant to the nucleation process that have been neglected in the present contribution e.g. material microstructure and localised plasticity at individual grain level [92]. It is envisaged that by adding microstructure details [93] and considering plasticity and damage at microscale(see e.g. [94]) this would help shed light on important issues, such as microstructure sensitivity [95] and the importance of material inherent length scales.

3 The Use of Static Reduction in Finite Element Solution of Two-Dimensional Frictional Contact Problems

3.1 Introduction

The general objectives of a numerical contact modelling are usually to determine the contact areas, the force transmitted and the relative displacement along the interface of contacting bodies. Numerically, the contact is a severe form of nonlinearity. Finite element solutions to the frictional contact problems are generally constructed by linking the finite elements model of contacting bodies through contact problems and using either Penalty or Lagrangian method to handle the discontinuous nature of contact boundary conditions. These models are often rather large and this can be a barrier to achieving good accuracy, particularly in cyclic loading problems where one would like to run a sufficient number of cycles to reach a steady state, and it is inefficient when multiple load cases are to be analysed. Additionally, there is no certainty whether unexpected features of the solution, which can arise in certain cases, reflect real features of the underlying continuum problem or are simply the remains of the regularization inherent in the contact elements.

An alternative, namely 'the reduced stiffness method', is particularly attractive in the case of two-dimensional frictional contact problems. By using the equilibrium equations for the degrees of freedom at the non-contact nodes I reduce the problem to a contact problem defined on N nodes. These N nodes consist of the contact nodes and those where the external loads are applied. This procedure is known as static reduction or substructuring.

By doing this, the problem then becomes equivalent to a system of N massless rigid blocks connected by a general N × N stiffness matrix, with each block in frictional contact with a rigid surface. In this formulation, the evolutionary contact problem can be defined and solved without the necessity of contact elements, using iterative applications of the contact inequalities or linear complementarity methods. Also, the reduced stiffness matrix provides a convenient way of exploring the limit loading factor, such as the maximum amplitude of cyclic external loads below which the system is capable of shaking down.

The purpose of the work is first to develop a procedure where one can convert a conventional finite element model to a reduced model. This can then be used to solve a wide range of two-dimensional frictional problems in significantly less time using the evolutional algorithm which will also be developed. This will be very useful for the finite element problems with large size or in the case where a high number of periodic loading cycles need to be run to investigate the steady-state behaviour of the systems.

3.2 Single elastic body pressed against a rigid body

In explaining the procedure for extracting the reduced stiffness matrix from the full finite element stiffness matrix, $\mathbf{K}$, it is convenient to start with the simplest case where there is only a single elastic body that makes frictional contact with a rigid obstacle at a set of contact nodes. I shall find that the more general problem where two elastic bodies make contact with each other can be solved using a series of steps for the two bodies separately. I discretize the body using the finite element method and characterise the resulting nodes as belonging to one of the three complementary sets, the contact node S_C , the externally loaded nodes S_E , and the unloaded nodes S_I . For the most general case, the set S_E should be further partitioned into S_U , where non-zero nodal displacements are prescribed, and S_T , where non-zero nodal forces are prescribed, but in most practical problems one of these sets will be null. In other words, the problems can be defined either as force-control or displacement-control ones. In all cases, I shall denote the nodal displacement by $\boldsymbol{u}$ and the nodal force by $\boldsymbol{f}$ with appropriate subscripts and superscripts.

3.2.1 Sign convention

Since the problem is two-dimensional, the contact nodal force $\boldsymbol{f}_j^C$ will have two components which are denoted by

$$\boldsymbol{f}_j^C = \begin{Bmatrix} q_j \\ p_j \end{Bmatrix}, \tag{3.1}$$

where p_j is the force normal to the contact surface and is defined as positive when compressive, and q_j is the component tangential to the surface with the sign convention of Figure 3.1.

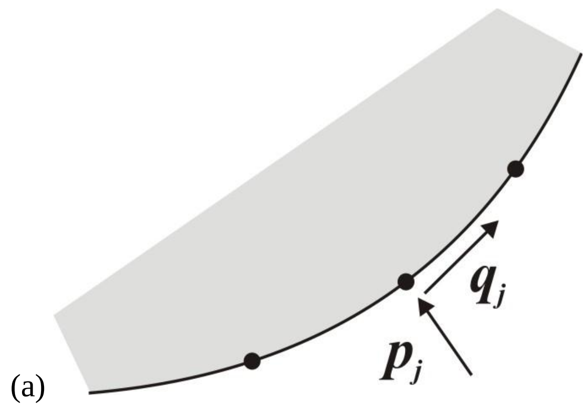

Figure 3.1: Sign convention for nodal forces.

The corresponding nodal displacements shown in Figure 3.2 are denoted by

$$\boldsymbol{u}_j^C = \begin{Bmatrix} v_j \\ w_j \end{Bmatrix}, \tag{3.2}$$

where w_j is normal to the contact surface and hence contributes to a positive gap, whilst v_j is a tangential (slip) displacement.

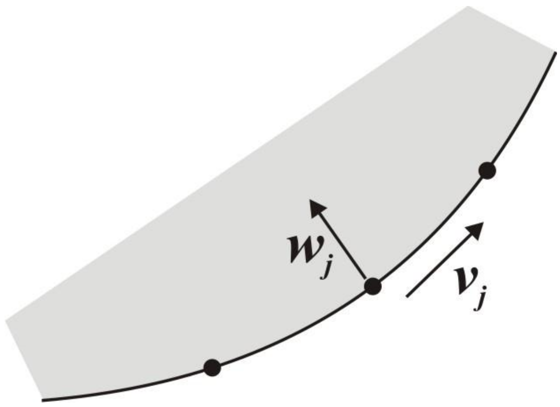

Figure 3.2(b): Sign convention for nodal displacements.

I then construct contact nodal force and nodal displacement vectors

$$\boldsymbol{f}^C = \left\{ \boldsymbol{f}_1^C, \boldsymbol{f}_2^C, \boldsymbol{f}_3^C, \ldots., \boldsymbol{f}_N^C \right\}^T ; \boldsymbol{u}^C = \left\{ \boldsymbol{u}_1^C, \boldsymbol{u}_2^C, \boldsymbol{u}_3^C, \ldots., \boldsymbol{u}_N^C \right\}^T, \tag{3.3}$$

where N is the number of contact nodes, and since the system is linear elastic, I can write

$$\boldsymbol{f}^C = \boldsymbol{f}^w + \mathbf{K}^C \boldsymbol{u}^C, \tag{3.4}$$

where $\mathbf{K}^C$ is a positive definite and symmetric *contact stiffness matrix* and $\boldsymbol{f}^w$ comprises the contact nodal forces that would be developed by the given external loading if the contact nodal displacements were all constrained to be zero $(\boldsymbol{u}^C = 0)$.

3.2.2 *Eliminating the displacements at the unloaded nodes*

Since S_C and S_E are sets of points on the boundary, whereas S_I includes all the nodes in the interior of the body (an area), most of the nodes will be in S_I and the dimensionality of the resulting matrices can be reduced by using the condition $\boldsymbol{f}^I = 0$ (zero nodal forces of the internal nodes) to eliminate these degrees of freedom. I first partition the full stiffness matrix such that

$$\boldsymbol{f} \equiv \begin{Bmatrix} \boldsymbol{f}^I \\ \boldsymbol{f}^E \\ \boldsymbol{f}^C \end{Bmatrix} = \mathbf{K}\boldsymbol{u} \equiv \begin{bmatrix} \mathbf{K}^{II} & \mathbf{K}^{IE} & \mathbf{K}^{IC} \\ \mathbf{K}^{EI} & \mathbf{K}^{EE} & \mathbf{K}^{EC} \\ \mathbf{K}^{CI} & \mathbf{K}^{CE} & \mathbf{K}^{CC} \end{bmatrix} \begin{Bmatrix} \boldsymbol{u}^I \\ \boldsymbol{u}^E \\ \boldsymbol{u}^C \end{Bmatrix}, \tag{3.5}$$

from which I conclude that

$$\boldsymbol{f}^I = \mathbf{K}^{II}\boldsymbol{u}^I + \mathbf{K}^{IE}\boldsymbol{u}^E + \mathbf{K}^{IC}\boldsymbol{u}^C \tag{3.6}$$

and

$$\begin{Bmatrix} \boldsymbol{f}^E \\ \boldsymbol{f}^C \end{Bmatrix} = \begin{bmatrix} \mathbf{K}^{EI} & \mathbf{K}^{EE} & \mathbf{K}^{EC} \\ \mathbf{K}^{CI} & \mathbf{K}^{CE} & \mathbf{K}^{CC} \end{bmatrix} \begin{Bmatrix} \boldsymbol{u}^I \\ \boldsymbol{u}^E \\ \boldsymbol{u}^C \end{Bmatrix}, \tag{3.7}$$

Substituting $\boldsymbol{f}^I = 0$ in equation 3.6, I have

$$\mathbf{K}^{II}\boldsymbol{u}^I = -\mathbf{K}^{IE}\boldsymbol{u}^E - \mathbf{K}^{IC}\boldsymbol{u}^C$$

and hence, solving for $\boldsymbol{u}^I$,

$$\boldsymbol{u}^I = -\left[\mathbf{K}^{II}\right]^{-1}\left[\mathbf{K}^{IE}\mathbf{K}^{IC}\right]\begin{Bmatrix} \boldsymbol{u}^E \\ \boldsymbol{u}^C \end{Bmatrix}. \tag{3.8}$$

Using this result to eliminate $\boldsymbol{u}^I$ in equation 3.7, I then obtain

$$\begin{Bmatrix} \boldsymbol{f}^E \\ \boldsymbol{f}^C \end{Bmatrix} = \left[- \begin{bmatrix} \mathbf{K}^{EI} \\ \mathbf{K}^{CI} \end{bmatrix} \left[\mathbf{K}^{II} \right]^{-1} \left[\mathbf{K}^{IE} \quad \mathbf{K}^{IC} \right] + \begin{bmatrix} \mathbf{K}^{EE} & \mathbf{K}^{EC} \\ \mathbf{K}^{CE} & \mathbf{K}^{CC} \end{bmatrix} \right] \begin{Bmatrix} \boldsymbol{u}^E \\ \boldsymbol{u}^C \end{Bmatrix}. \tag{3.9}$$

At this point, it is convenient to use these relations to define a reduced matrix

$$\boldsymbol{L} = \left[- \begin{bmatrix} \mathbf{K}^{EI} \\ \mathbf{K}^{CI} \end{bmatrix} \left[\mathbf{K}^{II} \right]^{-1} \left[\mathbf{K}^{IE} \quad \mathbf{K}^{IC} \right] + \begin{bmatrix} \mathbf{K}^{EE} & \mathbf{K}^{EC} \\ \mathbf{K}^{CE} & \mathbf{K}^{CC} \end{bmatrix} \right]$$

and partition it such that

$$\begin{Bmatrix} \boldsymbol{f}^E \\ \boldsymbol{f}^C \end{Bmatrix} = \begin{bmatrix} \boldsymbol{L}^{EE} & \boldsymbol{L}^{EC} \\ \boldsymbol{L}^{CE} & \boldsymbol{L}^{CC} \end{bmatrix} \begin{Bmatrix} \boldsymbol{u}^E \\ \boldsymbol{u}^C \end{Bmatrix}. \tag{3.10}$$

3.2.3 The force-control problem

In this case, the external nodal displacements are null and the external nodal forces $\boldsymbol{f}^E$ in S_E are known functions of time t. Equation 3.10 can be expressed as

$$\boldsymbol{f}^E = \boldsymbol{L}^{EE}\boldsymbol{u}^E + \boldsymbol{L}^{EC}\boldsymbol{u}^C \tag{3.11}$$

$$\boldsymbol{f}^C = \boldsymbol{L}^{CE}\boldsymbol{u}^E + \boldsymbol{L}^{CC}\boldsymbol{u}^C \tag{3.12}$$

and since $\boldsymbol{f}^E$ is known, I solve equation 3.11 for $\boldsymbol{u}^E$ obtaining

$$\boldsymbol{u}^E = \left[\boldsymbol{L}^{EE} \right]^{-1} \left[\boldsymbol{f}^E - \boldsymbol{L}^{EC}\boldsymbol{u}^C \right]. \tag{3.13}$$

Substituting this result in equation 3.12, I obtain

$$\begin{aligned} \boldsymbol{f}^{C} &= \boldsymbol{L}^{CE}\left[\left[\boldsymbol{L}^{EE}\right]^{-1}\left[\boldsymbol{f}^{E} - \boldsymbol{L}^{EC}\boldsymbol{u}^{C}\right]\right] + \boldsymbol{L}^{CC}\boldsymbol{u}^{C} \\ &= \mathbf{K}^{E}\boldsymbol{f}^{E} + \mathbf{K}^{C}\boldsymbol{u}^{C}, \end{aligned} \tag{3.14}$$

where

$$\mathbf{K}^{E} = \boldsymbol{L}^{CE}[\boldsymbol{L}^{EE}]^{-1} \tag{3.15}$$

and

$$\mathbf{K}^{C} = \left[\boldsymbol{L}^{CC} - \boldsymbol{L}^{CE}\left[\boldsymbol{L}^{EE}\right]^{-1}\boldsymbol{L}^{EC}\right] \tag{3.16}$$

is the contact stiffness matrix. Notice that equation 3.14 is of the form of equation 3.4, with

$$\boldsymbol{f}^{w} = \mathbf{K}^{E}\boldsymbol{f}^{E}. \tag{3.17}$$

In other words, this procedure determines the reduced nodal forces $\boldsymbol{f}^{w}$ due to prescribed external forces $\boldsymbol{f}^{E}$, as well as the contact stiffness matrix given by equation 3.16.

3.2.4 The displacement-control problem

If the nodal displacements $\boldsymbol{u}^{E}$ are prescribed functions of time, equation 3.12 still applies, and hence

$$\boldsymbol{f}^{C} = \boldsymbol{L}^{CE}\boldsymbol{u}^{E} + \boldsymbol{L}^{CC}\boldsymbol{u}^{C}. \tag{3.18}$$

Since in this case the $\boldsymbol{u}^{E}$ are known, I can write the equations in the form of equation 3.4, with

$$\boldsymbol{f}^{w} = \boldsymbol{L}^{CE}\boldsymbol{u}^{E} \text{ and } \mathbf{K}^{C} = \boldsymbol{L}^{CC}. \tag{3.19}$$

Notice that the contact stiffness matrix $\mathbf{K}^{C}$ is affected by whether the externally loaded nodes are force or displacement controlled. This is because the contact stiffness matrix is the solution of a problem in which the prescribed loading conditions are replaced by equivalent homogeneous conditions, traction-free in the force controlled case and zero displacement (fixed) in the displacement controlled case.

3.3 Contact of two elastic bodies

So far only the problem of a single elastic body in contact with a rigid surface has been treated. Now let us consider the cases when both bodies are elastically deformable. If two elastic bodies make contact at a set of N contact nodes, the first stage is to develop separate finite element models of the two bodies, taking care to locate the contact nodes at the same points on the interface. I use the sign convention of Figure 3.1 *for each body separately*, which implies that (for example) p_j^1 and p_j^2 are both compressive nodal forces. With this sign convention, when the two bodies are placed in contact, Newton's third law demands that $p_j^1 = p_j^2$, $q_j^1 = q_j^2$, or equivalently $\boldsymbol{f}_1^C = \boldsymbol{f}_2^C$ so I can conveniently drop the subscripts on these terms. In geometric terms, I can enforce this sign convention by defining local right-handed x, y coordinate systems at each contact node in each body, with the y-axis directed into the body, taking care to number the contact nodes in the same sequence in the two bodies.

In most cases, one of the contacting bodies will be externally supported and the other will have rigid-body degrees of freedom. In such cases, I shall use the index '2' to denote the externally-supported body and '1' for the free body. If both bodies are externally supported, the following procedure will work regardless of how the bodies are denoted. Since the two elastic bodies make contact at a shared set of N contact nodes, I first use the procedure of Section 3.2 to determine the matrices $\mathbf{K}_1^C, \mathbf{K}_2^C$ and the loading vectors $\boldsymbol{f}_1^w$, $\boldsymbol{f}_2^w$ for each body separately, defined as in equation 3.4, so

$$\boldsymbol{f}^C = \boldsymbol{f}_1^w + \mathbf{K}_1^C \boldsymbol{u}_1^C$$
$$\boldsymbol{f}^C = \boldsymbol{f}_2^w + \mathbf{K}_2^C \boldsymbol{u}_2^C . \tag{3.20}$$

With the sign convention of Figure 3.1, the opening nodal displacement in the full contact problem is $w_j = w_j^1 + w_j^2$ and the relative tangential (slip) displacement is $v_j = v_j^1 + v_j^2$, so

$$\boldsymbol{u}^C = \boldsymbol{u}_1^C + \boldsymbol{u}_2^C . \tag{3.21}$$

To make use of this result, I first solve equation (3.20)[2] for $\boldsymbol{u}_2^C$, obtaining

$$\left[\mathbf{K}_2^C\right]^{-1}\left(\boldsymbol{f}^C - \boldsymbol{f}_2^w\right) = \boldsymbol{u}_2^C .$$

I next premultiply by $\mathbf{K}_1^C$ obtaining

$$\mathbf{K}_1^C\left[\mathbf{K}_2^C\right]^{-1}\left(\boldsymbol{f}^C - \boldsymbol{f}_2^w\right) = \mathbf{K}_1^C \boldsymbol{u}_2^C .$$

Finally, adding this to (3.20)[1] and using (3.21), I have

$$\left[\mathbf{K}_1^C\left[\mathbf{K}_2^C\right]^{-1} + \boldsymbol{I}\right]\boldsymbol{f}^C = \mathbf{K}_1^C \boldsymbol{u}^C + \boldsymbol{f}_1^w + \mathbf{K}_1^C\left[\mathbf{K}_2^C\right]^{-1}\boldsymbol{f}_2^w ,$$

where $\boldsymbol{I}$ is the identity matrix. This equation can be inverted to yield a relation of the form in equation 3.4, with

$$\mathbf{K}^C = \left[\mathbf{K}_1^C\left[\mathbf{K}_2^C\right]^{-1} + \boldsymbol{I}\right]^{-1}\mathbf{K}_1^C \tag{3.22}$$

$$\boldsymbol{f}^w = \left[\mathbf{K}_1^C\left[\mathbf{K}_2^C\right]^{-1} + \boldsymbol{I}\right]^{-1}\left(\boldsymbol{f}_1^w + \mathbf{K}_1^C\left[\mathbf{K}_2^C\right]^{-1}\boldsymbol{f}_2^w\right). \tag{3.23}$$

Notice that if body 1 has rigid-body degrees of freedom, the matrix $\mathbf{K}_1^C$ will be singular. However, neither of the inversions in equation 3.23 will be ill-defined, but the reduced stiffness matrix $\mathbf{K}^C$ will also be singular. In fact it will have the same rank as $\mathbf{K}_1^C$ and the vectors defining the rigid-body modes of $\mathbf{K}^C$ will be the same as those for $\mathbf{K}_1^C$.

3.4 Partitioning the reduced stiffness matrix into normal and tangential components

The preceding operations will generate a $2N \times 2N$ stiffness matrix, whose components are ordered in nodal pairs. For example, the components of $\mathbf{u}^C$ the nodal displacement vector will be ordered as $\{v_1, w_1, v_2, w_2, v_3, w_3, ..., v_N, w_N\}$. For many purposes it is beneficial to reorder the vectors as

$$\boldsymbol{u}^C = \begin{Bmatrix} \boldsymbol{v} \\ \boldsymbol{w} \end{Bmatrix}; \quad \boldsymbol{f}^C = \begin{Bmatrix} \boldsymbol{q} \\ \boldsymbol{p} \end{Bmatrix}, \tag{3.24}$$

where $\boldsymbol{v} = \{v_1, \mathrm{v}_2, \mathrm{v}_3, ..., \mathrm{v}_N\}$, $\boldsymbol{p} = \{p_1, p_2, p_3, ..., p_N\}$ etc. The stiffness matrix must then be partitioned into sub-matrices $\boldsymbol{A}$, $\boldsymbol{B}$, $\boldsymbol{C}$ such that

$$\begin{Bmatrix} \boldsymbol{q} \\ \boldsymbol{p} \end{Bmatrix} = \begin{bmatrix} \boldsymbol{A} & \boldsymbol{B}^T \\ \boldsymbol{B} & \boldsymbol{C} \end{bmatrix} \begin{Bmatrix} \boldsymbol{v} \\ \boldsymbol{w} \end{Bmatrix} + \begin{Bmatrix} \boldsymbol{q}^w \\ \boldsymbol{p}^w \end{Bmatrix}, \tag{3.25}$$

Notice that the complete reduced stiffness matrix

$$\mathbf{K} = \begin{bmatrix} \boldsymbol{A} & \boldsymbol{B}^T \\ \boldsymbol{B} & \boldsymbol{C} \end{bmatrix} \tag{3.26}$$

must be symmetric, so $\boldsymbol{A}$, $\boldsymbol{C}$ are symmetric, but $\boldsymbol{B}$ is not generally symmetric. It is worth noting that a frictional elastic contact problem is described as '*uncoupled*' if and only if the matrix $\boldsymbol{B} = 0$. The coupling implied in the matrix $\boldsymbol{B}$ has important consequences for the behaviour of frictional elastic systems under cyclic loading.(see Section 3.8)

3.5 Algorithms for solving the reduced contact problem

Once the reduced stiffness matrix $\mathbf{K}^C$ and the time-varying external nodal forces $\boldsymbol{f}^w(t)$ have been determined, the problem becomes equivalent to that of a set of N massless blocks in frictional contact with a rigid surface. At any given point in the loading cycle, each node must be in one of four states which I designate by an integer state variable S_i. The conditions at each node are then defined by the relations

$S_i = 1$	Stick	$w_i = 0$; $\dot{v}_i = 0$;	$p_i \geq 0$; $\lvert q_i \rvert \leq fp_i$
$S_i = 2$	Separation	$p_i = 0$; $q_i = 0$;	$w_i > 0$
$S_i = 3$	Forward slip	$w_i = 0$; $q_i = -fp_i$;	$\dot{v}_i > 0$; $p_i \geq 0$
$S_i = 4$	Backward slip	$w_i = 0$; $q_i = fp_i$;	$\dot{v}_i < 0$; $p_i \geq 0$.

Notice that I have two equations at each node, so all the unknown nodal forces and displacements can be determined if the states S_i are assumed known. The solution of evolutionary contact problems will be obtained numerically using Gauss-Seidel principle[96]. In this algorithm, the nodal displacements are initially assumed to have the same values as at the previous time step. The nodes are then examined one by one in a Gauss-Seidel sense and the state and the nodal displacement at the node under examination are updated in accordance with the above governing inequalities. If a violation is detected the state change is made at the appropriate node and the calculation is repeated. The algorithm cycles through the entire set of nodes until the changes during one such cycle are less than some pre-defined convergence criterion. This algorithm requires the reduced stiffness matrix $\mathbf{K}^C$ to be arranged as in equation 3.26 where it has been partitioned into normal and tangential components. A similar algorithm was first developed by Ahn [58] for two-node discrete systems but here it has been extended to continuous systems including incomplete contacts as explained in section 3.6. The flow chart of the algorithm is displayed in Appendix D. Generally, the algorithm only requires a few iterations at each time step to obtain convergence to a self-consistent new state provided the loading increment is sufficiently small.

3.6 Incomplete contact problems

The discussion so far has focussed on ‘complete’ contact problems, where a defined set of nodes make contact when there are no external loads. Incomplete contact problems (also sometimes called advancing contact problems) arise when there is an initial gap between the bodies, the classical case being Hertzian contact between a quadratic surface and a plane. If the problem is to remain within the scope of linear elasticity, the magnitude of this gap must be small compared with other linear dimensions of the problem, notably the expected dimensions of the contact area. If the contact is incomplete, the first stage is to define a *nominal contact area* comprising the set of points that might come into contact during the loading process. If s defines a spatial coordinate along the nominal contact area, the initial gap will be a function $g(s)$ and I also require that the derivative $g'(s)$ be small compared with unity. This in turn ensures that I can establish a set of nodes on each of the two surfaces such that the line joining corresponding nodes is approximately perpendicular to each surface, as shown in Figure 3.3.

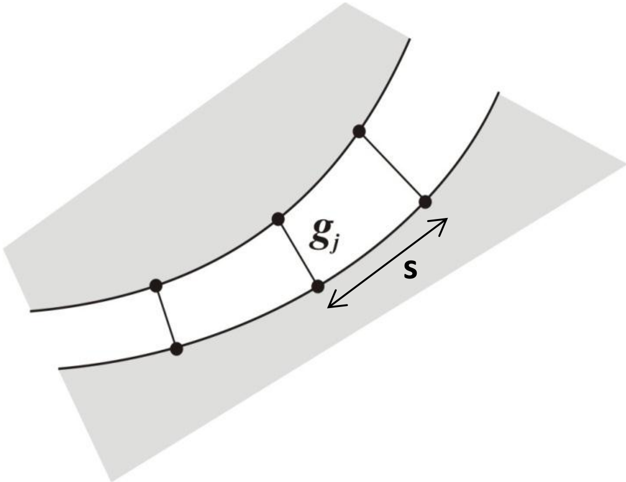

Figure 3.3: Definition of nodal gap.

In the finite element discretization, the length of this line for node j will be denoted by g_j .It then follows that the nodal gap after deformation is given by $g_i + w_i$ and hence the equations defining the contact algorithm of Section 3.5 needs be modified as shown below.

$S_i = 1$	Stick	$w_i + g_i = 0 \,;\, \dot{v}_i = 0 \,;$	$p_i \geq 0 \,;\, \lvert q_i \rvert \leq fp_i$
$S_i = 2$	Separation	$p_i = 0 \,;\, q_i = 0 \,;$	$w_i + g_i > 0$
$S_i = 3$	Forward slip	$w_i + g_i = 0 \,;\, q_i = -fp_i \,;$	$\dot{v}_i > 0 \,;\, p_i \geq 0$
$S_i = 4$	Backward slip	$w_i + g_i = 0 \,;\, q_i = fp_i \,;$	$\dot{v}_i < 0 \,;\, p_i \geq 0.$

With this formulation, the contact stiffness matrix $\mathbf{K}^C$ and the external loading vector $\boldsymbol{f}^w$ are the same as in the corresponding problem where there is no initial gap.

3.6.1 An alternative approach

An alternative approach, which does not require the contact algorithm in Section 3.5 to be modified, is to redefine the function $\boldsymbol{f}^w$ as the set of nodal forces needed to establish contact with no slip at all the nodes in the nominal contact area - including closing the initial gap. The way to determine these forces is to superpose the solution of two separate problems:-

1. The forces $\boldsymbol{f}^{w0}$ that would be generated by the external loads if there had been no initial gap $\boldsymbol{g} = 0$ - i.e. if the contact had been complete, and
2. The forces $\boldsymbol{f}^{wg}$ that are required to close the initial gap in the absence of external loads. These can be obtained using equation 3.25 as

$$\begin{Bmatrix} \boldsymbol{q}^{wg} \\ \boldsymbol{p}^{wg} \end{Bmatrix} = \begin{bmatrix} \boldsymbol{A} & \boldsymbol{B}^T \\ \boldsymbol{B} & \boldsymbol{C} \end{bmatrix} \begin{Bmatrix} 0 \\ -\boldsymbol{g} \end{Bmatrix}.$$

The required reduced external forces are then

$$\boldsymbol{f}^{w} = \boldsymbol{f}^{w0} + \boldsymbol{f}^{wg}.$$

The two methods are equivalent. To establish this, define a new contact nodal displacement vector

$$\boldsymbol{u}^* = \boldsymbol{u} + \boldsymbol{u}^g, \qquad \text{where} \qquad \boldsymbol{u}^g = \begin{Bmatrix} \boldsymbol{v} \\ \boldsymbol{w} \end{Bmatrix} = \begin{Bmatrix} 0 \\ -\boldsymbol{g} \end{Bmatrix}.$$

I then have

$$\boldsymbol{f}^{w} = \boldsymbol{f}^{w0} + \mathbf{K}^C \boldsymbol{u}^g$$

and hence

$$\boldsymbol{f} = \boldsymbol{f}^{w} + \mathbf{K}^C \boldsymbol{u} = \boldsymbol{f}^{w0} + \mathbf{K}^C (\boldsymbol{u} + \boldsymbol{u}^g) = \boldsymbol{f}^{w0} + \mathbf{K}^C \boldsymbol{u}^*.$$

The contact boundary condition at node i is $w_i = 0$, which therefore implies $w_i^* = -g_i$. Thus, I can use the original contact algorithm in Section 3.5 with the modified value of $\boldsymbol{f}^{w}$, or the modified algorithm (with contact boundary condition $w_i^* = -g_i$) and the original value $\boldsymbol{f}^{w} = \boldsymbol{f}^{w0}$.

3.7 Implementation of the reduced stiffness method

I turn, now, to the application of the static reduction technique to three example problems (Figures 3.3 and 3.9). Each was solved in two ways. First, by using the commercial finite element programme ABAQUS (ABQ), incorporating contact elements, and using the option of an artificial stiffness between sticking nodes, to help linearlise the problem. Secondly, the same model was generated in ABAQUS and the stiffness matrix abstracted (or matrices if both contacting bodies have finite stiffness) and processed using the reduced stiffness method (SR). In the latter case, the contact was solved within MATLAB so that the Signorini conditions are incorporated precisely in the solution using evolutionary algorithm.

3.7.1 Case I: single elastic body pressed against a rigid body

Figure 3.4(a) shows a square elastic punch, of side 2a, pressed onto a flat surface which is here taken to be rigid and the meshed finite element model is shown in Figure 3.4(b).
A two-dimensional, 4-noded (bilinear), plane strain quadrilateral (CPE4) element was used and the mesh size at the contact interface is $0.005a \times 0.005a$ where a is the contact half-width as shown in Figures 3.4. A normal force is first applied to the block by using a uniform distribution of pressure, giving a contact force P_o and this is held constant. Therefore P_o denotes the steady-state constant normal force applied to the contact before the application of the shear load. A shear traction is now subsequently applied to the upper surface, constant with position, but increasing monotonically in time, producing a shear force $Q(t)$. At the same time, a further pressure distribution (LP) , varying linearly with position and proportional in magnitude to the shear traction is applied, so that an anti-clockwise moment is developed which equilibrate the moment due to the shear load. This device is employed so that the detailed way in which the loads are exerted does not significantly influence the tractions distribution arising along the contact interface.

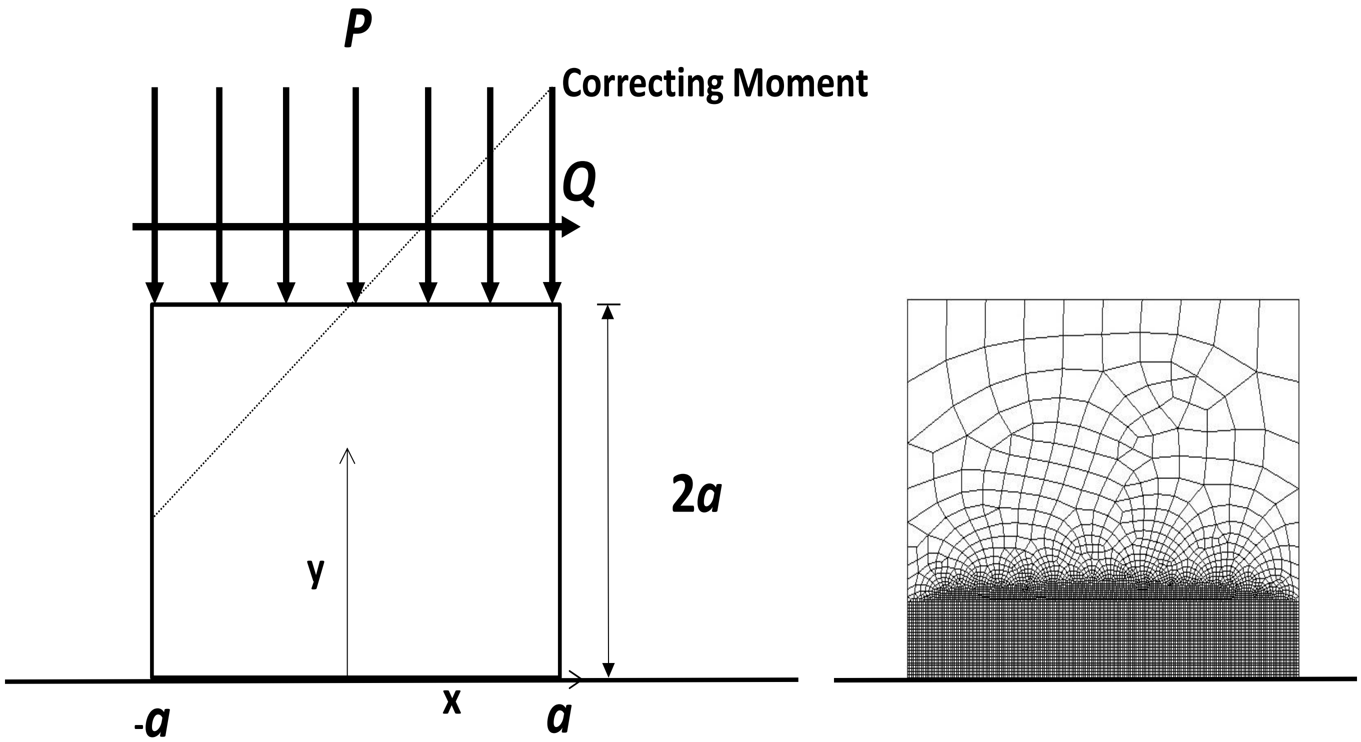

Figures 3.4: (a) A square elastic block pressed against a rigid surface by a constant normal load, *P*, and subsequently by a monotonically increasing shear force *Q*. (b) a finite element model.

The loading history of the problem is shown in Figure 3.5. The coefficient is initially chosen to be equal to 0.2.

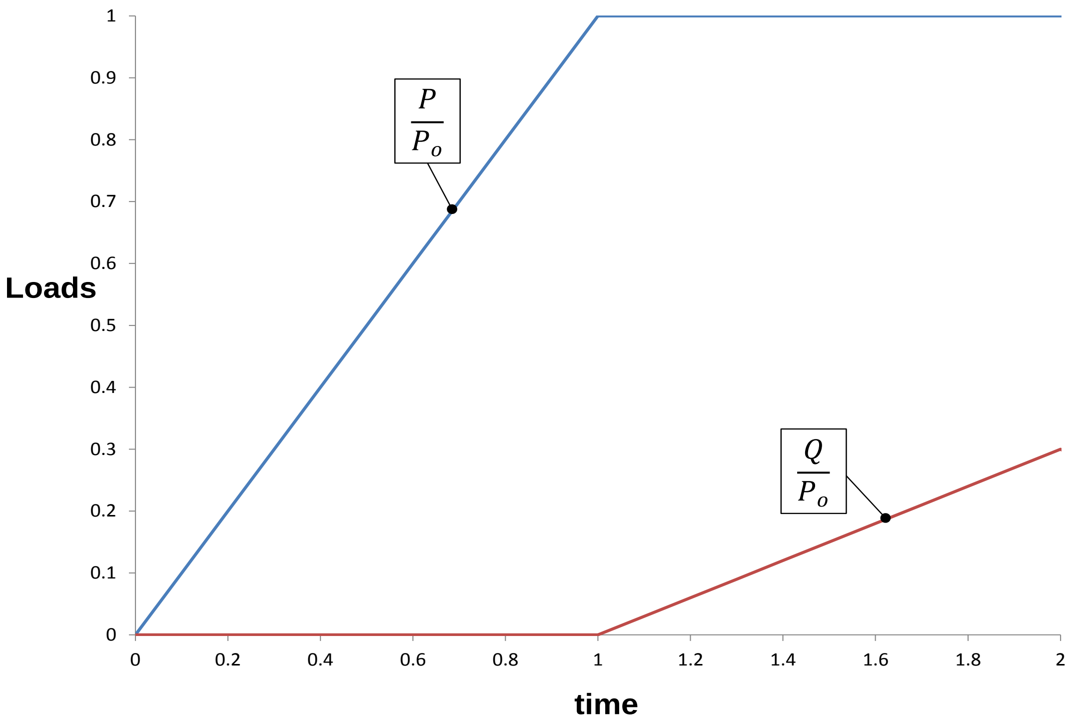

Figure 3.5: Loading History

The total number of nodes is 5,000 and the number of nodes present along the line of the contact interface is 101. Note that each node has two degrees of freedom so the total degree of freedom is 2N where N is the total number of nodes. By using the static reduction technique in this particular case, the full stiffness matrix size of 10,000 by 10,000 is reduced to 202 by 202. The comparison of the relative tangential (slip) displacement of contact nodes from the static reduction procedure (SR) and ABAQUS (ABQ) were made to see if there are any differences and the results are displayed in Figure 3.6 and 3.7. The results show that the relative tangential displacements of the contact nodes are the same. However, the computational cost is significantly less expensive in the case using the reduced stiffness method because the time taken is reduced by a factor of 60 in this particular case (i.e. 120 seconds to 2 seconds). The value of this factor increases rapidly if the total degree of freedom is increased. Figure 3.6 shows an interfacial slip displacement present when only the normal load is applied. As expected, it is anti-symmetric and there is a central stick zone.

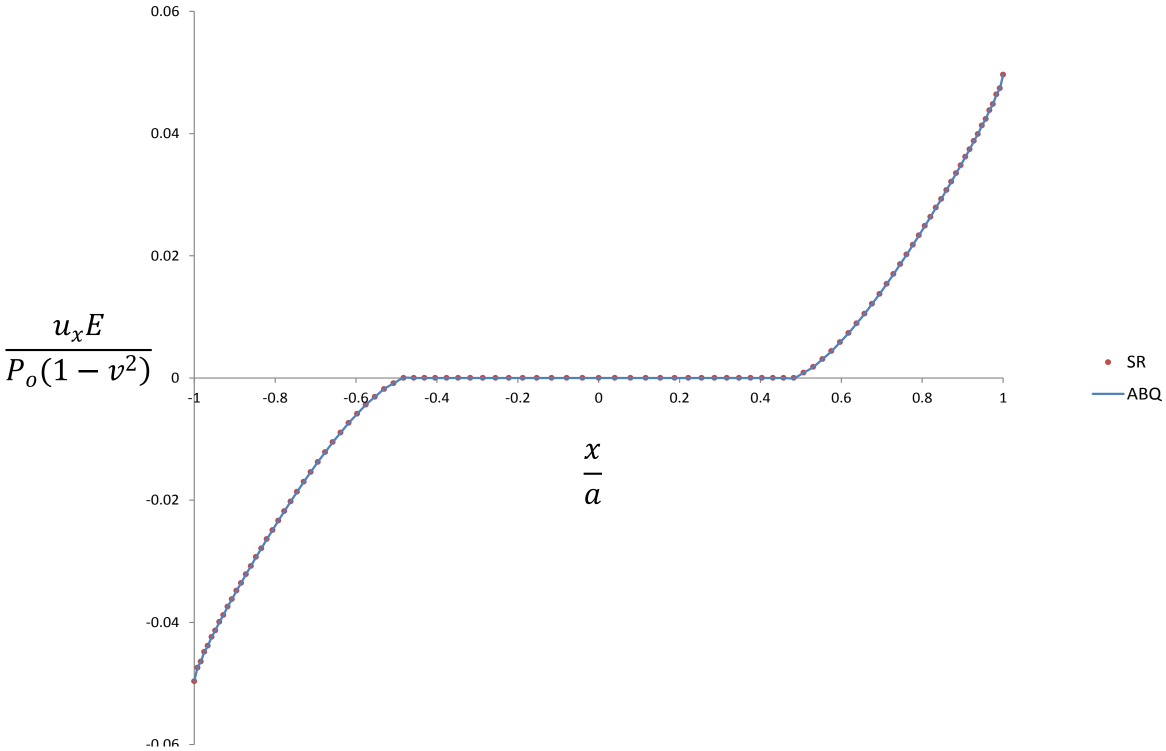

Figure 3.6: Relative tangential displacement of contact nodes when only normal load, *P*, is applied and friction coefficient *f* =0.2.

As the shear force is increased from zero what is now the trailing edge sticks upon application of an infinitesimal force locking in the reverse slip displacement already present, and this remains the case as the shearing force is increased in value. The forward slip zone attached to the leading edge increases in size, and the magnitude of the forward slip also increases as displayed in Figure 3.7. In Figure 3.6 and 3.7, the normalisation of the displacement is with respect to the 'plain strain modulus' with E Young's modulus and v Poisson's ratio. On this scale, local contact corner oscillatory behaviour is not apparent.

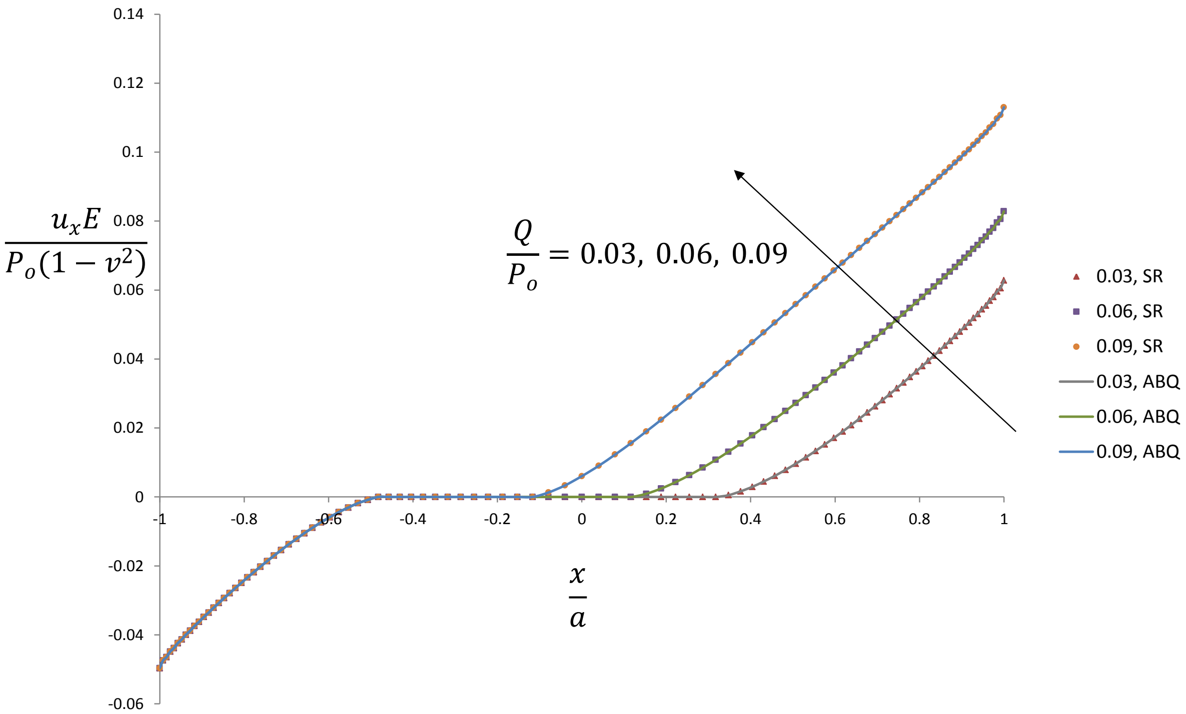

Figure 3.7: Relative tangential displacements of contact nodes when both normal load, *P*, and shear load, *Q*, are applied and friction coefficient *f* = 0.2.

Note that the results in the stick region are more accurate using the reduced stiffness method as there is no artificial compliance introduced. As a result, the values of the slip displacement are equal to zero precisely whereas the results from ABAQUS are not. However, this is not apparent in the Figures 3.6 and 3.7 because the magnitudes of the displacements are very small.

3.7.2 Case II: Contact of two elastic bodies

The problem depicted in Figure 3.4(a) was treated again, but this time the two bodies were given the same elastic constants, and with the coefficient of friction now set to 0.4. The elastic plane is chosen to be sufficiently large relative to the size of the square punch for it to be represented as a half-plane. The width and length of the elastic half plane is chosen to be larger than that of a contacting square by a factor of 200. A two-dimensional, 4-noded (bilinear), plane strain quadrilateral (CPE4) element was used. The mesh refinement was conducted to ensure independence of the results from the mesh and the mesh size at the contact interface is $0.005a \times 0.005a$ where a is the contact half-width.

Using the sign conventions in Figure 3.1 obtain both the full stiffness matrices of the square punch and that of half-plane. The procedure to obtain the global stiffness matrix is described Appendices B and C. In this case, since there are two elastic bodies, it is necessary to work out the combined reduced stiffness matrix and the problem can then be treated as a single elastic body against a rigid surface. The detailed explanation of the algebra to calculate the reduced stiffness matrix is in section 3.3.

The total number of degrees of freedom of a square punch and a half-plane are 10,000 and 17,000 respectively. Using the static reduction procedure, the combined reduced stiffness matrix is reduced to one of only 200 by 200. It is noteworthy to mention that the computational cost of matrix size reduction is very low provided that the computational power is sufficiently high. For instance, the time taken to reduce a stiffness matrix from 17000 by 17000 to 200 by 200 is equal to 3 seconds. This has been tested using a PC with a 2.66 GB dual-core processor with 4 GB of RAM. Figures 3.8 and 3.9 illustrate the slip displacement of the nodes along the contact interface at different points in the loading cycle in Figure 3.5. The results from both static reduction technique and ABAQUS are the same. The computational time to obtain the solution is significantly reduced from 130 to 2 seconds. Figures 3.8 show the slip displacement resulting from the application of the normal load and qualitatively similar to that found in the first example problem. Upon the application of an infinitesimal shear force what is now the trailing edge of the contact again instantaneously sticks, and as the force is increased in the value the leading edge slip zone increases monotonically in size as displayed in Figure 3.9.

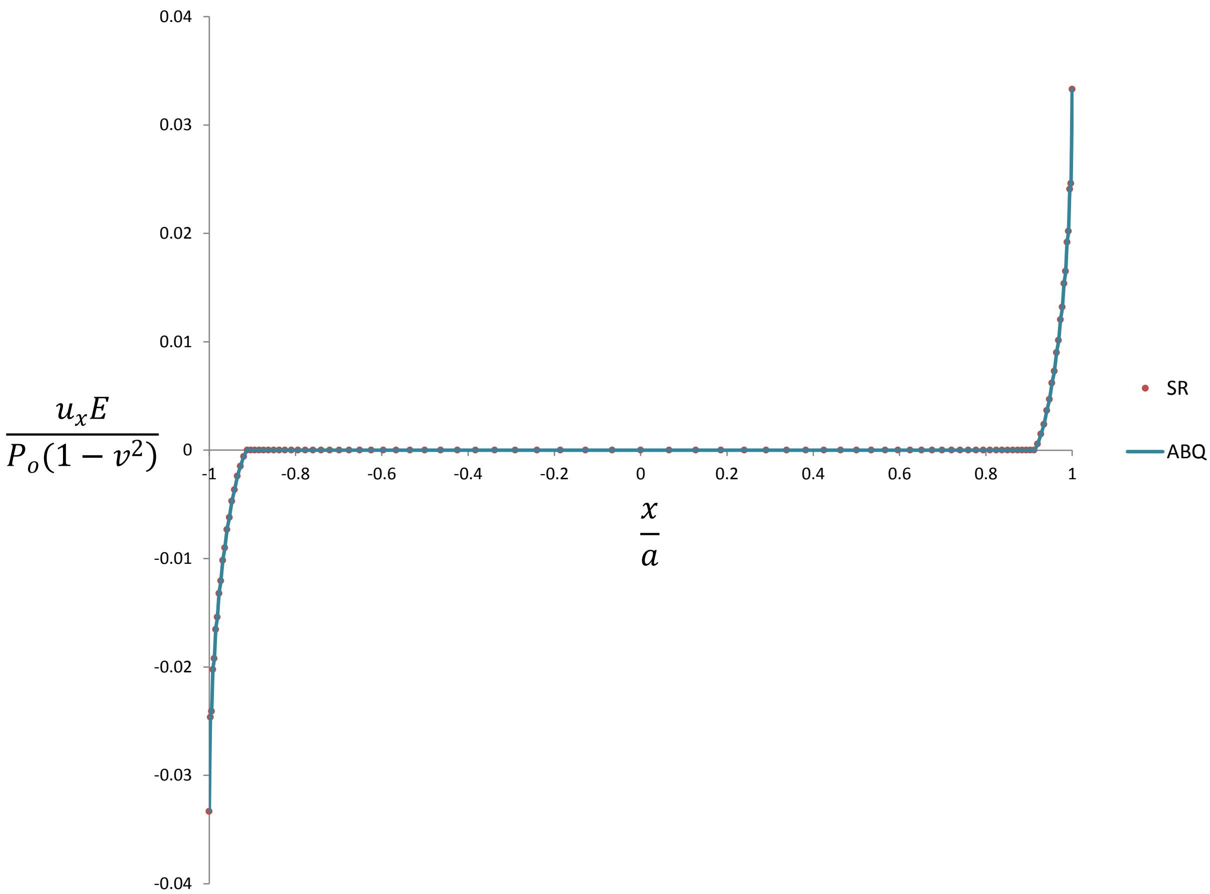

Figure 3.8: Relative tangential displacement of contact nodes when only normal load, *P*, is applied and friction coefficient *f* =0.4.

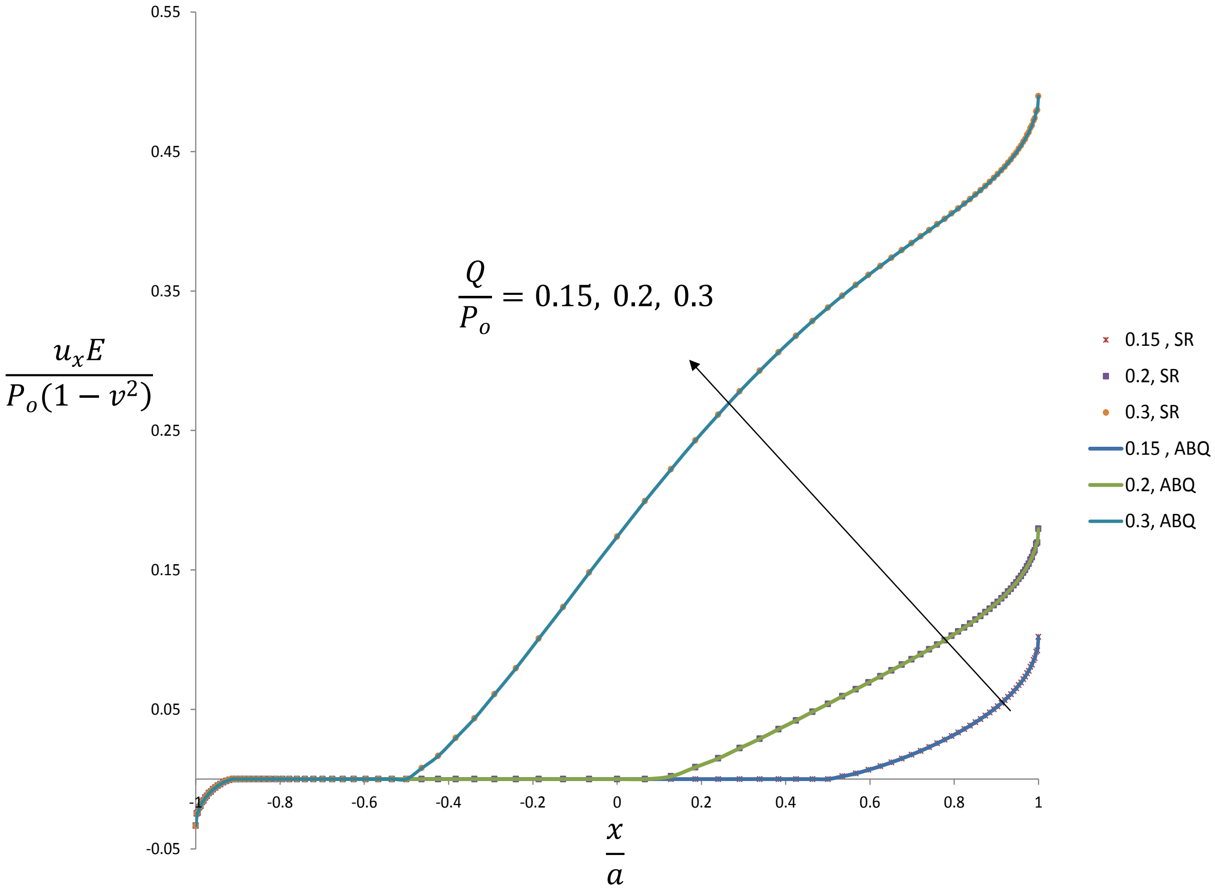

Figure 3.9: Relative tangential displacement of contact nodes when both normal load, *P*, and shear load ,*Q*, are applied and friction coefficient *f* =0.4 .

If the monotonically increasing shear load is now cycled between some maximum and minimum values, the solution from the ABAQUS can sometimes be less stable when the number of the loading cycle is large. However, the reduced stiffness method provides a more efficient and robust method to cope with problems of this kind. The simulations can be run with 100 plus loading cycles in a relatively short amount of time. This is particularly useful for the shakedown analysis in Chapter 4 where the high number of cycles will be run to ensure that the steady state of the system is reached.

3.7.3 Case III: Incomplete contact

So far I have only considered the problem where there is no initial gap between the two bodies. Let us now consider an incomplete contact where a cylindrical punch is pressed against an elastically similar half-plane as shown in Figure 3.10(a).The total number of degrees of freedom of a square punch and a half-plane are 10,000 and 17,000 respectively and the number of contact nodes is 101. The size of the elastic square punch and the elastically similar half-plane are kept the same as case II. The coefficient of friction is equal to 0.4.

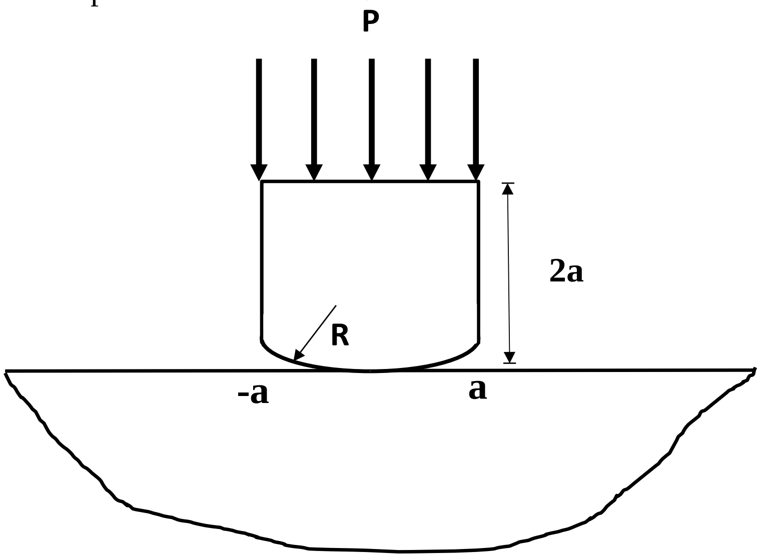

(a)

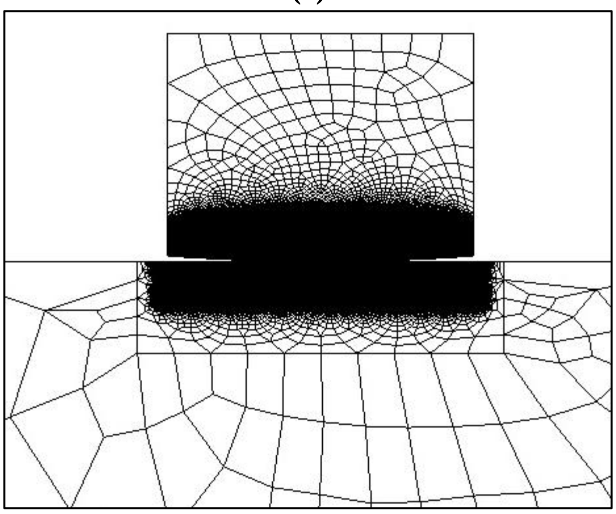

(b)

Figures 3.10: (a) A cylindrical punch against an elastically similar half-plane and (b) a finite element model.

A two-dimensional, 4-noded (bilinear), plane strain quadrilateral (CPE4) element was used and the mesh size at the contact interface is 0.005a × 0.005a (see Figures 3.10). To analyse this problem, the combined reduced stiffness matrix is obtained and the definition of nodal gap described in Section 3.6 is used. The relative surface normal separation of opposing contact nodes in the two bodies including that of the undeformed bodies, is shown in Figure 3.11, as a function of the applied load. Figure 3.12 shows the contact pressure distribution which is semi-elliptical in form. The results from the two methods are again compared and they are the same. Because of a significant reduction in stiffness matrix, the time taken to compute the results is much faster than ABAQUS as in case I and II. In this particular case, the computational time is reduced from 160 to 4 seconds. The two different approaches using reduced stiffness matrix described in Section 3.6 give the same results.

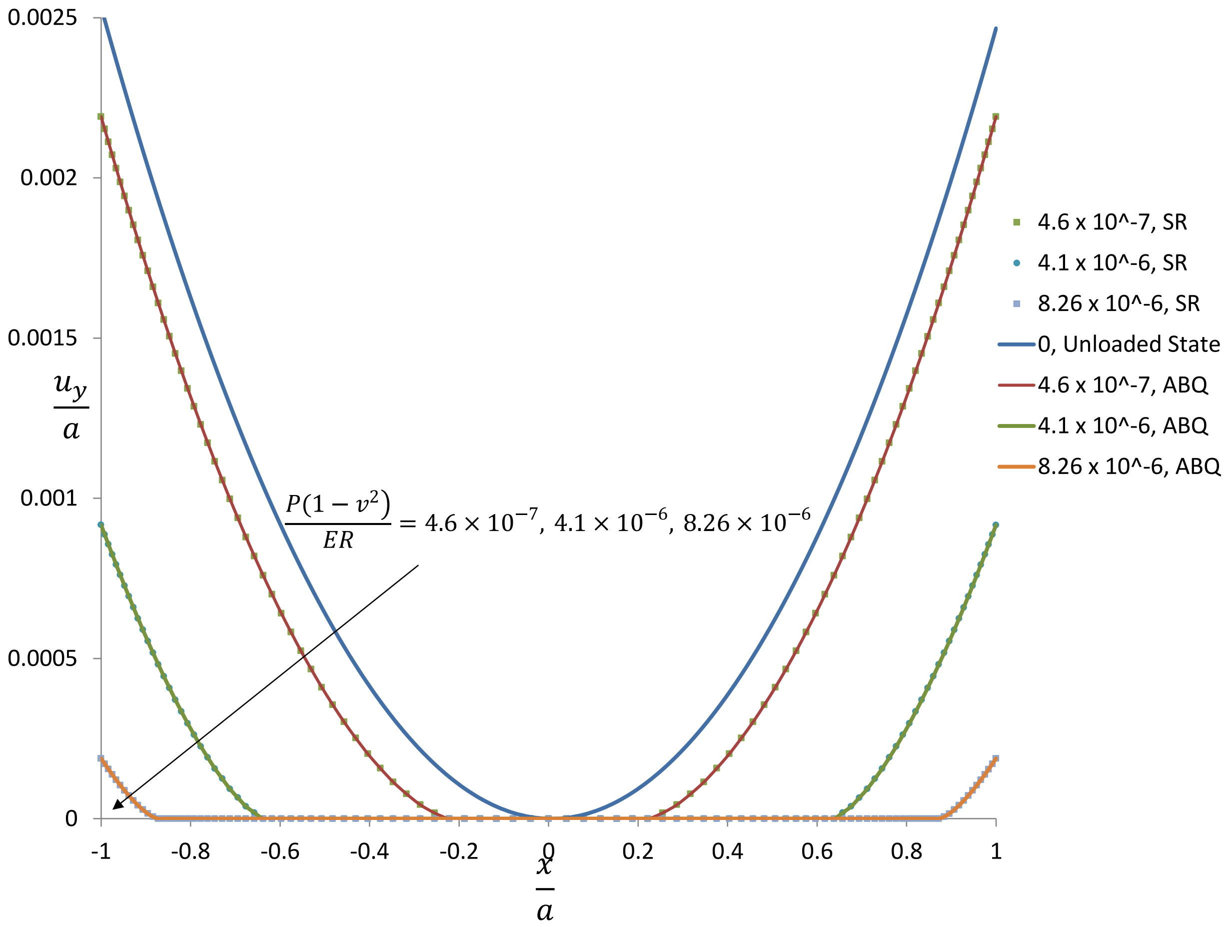

Figure 3.11: Relative surface normal separation of opposing contact nodes during the loading phase.

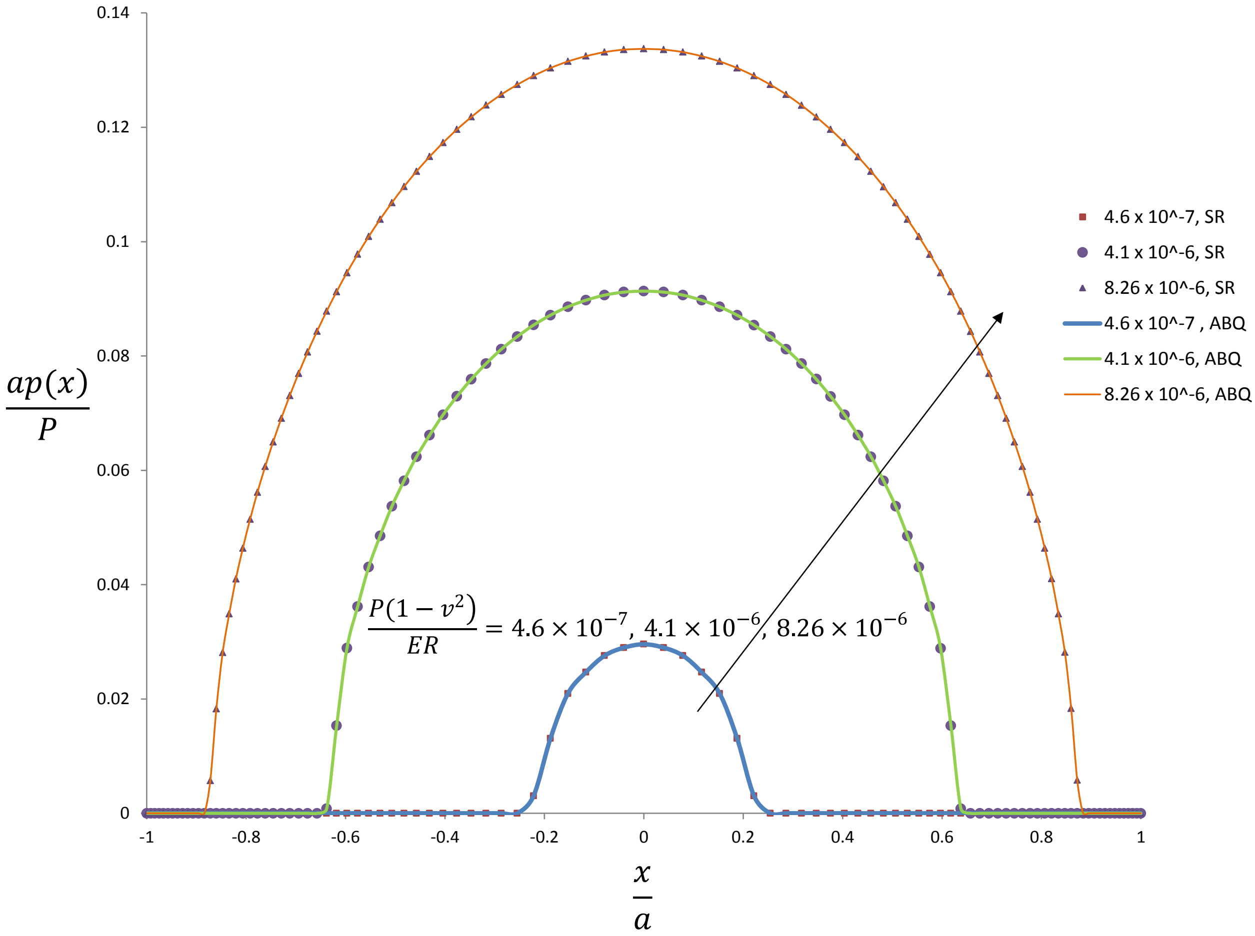

Figure 3.12: Pressure distribution of the contact nodes during the loading phase of the normal load.

3.8 Determining the shakedown limit

One of the other applications of the reduced stiffness method is the shakedown analysis of frictional elastic systems. If the external loading $\boldsymbol{P}(t)$ is periodic in time, the slip displacements during the first few cycles modify the behaviour in subsequent cycles, and in some circumstances can lead to a state of shakedown, where no slip occurs in the steady state. A necessary condition for shakedown is that there exists a time-independent tangential displacement vector v such that $|q_i| < fp_i$ for all nodes i and time t during the loading, and hence,

$$-fp_i^w(t) + B_{ij}v_j < q_i^w(t) + A_{ij}v_j < fp_i^w(t) + B_{ij}v_j \tag{3.27}$$

for all i and t. Others [56] in the field have shown that this is a necessary and sufficient condition for shakedown if and only if $\boldsymbol{B} = 0$. However, if the system is coupled ($\boldsymbol{B} \neq 0$), equation 3.27 defines a necessary but not sufficient condition for shakedown, so there will generally exist a class of periodic loading scenarios for which the occurrence of shakedown depends on the initial conditions. The procedures for defining the loading limits of this class can be achieved by the use of the reduced stiffness method and will be discussed in Chapter 4.

3.9 Conclusion

In this Chapter, a method of determining the reduced contact stiffness matrix has been developed. Once the reduced stiffness is determined, it can be used to develop a solution of the evolutionary contact problem using the direct implementation of Signorini and Coulomb friction contact inequalities. This is significantly more efficient than a direct finite element solution from the same problem. For examples analysed in section 3.7, computational time is significantly reduced. Another advantage of the proposed method is that the non-linearities associated with contact conditions are visible to and under control of the user. This facilitates trouble-shooting in complex problems and also permits the user to introduce alternative friction laws or experiment with different iterative strategies for the solution.

One of the other applications of this reduced stiffness matrix approach is the determination of the range of the alternating loads below which the system can shake down. With conventional time-marching finite elements solutions, these problems can only be explored by running numerous particular cases and this is likely to be prohibitively computer-intensive. However, when the number of remaining degree of freedoms is reduced to the number of the contact nodes, it becomes practical to use an optimisation code to determine (for example) the optimal set of time-independent slip displacements that will permit the maximum amplitude of the periodic loading without incurring further slip. This will be discussed more in Chapter 4. Lastly, the reduced stiffness method also provides a convenient way to obtain dislocation solutions. Note that the access to all MATLAB codes will be available in CD at the back of the thesis as well as the URL www.eng.ox.ac.uk/stress.

4 Shakedown Limit Algorithms

4.1 Introduction

Shakedown in continuum plasticity problems is well known. It was thought that the Melan theorem [55] for plasticity would equally apply to all elastic contacts governed by the Coulomb friction law regardless of whether the contacts are coupled or not. An example of an uncoupled problem would be one where the contacting bodies can be represented by elastic half-planes and they are elastically similar. They are uncoupled because the normal load does not induce slip displacements between the two bodies and the contact pressure distributions are not modified by the shearing load. Recent results of calculations on elastic discrete systems by Barber and co-workers [58] suggested that the Melan theorem cannot be applied rigorously to frictional contact problems when the normal contact reactions are coupled with the interfacial tangential displacements. This is mainly because of the non-associative nature of the frictional law [97]. Further, the results show that there generally exists two load factors which are the lower bound λ_1 and upper bound λ_2. The system will shake down regardless of the initial conditions for any load factor less than the lower bound $(\lambda < \lambda_1)$. For a load factor greater than the upper bound, $(\lambda > \lambda_2)$, the systems will undergo cyclic slip for all initial conditions. The systems may shake down or be in a state of cyclic slip depending on the initial conditions for any load factor between the lower and upper bounds($\lambda_1 < \lambda < \lambda_2$).

A thorough understanding of shakedown in continuum elasticity problems is vitally important because it is of direct relevance to the study of fretting fatigue in a wide range of applications. An example is the frictional contact which can be found in the gas turbine of the aeroplane engine such as dovetail joints where the fan blades are connected to the central discs. In this work, I will analyse the interfacial response of an elastic continuous system. As an example static frictional contact between a square elastic block and an elastically similar half-plane which is pressed by a steady-state constant normal load in the presence of friction and subject to a cyclically varying shear force will be studied. Since the two contacting bodies are in very different domains there is always considerable coupling present between the normal and shear loading. Three different algorithms have been developed to predict the likelihood of the frictional shakedown in the elastic continuous systems. In doing so, a number of questions may arise – Will the continuous systems under cyclic loading respond in the same way or merely a similar way to the results from the elastic discrete system? Does the interfacial response of contacts at steady state depend on the initial conditions? The analysis will be structured in the following way. First, two approximated methods will be developed together an exact-solution method using a mixed method between finite element analysis and mathematical programming. Note that in all algorithms particular values of load factors will be first chosen. Then the corresponding friction coefficients required for shakedown will be determined together with the residual tractions and their corresponding slip displacements. The results will then be used to investigate the effect of initial conditions on steady-state response of the system.

4.2 Monolith and monotonic shear loading

Consider an elastically-similar complete contact where a square elastic indenter, of side 2a, is pressed on an elastically similar half-plane as shown in Figure 4.1.

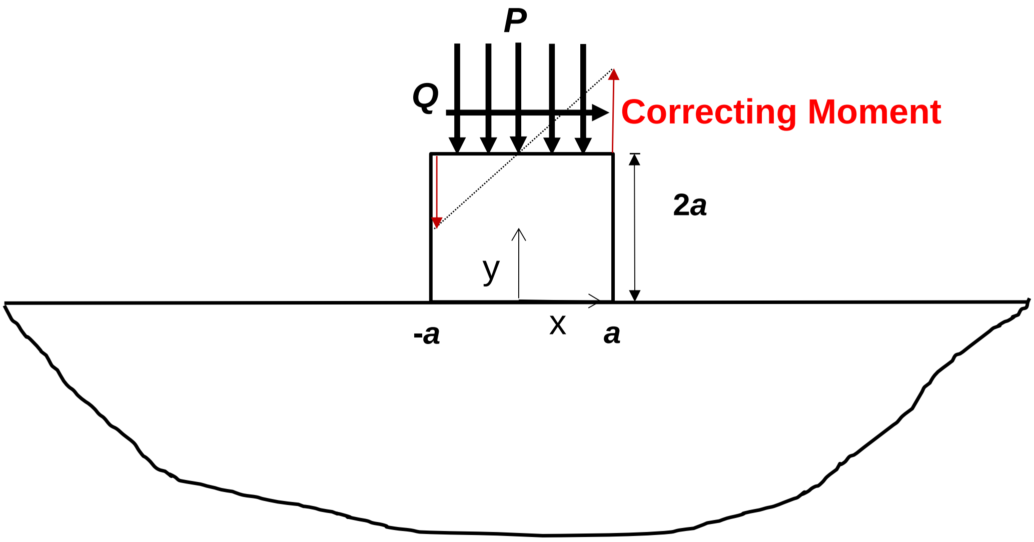

Figure 4.1: A square elastic punch pressed on an elastically half-plane subjected to a constant normal load, *P*, and a monotonically increasing shear load, *Q*.

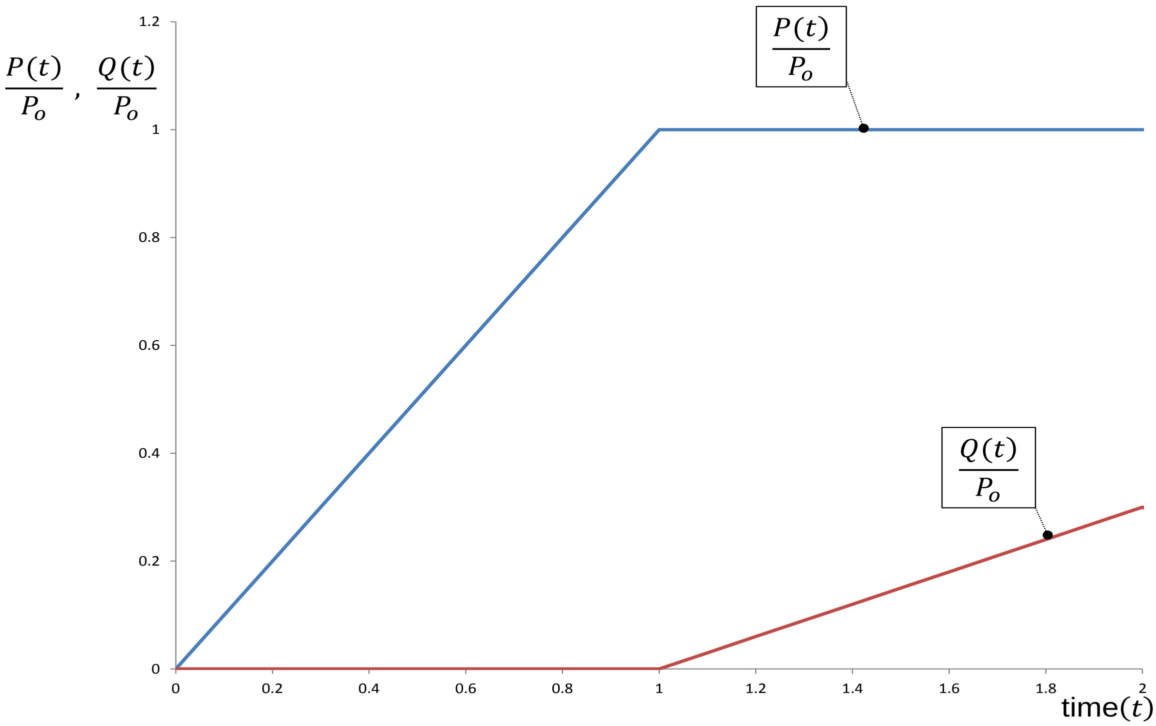

Figure 4.2: Loading History.

Before turning to a detailed steady-state analysis of the problem including frictional shakedown, I would first like to analyse interfacial behaviour of the complete contact subjected to a constant normal force and monotonic shear loading. Since a square elastic punch cannot be represented by half-plane it is not possible to obtain a closed form solution. Hence, a numerical method such as a finite element method has to be used to obtain the interfacial tractions. Wedges asymptotes [15, 19, 20] may be used to validate the solution near the contact edges where it may be difficult to attain convergences. The indenter is first subjected to a constant normal load followed by a monotonically shearing force and the load history is shown in Figure 4.2. A normal pressure varying linearly with position is also applied to satisfy the rotational equilibrium about the contact plane, i.e. to make the shear force be statically equivalent to one applied in the plane of the interface.

Let first assume that the coefficient of friction is sufficiently high to inhibit all slip so that the two bodies can be considered as a single entity. I will now explore different interfacial behaviour of this model under various values of maximum shear load. The problem geometry, portrayed in Figure 4.1, was initially modelled as a monolith and the investigation was carried out by employing the reduced stiffness procedure. First, I obtain the full stiffness matrices for each body. By using static reduction procedure, the size of the problem is reduced to the set of contact nodes and those where the external load is applied. (For more details, see Chapter 3). Convergence tests were also carried out to ensure that the results are independent of the mesh size.

For a monolithic model, an application of a normal load (P) and a monotonic increasing shear force (Q) will induce both normal, $p(x)$, and shear, $q(x)$ tractions. The normal and shear tractions are normalised as follows

$$\frac{p(x)}{p_o} = \tilde{p}_p(x) \qquad \frac{p(x)}{q_o} = \tilde{p}_q(x)$$

$$\frac{q(x)}{p_o} = \tilde{q}_p(x) \qquad \frac{q(x)}{q_o} = \tilde{q}_q(x)\,, \tag{4.1}$$

where $p_o = \frac{P_o}{2a}$ and $q_o = \frac{Q_{\max}}{2a}$ (P_o is the steady-state constant normal load and $Q_{\max}$ is the maximum shear load). The terms $\tilde{p}_q(x)$, $\tilde{q}_p(x)$ would be equal to zero in an uncoupled problem and are the first manifestation of the coupling phenomenon. The traction ratio is given by

$$\frac{q(x)}{p(x)} = \frac{p_o\tilde{q}_p(x) + q_o\tilde{q}_q(x)}{p_o\tilde{p}_p(x) + q_o\tilde{p}_q(x)} = \frac{\tilde{q}_p(x) + \lambda\tilde{q}_q(x)}{\tilde{p}_p(x) + \lambda\tilde{p}_q(x)} \tag{4.2}$$

where the dimensionless load factor $\lambda = \left(\frac{q_o}{p_o}\right) = \left(\frac{Q_{\max}}{P_o}\right)$ has been introduced.

Provided that $\tilde{q}_p(x) + \lambda\tilde{q}_q(x) > 0$, incipient slip occurs when

$$f = \left.\frac{\tilde{q}_p(x) + \lambda\tilde{q}_q(x)}{\tilde{p}_p(x) + \lambda\tilde{p}_q(x)}\right|_{\max} \tag{4.3}$$

where f is the coefficient of friction and the maximisation is with respect to position along the contact interface, x and the results are shown in Figure 4.3.

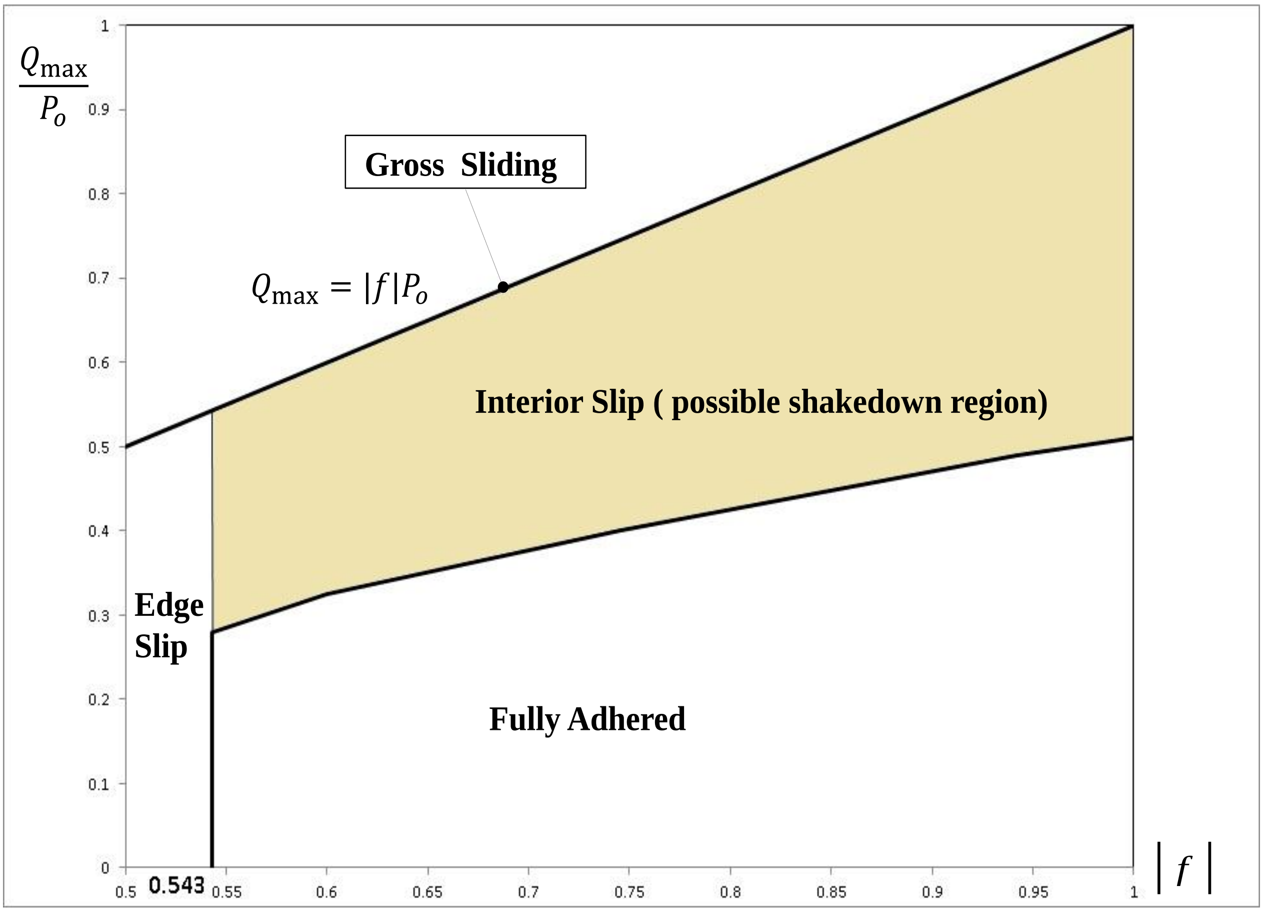

Figure 4.3 Interfacial behaviour map of a square punch for a range of load factor $\left(\frac{Q_{max}}{P_o}\right)$ and frictional coefficient, f .

Different classes of interfacial response found are displayed in Figure 4.3. The three classes can be summarised as followed.

1) Full Adhesion

When the normal load, P , is applied alone in loading step 1 the shear traction distribution is anti-symmetric about the centre of the contact and the normal traction is infinite at the edge of the contact (see Figure 4.4(a)).

Upon the application of a monotonic increasing shear load in loading step 2, the shear traction distribution is distorted considerably and it is no longer symmetric about the centre of the contact. In fact, the magnitude of the shear traction on the leading edge of the contact increases but decreases on the trailing edge of the contact. This is because, as displayed in Figure 4.4(b), when a shearing force is applied it increases the tendency of forward slip at both trailing and leading edges. It also reinforces the magnitude of the contact pressure at the leading edge and weakens it at the other end. However, it is worth noting that the ratio of interfacial shear $q(x)$ to normal traction $p(x)$ remains the same regardless of the maximum magnitude of the applied shear load as portrayed in Figure 4.5. This is a very useful result as it shows that the contact will undergo edged-initiated slip for any friction coefficient lower than 0.543 and the contact edge will remain fully adhered if the friction coefficient is greater than 0.543. I am interested only in cases where $f \geq 0.543$, so that no corner-initiated slip occurs. This is because the shakedown of frictional contacts will only take place for cases where the slip is initiated from the interior points within the contact.

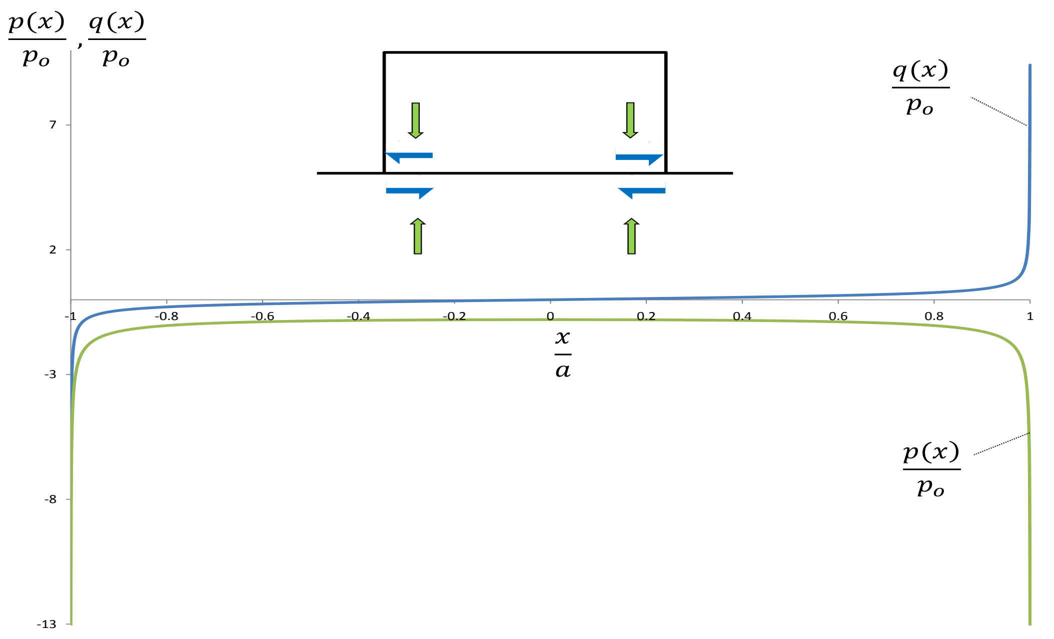

Figure 4.4(a): The normal and shear tractions as a result from the application of normal load (P) to the monolithic model.

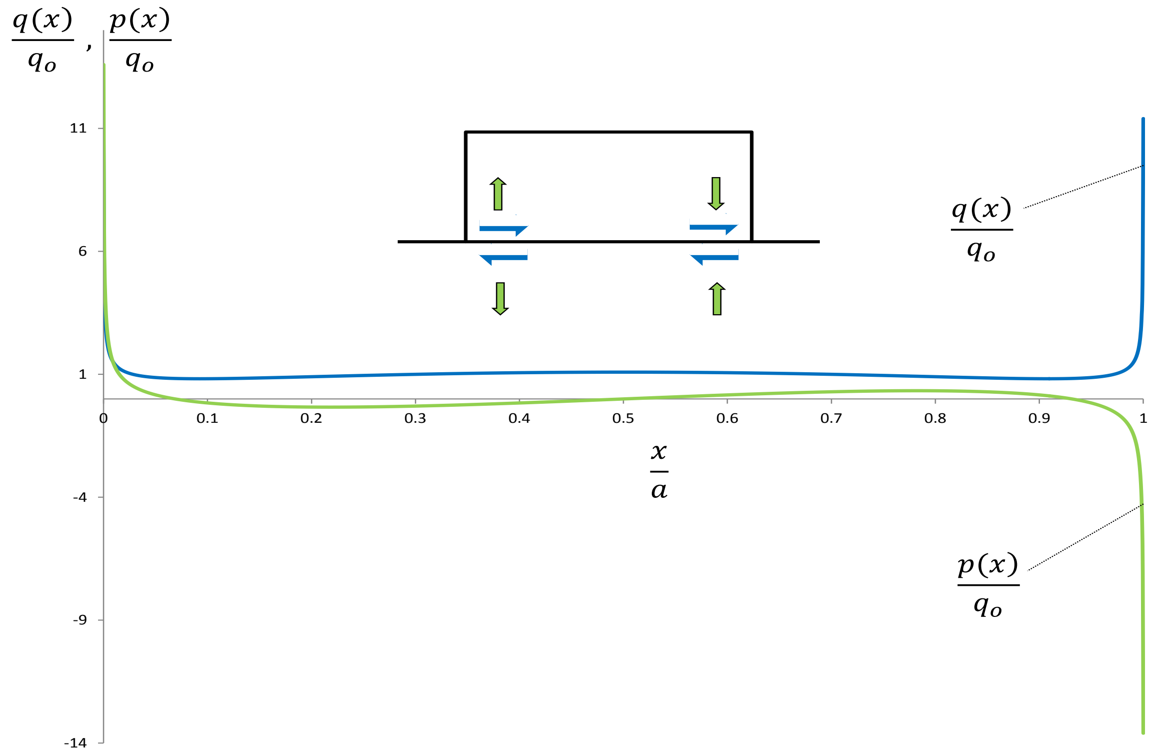

Figure 4.4(b): The normal and shear tractions as a result from the application of shear load (Q) to the monolithic model.

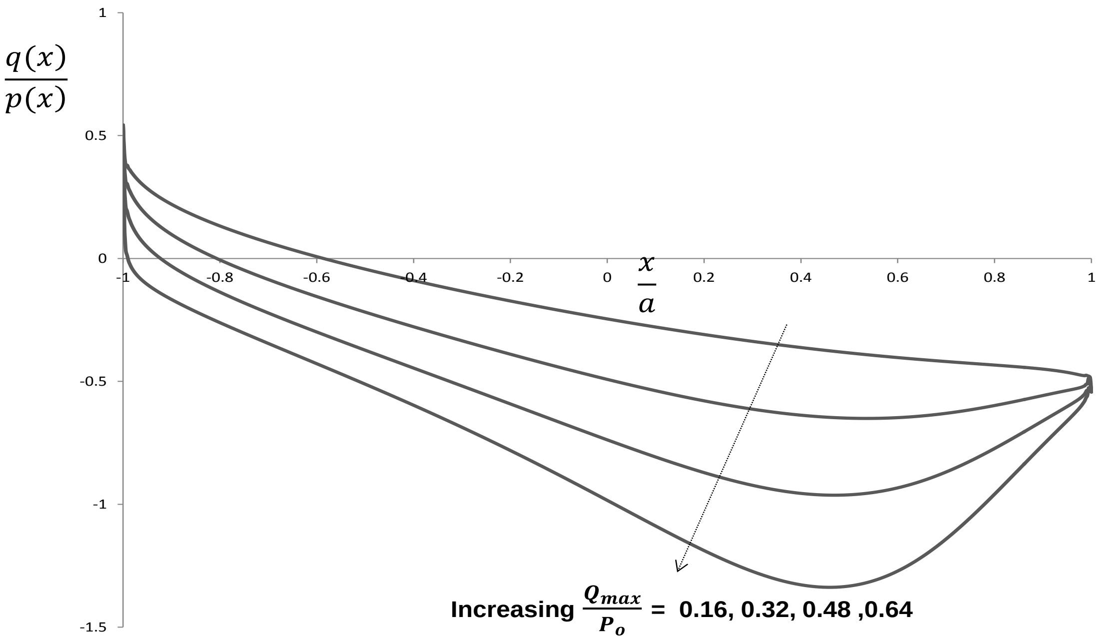

Figure 4.5: The ratio of shear to normal tractions $\frac{q(x)}{p(x)}$ as a function of $\frac{Q_{max}}{P_o}$ from a monolithic model in Figure 4.1.

2) Interior slip

Further increases in applied shear load in loading step 2, shifts the maximum of traction ratio from the edge of the contact to the interior point. For example, it can be seen from Figure 4.5 that the maximum is shifted from $\frac{x}{a} = 1$ to about $\frac{x}{a} = 0.5$ .This means the slip zone will be initiated from the interior point. This loading regime will be focussed on in this chapter.

3) Gross sliding

This is the case when a contact is in a full sliding state at the coulomb limit $Q(t) = fP(t)$. It is not possible for a contact to shake down when it is this loading regime.

4.3 Shakedown Calculation

4.3.1 Approximate solution methods

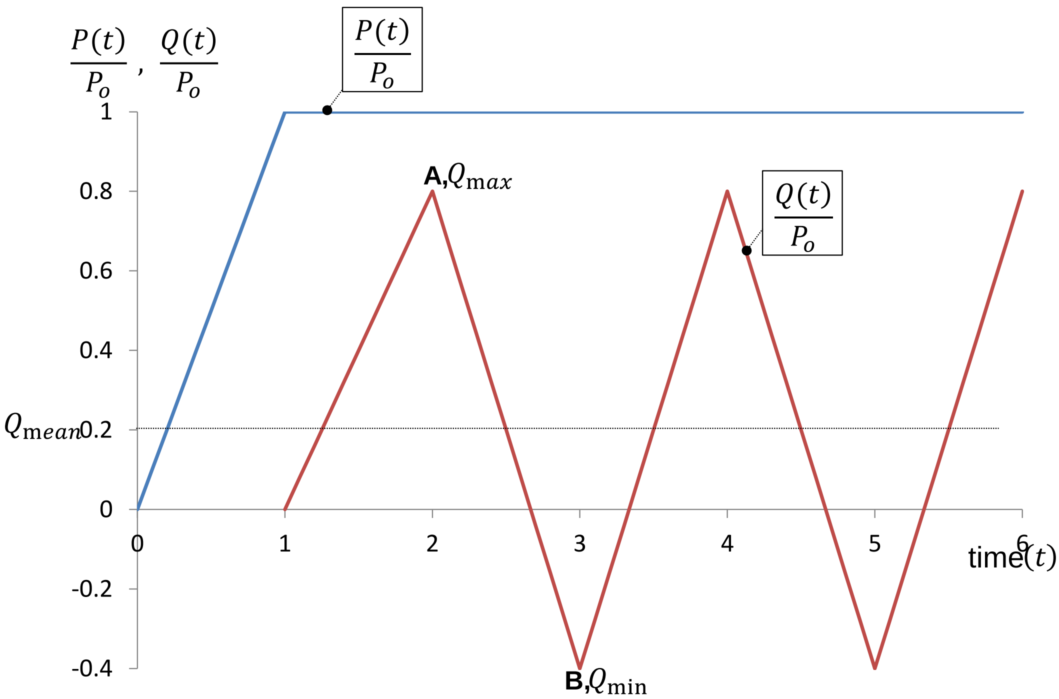

Figure 4.6: Loading History.

I will now turn to a detailed shakedown analysis of the example problem in Figure 4.1 under constant normal load P and cyclic shear loading $Q(t)$. The loading history of the problem is displayed in Figure 4.6.

4.3.1.1 No Coupling Effects

The problem in Figure 4.1 is treated again, but this time the shear load is cycled between some minimum values $Q_{\min}$ to maximum values $Q_{\max}$. I now attempt to predict the shakedown limit by an approximate procedure in which only the residual interfacial shearing traction is allowed to develop and the change of contact pressure distribution is approximated to be zero. In explaining the procedure for this estimate, it is convenient to start with the simplest loading history where the shearing force is varied from zero to a maximum value. Consider the interfacial tractions and admit the presence of an interfacial residual shearing traction distribution, $q_{res}(x)$. The resulting traction ratio is

$$\frac{q(x)}{p(x)} = \frac{p_o \tilde{q}_p(x) + q_o \tilde{q}_q(x) + q_{res}(x)}{p_o \tilde{p}_p(x) + q_o \tilde{p}_q(x)} \tag{4.4}$$

Divide by p_o and this gives

$$\frac{q(x)}{p(x)} = \frac{\tilde{q}_p(x) + \lambda \tilde{q}_q(x)}{\tilde{p}_p(x) + \lambda \tilde{p}_q(x)} + \frac{q_{res}(x) / p_o}{\tilde{p}_p(x) + \lambda \tilde{p}_Q(x)} \tag{4.5}$$

where $\lambda = \dfrac{q_o}{p_o}$. Since the shear force is cycled between 0 and a maximum value of $Q_{\max}$, the load factor varies over the range $[0 \quad \lambda_{\max}]$. I now set conditions of incipient forward and reverse slip at the point of maximum shear force in the cycle and the point of minimum shear force, so that

$$f = \frac{\tilde{q}_p(x) + \lambda_{\max}\tilde{q}_q(x)}{\tilde{p}_p(x) + \lambda_{\max}\tilde{p}_q} + \frac{q_{res}(x)/p_o}{\tilde{p}_p(x) + \lambda_{\max}\tilde{p}_q(x)} = -\frac{\tilde{q}_p(x)}{\tilde{p}_p(x)} - \frac{q_{res}(x)/p_0}{\tilde{p}_p(x)} \tag{4.6}$$

The implementation of this shakedown limit calculation consists of setting the maximum value of the traction ratio, $\frac{q(x)}{p(x)}$, equal to the minimum coefficient required to prevent slip in both directions, f_M, but also allowing for a residual shearing traction, $q_{res}(x)$, to self-develop, so that

$$f_M = \left|\frac{q(x)}{p(x)}\right|_{\max} = \left|\frac{q_A(x) + q_{res}(x)}{p_A(x)}\right|_{\max} = \left|\frac{q_B(x) + q_{res}(x)}{p_B(x)}\right|_{\max} \tag{4.7}$$

and,

$$\left(\frac{q_A(x) + q_{res}(x)}{p_A(x)}\right) = -\left(\frac{q_B(x) + q_{res}(x)}{p_B(x)}\right). \tag{4.8}$$

Next I use equation 4.8 to solve for the residual shearing traction distribution, $q_{res}(x)$, in terms of the normal and shearing tractions along the interface at the two extreme points in the loading cycle, $q(x), p(x)$. I then substitute this expression for $q_{res}(x)$ into the equation 4.7 and simplify to give

$$f_M = \left|\frac{q_A(x) - q_B(x)}{p_A(x) + p_B(x)}\right|_{\max} \tag{4.9}$$

I will now examine in detail an example problem when the coefficient of friction is 0.83 and where the corresponding shakedown load factor implied is $\lambda_{max} = \frac{Q_{max}}{P_o} = 0.8$ and $\lambda_{min} = \frac{Q_{min}}{P_o} =$ - 0.4. For this case, Figure 4.7 shows the shear traction $\frac{aq(x)}{P_o}$ and the direct traction distribution multiplied by the coefficient of friction $\pm\frac{afp(x)}{P_o}$ present along the contact interface at the $Q(t) = Q_{max}$ points in the loading cycle. Note that I normalise the tractions with respect to the steady-state constant normal load P_o and the contact half-width, a. The slip zone is between the position $\frac{x}{a} = -0.25$ and $\frac{x}{a} = 0.88$.

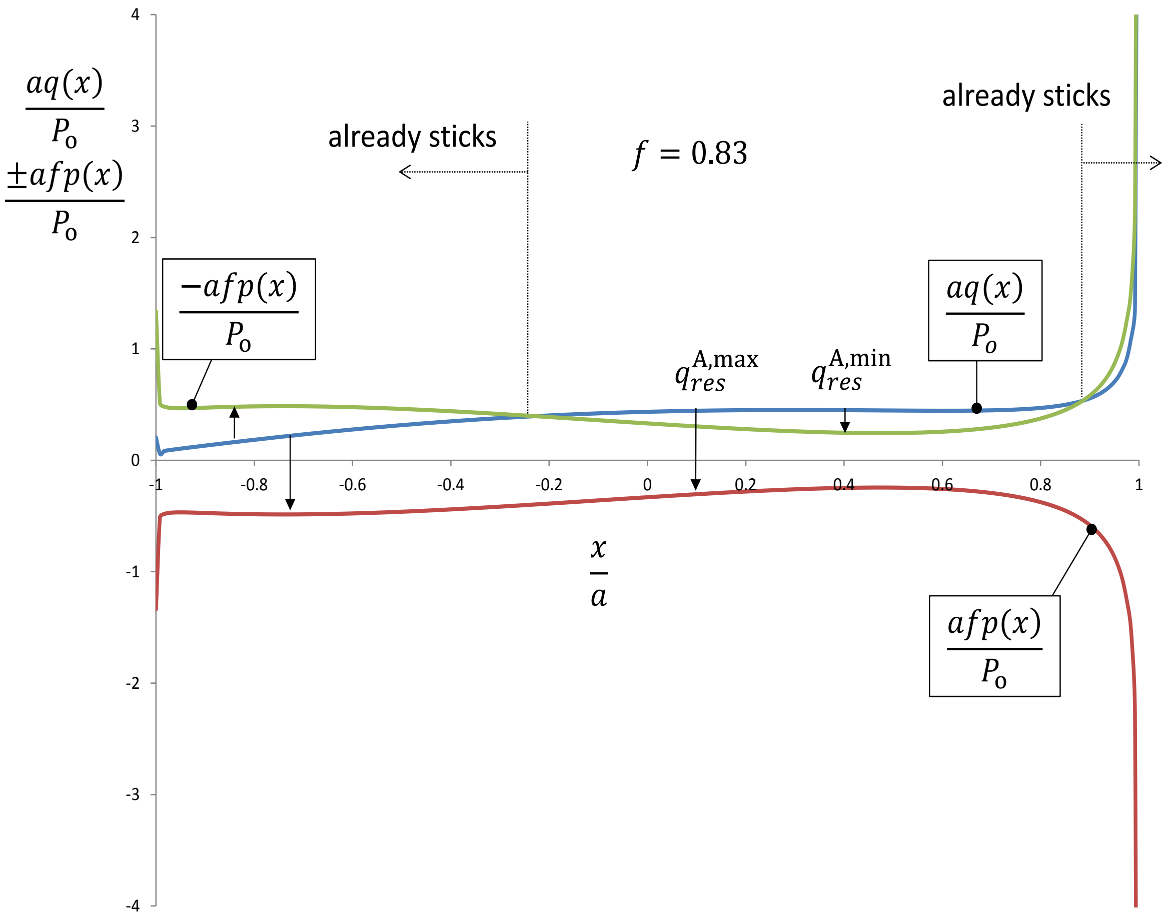

Figure 4.7: Interfacial shear and normal tractions at $Q(t) = Q_{max}$ in the loading cycle. (Point A in Figure 4.6)

This makes it clear, for all values of x, what permissible residual shearing tractions may be present to ensure full adhesion everywhere, and which I will denote by $\left(q_{res}^{A\,\min}(x) < q_{res}(x) < q_{res}^{A\,\max}(x)\right)$.

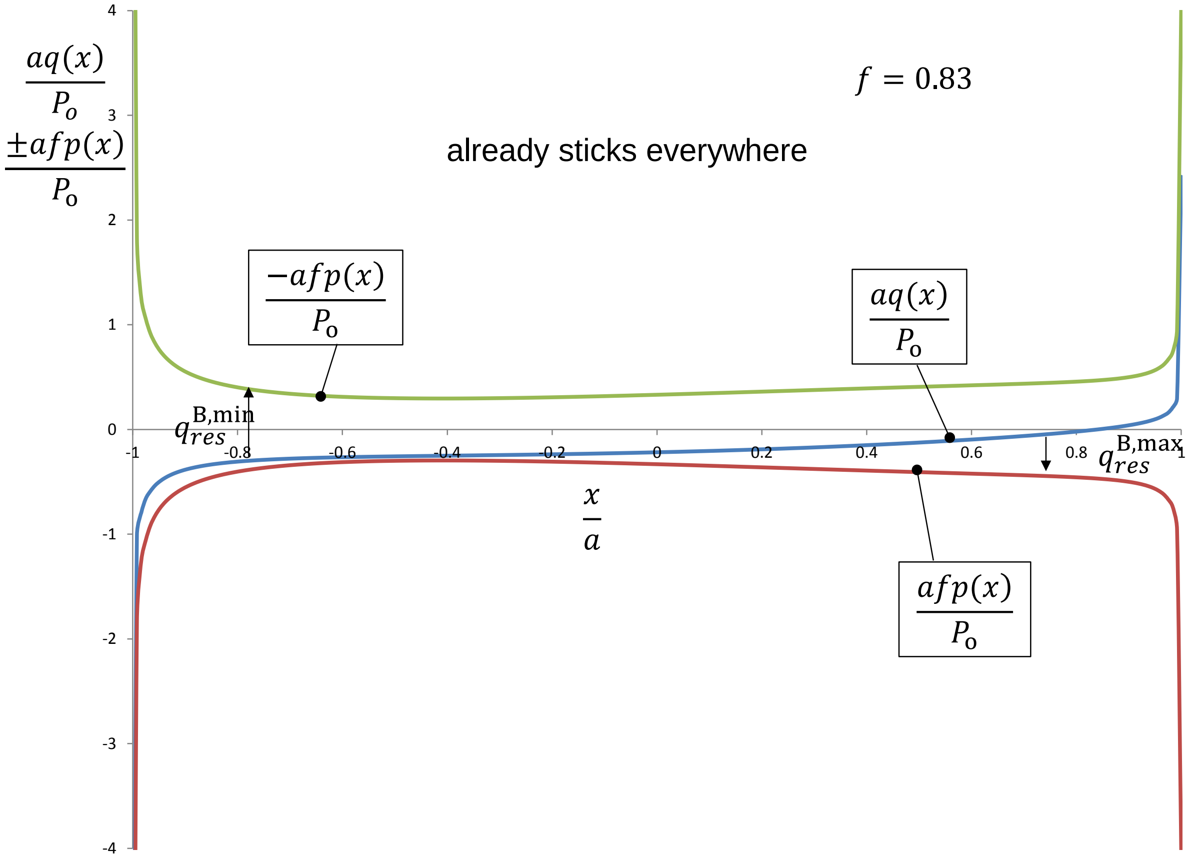

Figure 4.8: Interfacial shear and normal tractions at $Q(t) = Q_{\min}$ in the loading cycle. (Point B in Figure 4.6)

Similarly, Figure 4.8 shows the normalised shear traction distribution, $\frac{aq(x)}{P_0}$, and the normalised direct traction distribution, $\frac{ap(x)}{P_0}$, multiplied by coefficient of friction present along the contact interface, when the applied shearing force is minimum.

Notice that the shear traction distribution is below both limits, $\pm \frac{fap(x)}{P_0}$, and this suggests the contact interface already sticks everywhere. The range of permissible residual shear traction is denoted by $\left(q_{res}^{B\ \min}(x) < q_{res}(x) < q_{res}^{B\ \max}(x)\right)$. These four bounding lines are plotted together in Figure 4.9. This shows that, as expected, there is a unique value of residual shearing traction present at the critical point which permits all four inequalities to be satisfied but, elsewhere, there is a range of values of $q_{res}(x)$ all of which would be equally acceptable.

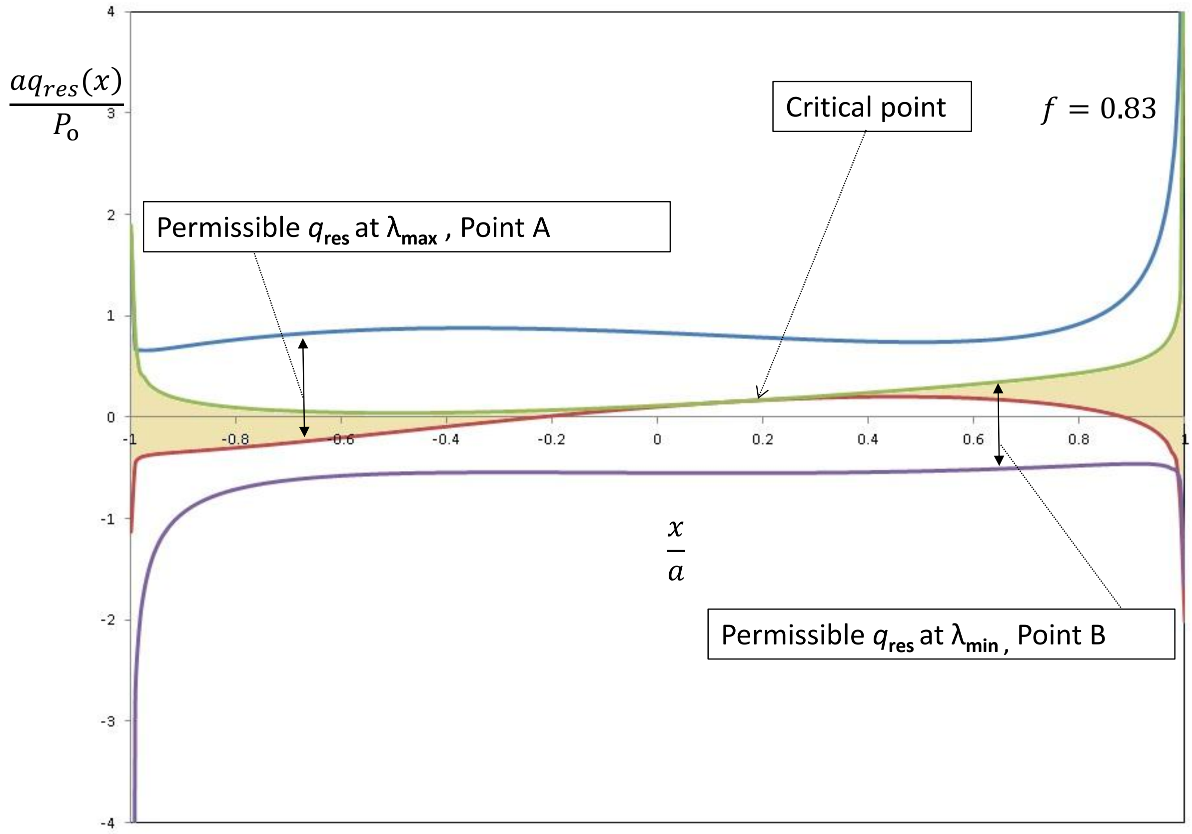

Figure 4.9: The range of permissible residual shearing tractions from the first calculation where only redistribution of shear traction is allowed.(f = 0.83)

In this initial calculation of an approximate algorithm, I developed the proposed residual shear traction distribution in a pointwise fashion. Therefore a resultant of shearing traction distribution may not be equal to zero. However, the shearing traction distribution, whose resultant is approximately equal to zero, will be selected. This will be used in the second calculation where I take the change of contact pressure into consideration as described in the next sub-section.

4.3.1.2 Allowance for Coupling Effects

Let now also take into account the effect of the change in contact pressure using the reduced stiffness method. First, I use the procedure described in Chapter 3 to work out the reduced stiffness matrices for each contacting body which are the square elastic block and an elastically similar half-plane. Each reduced stiffness matrix can then be employed to obtain the combined stiffness matrix. The stiffness matrix relates the slip displacement to interfacial shear and normal forces and it can be written as

$$\begin{Bmatrix} q_i(t) \\ p_i(t) \end{Bmatrix} = \begin{bmatrix} A_{ij} & B_{ij} \\ B^T_{ij} & C_{ij} \end{bmatrix} \begin{Bmatrix} v_j(t) \\ w_j(t) \end{Bmatrix} \tag{4.10}$$

where $v_j(t)$ is the slip displacement, $w_j(t)$ is the normal displacement, $p_i(t)$ and $q_i(t)$ are the normal and shear reaction forces respectively. Hence, the normal and shear tractions from previous calculations will be converted to forces by multiplying them by the average element area. The shakedown phenomenon of the contact will only take place if the relative normal displacements of the contact particles are equal to zero, $w_j(t) = 0$. This is mainly because if the normal contact reactions are equal to zero the self-generated residual interfacial shearing tractions along the contact interface cannot be sustained. Hence, the system of equations 4.10 is reduced to

$$\begin{Bmatrix} q_i(t) \\ p_i(t) \end{Bmatrix} = \begin{bmatrix} A_{ij} \\ B^T_{ij} \end{bmatrix} \{ v_j(t) \} \tag{4.11}$$

In this procedure, one of the residual shear traction distribution, $q_{res}(x)$, whose resultant is very close to zero, is selected as shown in Figure 4.10. This is because it is required that the residual interfacial shearing traction needs to be self-equilibrating.

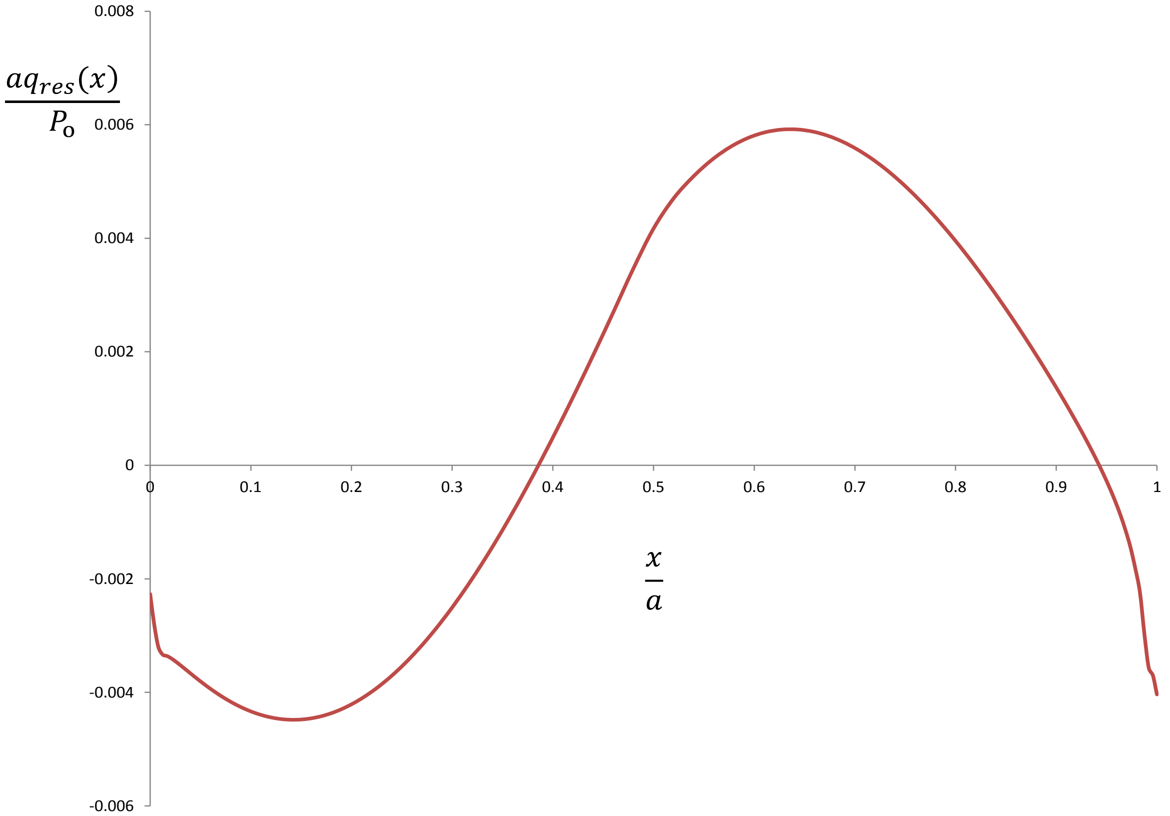

Figure 4.10: The permissible residual shearing traction whose resultant is very close to zero.

The selected shear traction $q_{res}(x)$ is then converted to a force $q_{res,i}$ by multiplying it by the average element area. I can now substitute $q_{res,i}$ in equation 4.12 and solve for the corresponding tangential displacement. The tangential displacement is calculated using single value decomposition because the stiffness matrix is singular. The slip displacement result is portrayed in Figure 4.11.

$$A_{ij} v_j = q_{res,i} \tag{4.12}$$

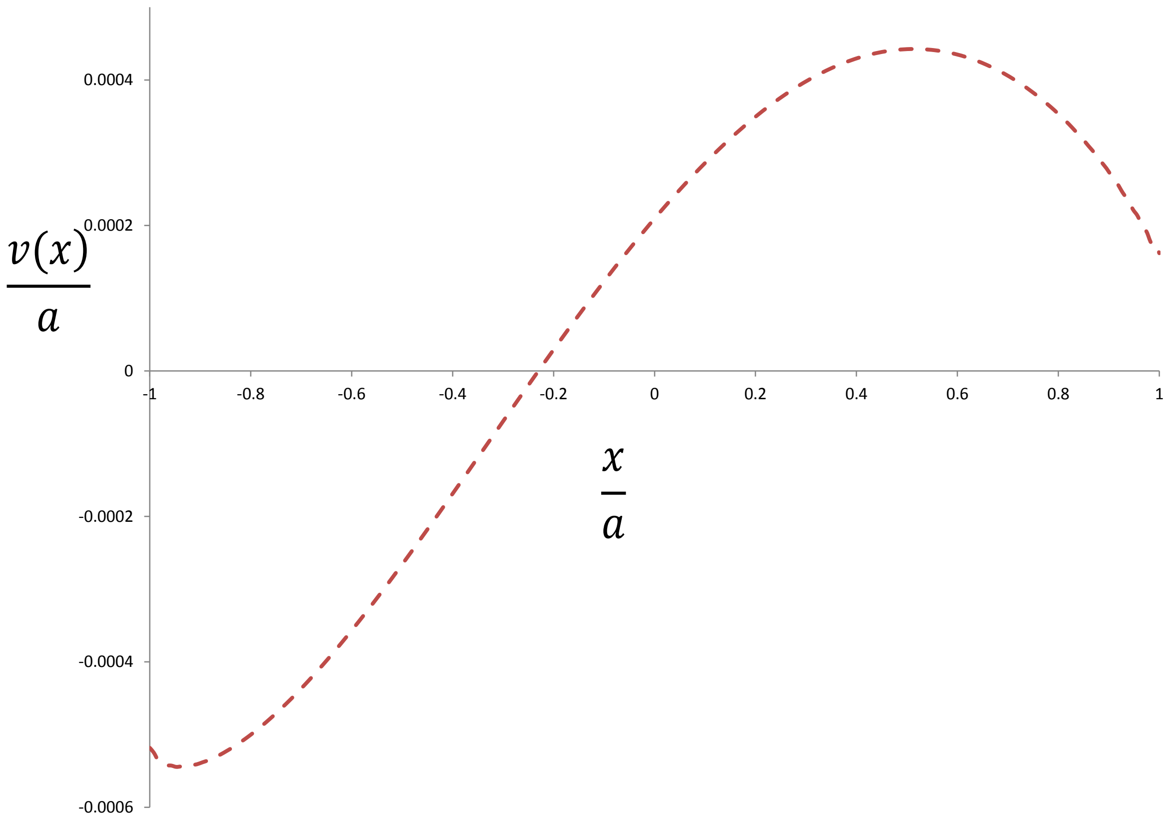

Figure 4.11: Tangential displacement associated with one residual shear traction distribution in Figure 4.10.

Then the corresponding tangential displacement v can then be substituted into equation 4.13 to find the corresponding value of $p_{res,i}$.

$$p_{res,i} = B_{ij}^{T} v_j \tag{4.13}$$

The change of nodal normal reaction force $p_{res,i}$ is now converted back to normal traction $p_{res}(x)$ by the division of the average element area. The results are plotted in Figure 4.12 and it can be seen that the sum of the residual normal traction is equal to zero so it is in self-equilibrium.

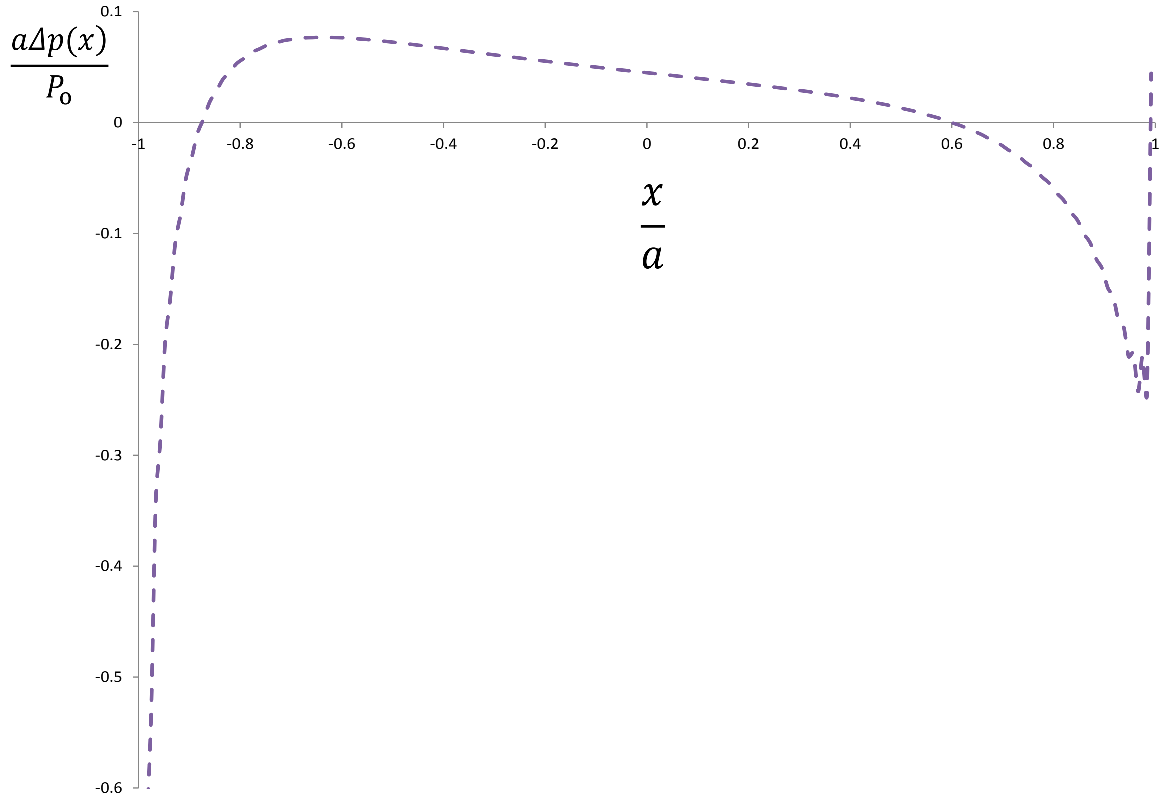

Figure 4.12: Change in contact pressure corresponding to the shakedown slip displacement.

The change of contact pressure is then superimposed on the results found. I can now plot the permissible range of residual interfacial shearing tractions at the same coefficient of friction as displayed in Figure 4.13. It shows that there is an overlapping region and this means the contact will not shake down at this friction coefficient, f = 0.83. For a contact to undergo a fully adhered state at steady state, I can either increase the coefficient of friction or reduce the load factor. For the load factors, I can either reduce the ratio maximum shear to normal loads, $\frac{Q_{max}}{P_o}$ or $\frac{Q_{min}}{P_o}$. However, the load factors are fixed for this calculation so that I will, instead, increase the friction coefficient. Graphically, this effect will result in a translation of the curves such that there is only one critical point where all four inequalities of the permissible residual shear tractions are satisfied.

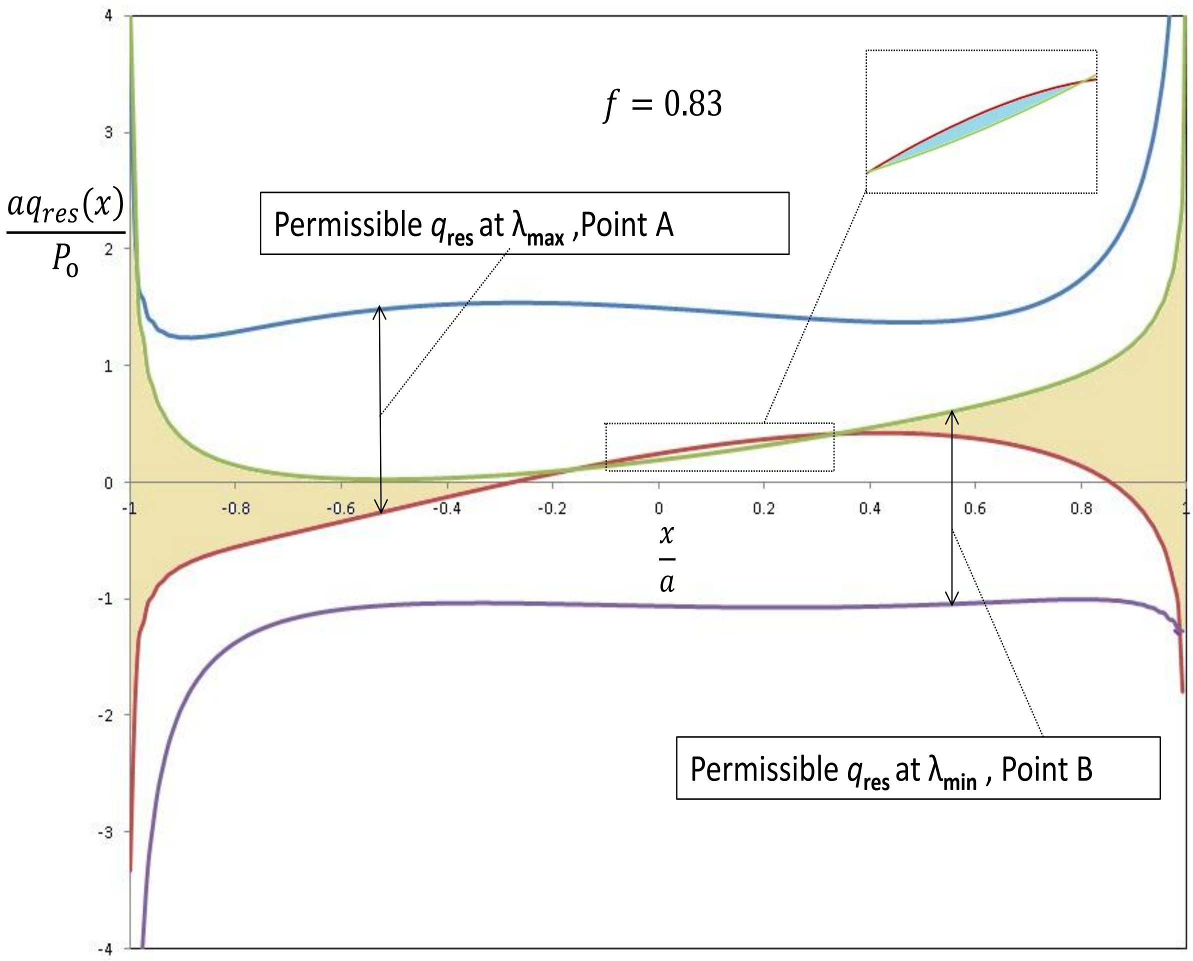

Figure 4.13: The permissible range of residual shear tractions at proposed shakedown limit obtained from the first calculation.(*f* = 0.83)

Using the equation 4.7, I can re-calculate the new minimum coefficient of friction needed for a contact to shake down and it is equal to 0.87. Let us now re-plot interfacial traction distributions at this new value of friction coefficient, Figure 4.14. By increasing coefficient of friction it shifts the bounding lines such that they touch at a point. This implies the contact will shake down at this coefficient of friction for these particular load factors $\lambda_{max} = 0.8$ and $\lambda_{min} = -0.4$.

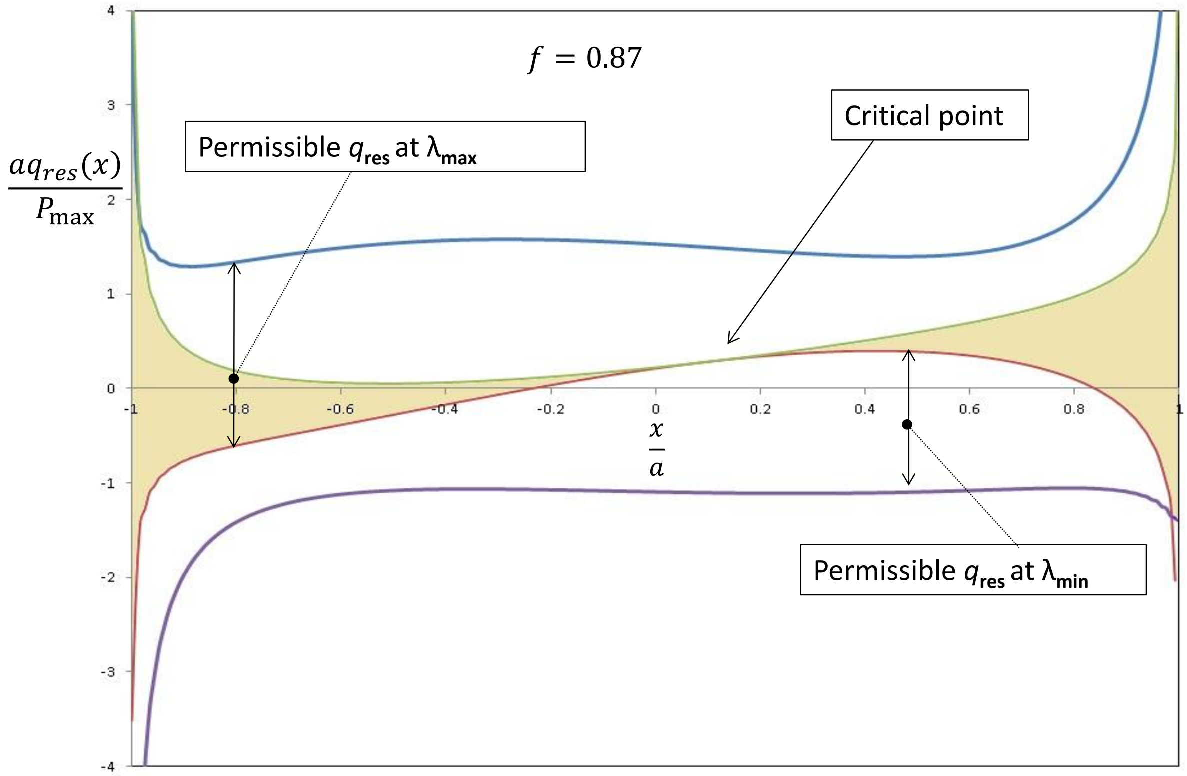

Figure 4.14: the permissible range of residual shear tractions at the shakedown limit obtained from the second calculation.(*f* = 0.87)

4.3.2 Exact-solution method

In the first approximated algorithm, only one of the manifestations of the coupling phenomenon is taken into account which is the redistribution of interfacial shearing traction. The change of contact pressure is then taken into consideration for the second approximated algorithm. However, this is not an optimal solution because the residual shear and normal tractions cannot be chosen independently.

I will now attempt to find the actual optimal conditions under which the interface will shake down to a fully adhered state after some initial slip. In this exact solution algorithm, I consider the development of an interfacial tangential displacement which can vary along the contact interface but remains constant with time. The tangential displacement is modelled by an array of glide dislocations and this would give rise to both interfacial shear and normal tractions. For a given set of tangential displacement distribution, the corresponding residual tractions can be calculated using the reduced stiffness procedure. By doing it in this way, I allow redistribution of both interfacial shear and normal tractions. The optimal tangential displacement distribution is the one which would enable the contact to achieve a fully adhered state for the highest possible load factor. This is regarded as a shakedown limit and this algorithm is a rigorous implementation of the Melan shakedown theorem[98].

Let us now consider the example problem, Figure 4.1, again where a square elastic punch is pressed against an elastically similar half-plane by a constant normal load P and also subjected to a cyclically varying shear force Q (see Figure 4.6). Suppose the coefficient of friction is artificially large such that all the particles along the contact interface are prevented from moving. The interfacial shear and normal forces due to the time-varying external loads are given by

$$p_i(t) = p_i^w(t) \tag{4.14}$$

$$q_i(t) = q_i^w(t) \tag{4.15}$$

If, now, the friction coefficient becomes finite so that the contacting particles are allowed to move then the change in either normal or tangential displacements will modify both shear and normal forces. This is because there is a considerable degree of coupling in this example problem and this effect can be described by equation 4.16 and 4.17.

$$q_i(t) = q_i^w(t) + A_{ij}\sum_{j=1}^{N} v_j(t) + B_{ij}\sum_{j=1}^{N} w_j(t) \tag{4.16}$$

$$p_i(t) = p_i^w(t) + B_{ij}^T\sum_{j=1}^{N} v_j(t) + C_{ij}\sum_{j=1}^{N} w_j(t) \tag{4.17}$$

where N is the total number of contact nodes, q_i is tangential force and p_i is the normal force. The constants $A_{ij,}$ $B_{ij,}$ B_{ij}^T and C_{ij} are the sub-matrices of the reduced stiffness matrix as defined in equation 3.26 (Chapter 3). For an uncoupled system the sub-matrices B_{ij} will be equal to zero where the residual normal traction is not affected by the presence of tangential displacement. This is sometimes known as a coupling term. For a contact to shake down (to a fully adhered state), all contact particles must remain on the plane of the contact interface. This 'no separation' constraint can be described by

$$w_j(t) = 0 \tag{4.18}$$

$$p_j(t) > 0 \tag{4.19}$$

Using the required condition, equations 4.16 and 4.17 can be written as

$$q_i(t) = q_i^w(t) + A_{ij}\sum_{j=1}^{N} v_j(t) \tag{4.20}$$

$$p_i(t) = p_i^w(t) + B_{ij}^T\sum_{j=1}^{N} v_j(t) \tag{4.21}$$

The optimal solution can be calculated by finding a set of tangential displacement which maximises the possibility of shakedown. The optimal tangential displacement can be defined as the time-independent displacement which minimises the maximum of total shear to normal tractions $\left|\frac{q(x)}{p(x)}\right|_{\max}$. Note that the nodal forces are converted to tractions by division of the element area. This is a non-linear optimisation problem subjected to constraints. The optimal displacement is calculated in MATLAB using the 'fmincon' function and interior point algorithm as an optimisation method. The lower and upper bounds of nodal displacement at each contact node is ± 10% of the element width.

First, assemble the matrix in equation 4.20 and 4.21 so that they are in the form

$$A_{eq}x = B_{eq}, \tag{4.22}$$

where A_{eq} and B_{eq} are matrices and x is the vector. This gives

$$\begin{bmatrix} 1 & 0 & -A_{ij} \\ 0 & 1 & -B_{ij}^{T} \end{bmatrix} \begin{bmatrix} q_i(t) \\ p_i(t) \\ v_j \end{bmatrix} = \begin{bmatrix} q_i^w(t) \\ p_i^w(t) \end{bmatrix}. \tag{4.23}$$

The inputs A_{ij}, B_{ij}^{T}, $q_i^w(t)$ and $p_i^w(t)$ are obtained from the reduced stiffness method explained in Chapter 3. The loading conditions of the problem will be kept the same as those analysed in the first two approximated method ($\lambda_{\max} = 0.8$ and $\lambda_{\min} = -0.4$). The function will then attempt to search the time-independent v_j which leads to a minimum value of $\left|\frac{q(x)}{p(x)}\right|_{\max}$ subjected to the constraints. This minimum value is the friction coefficient required for a contact to shake down because the magnitudes of maximum traction ratios at two extreme points in the loading cycle are equal to this value. The output of optimal tangential displacement is shown in Fig.4.15 and the minimum friction coefficient needed for a shakedown for the case when $\lambda_{max} = 0.8$ and $\lambda_{min} = -0.4$ is 0.85. This value is actually between the predicted values from the first two calculations. In the first calculation I approximate the change of contact pressure to be equal to zero and this shows that the predicted shakedown calculation is slightly overestimated. This means the contact will not shake down at the predicted load factor but it will at a lower load factor. In the second calculation, I estimate the change of contact pressure based on one of the residual shear distribution whose resultant is close to zero. It shows that the shakedown limit is slightly underestimated so that the contact can actually shakedown at a higher load factor.

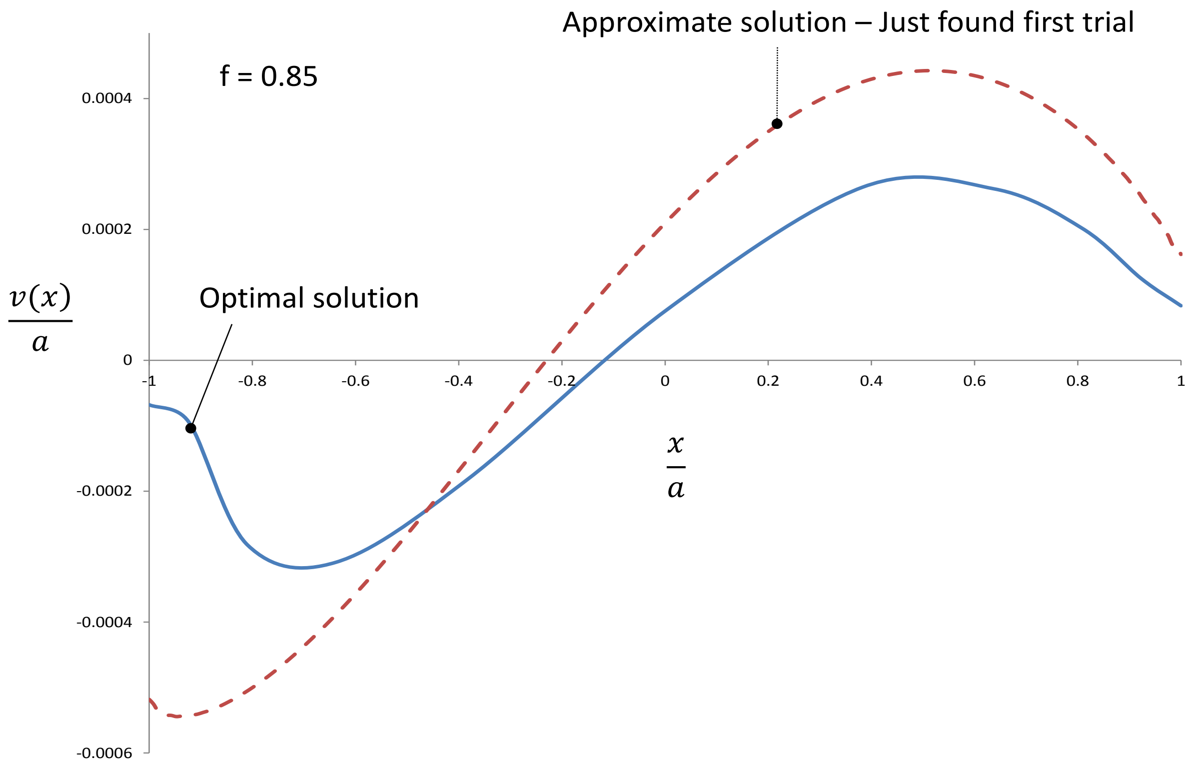

Figure 4.15: The comparison of the optimal and approximated tangential (slip) displacement distributions.

I can then work out the corresponding residual normal and shear tractions. The results are displayed in Figure 4.16.

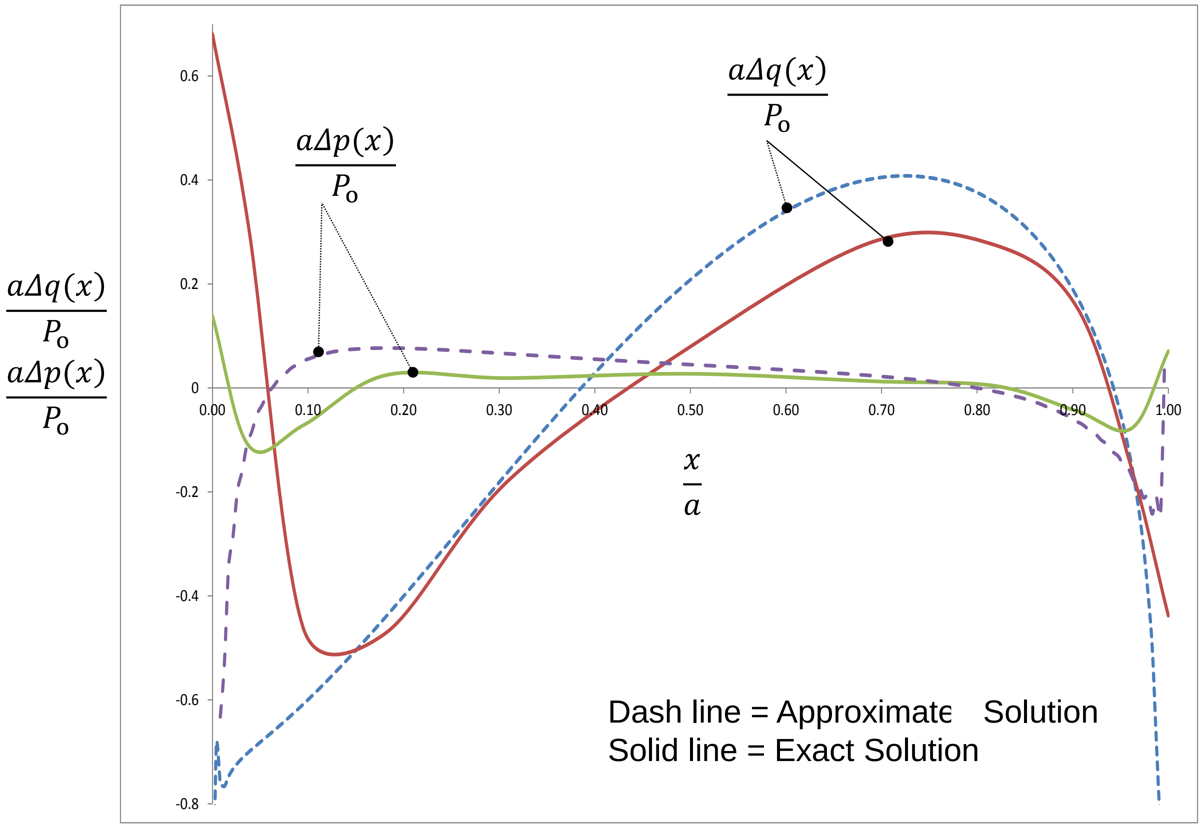

Figure 4.16: The comparison of the residual shear and normal tractions from the first approximate method and exact-solution method.

Using the residual interfacial traction corresponding to the optimal displacement in Figure 4.16, I can plot the permissible range of the residual shear traction as shown in Figure 4.17. The optimal residual shear traction is also plotted as a dashed line and it is in the permissible region as expected.

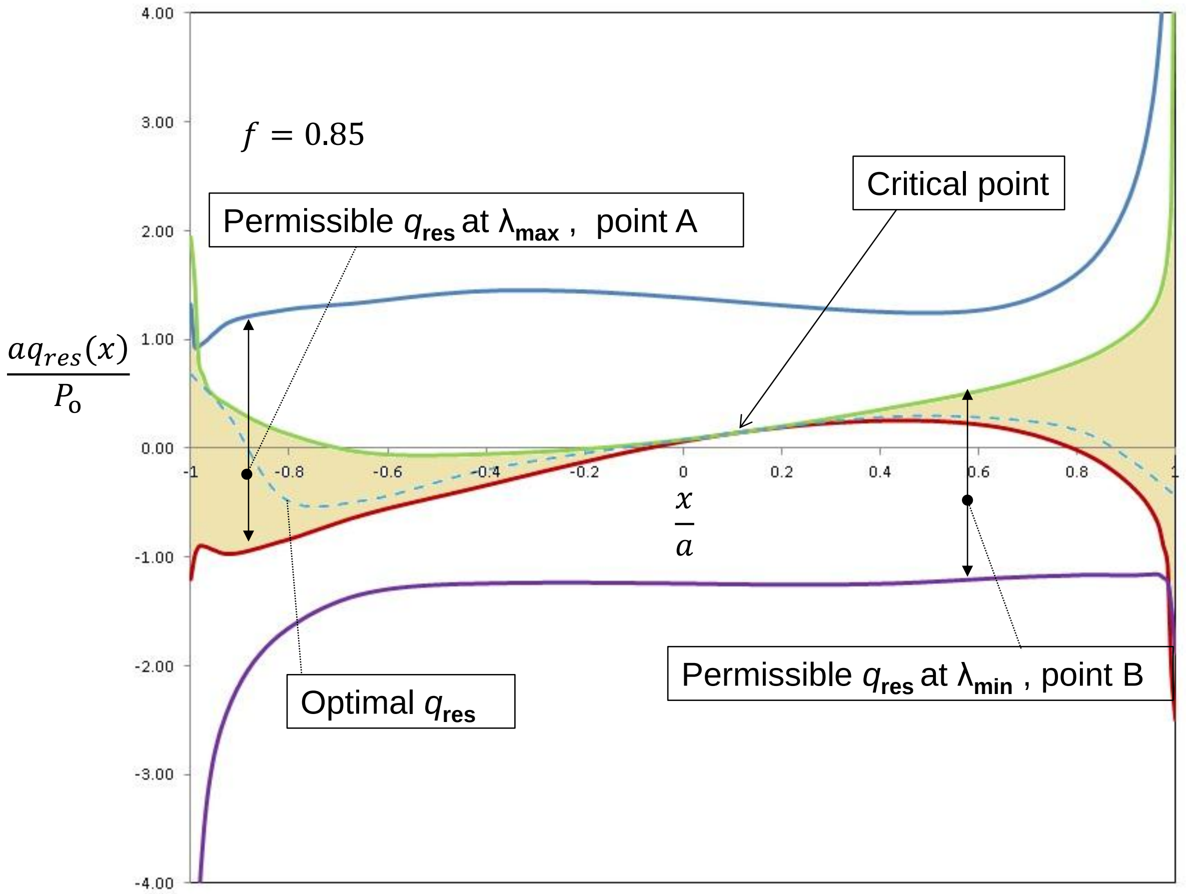

Figure 4.17: The range of permissible residual shearing tractions as well as an optimal residual shear traction distribution from the exact-solution method.(f = 0.85)

So far I have only analysed one example case but the procedures can be applied to other loading conditions. Before proceeding to the shakedown analysis of other loading conditions, let us define a dimensionless parameter, R , which represents the degree of shear load reversal.

$$R = \frac{Q_{min}}{Q_{max}} \quad , \qquad -1 \le R < 1 \tag{4.24}$$

I will now calculate the true shakedown limit of other loading conditions using the exact solution algorithm and a summary of the results is plotted in Figure 4.18.

For a higher degree of shear load reversal, it is more difficult for a contact to shake down and therefore the coefficient of friction increases. The most extreme case is when the value of R

is equal to a negative one ($Q_{max} = -Q_{min}$) where the shear load is fully reversed at successive time steps. Conversely, when the value of R becomes more positive the minimum frictional coefficients required for shakedown decreases. As the value R approaches a positive one the minimum coefficient required for shakedown is just slightly greater than the limiting frictional coefficients. The shakedown limit boundaries for three different loading histories (R = -0.5, -0.75 and -1) are shown in Figure 4.18 and the results can be used to predict the steady state behaviour of the problems with similar geometries and loading conditions. As an example in interpreting Figure 4.18, suppose that the problem is under fully reversing shear load $(R = -1)$, the contact will shake down if $\frac{Q_{max}}{fP_o} < 0.68$.

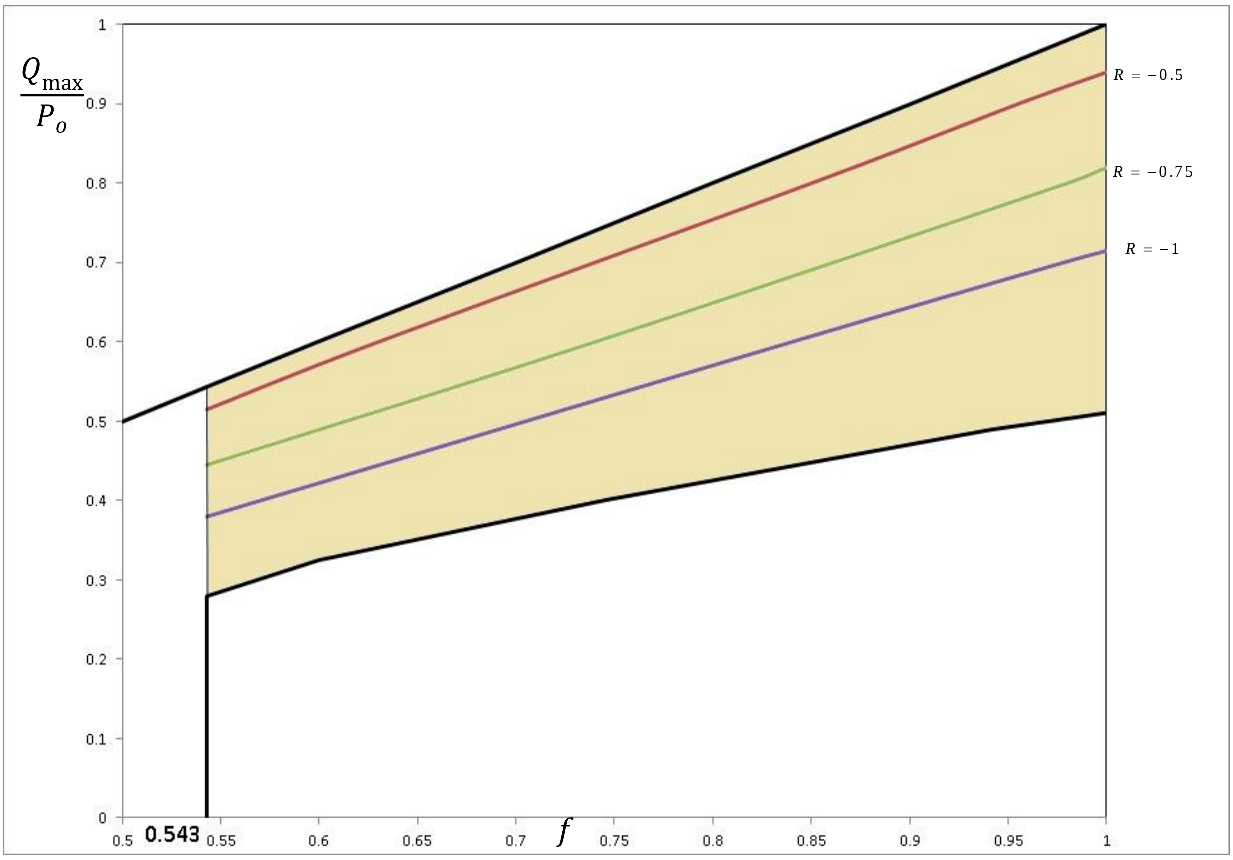

Figure 4.18: Interfacial response at steady state of the complete contact as shown in Figure 4.1 and subject to loading history in Figure 4.6.

In summary, the contact will shake down to a fully adhered state provided that the points in

f , $\frac{Q_{max}}{P_o}$ space of Figure 4.18 are below or to the right of the corresponding shakedown line with the degree of shear load reversal, R . The contact will exhibit cyclic response if the points lie above the shakedown line.

4.4 Marching in time solution and steady state response

Marching in time numerical solutions by the finite element method are then obtained using the evolutionary algorithm developed in Chapter 3 and permitting the particles to move along the contact interface in both tangential and normal directions.

The Melan theorem, which was originally postulated for plastic shakedown, stated that if shakedown is possible then the contact would shake down regardless of all initial conditions. However, Barber[58] has shown that there are a range of load factors in which the shakedown of a contact depends on the nature of pre-existing residual stresses. As stated before, he defined these load factors as λ_1 and λ_2 . From previous section 4.3.2, I know values of λ_2 for different coefficient of friction as displayed in Figure 4.18. Consider an example case when $f = 0.85$, $\lambda_{max} = 0.8$ and $\lambda_{min} = -0.4$. To investigate the effect on initial conditions on steady state, different sets of initial tangential(slip) displacements will be inserted to generate pre-existing residual shear and normal stresses. These results will now be investigated to see if the interfacial response at steady state depends on any pre-existing conditions. The loading history of the model, which can be regarded as the service loading on the contact, is shown in Figure 4.6.

The frictional energy dissipation per unit cycle is

$$W = \frac{1}{T}\int_{o}^{T}\int_{-a}^{a} q(x,t)\Delta u(x,t)\,dx\,dt \tag{4.25}$$

where $q(x,t)$ is the interfacial shearing traction at position x along the contact plane and $\Delta u(x,t)$ is the tangential displacement at position x along the contact interface, a is the semi-contact width and T is the time period of the loading cycle.

The minimum coefficient of friction required for shakedown $f = 0.85$ at load factors of $\lambda_{max} = 0.8$ and $\lambda_{min} = -0.4$, which calculated from the exact-solution algorithm, will be fixed. The only variable will be the initial tangential displacement distribution. Three different sets of the initial tangential displacement will be inserted which are:

(1) zero initial condition

(2) optimal condition (as shown Figure 4.15)

(3) negative-optimal condition

I then carry out the marching in time numerical solutions of the problem and calculate the corresponding frictional energy dissipation. The results show that the contact shakes down after a number of loading cycles in case 1 and it can be seen in Figure 4.19 that there is no additional energy dissipation when the contact has shaken down. In case 2, there is no energy dissipation as the optimal residual stresses inhibit the development of the microslip zone. In case 3, the amount of the energy dissipation increases significantly because this initial condition reduces the normal reactions. Subsequently, the amount of dissipation per cycle decreases and cyclic slip occurs. Therefore this seems to suggest that the steady state behaviour of contacts depends on the initial conditions. However, the oscillation is very small as shown in Figure 4.19.

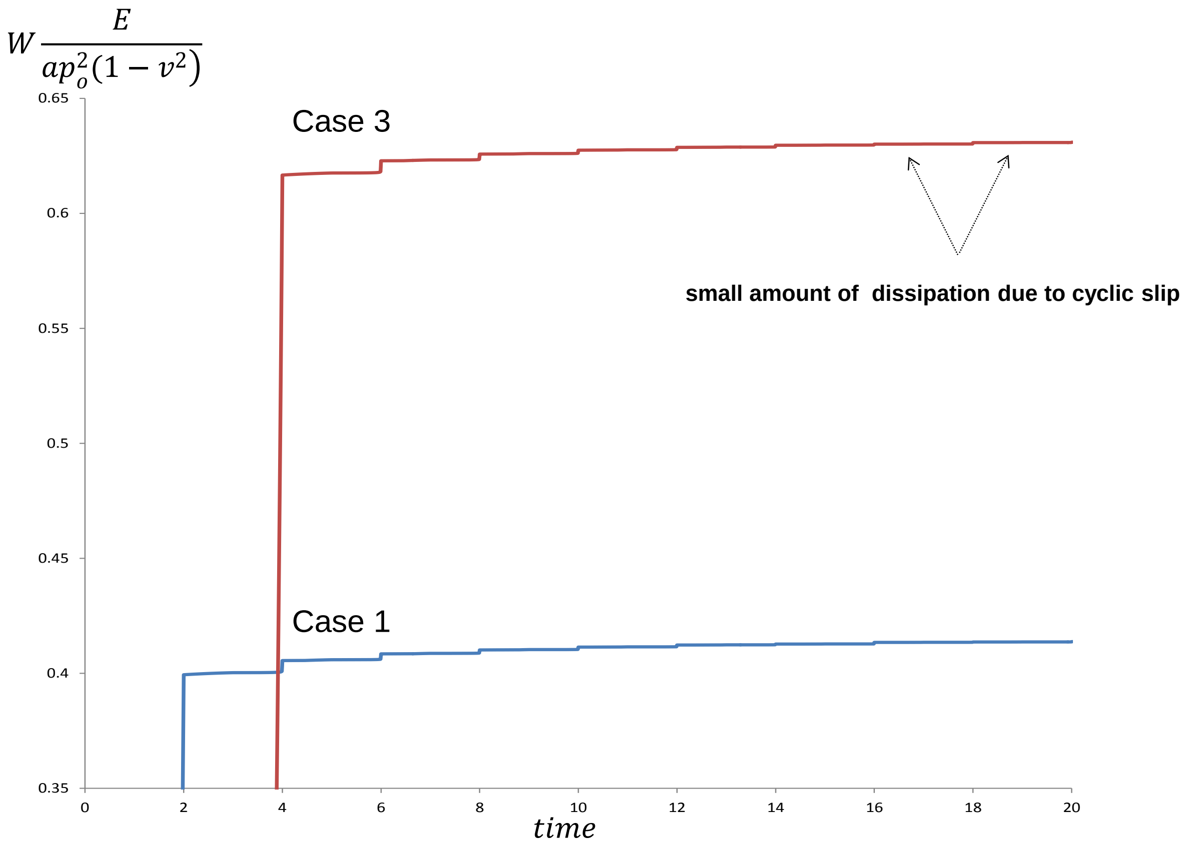

Figure 4.19: Total frictional energy dissipation of the different pre-existing residual stresses; case 1 and case 3.

Note that the marching in time numerical solution of the model can also be obtained using ABAQUS. However, the computational cost is much greater due to the need to run a high number of loading cycles and small time steps until the contact reaches the steady state. Plus, the solution in ABAQUS can sometimes be less stable when a considerable number of loading cycles is required to be run. It is difficult to tell whether this result reflects a real feature of the problem or is the remains of the regulation inherent in the contact elements.

4.5 Conclusion

The partial slip contact problem of a square elastic punch pressed on an elastically similar half-plane is studied. I restricted ourselves to the cases where the slip zone is initiated from the interior points, remote from the contact edge. This occurs when the coefficient of friction is greater than a critical value 0.543. If the complete contact exhibits edge slip then it is not possible for a contact to shake down because a reversing shear stress will cause separation. It follows that the contact pressure will fall to zero at the contact edge and therefore it prevents the development of any locked-in residual shear stress. Therefore only the cases whose values of friction coefficient are greater than the critical value were analysed in the shakedown analysis.

In this chapter, I have developed three different methods for shakedown calculations, without the computational expense of marching in time numerical solutions. The example problem of complete contact is analysed which may be the representation of the contact of a spline connection used to couple the shafts in the jet engine. It was shown that the first approximate algorithm for shakedown overestimated the true shakedown limit. The contact will only be able to shake down at a slightly lower load factor than the predicted value. This is because the redistribution of contact pressure had been neglected and the analysis was conducted in a pointwise fashion. In the second calculation, I allow for the coupling effect based on one of the permissible residual shearing traction distributions and re-calculate the approximate shakedown limit. It was observed that this second calculation underestimated the true shakedown limit because the shear and normal traction distributions cannot be chosen independently. In the second algorithm, I calculate the true shakedown limits using the tangential displacement which is modelled as a glide dislocation array. It can vary from point to point along the contact interface but remains constant in time. The tangential displacement gives rise to a self-consistent set of normal and shear tractions so that redistributions of both residual shear and normal tractions are taken into consideration. The true shakedown limit is calculated by finding the optimal set of tangential displacement. As expected, it was shown that the true shakedown limit is in the range of the limits based on the first two calculations. The analysis was then repeated with other loading conditions and the summary of the results are plotted in Figure 4.18 which shows shakedown limit boundaries for different loading conditions and friction coefficients.

I then take results from Figure 4.18 and carry out the marching in time cyclic loading analyses. Then investigate whether the contact will always shake down or is dependent on the initial conditions by inserting different sets of tangential displacements. It was found that the interfacial response of a contact at steady state seems to depend on the initial conditions. However, the energy dissipation due to cyclic slip is relatively small.

5 Plane Receding Contact

5.1 Introduction

There is considerable interest, currently, in the performance of bolted joints subject to vibratory loading, and how frictional damping affects the structural response. Bolted joints come into the category of 'receding' contacts, i.e. those where the initial application of a normal load leads to a reduction in the notional area of contact. Most are also 'coupled' in the sense that the normal load induces interfacial shearing traction because of a difference in the domains. As discussed in Chapter 4, Melan shakedown theorem [55] may not be applied in these cases, as the possibility of shakedown depends, critically, on the nature of any pre-existing residual stress. This, in turn, is very important practically because a shaken down contact provides little damping, whereas a contact undergoing cyclic slip provides considerable damping.

Relatively little is known about receding contacts. Pioneering work was undertaken by Dundurs and co-workers [49] in 1970s when the finite element method was still in its early stages of development and computational power was limited. Therefore, it was not easy to obtain accurate results. The purpose of this chapter is to provide a definitive solution to the plane receding contact problem, as shown in Figure 5.1. It consists of a semi-infinite elastic strip, of thickness t, pressed onto an elastically similar half-plane by a uniform normal load, P, and which is present up to distance *nt* from the strip end. The applied normal load is increased monotonically from zero to P_o and held constant. Hence, P_o is the steady-state normal load applied to the contact and corresponding constant pressure is $p_o = \frac{P_o}{w}$ where w is the length at which the load is distributed as shown in Figure 5.1(a). The motivation for studying this geometry is partly its simplicity and also because, under some circumstances, it will provide useful information about the performance of clamped flange assemblies. For example, it will enable us to infer how close to a flange edge bolts have to be mounted to inhibit separation and slip. It also reveals the 'starting conditions' when a bolted joint of what is sometimes called the 'high strength friction grip' kind is subjected to shear.

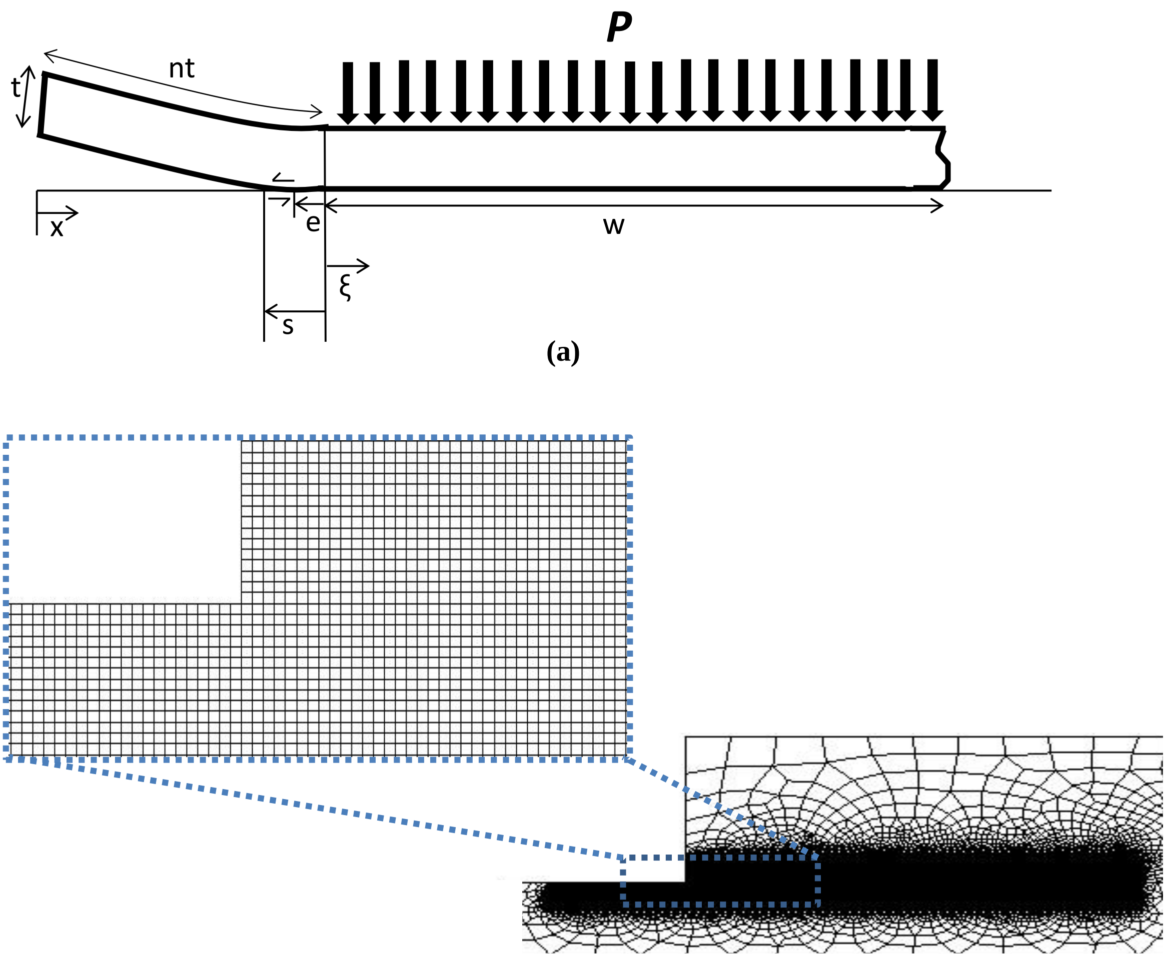

(a)

(b)

Figure 5.1: (a) Plane receding contact subjected to a constant normal load, *P* and (b) a finite element model.

5.2 Fully adhered problem

The problem is tackled using the well-known commercial finite element programme ABAQUS, with a very well refined and graded mesh, particularly in the neighbourhood of potential separation. A two-dimensional, 4-noded (bilinear), plane strain quadrilateral (CPE4) element was used. The convergence test was carried out to ensure the model is fully converged with different loading conditions and the mesh size at the contact interface is chosen to be $0.005t \times 0.005t$ where t is a thickness of the elastic strip as shown in Figures 5.1. As contact elements introduce difficulties of their own - for example the 'stiffness in stick' property has to be properly quantified, but for a mathematically perfect problem I would like it to be as high as practicable - I start the investigations by considering the layer and half-plane as a bonded homogeneous monolith. Then I look for the violations of the requirements that the interfacial direct traction must be negative everywhere, and where the magnitude of the shear traction, $q(x)$, exceeds $fp(x)$ where f is the coefficient of friction and $p(x)$ the contact pressure.

For small values of n no separation occurs, so that intimate contact is maintained right up to the end of the strip, and Figure 5.2 displays the ratio of $q(x)/p(x)$. The origin of the x-axis is set at the tip of the re-entrant corner as shown in Figure 5.1(a). Curves are plotted for various values of n. It will be seen that, by the time n has reached 0.8, maintenance of full adhesion would already require a coefficient of friction exceeding unity, and so results are not plotted for higher values of n. It should be noted that if the coefficient of friction were extremely high then the separation would finally occur when $n = 1.89$.

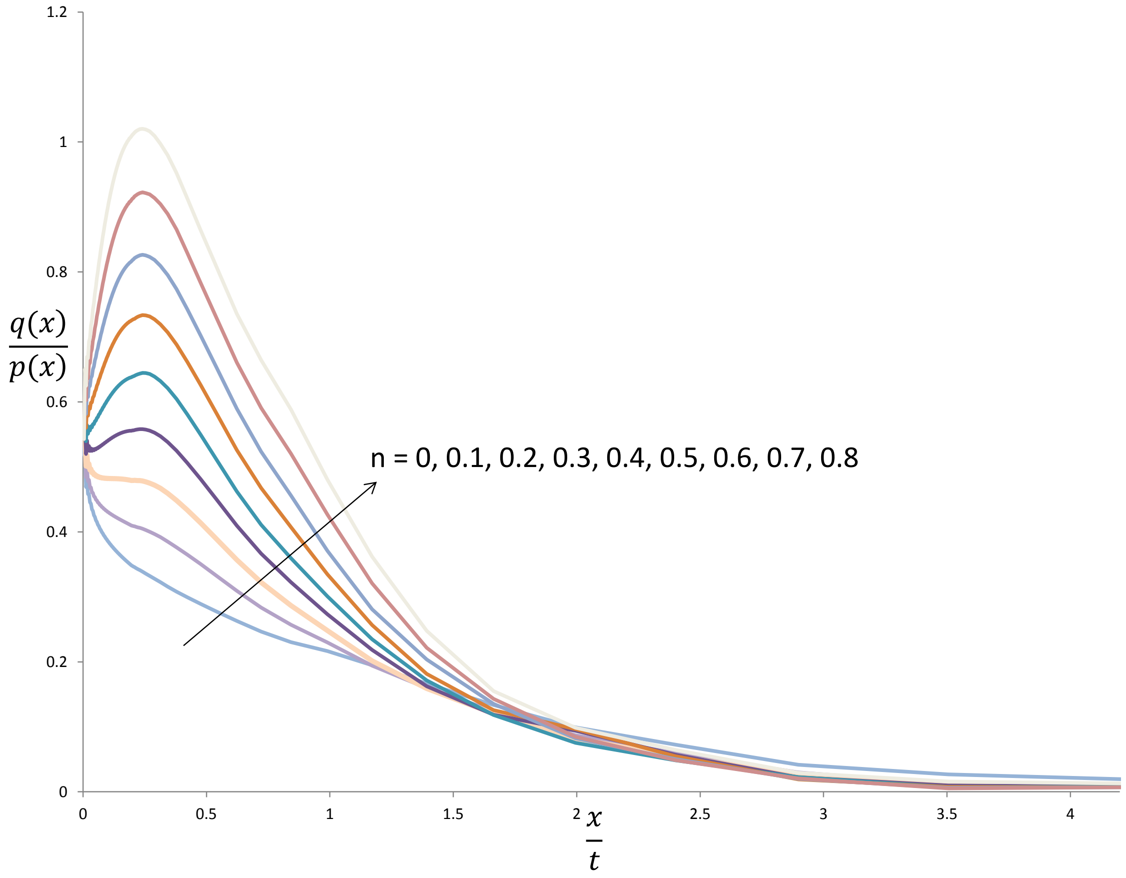

Figure 5.2: Ratio of shear to normal tractions of a monolith in Figure 5.1.

At the extreme internal corner of the adhered strip/half-plane geometry the state of stress must asymptotically match William's solution[15] for a semi-infinite wedge, and it is therefore possible to infer the value of traction ratio for $x << t$ in closed form. A general notch in a homogeneous medium experiences a state of stress in the form

$$\sigma_{ij}(r,\theta) = K_I r^{\lambda_I - 1} f_{ij}^{I}(\theta) + K_{II} r^{\lambda_{II}-1} f_{ij}^{II}(\theta) + \text{bounded terms} \tag{5.1}$$

where (r,θ) are polar coordinates centred on the internal corner and 'notch' bisector, $0 < \lambda_{\mathrm{I}} < \lambda_{\mathrm{II}} < 1$ are the eigenvalues, and $f_{ij}^{k}(\theta)$ are the eigenvectors. All of these parameters are explicitly known and depend only on the wedge internal angle, here $3\pi/2$.

Along the interface I have

$$p(x) = K_I^* x^{\lambda_I - 1} + K_{II}^* x^{\lambda_{II} - 1} + \text{bounded terms} \tag{5.2}$$

$$q(x) = K_I^* g_{r\theta}^I x^{\lambda_I - 1} + K_{II}^* g_{r\theta}^{II} x^{\lambda_{II} - 1} + \text{bounded terms} \tag{5.3}$$

so that the ratio $\frac{q(x)}{p(x)}$ is given by

$$\frac{q(x)}{p(x)} = \frac{K_I^* g_{r\theta}^I x^{\lambda_I - 1} + K_{II}^* g_{r\theta}^{II} x^{\lambda_{II} - 1}}{K_I^* x^{\lambda_I - 1} + K_{II}^* x^{\lambda_{II} - 1}} \tag{5.4}$$

and, in the limit $x \to 0$, I find simply that $\frac{q(0)}{p(0)} = g_{r\theta}^I$. For a $\frac{3\pi}{2}$ internal corner $g_{r\theta} = 0.543$,and I see, in Figure 5.2, that the traction ratio does go to this ratio for all values of *n*. Numerical results show that, when n is sufficiently small (≤ 0.18), the traction ratio decreases monotonically with distance from the corner, so that a coefficient of friction of at least 0.543 guarantees the strip remains adhered along the entire substrate.

For 0.18 ≤ n ≤ 1.89, the traction ratio has a maximum at a nearby interior point $x > 0$ (Figure 5.2). Consequently, the coefficient of friction needed to maintain full adhesion rises rapidly with n, and soon exceeds typical values of realistic materials. Although these results may suggest that, if the actual coefficient of friction present is just slightly less than the maximum needed to maintain full adhesion, a small detached slip region might develop, in practice the turning point is located so close to the strip end that, once slip starts, the re-distribution of tractions gives rise to a small slip region which propagates up to the free end. Further, the presence of the slip modifies the value of n at which separation occurs.

It is important to note that the investigation of this problem could have been carried out using a reduced stiffness method developed in chapter 3 but the analysis was started before the development of the reduced stiffness method. Nevertheless, it is useful to investigate whether the results will be the same and it has been found that the results from the two methods are the same. (see section 3.7 for the comparison of the results from a conventional finite element method and static reduction procedure)

5.3 Slipping interface

5.3.1 Loading phase

The finite element model was modified by including contact elements along the interface between the strip and the half-plane, with the intention of investigating in more detail slip and separation. Contact elements which utilise the augmented Lagrangian method was used to handle the discontinuous nature of the contact boundary conditions. Convergence tests were carried out to ensure independence of the results from the mesh and the mesh size at the contact interface is chosen to be $0.005t \times 0.005t$.

When separation occurs, the contact becomes incomplete and, since the contact pressure falls smoothly to zero at the location where the elastic strip is separated from the half-plane, there is always a slip zone present. Also, as the point of lift-off is independent of the magnitude of the contact pressure, p_o, a degree of linearity is restored to the problem, in the sense that the state of stress is proportional to p_o, and the actual amount of lift-off, which is governed by the displacement field, is also proportional to the load, in turn. Figure 5.3(a) displays the extent of separation and the size of the stick zone as a function of n and the coefficient of friction, f.

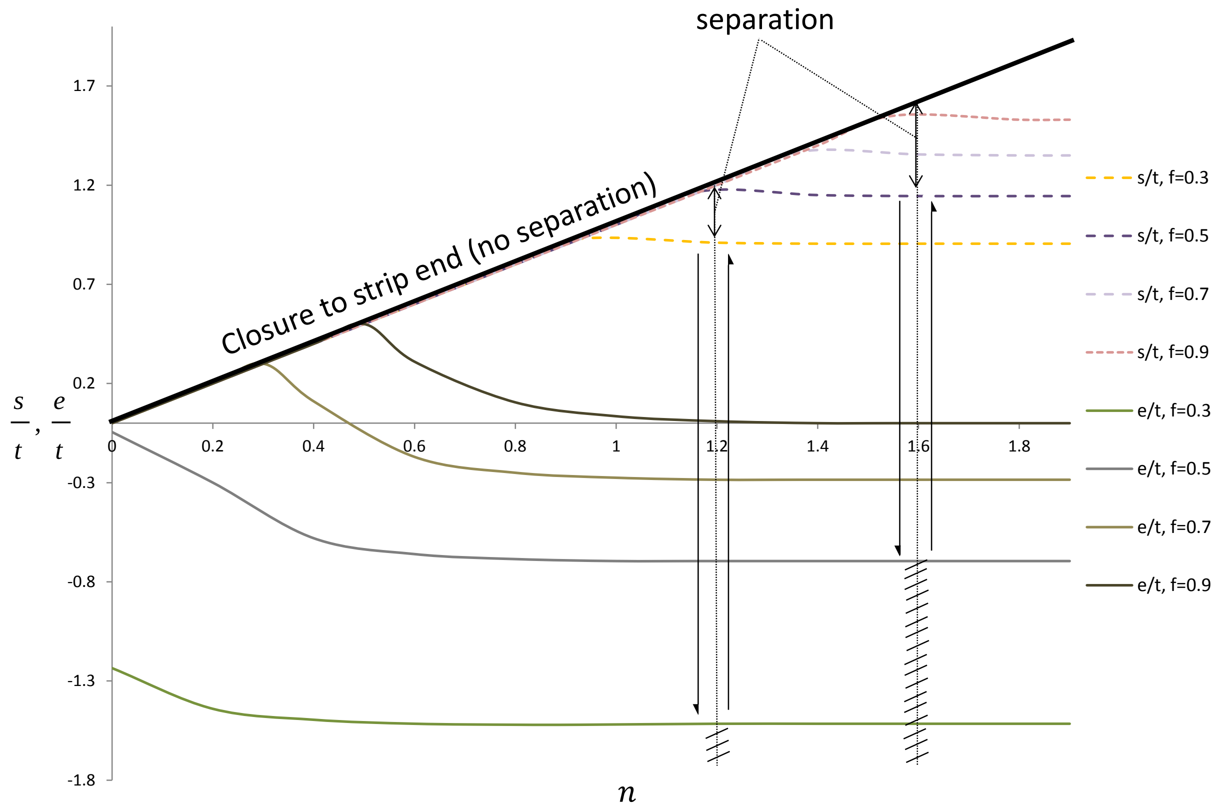

Figure 5.3(*a*): Extent of separation and the size of separation as a function of *n*. (Small *n*)

The coordinates *e*, *s* are defined in Figure 5.1 and each is measured from the point where the contact pressure stops. They are positive in a sense directed towards the strip free end, and *e* is the point of stick/slip transition whilst *s* is the point of separation. The separation point is invariably nearer the free end than a point at which the pressure stops($s > 0$), but the stick/slip transition point may lie beneath the pressure-loaded region ($e < 0$) for low coefficients of friction, and nearer to the free end ($e > 0$) for lower friction, and for sufficiently small values of *n*. As an example of the interpretation of Figure 5.3(*a*), if I chose $n = 1.6$ and have a coefficient of friction, $f = 0.5$, adhesion occurs at all points inboard of $e/t = -0.7$, and slip occurs between this point and $s/t = 1.1$, which is the point of separation. With coefficient of friction $f = 0.3$ if I choose $n = 1.2$ then $e/t = -1.45$ and $s/t = 0.9$. If I maintain $n = 1.2$ but increase the coefficient of friction to $f = 0.5$, no separation occurs.

It is apparent that the stick-slip transition point is only very weakly dependent on n and that the position of the separation point depends on n only up to about 1.0. In fact, for low coefficients of friction the separation point stabilises at even lower values. It follows that, when the length of strip projecting beyond the end of load exceeds about twice the strip thickness, the solution is entirely independent of n. The large n solution is therefore of interest because of its universality, and in Figure 5.3(b) the variation of s/t and e/t with coefficient of friction is displayed where the solution has become insensitive to its value.

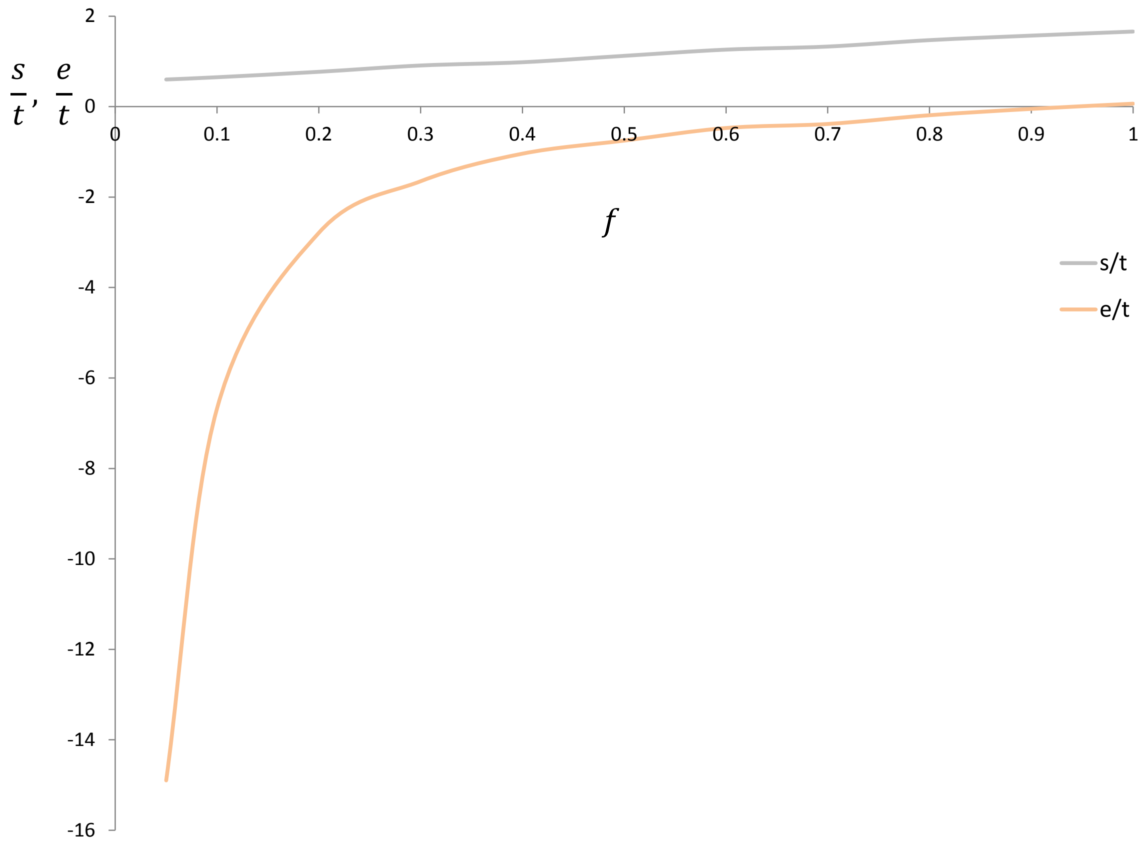

Figure 5.3(*b*): Extent of separation and the size of separation as a function of *f*. (Large *n*)

At very large coefficients of friction the stick/slip point lies directly beneath the end of the pressure load and the slip extent is almost twice the strip thickness. At the other extreme, for a very low coefficient of friction the slip zone ends a long way under the loaded portion of the strip whilst the separation point is approximately underneath the end of the pressurised region

Figure 5.4, which is plotted for the case of a coefficient of friction of 0.7, displays the variation of contact pressure and shearing traction as a function of position. The coordinate origin is now taken as immediately beneath the edge of loading, and hence $\xi/t = x/t - n$.

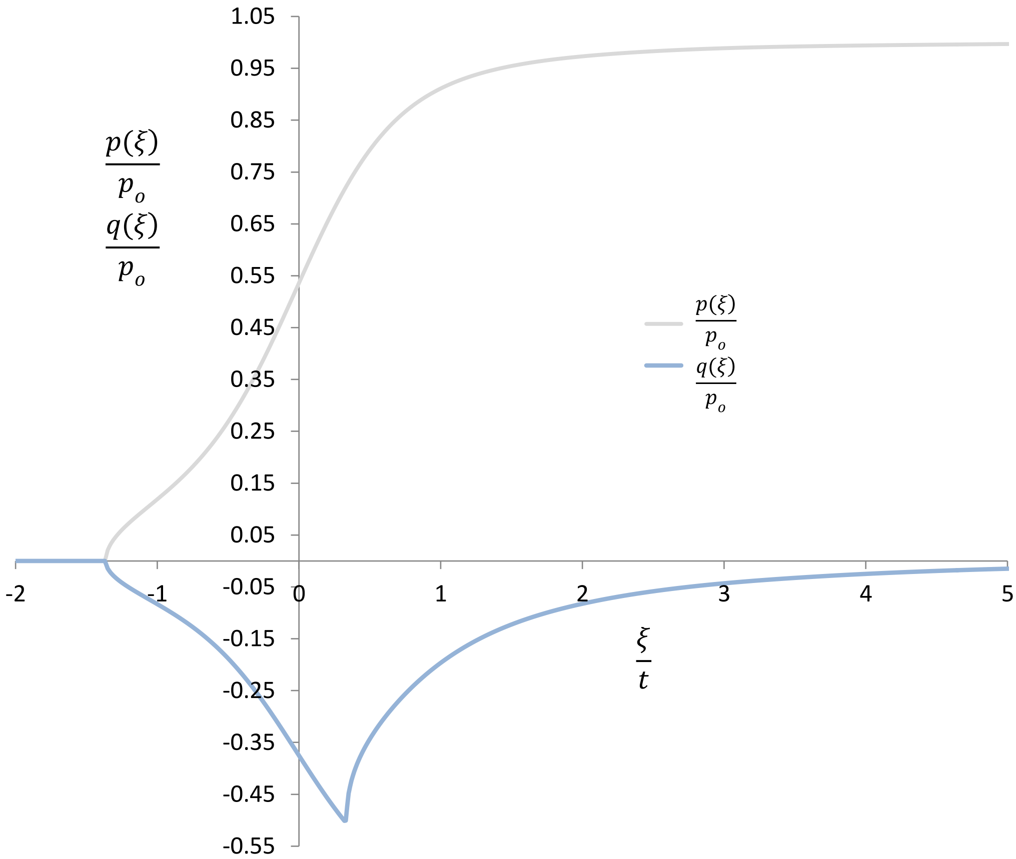

Figure 5.4: Interfacial pressure and shear tractions distribution during loading phase.

5.3.2 *Unloading problem*

In many ways it is the unloading phase of this problem which produces unexpected properties. In order to reduce the number of unknowns I will examine, in detail, only the 'large n' solution, and concentrate first, on the response when f = 0.7. Suppose that I have applied a monotonically increasing contact pressure until a maximum value, p_o is attained, so that the tractions are as shown in Figure 5.5, $p/p_o = 1$. The contact loading is now gradually removed, and the tractions present when unloading to pressures of 0.9, 0.5, and $0.1 \times p_o$ are also shown in Figure 5.5.

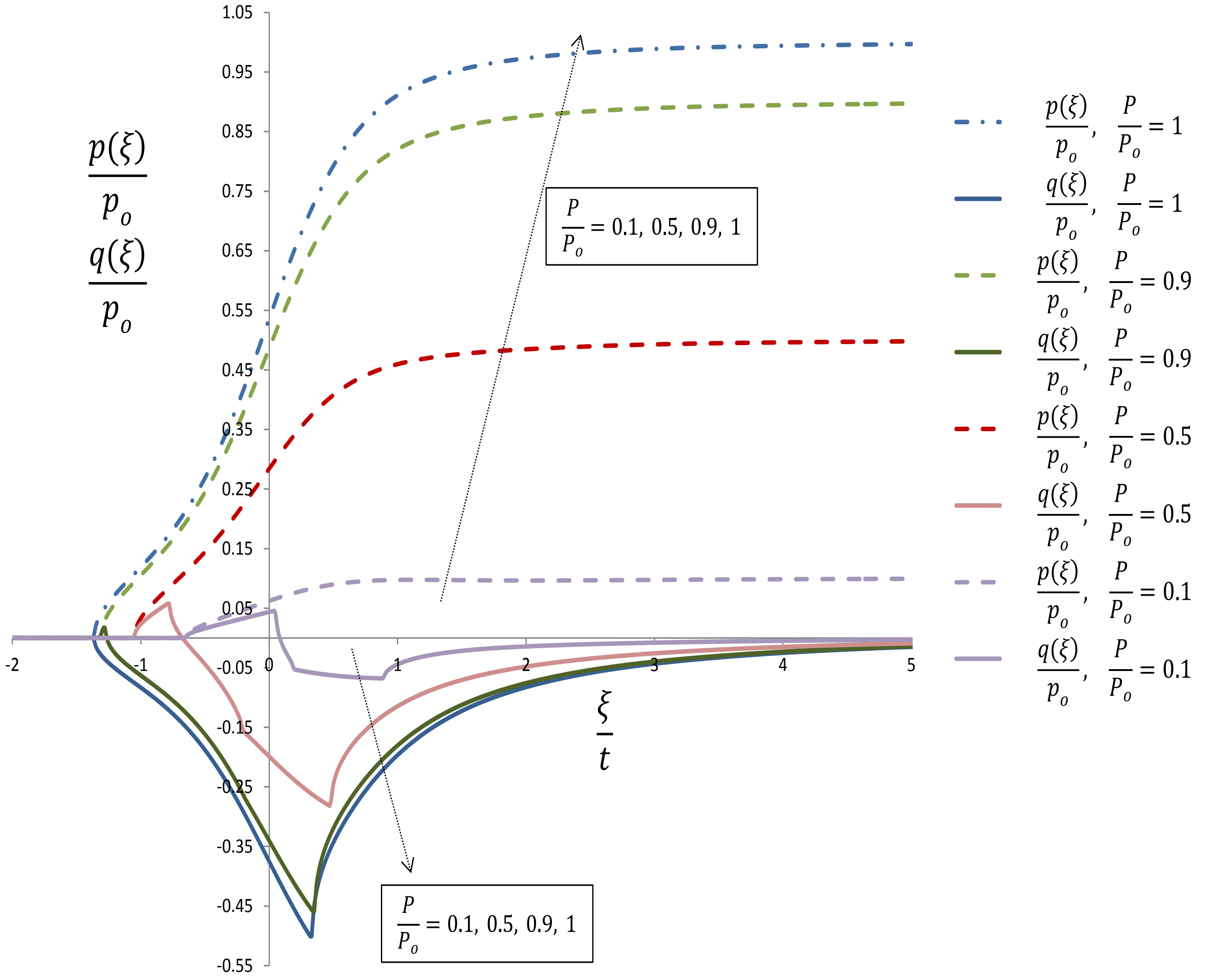

Figure 5.5: Interfacial pressure and shear tractions distribution during unloading phase.

This shows the following properties;

1. During the loading phase (s/t) =1.4 and (e/t) = -0.3.

2. The contact continues to recede as the load is reduced and eventually the layer simply falls back into contact along the half-plane surface as the applied pressure load tends to zero.

3. An infinitesimal reduction in load causes the entire slip region present during loading to become adhered.

4. For finite reductions in the applied load a *reverse* slip region, attached to the point of separation, develops and gradually gets bigger. A second slip region, of forward slip, develops from the initial point of slip-stick transition.

The traction plot is useful but it is difficult to distinguish the stick/slip/separation regime, and this is plotted out in detail in Figure 5.6. I now consider, in detail, an accumulative loading cycle starting from an unloaded state. An infinitesimal load is applied, and the contact suddenly snaps from being continuous along the range ($0 < x < \infty$) to being in contact only for ($x > 0.6t$ or $\xi > -1.4t$), and to be adhered only for ($x > 2.3t$ or $\xi > 0.3t$). Finite increases in the contact pressure causes the internal stresses and displacement to increase in proportion to the applied normal load, but the slip and separation points remain fixed. Upon an infinitesimal removal of load, the requirement that the sign of the shear traction be consistent with an increment in slip displacement is violated, and the slip region instantly sticks. This point is just to the right of the left hand axis in Figure 5.6. Finite removal of the contact pressure causes the stick region just formed from within the original forward slip region to contract, as a reverse slip region develops at the contact edge and a new forward slip region develops at the former stick/slip transition point.

As an example in interpreting Figure 5.6 for a finite reduction in load, suppose I have removed 50%, i.e. p/p_o = 0.5, and I see that I have

1. Separation $x \leq 0.9t$ or $\xi \leq -1.1t$
2. Forward slip $0.9t \leq x \leq 1.3t$ or $-1.1t \leq \xi \leq -0.7t$
3. Stick $1.3t < x < 1.8t$ or $-0.7t < \xi < -0.2t$
4. Backward slip $1.8t < x < 2.5t$ or $-0.2t < \xi < 0.5t$
5. Stick $2.5t < x$ or $0.5t < \xi$.

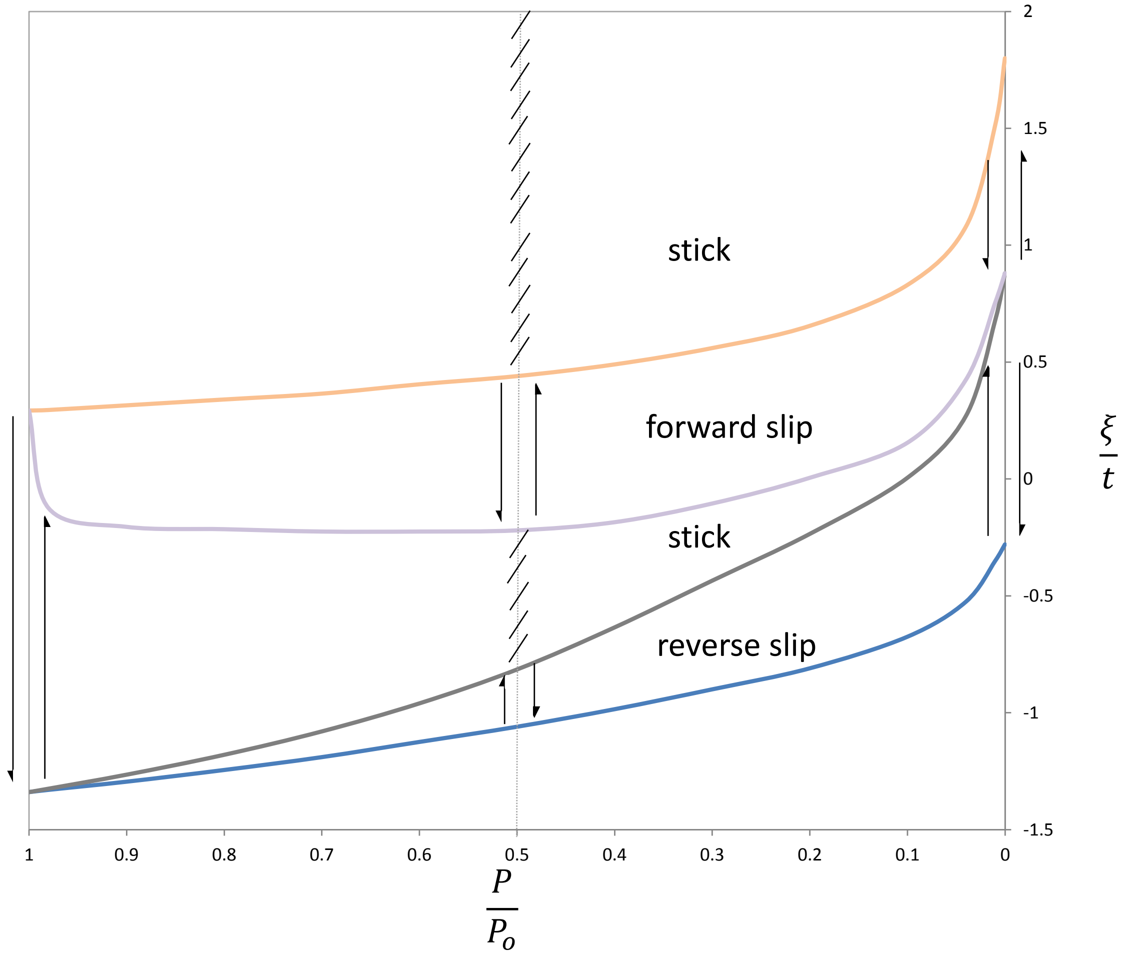

Figure 5.6: Evolution of slip/stick zone during unloading for *n*= 2 and *f* =0.7.

The cycle ends with the complete removal of all normal loads, so that the final state is that the pair is again unloaded, but the slip displacement history is really quite complicated. All points in the range $0.6 < x/t < 2.3$ or $-1.4 < \xi/t < 0.3$ show advancing slip as the contact pressure is increased. It is during unloading that the real differences emerge:

1. In the range $0.6 < x/t < 1.8$ or $-1.4 < \xi/t < -0.2$ the initial stick is followed by a period of reverse slip, then separation.
2. There are some points, in the range $1.8 < x/t < 2.3$ or $-0.2 < \xi/t < 0.3$ where the initial adhesion upon unloading is followed by further forward slip, a second period of adhesion, and a period of reverse slip which endures until all load is removed.
3. Also, for $2.3 < x/t < 3.8$ or $0.3 < \xi/t < 1.8$ there are particles which exhibit neither separation nor slip during the application of the load, but which slip, in the forwards direction, only during unloading.

Example plots of slip displacement corresponding to these responses are shown in Figure 5.7. Figure 5.7(*a*) shows the relative slip displacement history at point $x/t = 1.5$ or $\xi/t = -0.5$, Figure 5.7(*b*) is the response of a point $x/t = 2$ or $\xi/t = 0$, and Figure 5.7(*c*) the response at point $x/t = 2.5$ or $\xi/t = 0.5$.

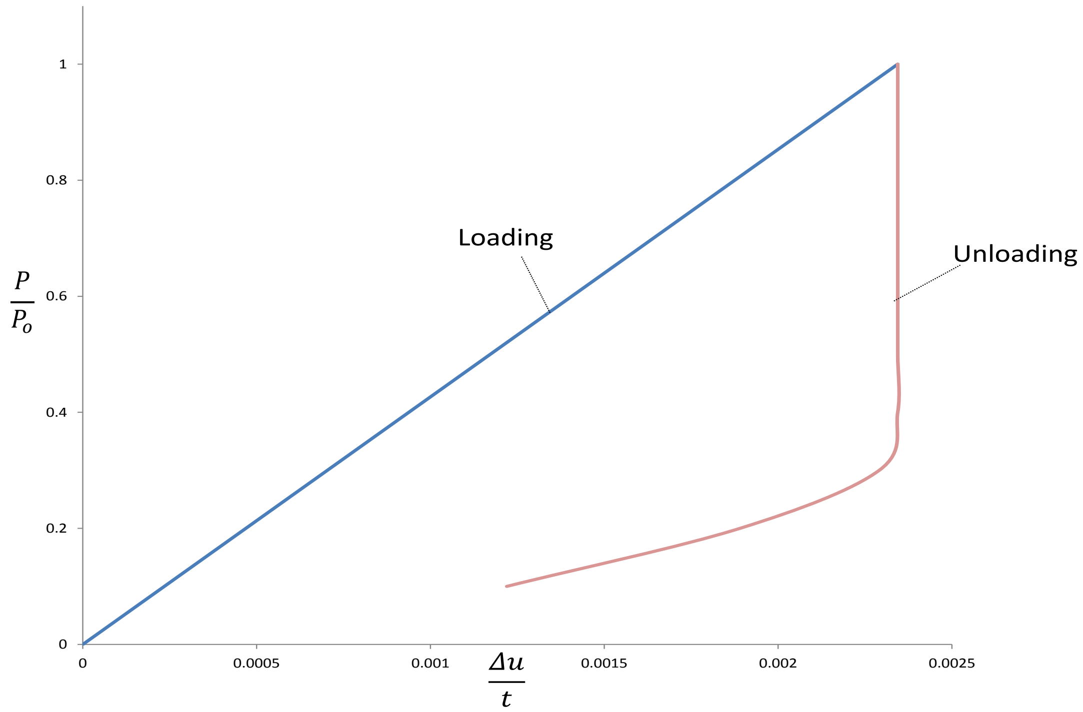

Figure 5.7(a): $-1.4 < \frac{\xi}{t} < -0.2, \quad \left(\frac{\xi}{t} = -0.5\right)$

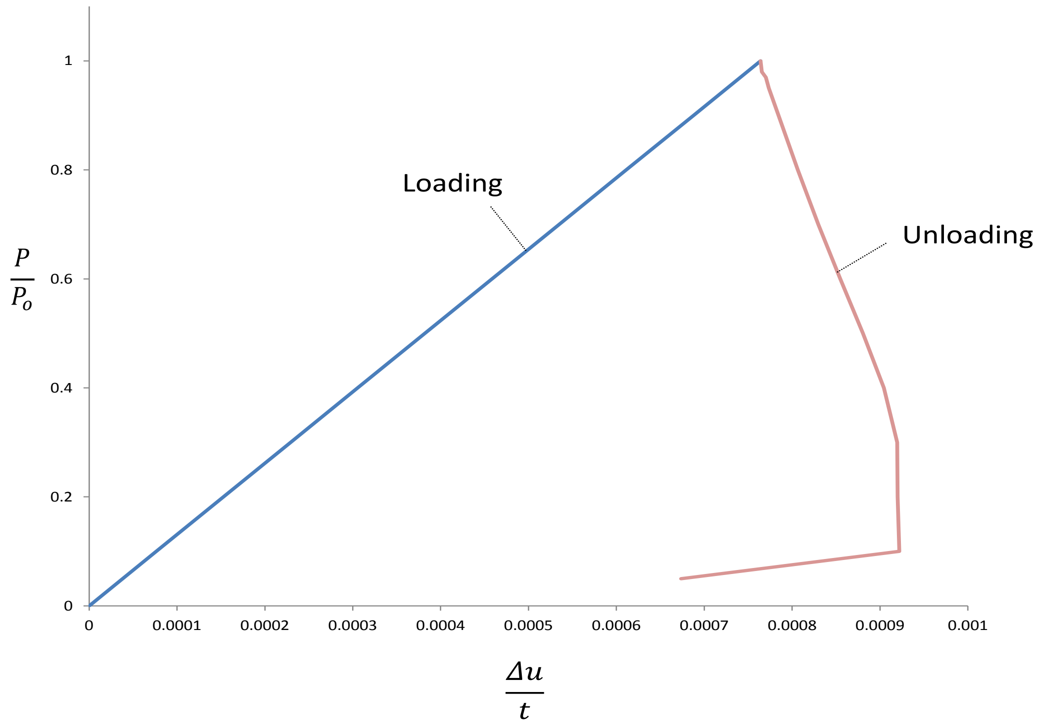

Figure 5.7(b): $-0.2 < \frac{\xi}{t} < 0.3, \quad \left(\frac{\xi}{t} = 0\right)$

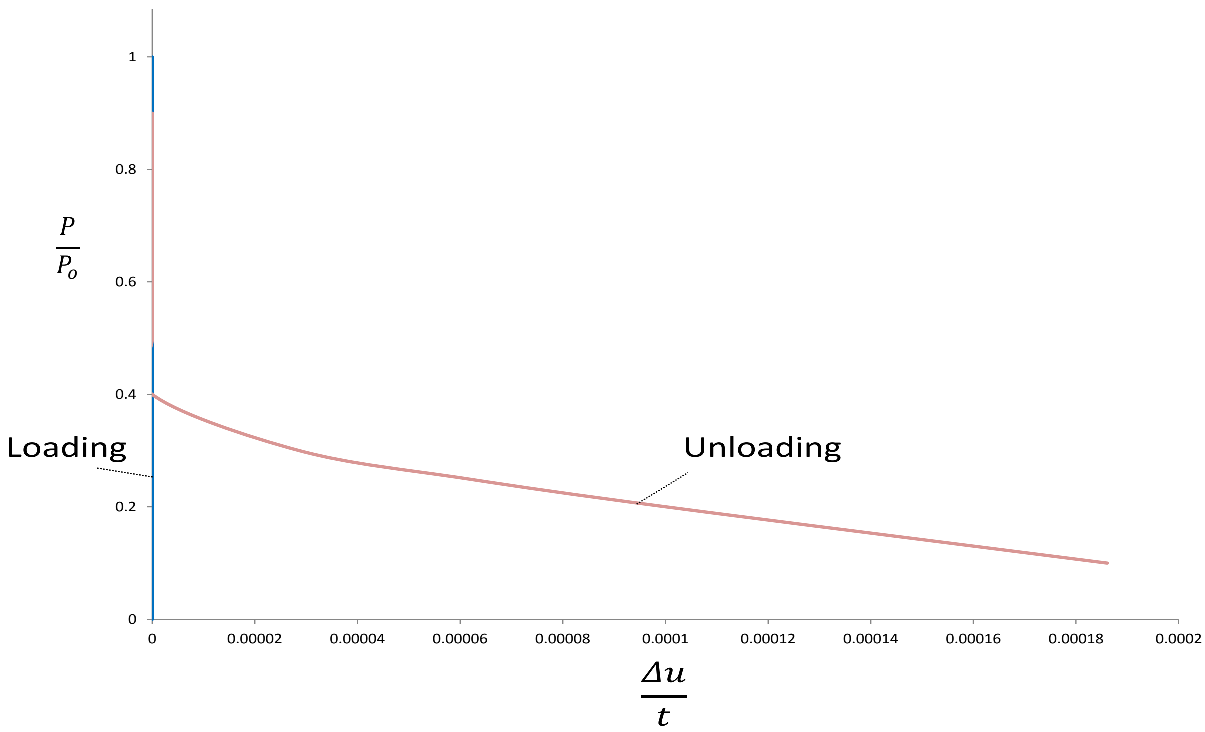

Figure 5.7(c): $0.3 < \frac{\xi}{t} < 1.8, \left(\frac{\xi}{t} = 0.5\right)$

5.4 Conclusion

The apparently simple plane problem of receding contact between a layer and a half-plane, made from the same material, and where pressure load is applied over part of the top surface of the layer or strip, has been studied. If the contact pressure extends up to a point close to the contact edge full contact may be maintained, and either the contact is fully adhered or, if the coefficient of friction is less than 0.543 a slip region will develop. If the pressure stops further away from the contact edge than this critical distance the contact recedes, and is seen to snap to a configuration of incomplete contact upon the application of an infinitesimal load. As the contact now becomes incomplete and hence the interfacial normal distribution falls smoothly to zero as the contact edge is approached, there will always be an attendant forwards slip region. Further increases in normal load leave the points of separation and stick/slip transition unchanged but the stress and the displacement fields are proportional to the applied normal load. Upon removal of the load the contact recedes further, and a complicated stick slip pattern develops which changes smoothly as the load is removed.

6 Frictional Lap Joint

6.1 Introduction

Lap joints formed using standard high strength friction grip bolts are very widely used in both basic structural steelwork, and in rather more sophisticated mechanical assemblies such as gearboxes, gas turbines and many flanged constructions. Lap joints can act as a good source of frictional damping which prevents or diminishes the resonance effect of structures subjected to some oscillatory loads. However, the lap joints are usually associated with wear and reduced fatigue life. This often gives rise to difficulties in many engineering designs which can also result in an increase in manufacturing and maintenance costs. A thorough understanding of the interfacial behaviour of the mechanical lap joints, and, particularly the slip-stick regime, the traction distributions and the relative slip displacement will improve the engineering design approach significantly.

In the context of structural steelwork the design of the joint is based on a very simple determinate procedure, and most of the construction codes are concerned with estimating the individual shear force transmitted through each bolt comprising the connexion.

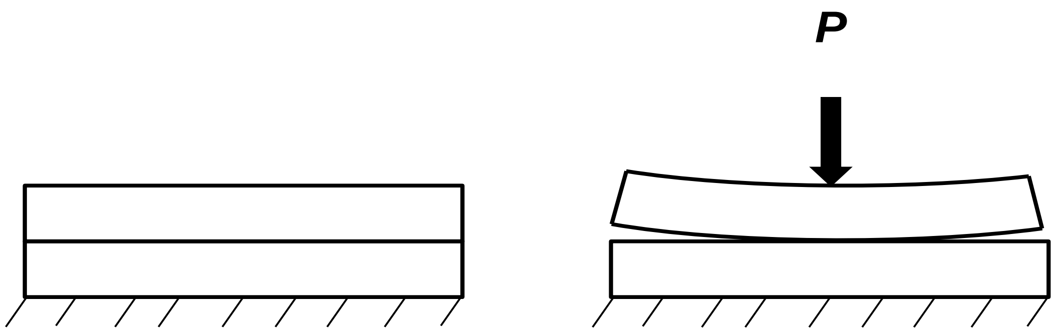

(a) Unloaded configuration **(b) Loaded configuration**

Figure 6.1: Receding contact

The intention here is quite different, and focuses on determining the detailed nature in which the shear load is transmitted between the laps of the joint at each individual contact, in a similar fashion to the early attempts to estimate the friction energy dissipation in lap joints performed by Earles [99]. It should also be stated that no attempt here is made to study the details of the compressive load under the bolthead/washer/nut either. Instead, this chapter aims to provide some insight into the basic nature of the contact itself, which is of the class called receding, the name coined by Dundurs [47, 49]. Receding contacts, Figures 6.1, are those where the application of a normal load, P, alone causes the contact area to jump. This jump is between that implied by placing together the unloaded components, and where the contacting area is normally very extensive, to a much smaller value comparable in size with the thickness of the laps or extent of loading. A particular feature of the contacts is that the jump occurs at an infinitesimal load, and, for increasing value of the normal load, the contact extent is constant, so that some features of linearity are then restored as shown in Chapter 5. This contrasts with those problems where an increase in load causes a smooth reduction in the size of the contact, which Barber and Ciavarella refer to as 'regressive' [100].

In this chapter, I take a simple representation of a lap joint and, for a typical geometry (see Figure 6.2), explore the local contact behaviour as the joint is put under oscillatory remote loading. The range of magnitude of the remote loading will be restricted to the sliding limit as this enables the contact interface to exhibit partial slip behaviour. The results found display a characteristic behaviour which will be useful in understanding how problems with similar loading histories, but having a different geometry, may be expected to behave. The geometry is strictly two-dimensional, so the 'pinching pressure', $p_o = \frac{P_o}{w}$, where P_o is the steady-state constant normal load applied to the joint (see Figure 6.2) and w the width over which it is distributed, is simply taken to be spatially uniform. I use as the reference dimension the thickness of the laps, *t*, and the extent of the pinching pressure is measured using $\frac{w}{t}$, whilst the length of the laps beyond the pinch-point is $16t$. The loading history of the normal load, P, and remote tension, T, at the free end of the lap joints is shown in Figure 6.3. Note that the normal load is first monotonically increased from zero to P_o and then kept constant throughout the simulation; hence P_o denotes the constant clamping force applied to the bolted connection before cycling the remote load.

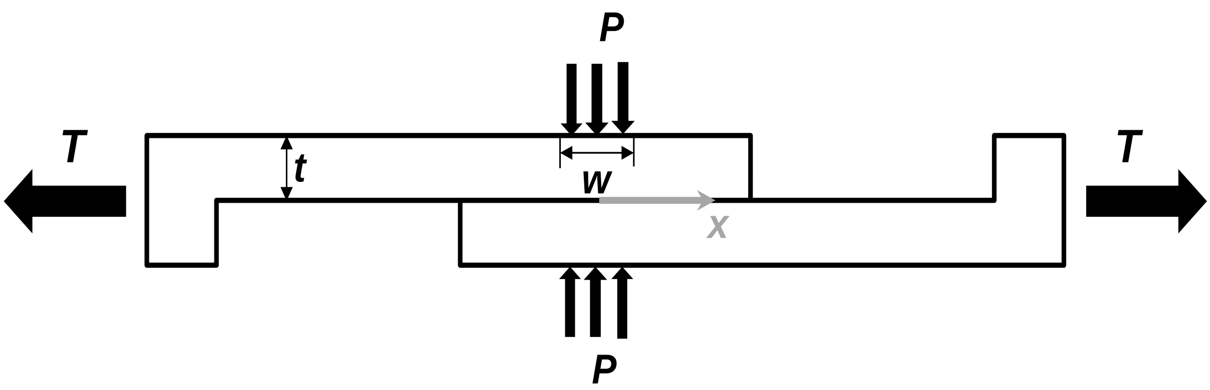

(a)

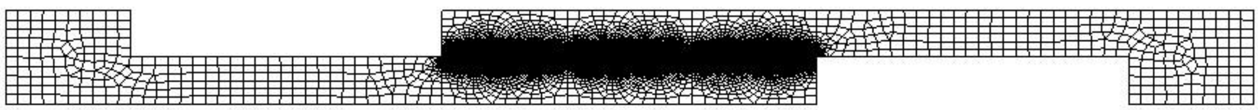

(b)

Figures 6.2: (a) Frictional lap joint subject to constant normal load, *P*, and oscillatory bulk tension, *T*. (b) a meshed finite element model.

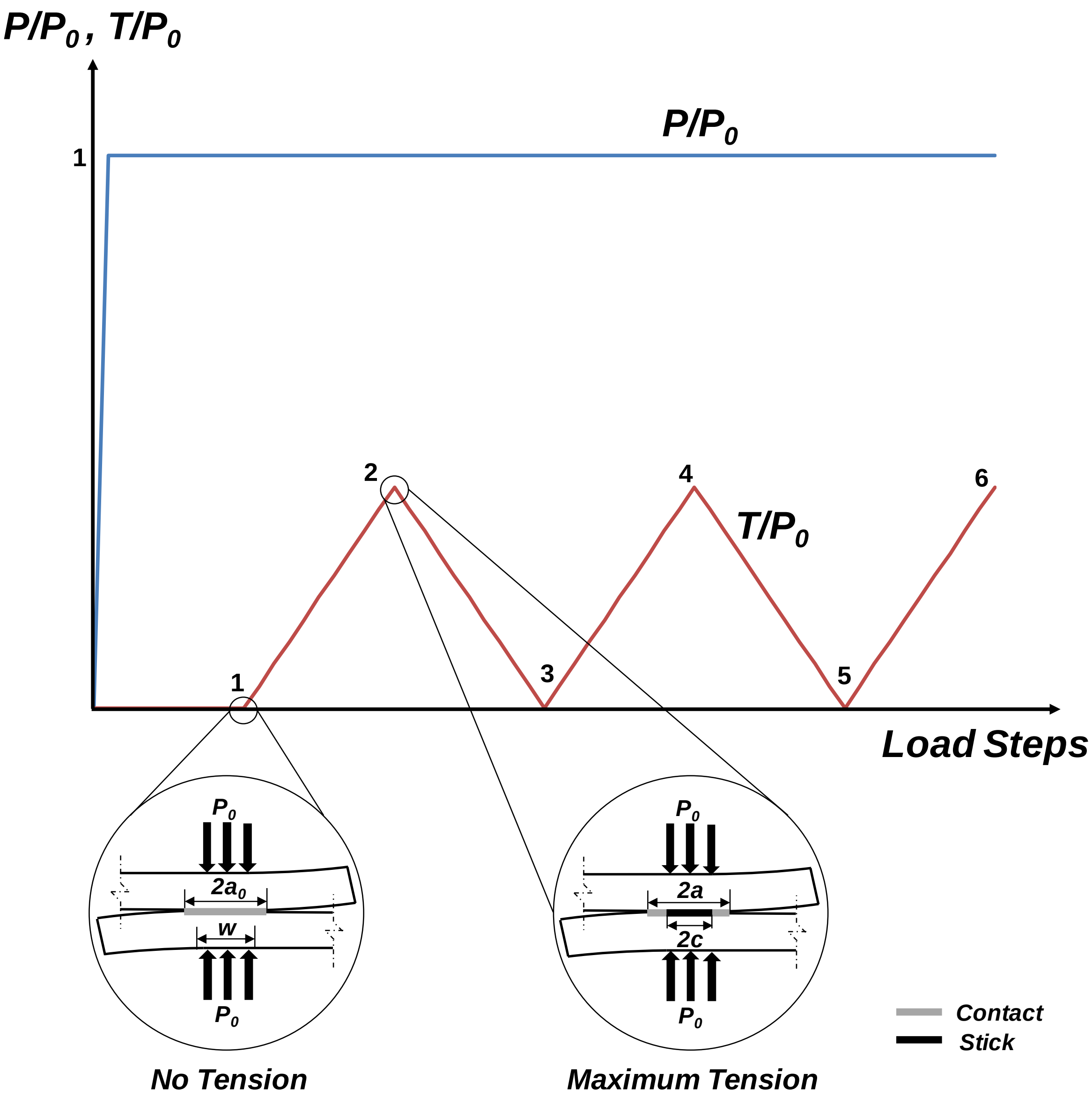

Figure 6.3: Loading history for tensile loading case and schematic of the contact configurations at different points during the loading cycle.

6.2 Model formulation and results

It does not seem possible to use an analytical approach to investigate the problem, and so a commercial finite element code, ABAQUS [101, 102] is employed. The usual precautions were taken of grading the mesh finely at all the appropriate key points - although the separation effects mean that there are no singularities, and the stress field is generally well behaved. Tests were carried out to ensure independence of the results from the mesh and the model is well converged with all the load conditions employed in the analysis. Contact elements were chosen which utilise the augmented Lagrangian method to handle the discontinuous nature of the contact boundary conditions. A two-dimensional, 4-noded (bilinear), plane strain quadrilateral (CPE4) element was used and the mesh size at the contact is $0.005t \times 0.005t$ where t is a thickness of the lap joint as displayed in Figures 6.2. Each loading cycle is solved using at least two-hundred increments using an implicit solver to accurately capture the evolution of the contact area, slip region and stick region throughout the simulations. Although the effect of varying $\frac{w}{t}$ was investigated, the results reported in this chapter refer to the case $\frac{w}{t} = 1$ unless different values for this parameter are explicitly mentioned. It is worth noting that the problem could have been analysed using the reduced stiffness method in chapter 3 because the procedure is applicable to all two dimensional frictional contact problems. However, the investigation of the problem in this chapter was conducted before the development of the reduced stiffness method. The analysis was carried out using the reduced stiffness method and the results are the same (see section 3.7 for comparison of the results from a conventional finite element method and the static reduction procedure).

6.2.1 *Tensile remote loading*

First, consider the case when the remote loading is tensile. When the pinching pressure is applied, the receded contact occupies a length $\pm 0.71t$ ($\frac{a_o}{t} = 0.71$) either side of the 'bolt' centreline, and the contact pressure distribution is as shown in Figure 6.4. Its peak value is $1.05p_o$. A tension is now applied to the laps, and this is increased up to a maximum value of $0.04P_o$. As this is done the contact smoothly recedes (regresses in Barber and Ciavarella terms [100]) to a length $\pm 0.67t$.

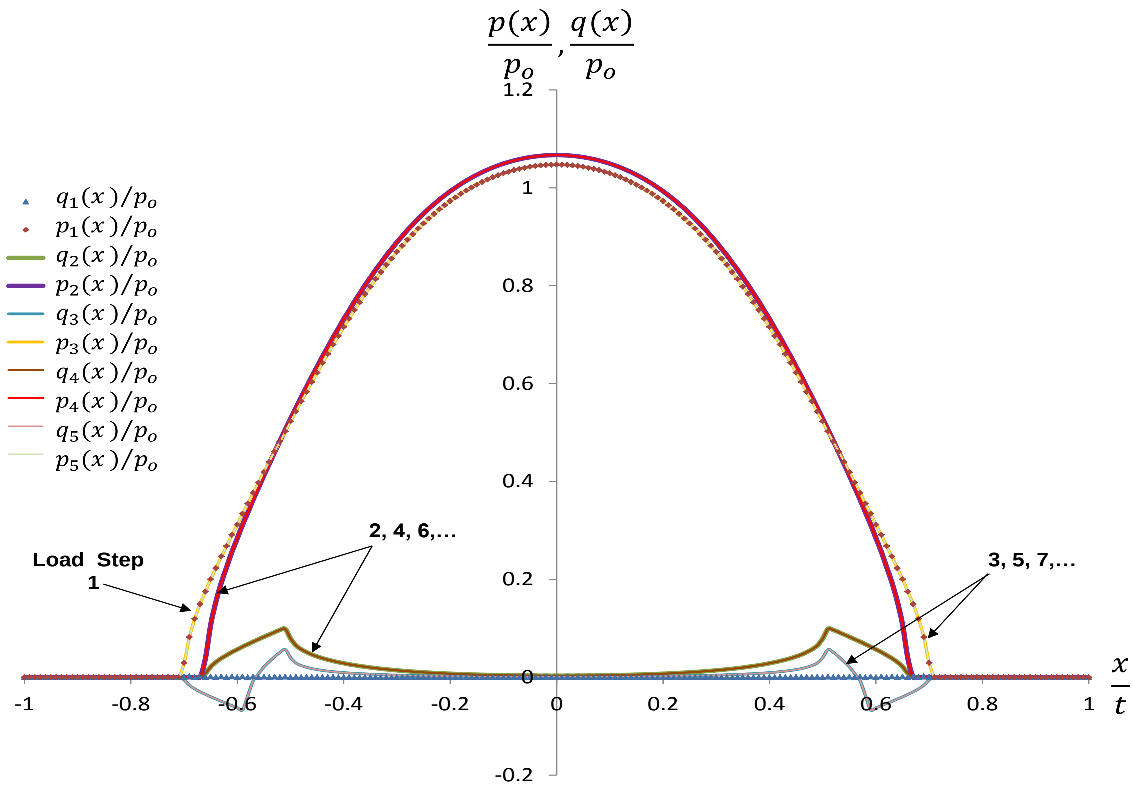

Figure 6.4: Interfacial Tractions at different points in the loading cycle (*T/P$_o$*= 0.04, *f* = 0.2). See Figure 6.3 for load steps 1-7.

The remote tension effectively also puts the contact in shear, and slip zones develop at each edge of the contact, whilst the central part remains stuck (see Figure 6.4). Qualitatively, the shear traction distribution is rather like that in a Cattaneo-Mindlin contact [63, 103]. Note that, whilst 'bulk tension' is also present, it takes the same value in each lap, and hence symmetry is maintained, so that the pressure and shear traction distribution remain symmetrical themselves. With a coefficient of friction of $f = 0.2$, and a ratio of shear load T to normal load, P_o of 0.04, the dimensionless ratio of stick half-width, c, to contact half-width, a, is 0.78 and this compares with a value of 0.89 in a Cattaneo contact subjected to the same $\frac{T}{P_o}$ ratio, i.e. $\frac{c}{a} = \sqrt{1 - \frac{T}{fP_o}}$.

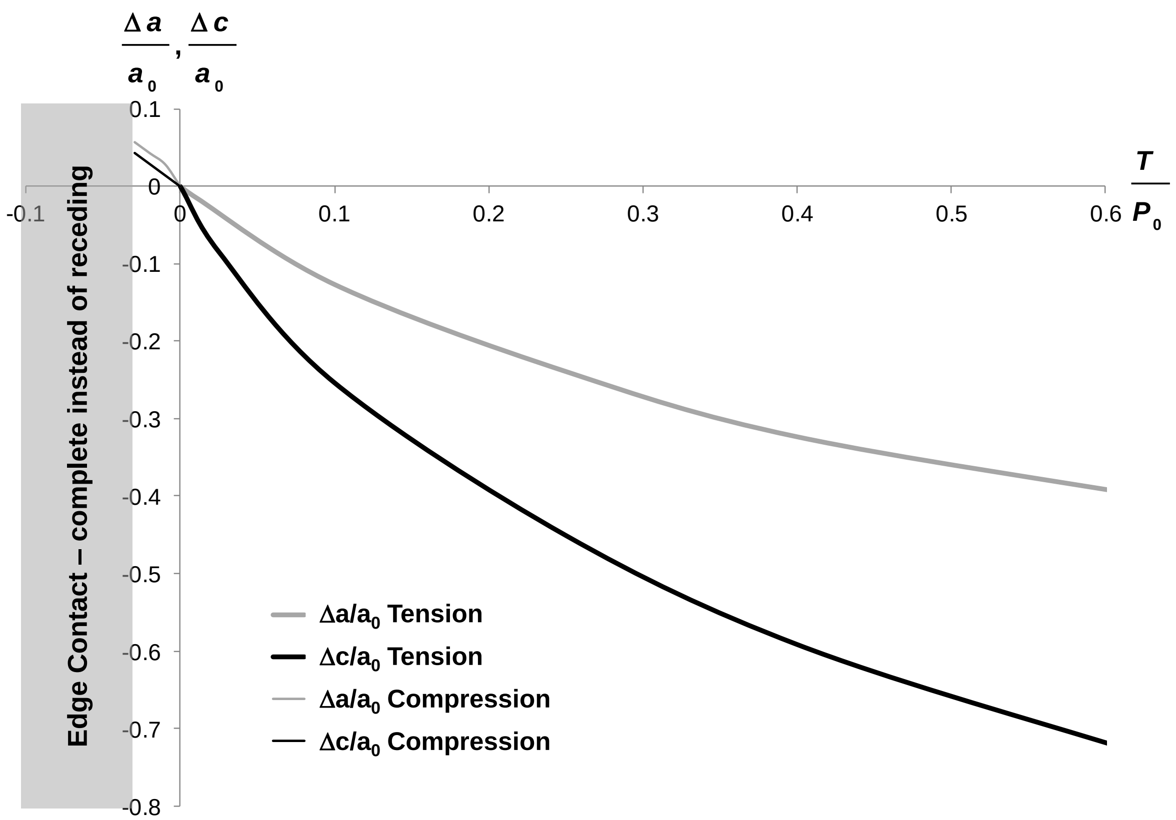

Figure 6.5: Effect of remote loading on the semi-contact half width, *a*, and the stick/slip interface, *c* at *f* = 0.8.

Figure 6.5 shows how the semi-contact half width, a, and the stick/slip interface, c, are influenced by a change in remote loading at steady state cycle. The results when the remote load is in tension are shown in the fourth quadrant of Figure 6.5: the contact recedes further as the magnitude of tensile load increases. The remote load applied to the laps is now removed, and the contact size increases smoothly to its original value, whilst the contact pressure distribution also reverts to its original distribution. However, the shear traction does not vanish, but leaves a locked in distribution with reverse slip present at the outer edges, Figure 6.4. It is also noteworthy that the locked-in shearing traction seems to have no influence on either the contact extent or the pressure distribution, as it might be expected to in, for example, a ‘coupled’ half-plane problem [104]. Upon re-application of the remote tension the contact becomes smaller to the same extent as the first cycle and the contact pressure and shearing traction distribution are as shown in Figure 6.4. Note that the second cycle of loading is also the same as the steady state solution. Details of the evolution of the contact extent and slip zone size are portrayed in Figure 6.6a for f = 0.2 and Figure 6.6b for f = 0.8, which shows the steady state extent of slip is smaller than that observed in the first cycle. This effect is caused by the locked-in shearing tractions.

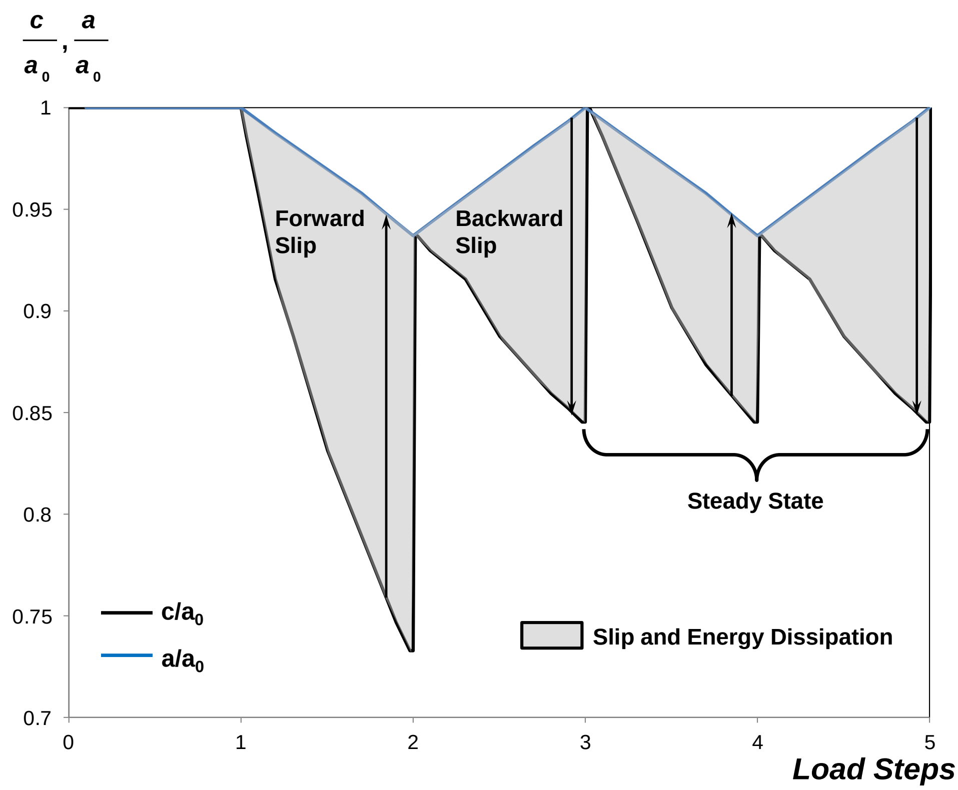

Figure 6.6a: Evolution of stick and slip zones. (*T*/*P*$_o$ = 0.04, *f* = 0.2).

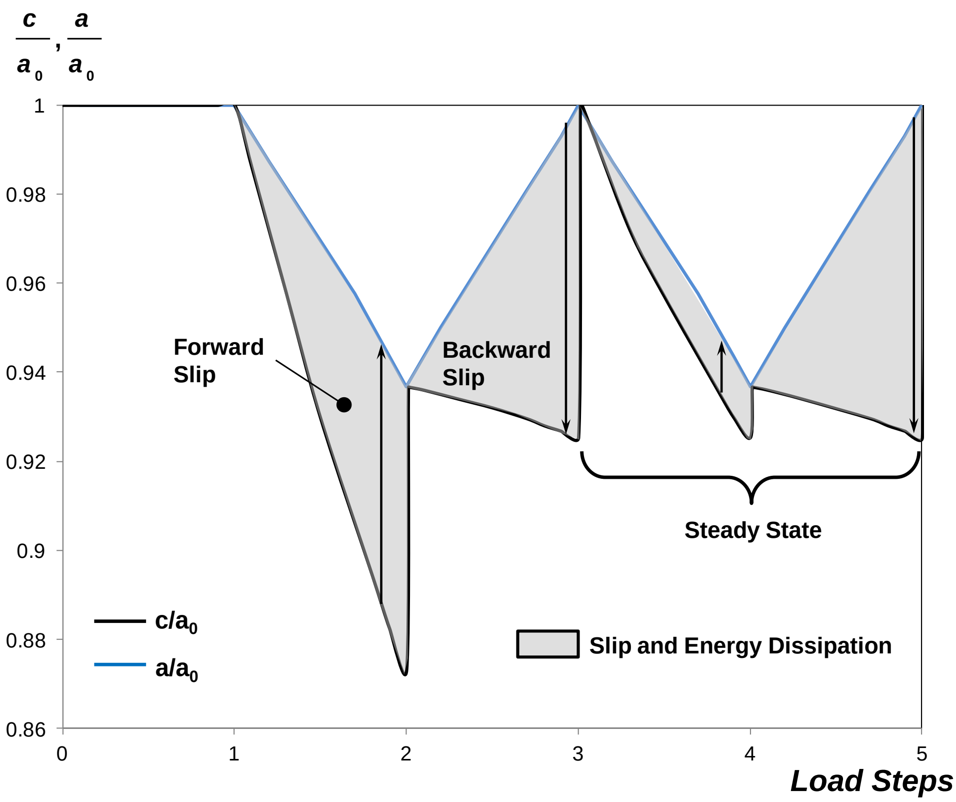

Figure 6.6b: Evolution of stick and slip zones. (*T/P*$_o$ = 0.04, *f* = 0.8)

The plots in Figures 6.6 show that the contact starts to slip in the forwards direction as soon as the bulk tension is applied and increases smoothly up until the bulk tension reaches its maximum. Upon an infinitesimal reduction in tension the contact sticks everywhere and then exhibits backward slip, but not to the same extent as the forward slip in the first half of the loading cycle. The steady state is reached after point t = 2 and the position of slip/stick interface, $\frac{c}{a_o}$, at the extreme points in the loading remain the same for subsequent loading cycles. This is similar to what is observed for the equivalent Cattaneo-Mindlin problem [105], and is typical of systems which are inherently uncoupled. It should also be noted that when friction coefficient is increased the slip regions reduce significantly. This has a significant impact on the amount of dissipation (see section 6.3).

6.2.2 *Remote compression and alternating loads*

It is fully appreciated that the slenderness of the lap arrangement as analysed means that buckling would occur if the unrestrained arrangement were put under significant compression. However, it is expected that the phenomenon investigated here would also be present, in some more complex form, in a structural steelwork connexion. Note that the only fundamental difference between this and the tensile loading case is that here the load is acting *towards* the free end of the lap, whereas in the tension case it is acting away from the free end of the lap as shown in Figure 6.2.

For the remote compression case, there is a very limited range of the compressive bulk that can be applied to the joint before the laps start to touch at the edges- in fact this occurs at a value of the compressive remote loading, $T = 0.04P_o$. The effect of compressive remote loading on the semi-contact half width, a, and stick/slip interface are displayed in the second quadrant of Figure 6.5. When the compressive remote loading increases the interfacial contact area of the lap joint increases and this also increases the extent of the backward slip region. As a result, both changes of the semi-contact half width, a , and the stick/slip interface, c , are positive.

Details of the contact pressure and shearing tractions are shown in Figure 6.7 and an increase in compression is accompanied by backward slip. The interesting additional phenomenon observed here is that the contact actually increases in size until the remote load reaches the maximum value, which is the opposite effect to the tension case. The contact will start to contract as the load is reduced and resumes its initial size as the remote load is completely removed. At the same time a forward slip zone develops.

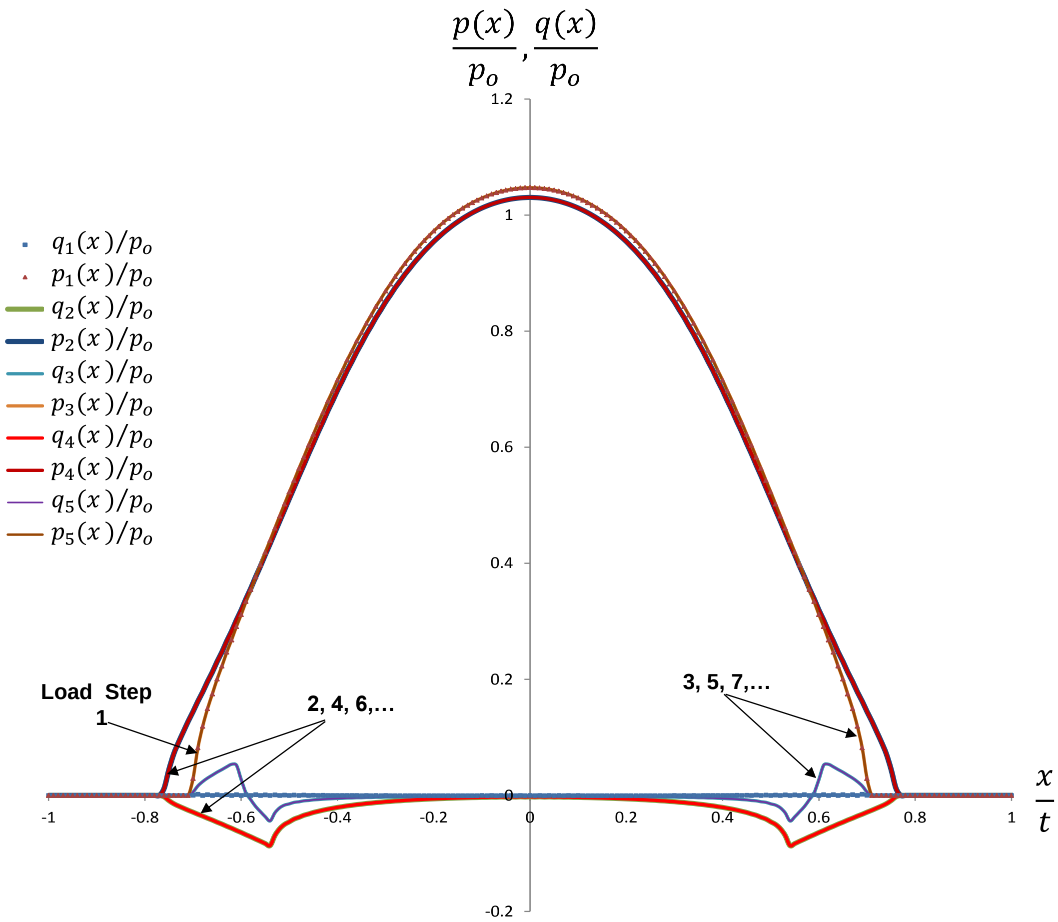

Figure 6.7: Interfacial Tractions at different points in the loading cycle. (*T/P$_o$*= -0.04, *f* =0.2).

Figures 6.8a and 6.8b show the evolving contact size and slip zone, both during the first and subsequent cycles for friction coefficients, *f* = 0.2 and *f* = 0.8 respectively. The steady state is again reached after point 2.

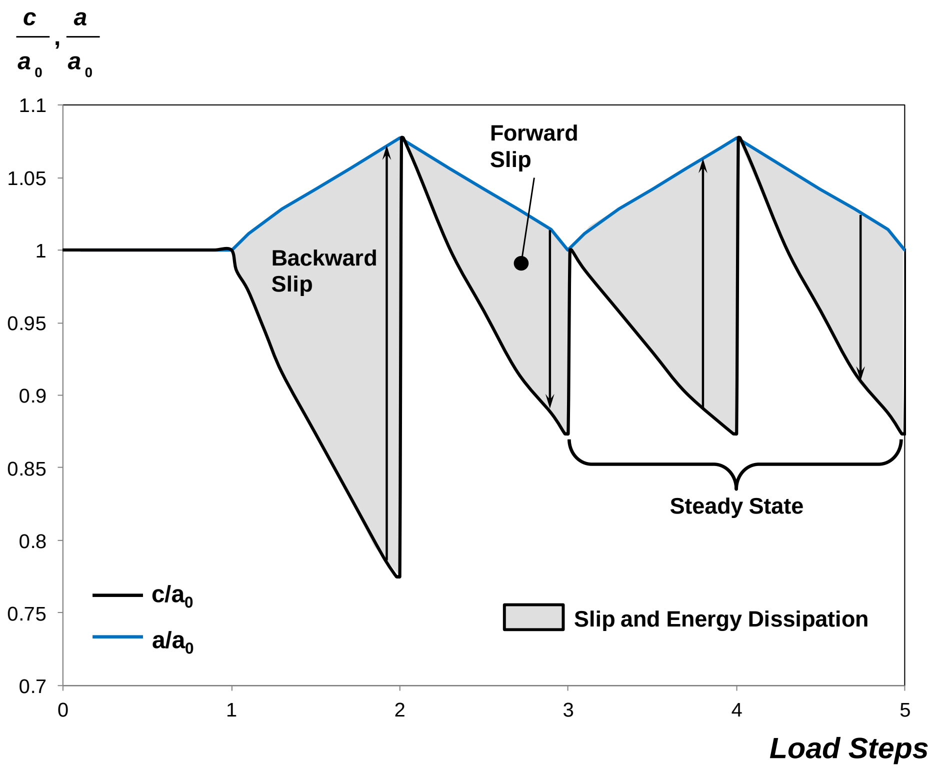

Figure 6.8a: Evolution of stick and slip zones. (T/P_o = - 0.04, f = 0.2).

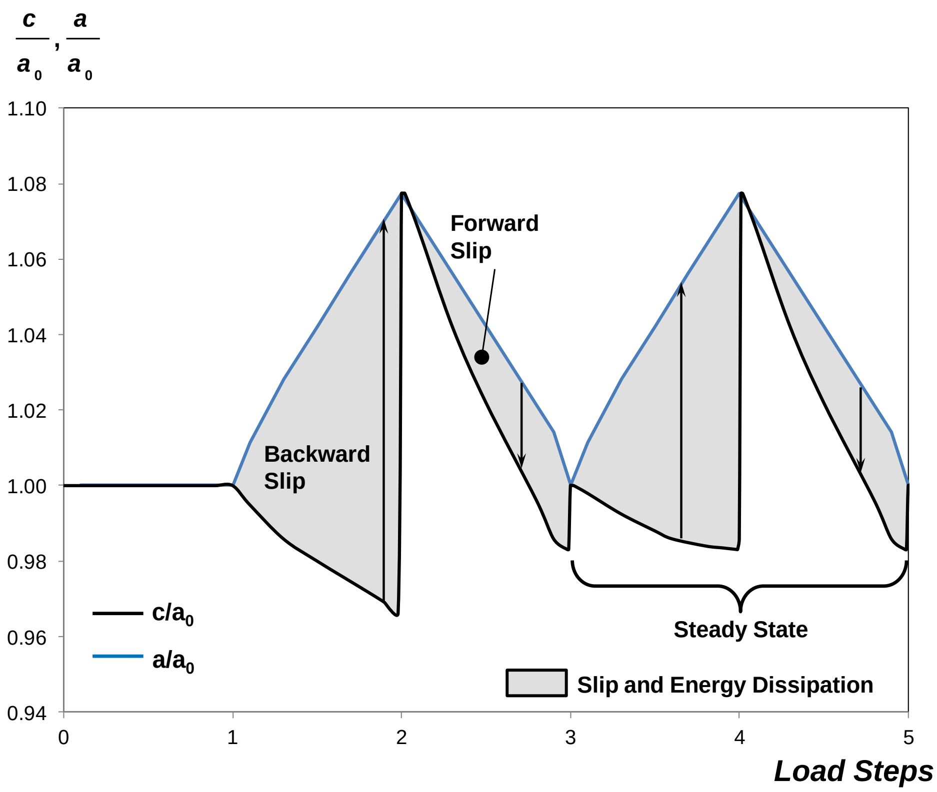

Figure 6.8b: Evolution of stick and slip zones. (T/P_o = -0.04, f = 0.8).

6.3 Energy expenditure

An important feature of these lap joints is that they clearly show hysteresis, and hence, under the application of any kind of fluctuating remote load, they display damping. This is usually viewed as a desirable property, but it also causes damage [106, 107, 108] and one possible measure of the damage may be the maximum density of work done, i.e. the maximum work done per unit area. One feature of this problem which is rather different from the standard Cattaneo-Mindlin one is that the contact pressure is not constant at a particular position, because of the changing contact size. It is simplest to note that the rate of doing work per unit time and per unit area, $\dot{W}(x)$, is the product of the shear traction and slip velocity $(fp(x) \times \dot{u}(x))$. This quantity has been integrated up with respect to time over a steady state cycle, to show how the 'damage' is localised within the contact which may lead to failure due to fretting fatigue [64]. As the pressure falls smoothly to zero at the contact edge and the slip velocity falls to zero at the stick-slip interface, the maximum is clearly at some intermediate point along the slip region. For the example problem treated the work done per unit area per cycle of load is shown in Figure 6.9a for the tension loading case and Figure 6.9b for the compression case. These figures also show the effect the friction coefficient has on the localisation of energy dissipation (and, hence, damage): for the tension case, shown in Figure 6.9a, when the friction coefficient is increased, the extent of the slip region decreases and so does its magnitude; for the compression case shown in Figure 6.9b, both the extent of the slip region and its magnitude reduce significantly as the friction coefficient is increased. As a result, the amount of frictional energy dissipation decreases for higher friction coefficients in the case of both tension and compression. Figures 6.9a and 6.9b show the 'location and the magnitude of the frictional energy dissipated' for tensile and compressive loading respectively.

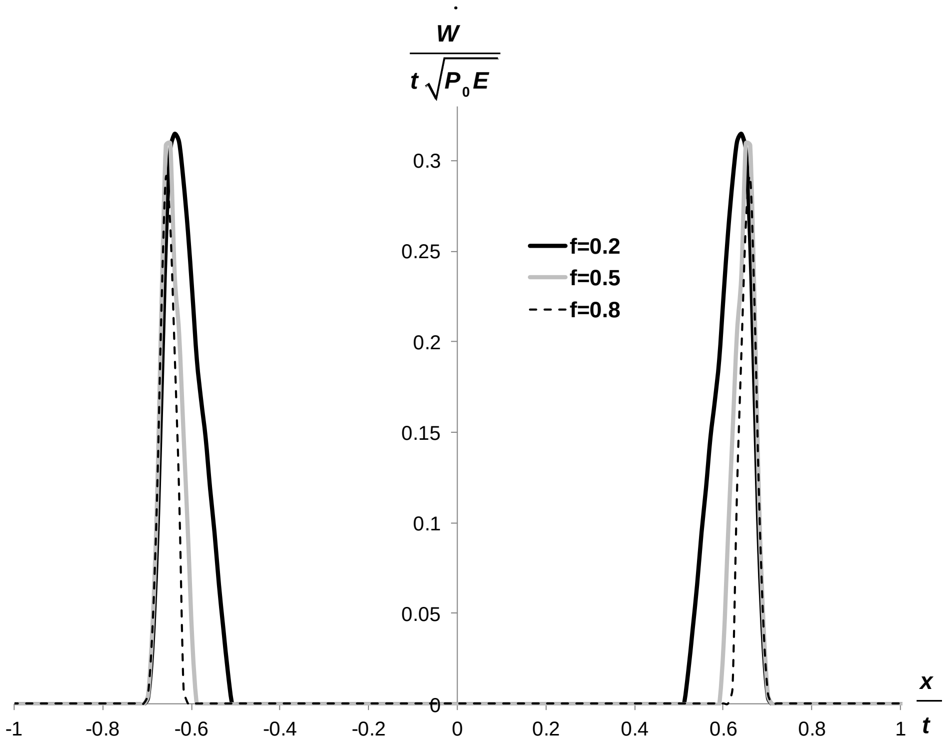

Figure 6.9(a): Energy dissipation per unit area for the tensile bulk T/P_o = 0.04 and f = 0.2, 0.5 and 0.8.

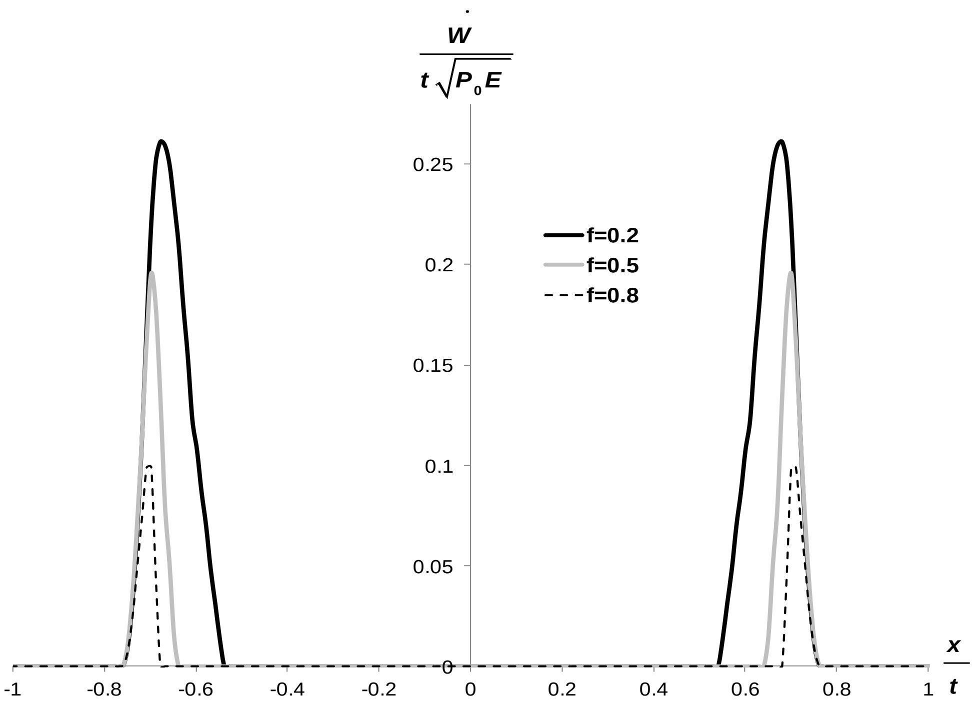

Figure 6.9(b): Energy dissipation per unit area for the compressive bulk, T/P_o = -0.04 and f = 0.2, 0.5 and 0.8.

For the tension case, Figure 6.9, the extent of the slip region as well as its absolute value decrease for an increasing friction coefficient. A similar trend applies to the compressive bulk load but the extent of slip and its magnitude decreases more significantly for an increasing friction coefficient. Note that it may be expected that an increase in the coefficient of friction leads to a greater expenditure of energy. However, it is not applicable for this case because an increase in friction coefficient has two effects. First, an increase in friction would lead to an increase in shearing traction in the slip zone. At the same time, the slip displacement decreases for higher friction coefficients and this seems to have a more significant effect.

A second level of integration may now be performed with respect to position to determine the work done per cycle of loading, and hence the damping property of the joint. This quantity has also been found by a different method, which avoids integration, and is in the spirit of the procedure devised by Mindlin, viz. the work done by the remote external loads applied to the laps was found, first with a finite coefficient of friction, and secondly with an artificial extremely high value of frictional coefficient. In the latter case the work done over a loading cycle is recovered and is associated with the reversible elastic strain energy, whilst in the former case there is an additional component equal to the frictional work. The difference is the frictional work alone, and this was found to agree well with the value found by pointwise integration. Figure 6.10 is a comparison of the effects of compressive and tensile bulk loads at various friction coefficients 0.2, 0.5 and 0.8. It shows that the energy dissipation decreases as friction coefficient increases because a higher friction coefficient prevents the joint interfaces sliding relative to each other. For the same friction coefficient and magnitude of remote load, the results show that tension dissipates more energy than the corresponding compression case because the slip region between the contact interface is larger when the joints are in tension. Increases in both compressive and tensile remote loads lead to the greater amount of energy expenditure (see Figure 6.10). The same trend continues until the value of the remote load reaches incipient sliding.

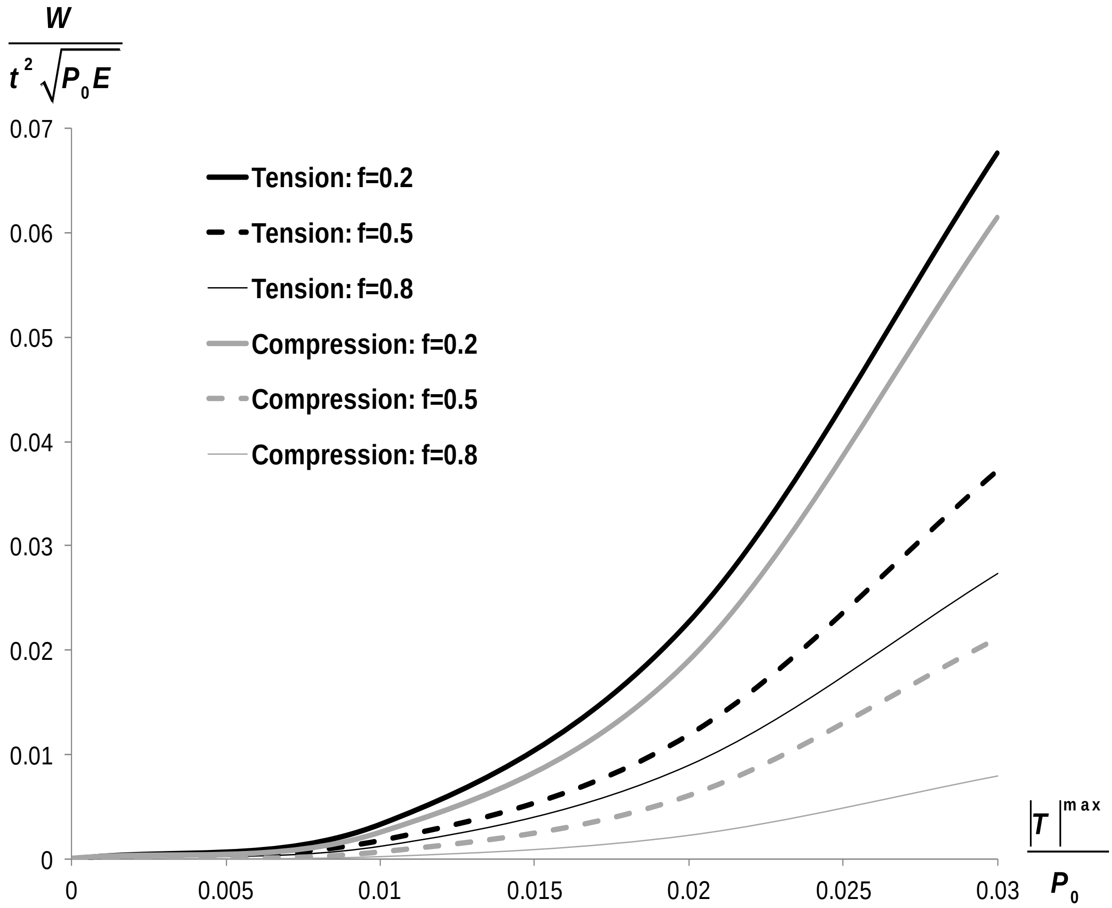

Figure 6.10: Frictional dissipation as a function of compressive and tensile bulk for three different friction coefficients *f*=0.2, 0.5, and 0.8 and the same value of *w/t* = 1.

In practice, the width of the pinching pressure, w, varies depending on the size of the bolt so an investigation to analyse the effect of energy dissipation for different values of $\frac{w}{t}$ was also carried out. All the variables are kept constant apart from the values of $\frac{w}{t}$. Figure 6.11 illustrates that as the pinching pressure width is increased the energy dissipation decreases. This phenomenon applies both when the lap joints are in tension or compression. For the same value of $\frac{w}{t}$, an increase in pressure also reduces the energy dissipation. It should be noted that the results reported in this chapter are in agreement with the experimental findings reported by Eriten and co-workers [109] in terms of both the evolution of energy dissipation as a function of applied maximum remote load and the effect of bolt pre-load.

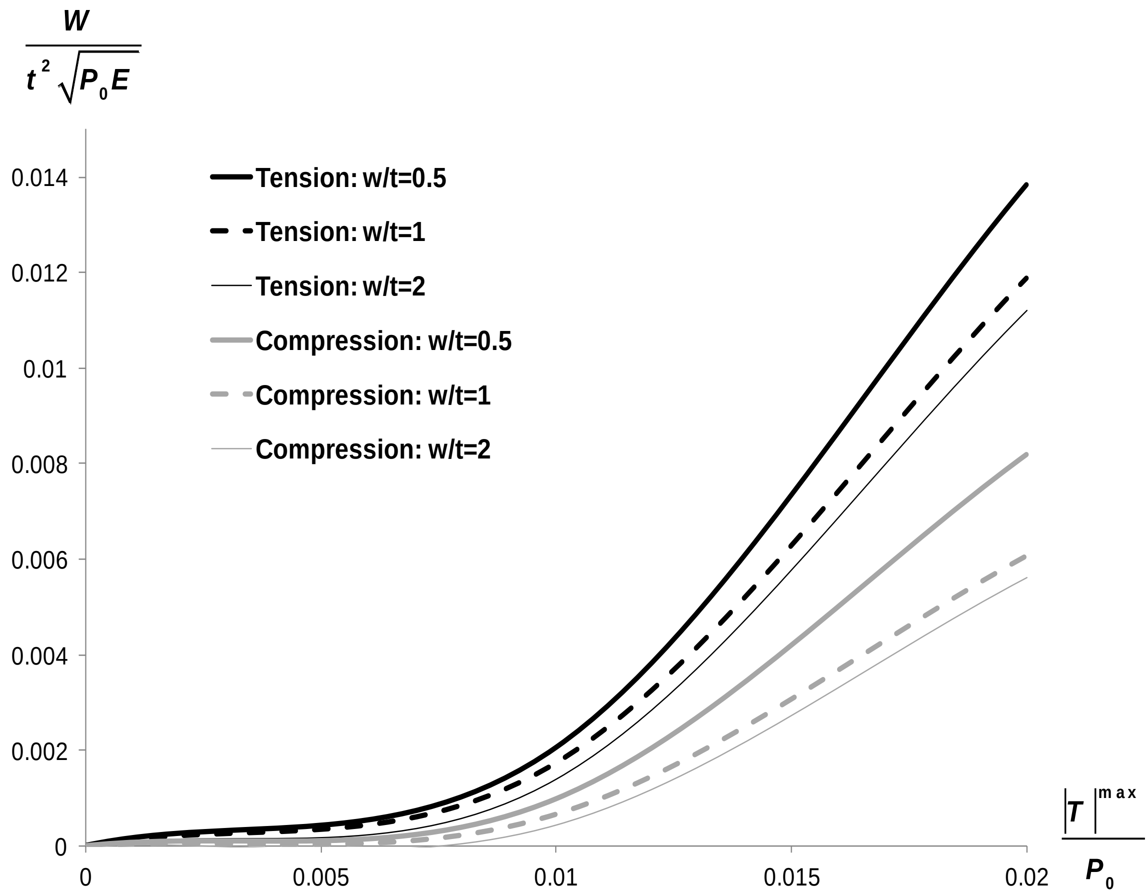

Figure 6.11: Frictional dissipation as a function of pinching pressure width to the thickness, *w/t* = 0.5, 1 and 2 for friction coefficients, *f* = 0.5.

6.4 Conclusion

A lap joint, idealized as a two dimensional problem, has been analysed and the clamping pressure assumed to be uniform. With this as the starting point, it has been shown that, while the normal load causes the contact to snap to a fixed size, comparable with the thickness of the strips or width of the imposed contact loading (whichever is the smaller), a remote tensile loading causes a smooth change in the size of the contact. The size of the remote loading was chosen to simulate partial slip. The partial slip contact problem which results is coupled, with a direct load applied away from the shorter length protrusion giving rise to a broadening of the contact patch, and vice versa. Cyclic loading produces a cyclic slip state which reaches steady-state after one cycle, and the trends in dissipation with extent of contact and magnitude of tension and compression force have been found. The tensile remote load dissipates more energy since both magnitude and extent of slip zone are greater than that arising in compression. However, there is a similar trend in an increase of energy dissipation when the magnitudes of both tensile and compressive remote loads are increased. The highest degree of damping occurs when the friction coefficient is infinitesimally greater than limiting friction coefficient.

7 Axisymmetric Receding Contact

7.1 Introduction

There seems to be relatively little research work on frictional receding contact in the open scientific literature. Receding contact problems are contacts where, when the load is applied, the contact area decreases from that which arises when the components are brought together before being loaded. This type of contact can be found in many engineering components such as flange joints in the aerospace industry and high strength frictional grip bolted connexions. I am interested in the interface response when the receding contact is subsequently torsion. The work of this chapter is to analyse the axis-symmetric form of the receding contact in which the circular elastic disc is pressed against an elastically similar half-space by a normal load whose value increases steadily from zero to a steady-state constant value, Figure 7.1. The torque is then applied about the axis of the disc.

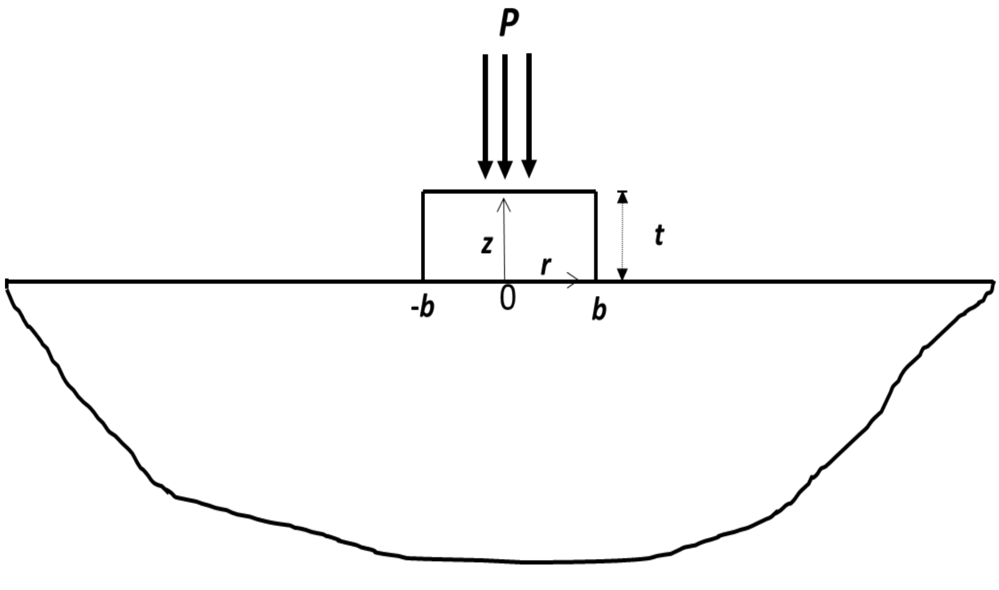

Figure 7.1: A circular elastic disc pressed against an elastically similar half-space by a constant normal load, *P*.

7.2 Problem formulation

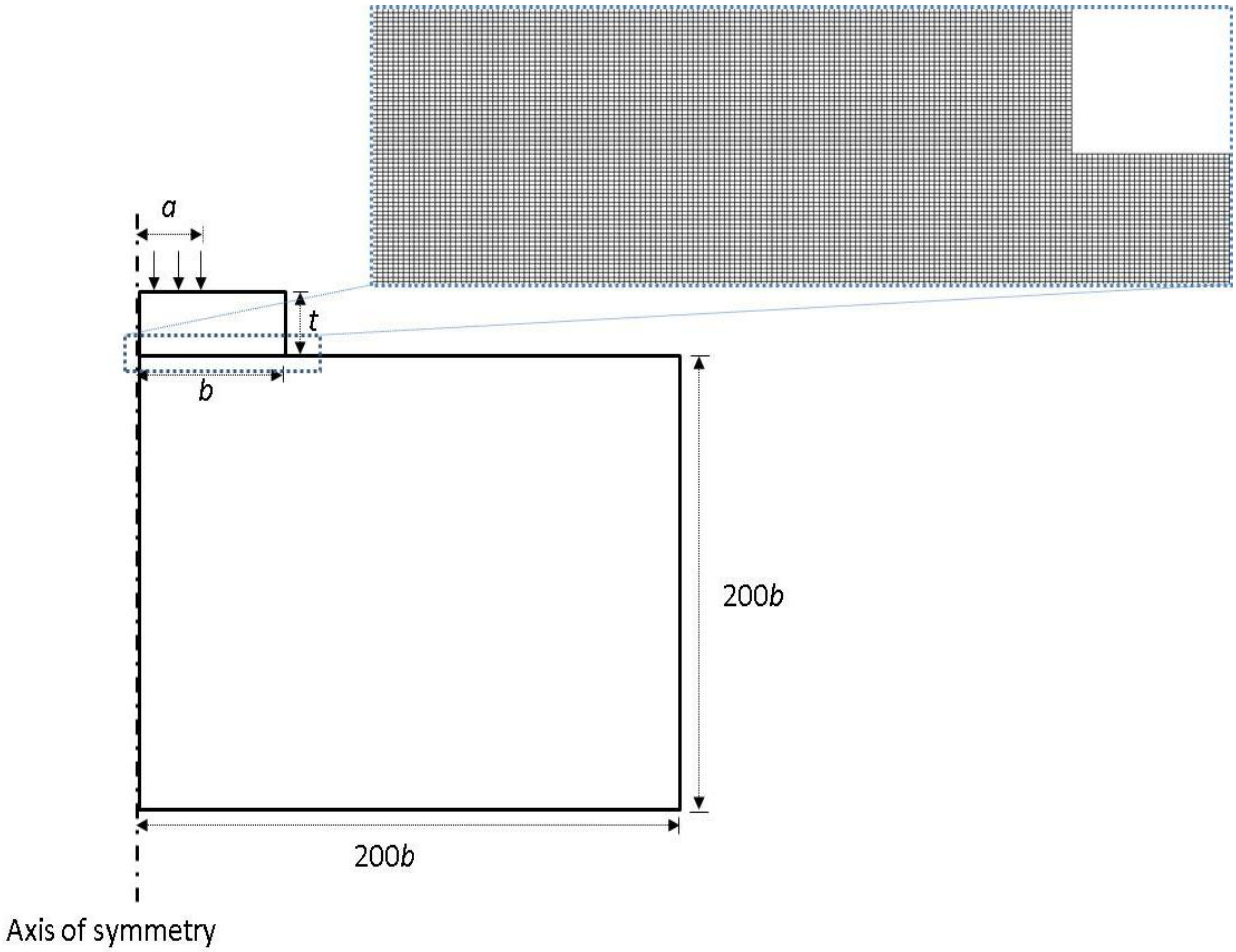

Figure 7.2: Axisymmetric finite element model of the problem.

The problem consists of a circular disc of radius, b , an height t. The size of the lower body is chosen to be sufficiently large for it to be regarded as a half-space. The geometry is three-dimensional and the circular disc is pressed down by a constant pressure, $p_o = \frac{P_o}{\pi a^2}$, where P_o is the steady-state constant normal load and a is the radius of the area in which the pressure acts upon. Exploiting the nature of the axis-symmetric contacts the three dimensional problem can be represented by an axisymmetric finite element model, as shown in Figure 7.2, thereby reducing the computational cost significantly. The finite element model will be analysed using the commercial finite element analysis software, ABAQUS. The mesh is well refined and graded in the area where separation may occur upon the application of the load. There are no singularities in this problem since the contact pressure will drop to zero at the location where separation occurs. Tests were carried out to ensure that the results are independent of the mesh size and the finite element model is fully converged with all interfacial boundary conditions and applied load conditions. A 4-noded (bilinear), axisymmetric solid element (CGAX4) is used and the mesh size at the contact interface is $0.005t \times 0.005t$ where t is a thickness of the disc as shown in Figure 7.2. Contact elements, which link the finite element models of the contact bodies, were chosen which utilise the augmented Lagrangian method to handle the discontinuous nature of the contact boundary conditions.

7.3 Bilateral solution

One of the purposes of this work is to investigate how the results from a bilateral model, which is easier to model, can be used to predict the behaviour of the contact model. Suppose, therefore, that the interfacial coefficient of friction is artificially very large to prevent all slip between the disc and an elastically similar half-space so that the two contacting bodies are bonded together. I can then treat the problem as one single entity. I can find the location of the contact interface at which it separates by considering the pressure distribution. The location where the separation is likely to take place is when the axial stress, $\sigma_{zz}(r)$, becomes zero. As an example, suppose that a particular dimension of the disc is chosen, $\frac{b}{t} = 5$. It is possible to find the critical radius of the area beyond which the normal pressure must act in order to ensure complete contact interface between the disc and the half-plane. In fact, the critical radius, $\frac{a}{t}$, is equal to 2.1 in this particular case. It can be seen from Figure 7.3 that pressure distribution is just equal to zero at the outer edges of the disc. This means that the normal pressure needs to act over an area with radius, $\frac{a}{t}$, whose value is greater than 2.1 to avoid any separation along the contact interface. When the radius of the loaded, $\frac{a}{t}$, is greater or less than this critical value, 2.1. It shows that if $\frac{a}{t}$ is equal to 3 the pressure distribution at the outer edge of the disc is non-zero whereas the separation point is at the interior point in the case when $\frac{a}{t}$ is equal to 1.5 as displayed in Figure 7.3.

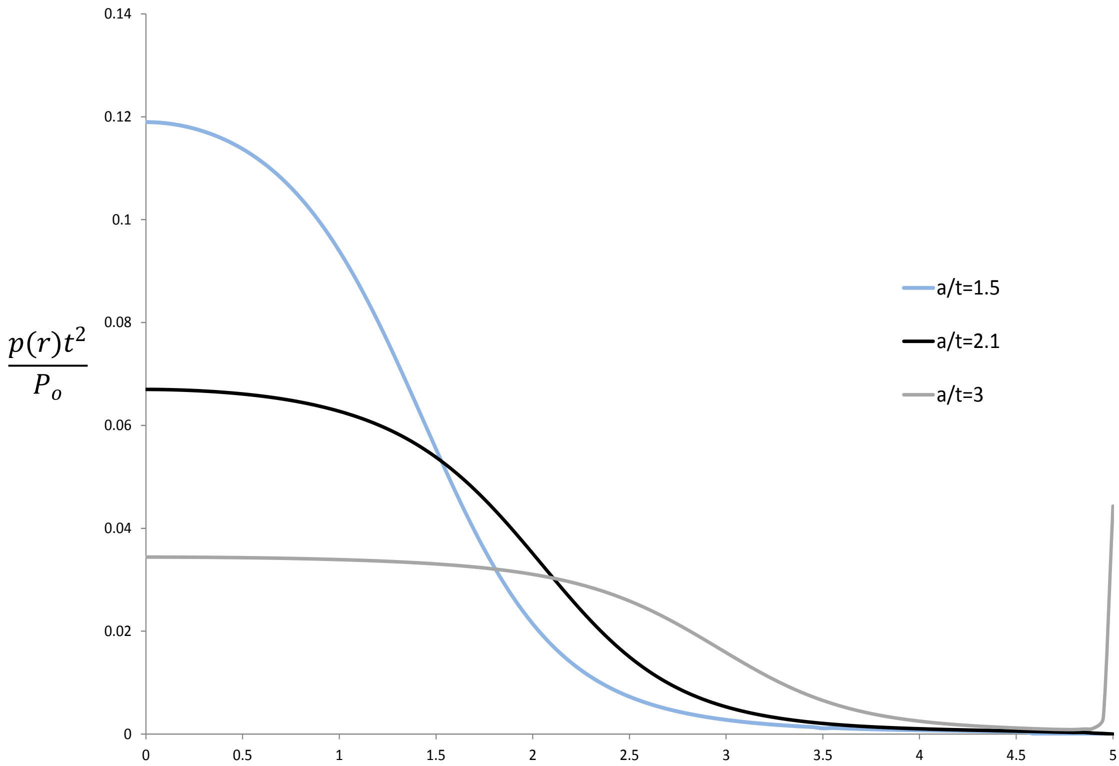

Figure 7.3: Interfacial pressure distribution for *b/t* = 5 and *a/t* = 1.5, 2.1 and 3.

The procedure was then repeated with other dimensions, $\frac{b}{t}$, of the circular disc. The results are displayed in Figure 7.4 which shows a boundary between separation and non-separation. This suggests that contact will remain complete if the points in $\frac{a}{t}, \frac{b}{t}$ space of Figure 7.4 are below the boundary line. The results in Figure 7.4 show a linear relationship between the radius of the disc and the critical radius needed to ensure complete contact. As predicted, a larger loaded area is required as the disc radius increases. The results are practically useful as it provides information on how all separation can be avoided which will be discussed in detail in the next section 7.4 together with the cases of finite friction coefficients and other limiting cases.

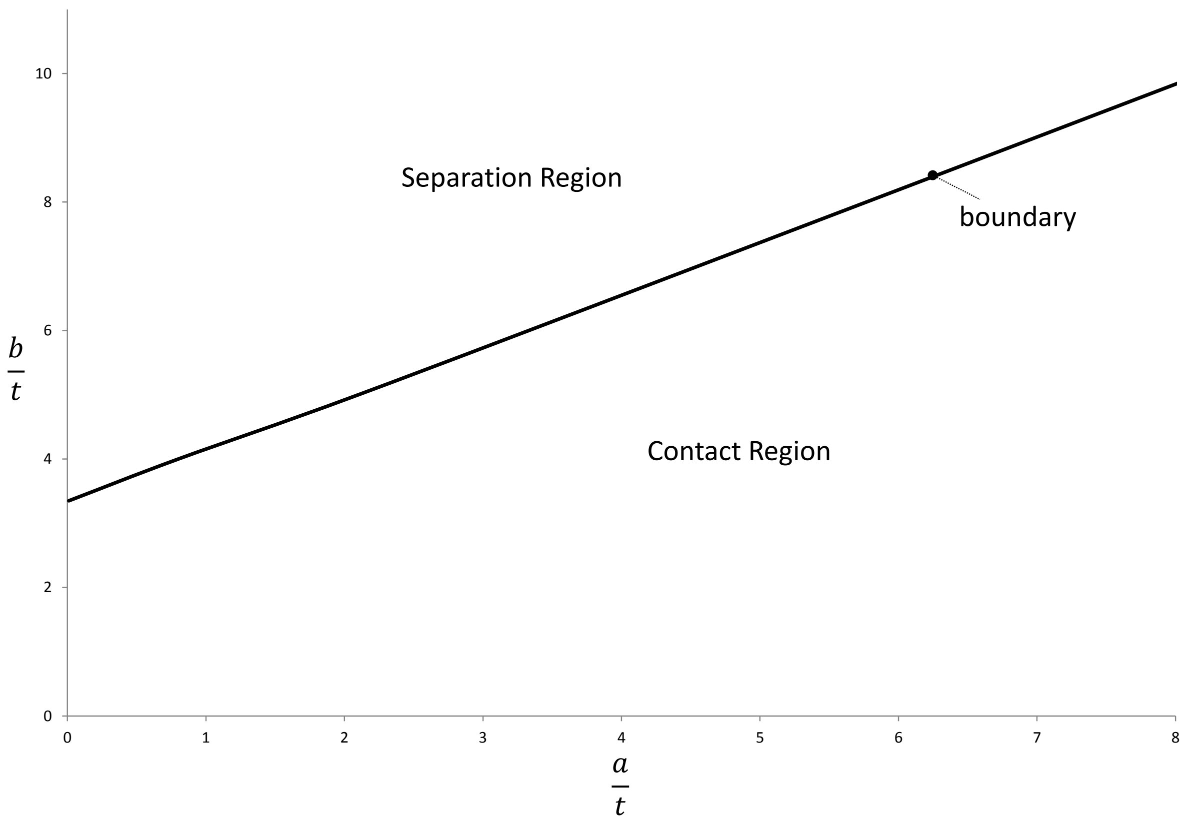

Figure 7.4: Interfacial behaviour map of a monolith for separation and non-separation boundary.

7.4 Contact model

The contact elements are now inserted and the finite element models are re-run. A 4-noded (bilinear), axisymmetric solid element (CGAX4) is used and the mesh size at the contact interface is $0.005t \times 0.005t$. The circular disc is pressed against an elastically similar half-plane by an axis-symmetric normal load, P, whose value increases from zero to a constant value P_o with respect to time. Each loading cycle is solved using at least two-hundred increments using an implicit solver.

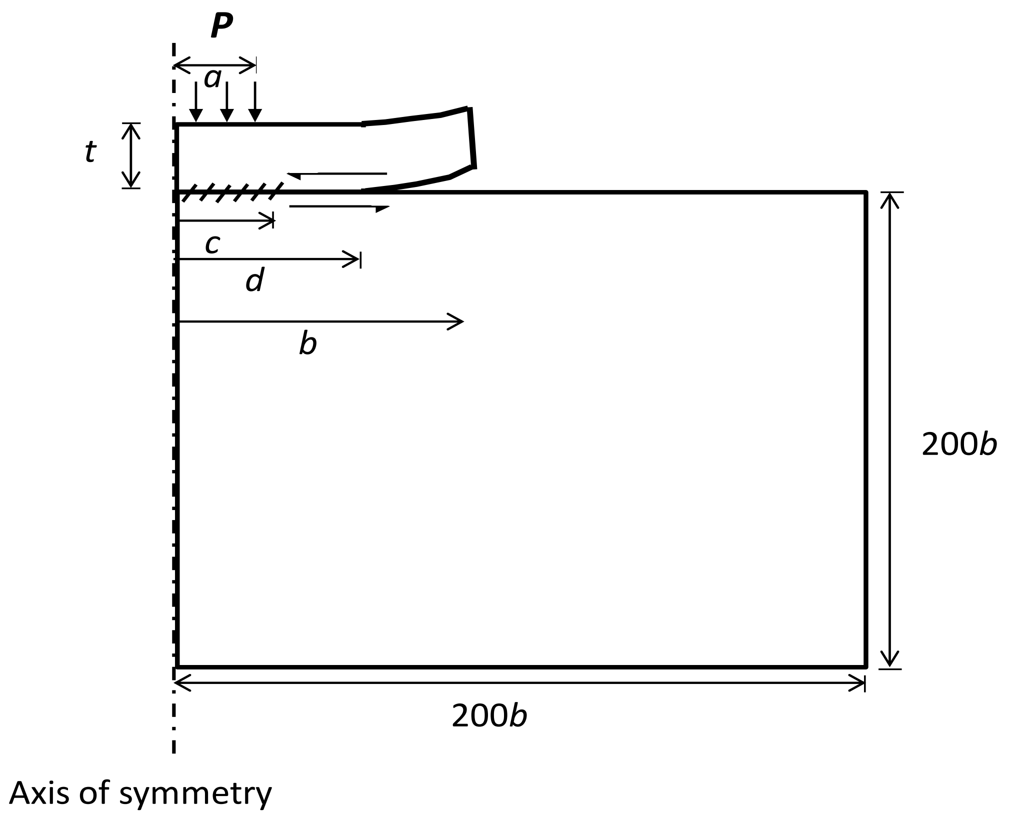

Figure 7.5: Axisymmetric finite element model of the problem and definition of symbols.

For a particular radius of the circular disc, $\frac{b}{t}$, and coefficient of friction, f, the contact interface between the disc and half-plane will separate provided that the radius of the circular area, $\frac{a}{t}$, which the pressure acts upon, is less than the critical size. If the separation occurs the pressure distribution will drop to zero at the locations where the disc is separated. This implies that there must be a slip zone which is followed by the central stick zone toward the centre of the disc. The extent of the contact area and the length of stick zone are denoted as d and c respectively as shown in Figure 7.5. Hence, the length of slip zone is the difference between the extent of contact area and the length of the stick zone, $d - c$.

Let now consider an example case where the radius of the circular disc, $\frac{b}{t} = 5$, and the radius of the loaded area, $\frac{a}{t} = 0.5$. The comparison of the results from two different models, a monolith and a contact model, will be made. Figure 7.6 shows the pressure and shear traction distributions from a monolith. It predicts that the contact interface will be separated at the location where the radius of the circular disc is equal to $0.65b$. Exactly the same model was re-run with contact elements inserted and coefficient of friction is equal to 0.9. The pressure and shear traction distribution of the contact model are shown in Figure 7.7. It shows that the actual location where the circular disc is separated from the half-plane is equal to $0.52b$. The actual point of separation is slightly lower than the predicted result, $0.6b$, from the monolith model. This shows that the result of the monolith provides a reasonable estimate of the interface behaviour in the contact model. Note that this procedure is applicable to other dimensions of the disc and the loaded area. The difference between the predicted and actual results increases as the friction coefficient decreases.

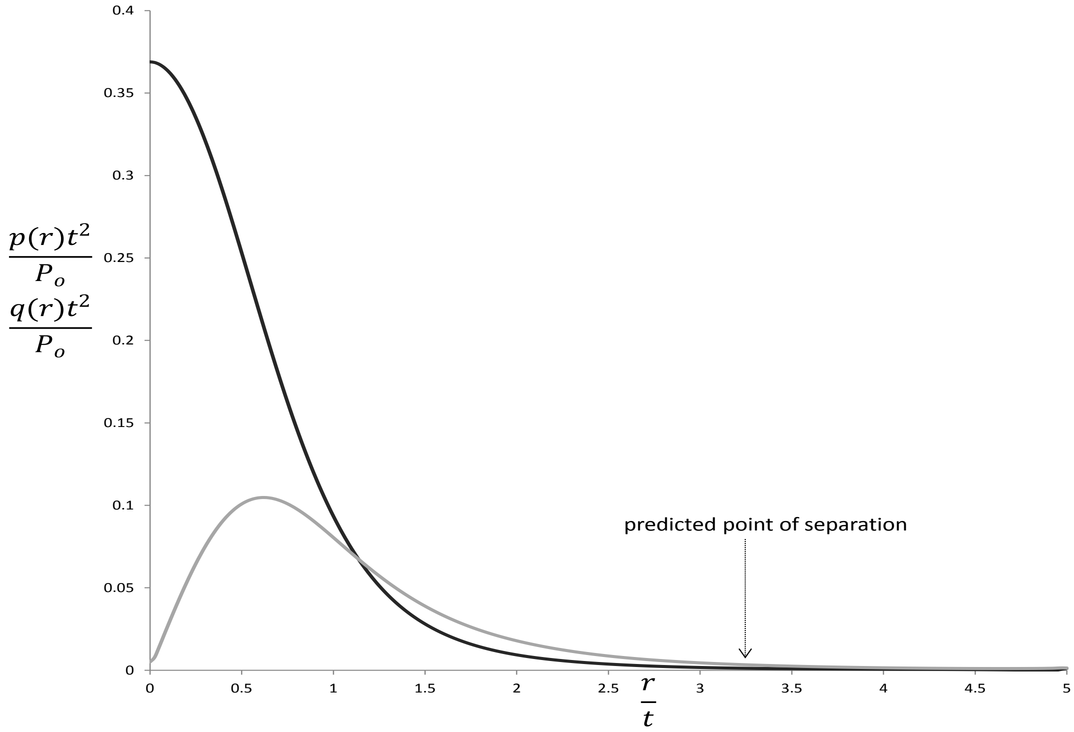

Figure 7.6: Interfacial pressure and shear traction distributions from a monolith when *b/t* = 5 and *a/t* = 0.5.

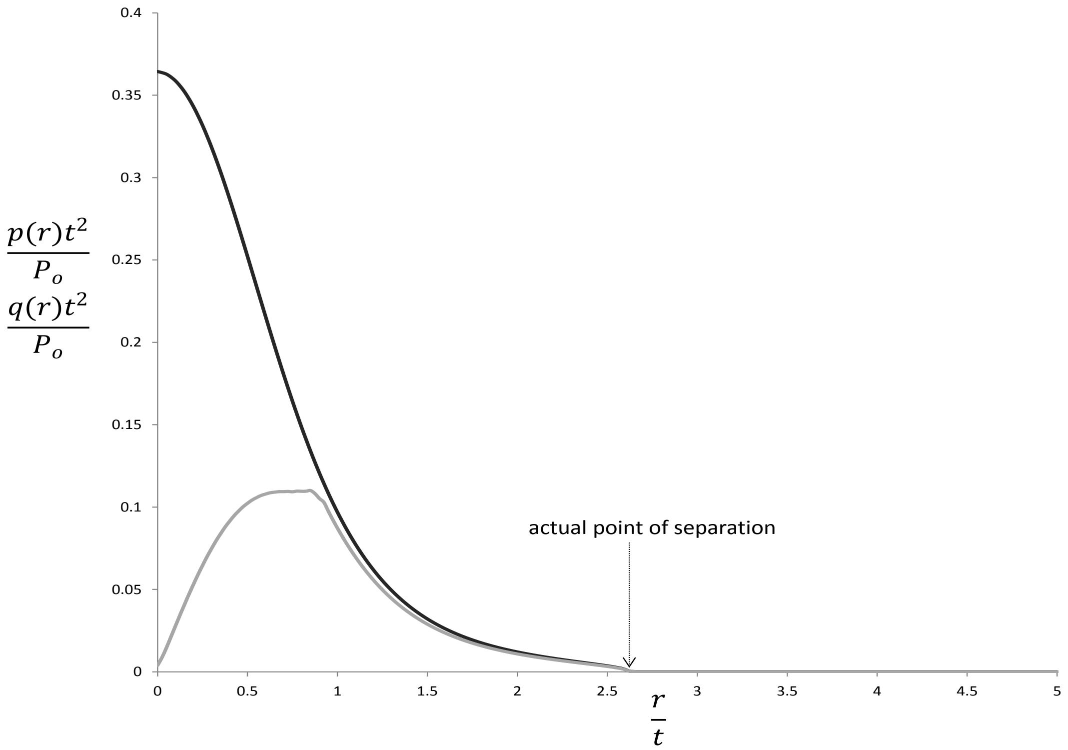

Figure 7.7: Interfacial pressure and shear traction distributions of a contact model when *b/t* = 5, *a/t* = 0.5 and *f* = 0.9.

I can follow the same analysis as in the bilateral solution where the critical radius of the disc needed to avoid separation can be found for a particular disc radius. The cases when friction coefficients are finite are considered as well as the limiting case when there is no friction present along the contact interface. The results are plotted in Figure 7.8. The line AB represents the cases in which the normal pressure is fully extended up to the outer edge of the disc and therefore no separation occurs. The line CD is the critical radius for different values of the disc radius when the contact interface becomes frictionless. The shaded region ABCD is the unconditional contact region. This implies that the separation can be avoided for all friction coefficients provided that the points in $\frac{a}{t}, \frac{b}{t}$ space of Figure 7.8 are below or to the right of the line CD.

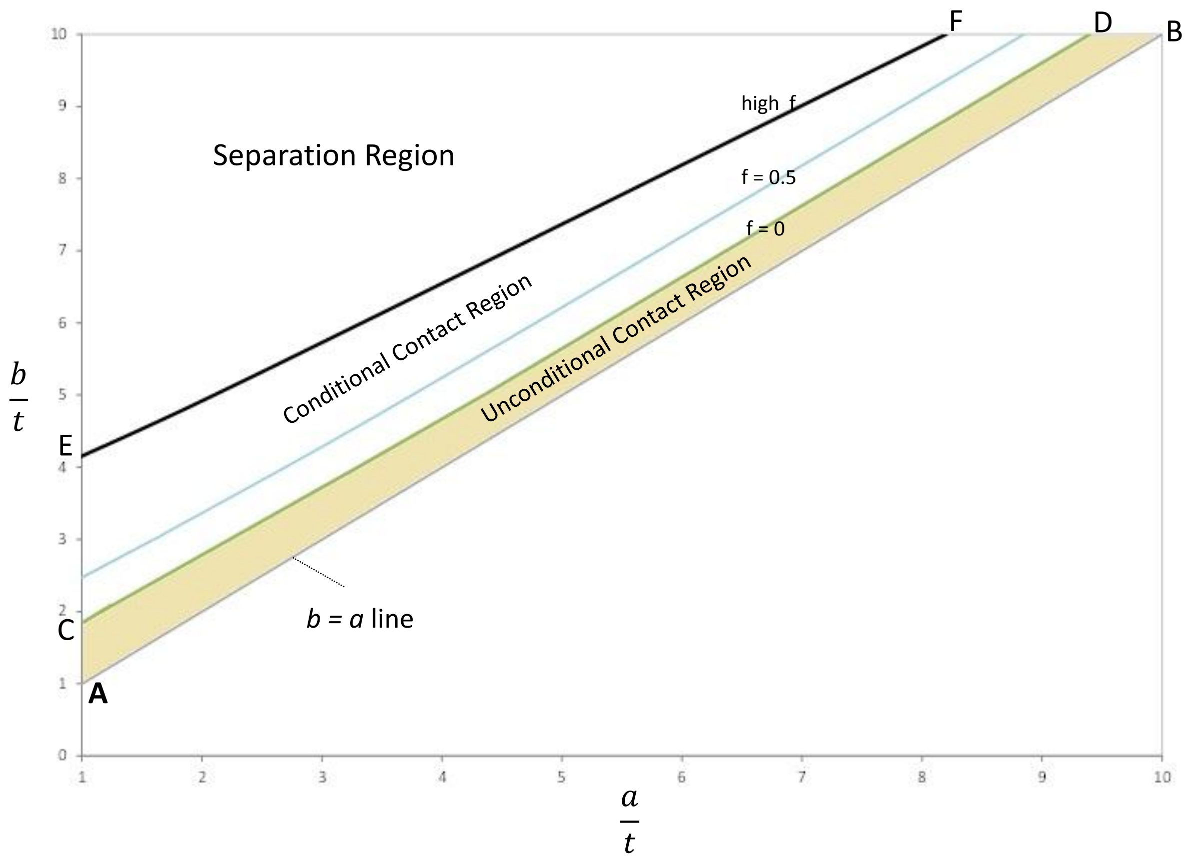

Figure 7.8: Map of interfacial behaviour of the contact shown in Figure 7.5. The separation boundaries are given for *f* =0 , *f* = 0.5 and when *f* is extremely high.

It is worth noting that these results are practically useful as it can be used as a design criterion against separation. If the contact interface does not separate there is no edge slip provided that the coefficient is greater than a critical value, 0.543. It was explained in Chapter 5 that this is the value of friction coefficient required to ensure that the edge of the contact is fully adhered. This increases a possibility of a contact to shaking down to an adhered state. If there is no slip present then the fretting fatigue failure may be avoided. The other limiting case considered is when the relative radial displacement is inhibited whilst permitting for the relative normal displacement. This gives exactly the same results as the monolith denoted by line EF in Figure 7.8. When the friction coefficients become finite the critical radius are between the line CD and EF as shown for the case of friction coefficient, f = 0.5, in Figure 7.8. As an example in interpreting the figure for the case of $f = 0.5$, the pressure needs to act upon an area whose radius has to be equal or greater than the critical radius $\frac{a}{t}$ (i.e. to the right of line $f = 0.5$) and the value of f must not be less than 0.5 in order to avoid any separation. The area CDEF is the conditional contact region where the result is dependent on the values of friction coefficients.

Let us now consider another example case when the radius of the disc, $\frac{b}{t} = 5$, the radius of the loaded area, $\frac{a}{t} = 2.5$ and the frictional coefficient, $f = 0.5$. One other observation during the loading phase is that the circular disc will snap to a certain configuration upon the application of the load. The location where it separates from the half-plane $\left(\frac{r}{t} = 3.75\right)$ is independent of the magnitude of the load as displayed in Figure 7.9.

However, the state of stresses and displacement are proportional to the applied load. This is also what happens during the loading phase of the plane receding contact[110].

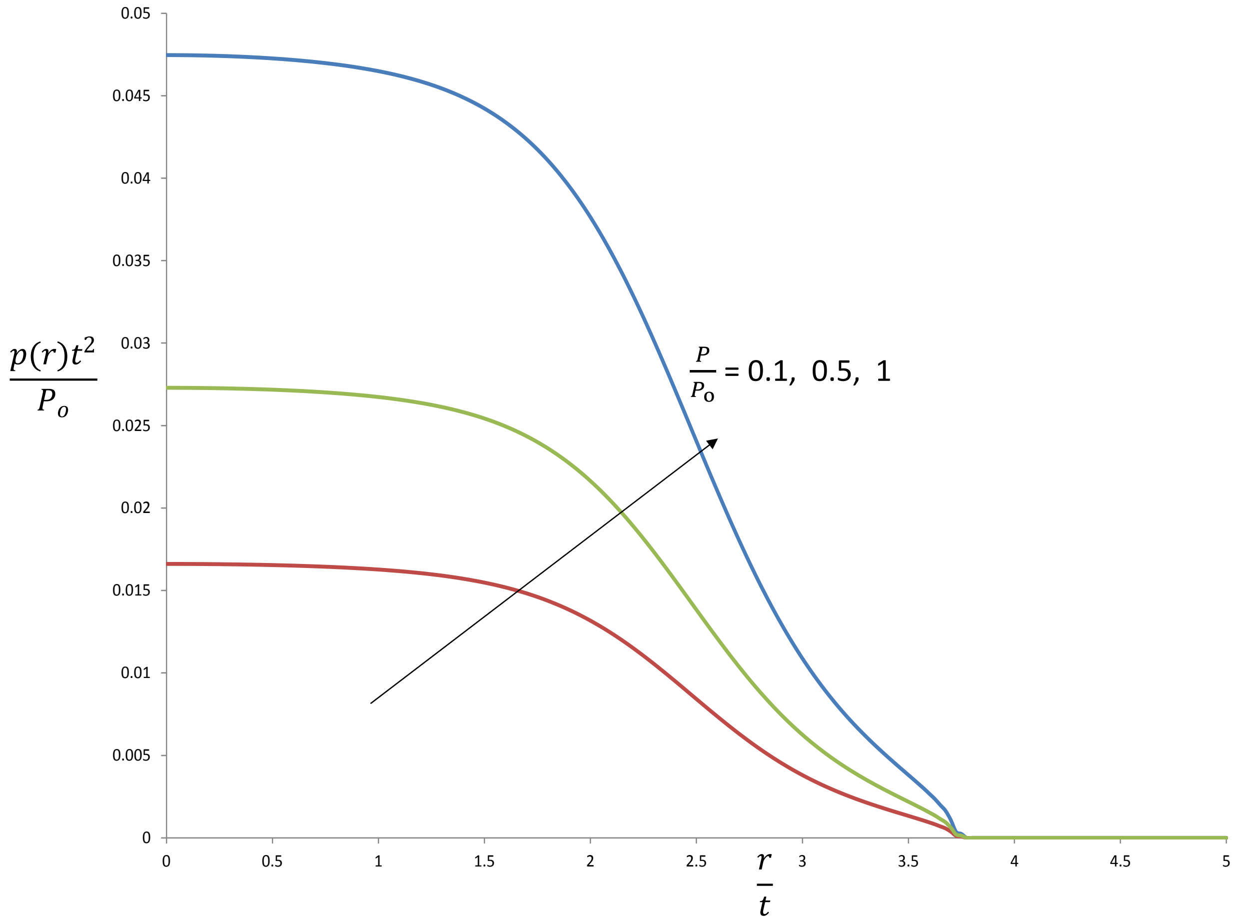

Figure 7.9: Interfacial pressure distributions of the contact during the loading phase for *b/t* = 5, *a/t* = 2.5 and *f* = 0.5.

I will now investigate the development of stick and slip zones in detail. In this example case, the value of the disc radius, $\frac{b}{t}$, is chosen to be 5 and the coefficients of friction are equal to 0.5 and 0.8. Figure 7.10 displays the extent of separation and the size of the stick and slip zones as a function of a radius of the loaded area, $\frac{a}{t}$, and the coefficient of friction, f. The coordinates c, d are defined in Figure 7.5 and each is measured from the centre of the circular disc. Note that the transitional point between stick and slip zones is denoted as *c* and the point where the circular disc separates from the half-space is denoted as d. As the coefficient of friction is reduced from 0.8 to 0.5 the extent of contact area decreases as the contact recedes further. The length of the slip zone increases slightly whereas the length of the stick zone decreases.

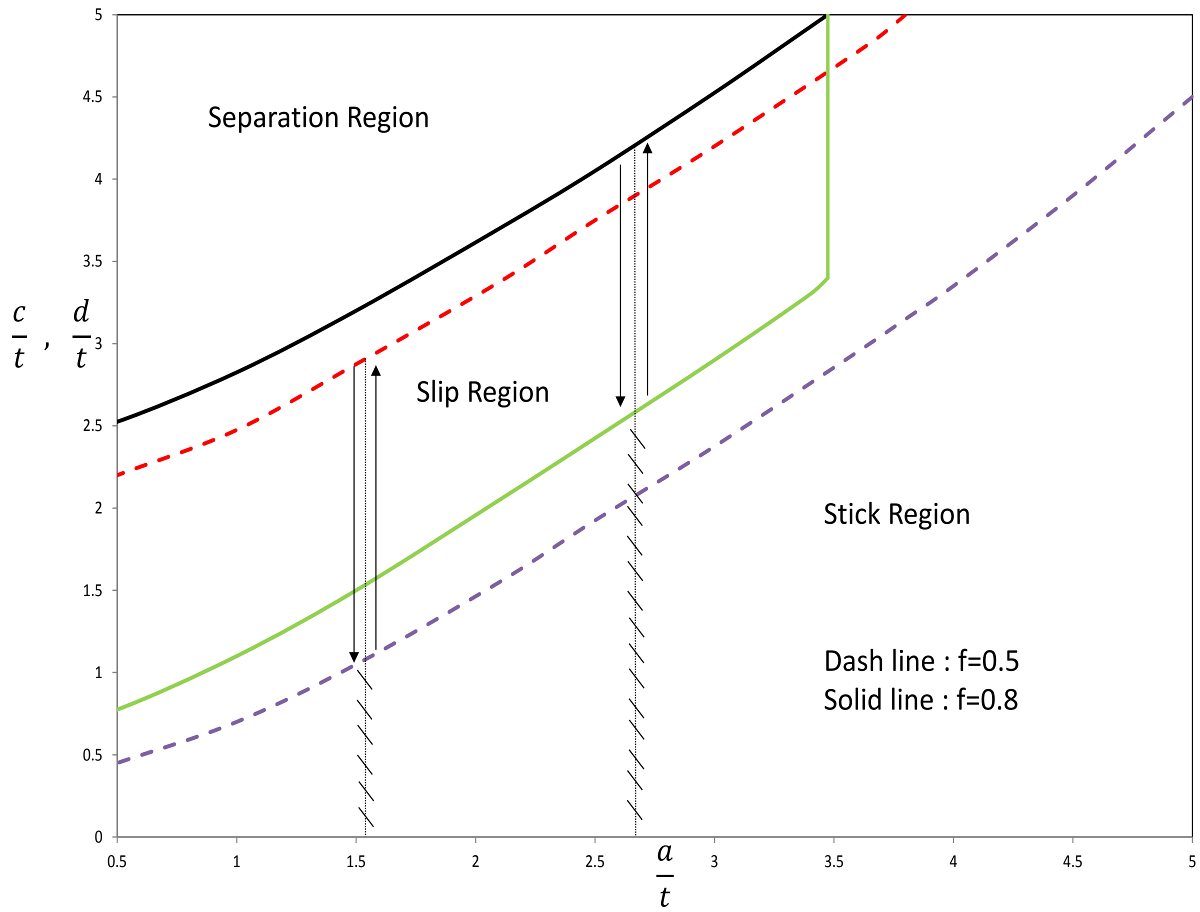

Figure 7.10: Interfacial behaviour map of a contact in Figure 7.5 at f = 0.5 and 0.8 when b/t = 5.

When the radius of loaded area is sufficiently large such that the contact interface becomes complete, the edge slip will still be present at the edge of the contact provided the coefficient of friction is less than a critical value 0.543. It can be seen in Figure 7.10 that there is still a slip region at the contact edge when disc/half-space geometry becomes a complete contact in the case of friction coefficient equals 0.5 (see dash line in Figure 7.10). However, the contact interface is fully adhered in the case of friction coefficient equals 0.8.(see solid line in Figure 7.10). To avoid any slip, the loaded area needs to be sufficiently large and coefficient of friction has to be greater than 0.543.

I now consider the unloading phase of the problem and investigate how this has an effect on the interfacial behaviour of the contact. The magnitude of the applied pressure load is gradually reduced to zero from a maximum value, P_o. The corresponding normal and shear traction distributions when $P = P_o$ are shown in Figure 7.11(see solid line). The contact loading is now gradually removed, and the tractions present when unloading to pressure load of 0.5 and 0.1 $\times P_o$ are also shown in Figure 7.11.

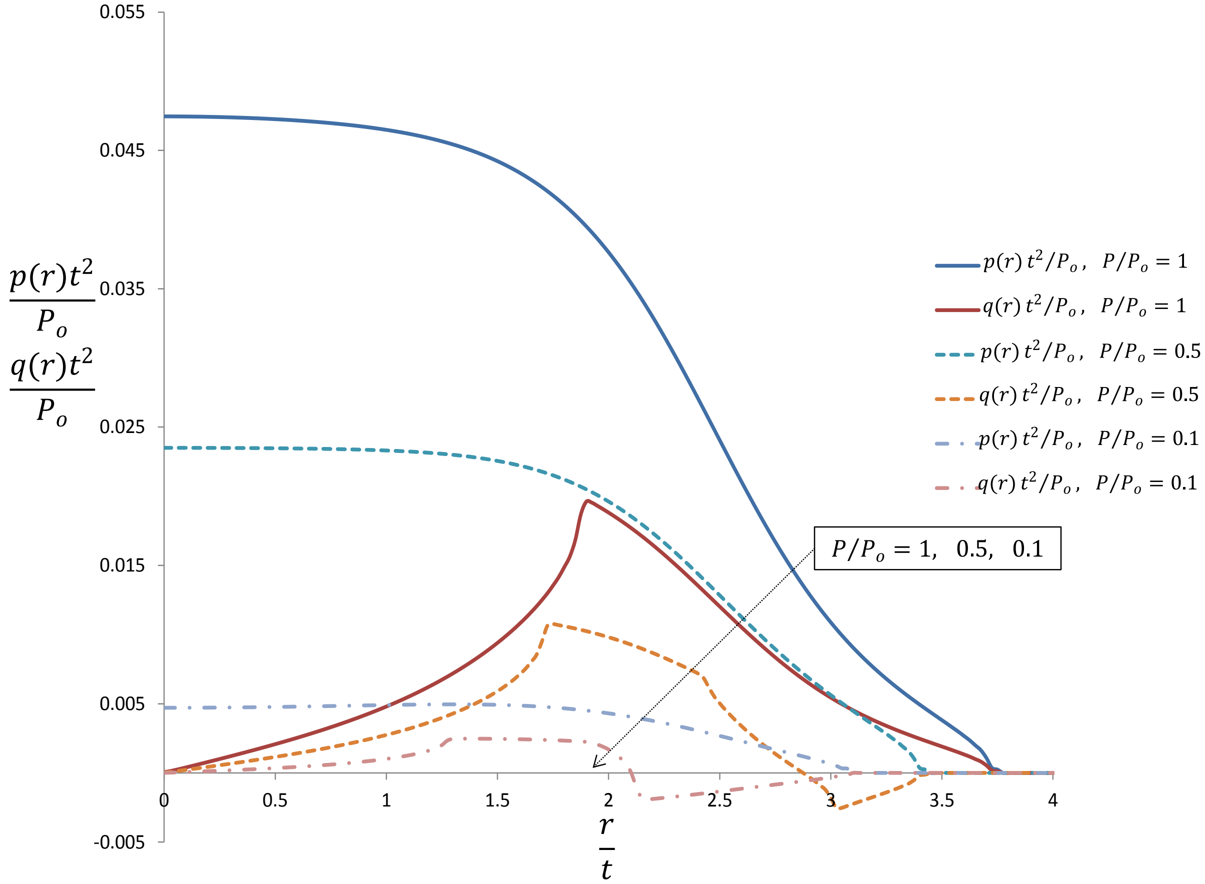

Figure 7.11: Interfacial pressure distributions during the unloading phase for *b/t* = 5, *a/t* = 2.5, and *f* = 0.5.

Upon an infinitesimal removal of load the slip region instantly sticks. Finite removal of the applied load causes the contact to recede further. A reverse slip region attached to the point of separation develops and gets bigger as the load is further removed. A forward slip region is also developed from an initial point of slip-stick transition. The circular disc will fall back into contact along the half-space surface when it is completely unloaded. It is worth noting that this problem exhibits similar behaviour to that observed in the plane receding contact problem during its unloading phase. It is useful to plot the evolution of the stick/slip/separation regimes because it is easier to visualise the interface response as portrayed in Figure 7.12.

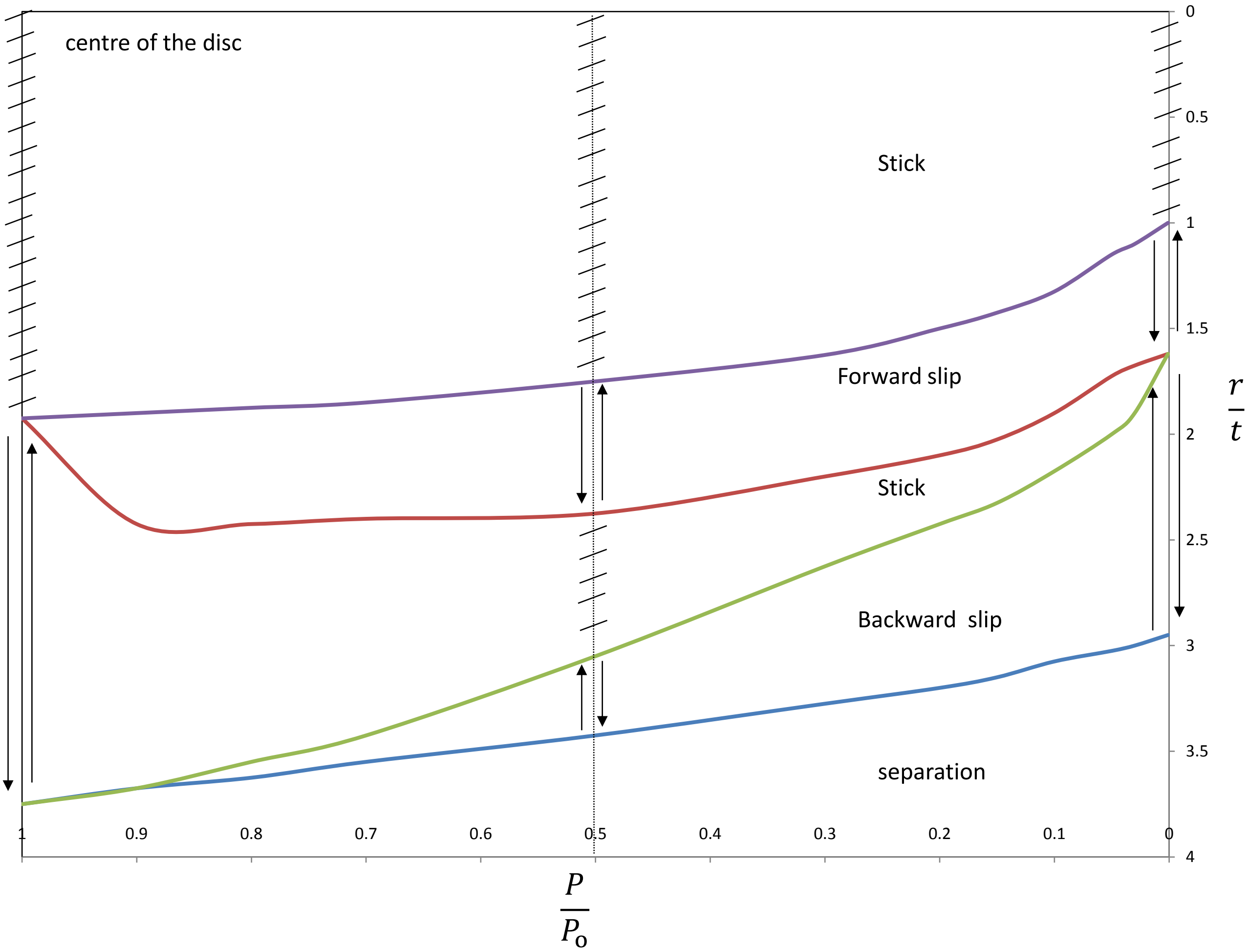

Figure 7.12: Evolution of slip/stick zones during unloading phase for *b/t* = 5, *a/t* = 2.5 and *f* = 0.5.

The extent of contact between the disc and half plane reduces from $0 < r < 5t$ to $0 < r < 3.75t$. The left hand-side in Figure 7.12 shows the state at which the normal applied load is equal to its maximum value during the loading phase. The contact snaps to a particular configuration of incomplete contact when an infinitesimal load is applied. Further increases in applied load do not alter the slip and separation points. However, the internal stresses and displacements are proportional to the applied contact pressure. Upon the infinitesimal removal of load, the contact interface instantly sticks. Further removal of load causes this stick region to contract. The contact recedes further and the extent of contact area decreases. A reverse slip is also developed at the contact edge and a forward slip region develops at the former stick/slip transition point. As an example in interpreting the figure for a finite reduction in load, if the applied load is reduced to 50% of its maximum value, $\frac{P}{P_o} = 0.5$ in Figure 7.12. The following information can be read from Figure 7.12.

1. Separation $r > 3.4t$
2. Backward slip $2.9t < r < 3.4t$
3. Stick $2.3t < r < 2.9t$
4. Forward slip $1.6t < r < 2.3t$
5. Stick $r < 1.6t$

7.5 Torsion model

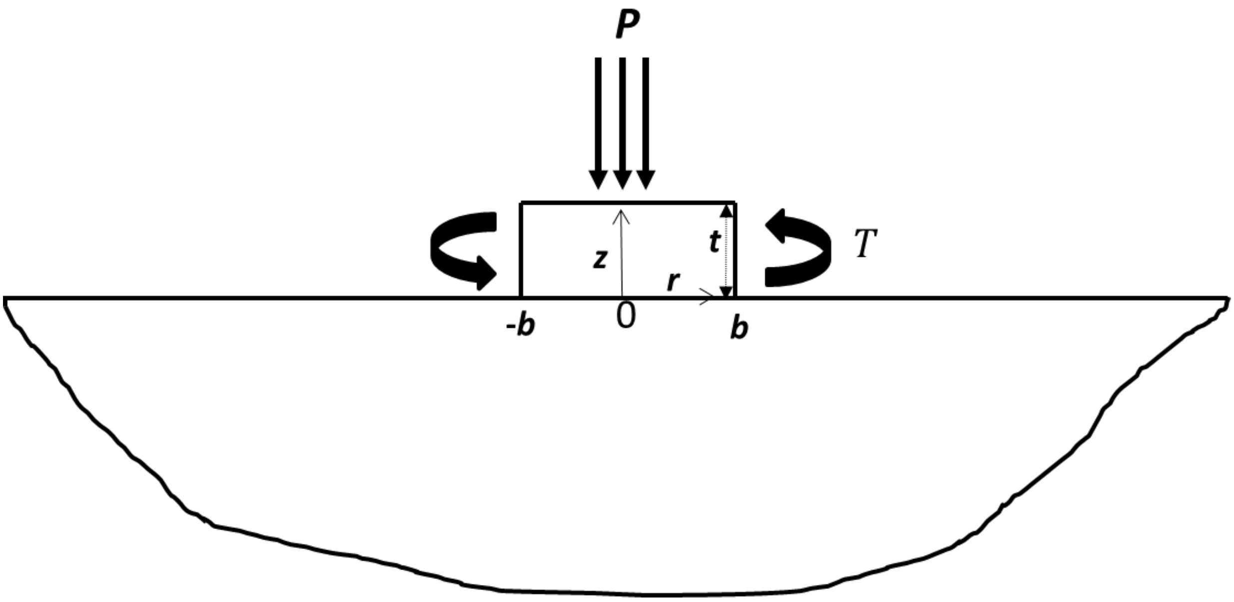

Figure 7.13: A circular elastic disc against an elastically similar half-plane under a constant normal load and subsequently to a torque, *T*, about the disc axis.

I now introduce the application of the moment about the disc axis in the clockwise direction. The circular disc will be first pressed against an elastically similar half-space by a constant normal force, followed by torsion. The torque is introduced by applying an angular displacement around the disc axially. I can work out the corresponding torsion from the shear stress induced by the angular displacement as shown in equation 7.1.

$$T_s = \int_0^r \int_0^{2\Pi} q_\theta(r) r . r d\theta dr \tag{7.1}$$

During the loading phase of the normal load, I know that the disc snaps to a particular configuration when an infinitesimal normal load is applied. The applied torque is then increased monotonically to the value slightly below the spinning limit.

The dimension of the disc and loading condition will be kept the same as the previous example where b/t = 5, a/t = 2.5. Figure 7.14 shows how the contact pressure and the resultant shear traction distributions vary during the application of torque. Upon the application of torsion, a tangential shear stress, q_θ , is induced and this will change the extent and the direction of the slip zone. As a result, the interface between stick and slip zone is shifted towards the centre of the disc as the length of slip zone increases. Since the domains of the two contacting bodies are different there is a considerable degree of coupling present.

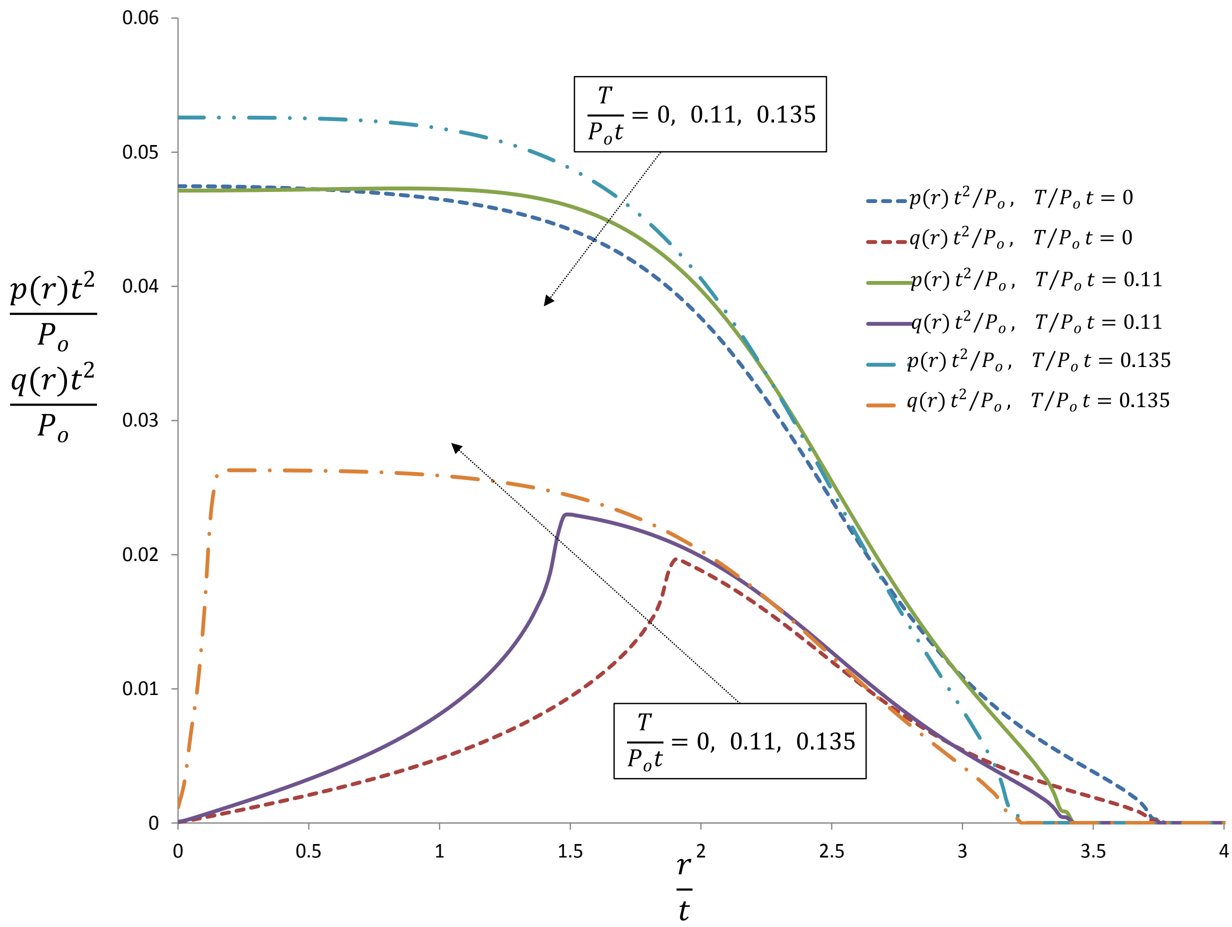

Figure 7.14: Interfacial normal and the resultant shear traction distributions when the disc under the application of different torsions T at f = 0.5.

An increase in slip zone will change the distribution of the radial shear traction. This also has an effect on the normal traction distribution and therefore the point of separation as displayed in Figure 7.14. Note that this would not be the case if no coupling were present [111] i.e. if the domains of the problem were the same. The tangential slip will not alter the profile of the radial stress. The pressure distribution will, therefore, remain the same. This implies that the point of separation remains unchanged when the disc is subjected to torsion. When the disc is in a full spinning state the resultant shear traction distribution will be purely tangential and it is equal to the product of the friction coefficient and normal traction. The freely spinning limit of the torsion, T_s, can be calculated by performing the integral in equation 7.2.

$$T_s = 2\pi f \int_0^r p(r) r^2 dr \tag{7.2}$$

The two components of the slip displacement are in radial and tangential directions. The corresponding resultant slip displacement, when the disc is under different magnitude of torsion in Figure 7.14, can be calculated using equation 7.3.

$$u^2 = u_\theta^2 + u_r^2 \tag{7.3}$$

where u_θ and u_r are the relative displacement in tangential and radial direction respectively. The result is displayed in Figure 7.15. The magnitude of the resultant displacement increases from the stick/slip interface to the point of separation. As the torsion is increased the resultant slip displacement increases at all locations up to the point of the separation. The direction of the resultant slip with respect to the radial direction can be found by using equation 7.4 and the result is shown in Figure 7.16.

$$\theta = \arctan\left(\frac{u_\theta}{u_r}\right) \tag{7.4}$$

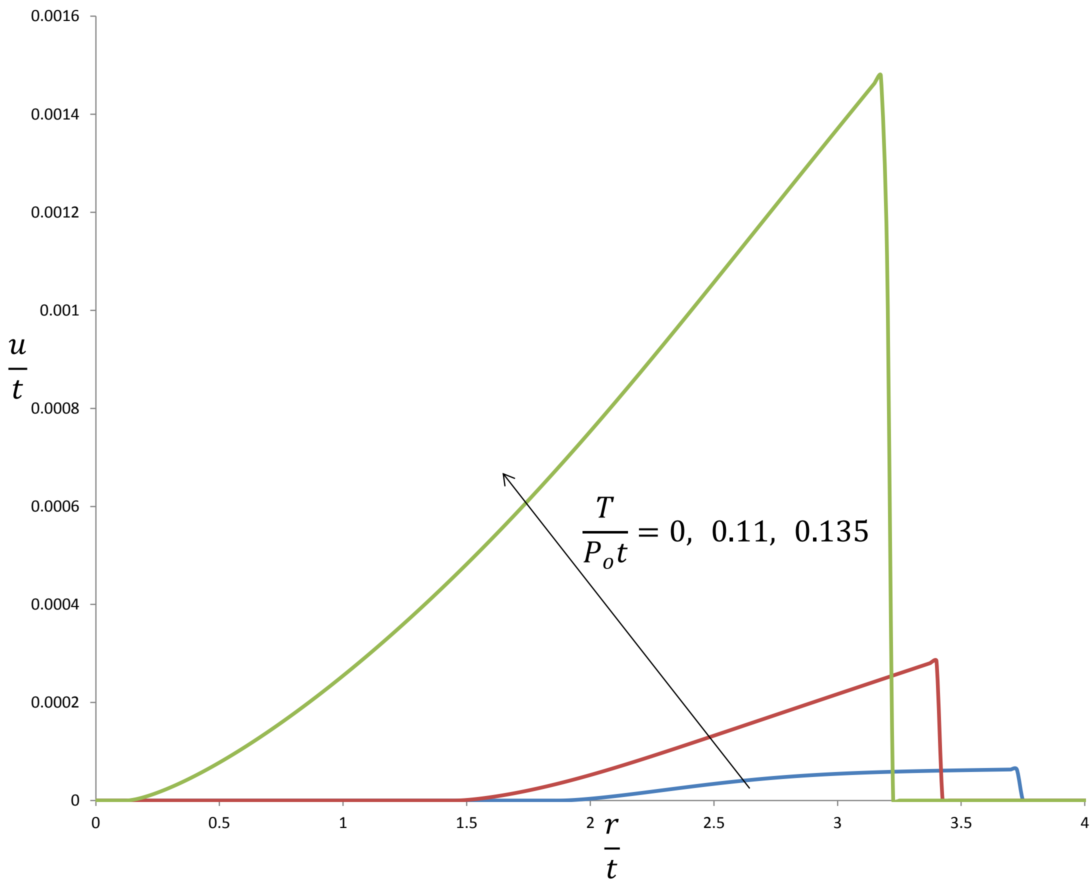

Figure 7.15: The resultant slip displacement of the contact interface when the disc subjected to different torsion, *T at f = 0.5*.

It is difficult to illustrate the direction of the resultant slip displacement in Figure 7.15 and this is plotted in Figure 7.16. The results in Figure 7.16 illustrate the evolution of contact behaviour and the direction of the resultant slip. The origin (0,0) represents the centre of the disc. The bottom line is the state at which the normal load reaches its maximum value during the loading phase. All slip direction is in radial direction at this stage. Upon the infinitesimal torsion, the resultant slip changes direction slightly. However, the separation point and stick/slip boundary remain fixed. Further increases in torsion cause the central stick region to contract as the length of the slip zone increases. At the same time, the separation points move towards the centre of the disc due to the coupling effect. The direction of resultant slip continues to change towards the tangential direction. The amount by which the slip changes direction increases with position from the stick/slip interface to the point of separation as displayed in Figure 7.16 when the normalised torsion is equal to 0.09. As expected, when the torsion reaches its spinning limit the direction of the resultant slip will be in the tangential direction.

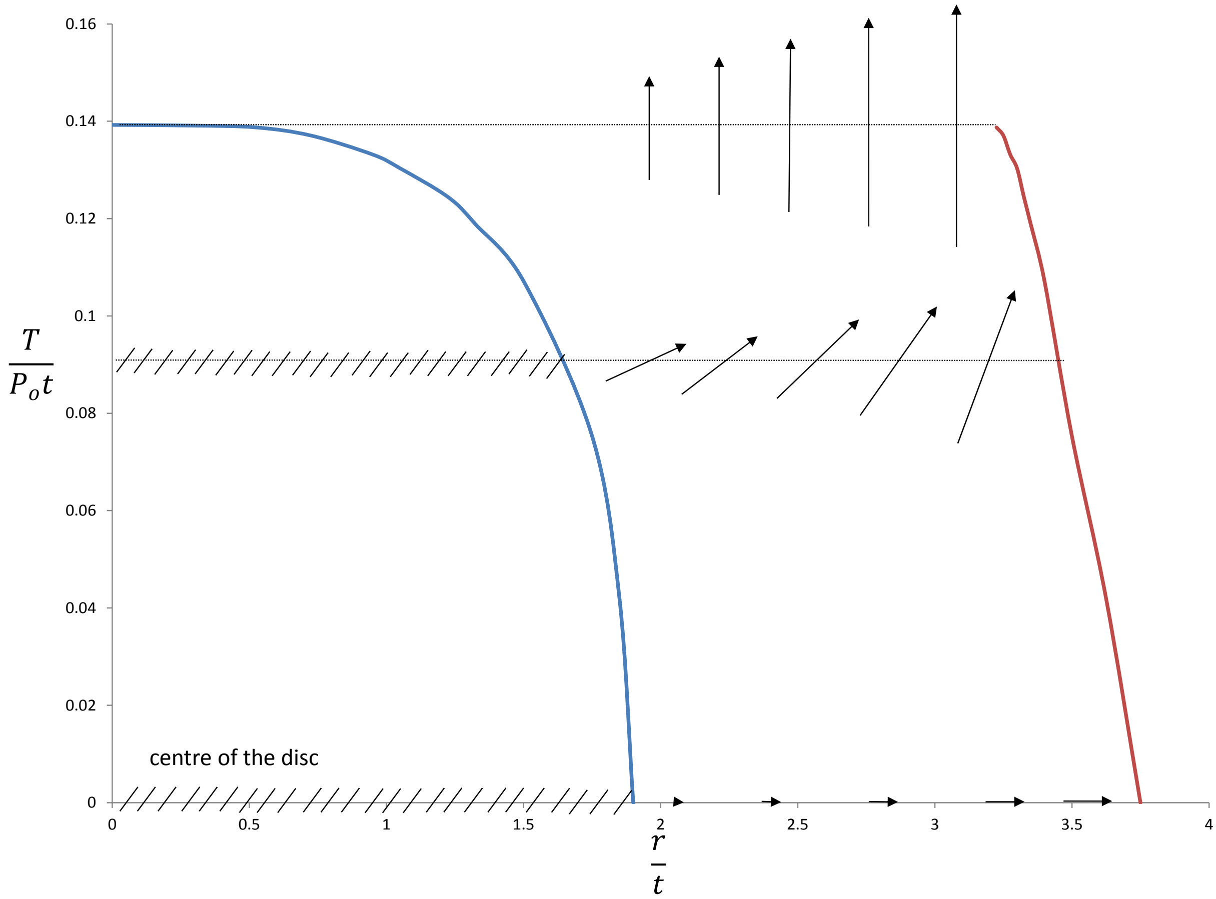

Figure 7.16: Evolution of slip/stick zones and separation when the disc in under torsion, *T* at *f* = 0.5.

It is important to note that the results are the same if the direction of the applied torsion is reversed i.e. anti-clockwise direction. The only difference is the reversed direction of the resultant slip. The aerial view of the interfacial response when the circular disc is subjected to torsion is portrayed in Figure 7.17.

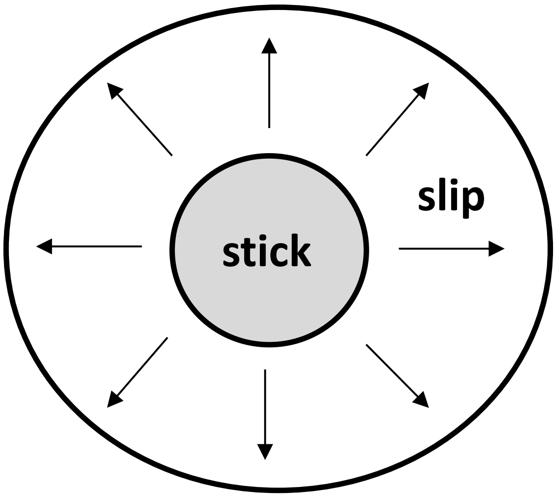

(a)

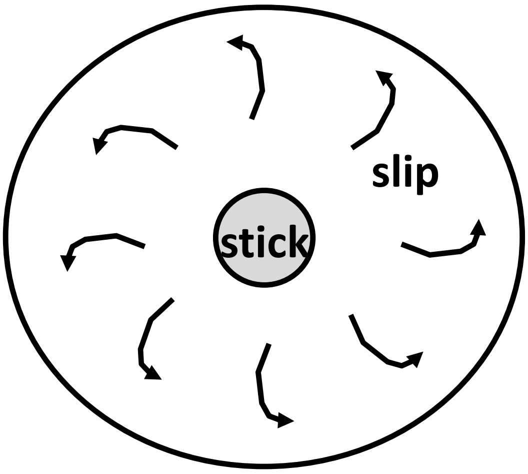

(b)

Figure 7.17: Aerial view of the evolution of stick and slip zones before and after the disc is subjected to a finite torsion: (a) no torsion, (b) finite torsion.

7.6 Conclusion

The axisymmetric form of receding contact between a circular disc and elastic half-plane, made from the same material, and where the uniform pressure load is applied over part of the top surface of the circular disc has been studied. If the radius of the loaded area is sufficiently large the contact interface may remain complete. The complete contact will either be fully adhered or, if the coefficient of friction is less than 0.543 a slip region will develop. If the radius of the loaded area is smaller than the critical value the contact will recede as shown in Figure 7.8. It has been shown that contact interface will snap to a particular configuration upon the infinitesimal normal load. The pressure distribution will drop smoothly to zero at the edges of the contact because of the separation in the contact interface. This means there will always be a radial slip region. Further increases in normal load do not alter the point of separations but the stress and displacements are proportional to the applied load.

During the unloading phase, the contact will further recede which alter both slip and stick zones. This shows similar properties to the plane receding contact. The application of torsion causes the length of slip zone to grow inwards and, as a result, extent of contact area decreases. This also has a significant effect the magnitude and direction of resultant slip displacement. The direction of resultant slip is perpendicular to the radial direction when the disc is about to spin.

8 Conclusion and future work

8.1 Conclusion

Fretting fatigue failure has been a major source of premature failures in many mechanical assemblies and this can cause catastrophic damage and loss of life. This thesis provides a series of useful tools to aid in the investigation of fretting fatigue and procedures for designing against fretting fatigue.

It is important to find lifting criteria for design against fretting fatigue. The first part of this thesis focuses on crack initiation and early stages of crack growth as well as the boundary between the finite and infinite life for incomplete contacts. An asymptotic approach was employed to quantify the state of stress and displacement at the edges of contact. It can be used as a way to compare the measured values of fatigue strength during fretting experiments and to predict the strength of a more complex prototype. Four potential correlators of fretting fatigue were considered. First, the S-N diagram was used. In this correlator, the information on size of the contact, where it is subjected to severe contact stress, is absent and therefore there is a considerable spread of results. The second correlator is based on the K-T approach where a length scale is defined by the intrinsic material properties. Assume that the crack, of depth c, normal to the surface is formed at the edge of the contact. The crack tip stress intensity factor is then calculated. The boundary between long crack propagation and short crack arrest was determined. It is important to note that this correlator is applicable for any incomplete contact where the asymptotic representation is appropriate. This was very useful in the analysis because both cylindrical and flat-rounded pads were used in the available fretting fatigue experimental data. It was shown that this correlator satisfactorily predicts the boundary between finite and infinite lives. Although the K-T method provides the boundary between finite and infinite lives it is not possible to predict the component life when it is finite. The values of ΔK_T may be considered as a potential correlator especially in the case where the process zone is relatively large. It was thought that the threshold for growth of a model II crack may be appropriate to the nucleation condition at the contact edge and mode II crack threshold was assumed to be $\Delta K_{II}^{th} = 0.8 \times \Delta K_{I}^{th}$. The life correlation based on ΔK_T shows a big improvement over the stress-based criteria. The last correlator considered is the maximum of irreversible frictional energy expended per unit area within the slip region and the results are correctly ranked with a few outliers and the thresholds are distinct.

Chapter 3 of the thesis focuses on the developments of a reduced stiffness method and an evolutionary algorithm for use with finite element analysis. It provides an efficient and robust method of solving frictional contact problems as computational time is significantly reduced. This method also provides more accurate results than a traditional finite element approach.
It also enables us to formulate and solve other categories of problem that cannot be conveniently treated using conventional finite element methods such as shakedown analysis and dislocation solutions.

Three shakedown limit algorithms for coupled contacts have been discussed in chapter 4. An example of an elastic complete contact subjected to cyclic shear loading was used to illustrate how these algorithms can be applied to calculate the shakedown limit. The exact-solution algorithm was used to determine the correct shakedown limits for various loading conditions and coefficients of frictions. The corresponding optimal residual traction and slip displacement distributions have also been found. The results were then tested by conducting a marching in time solution using the evolutionary algorithm and they also show that the steady state response of the complete contact seems to depend on pre-existing residual tractions. The initial condition here may be determined by assembly protocol e.g. the order in which the bolts are tightened. By knowing the residual stresses needed to cause the contact to shake down the steady response can be predicted. This may be used to determine the order by which the bolts should be tightened up in order to maximise the possibility of contact shakedown.

In chapter 5, the results of analysis on the plane receding contact where a layer is pressed against a half-plane by a normal pressure has shown that full contact is maintained only if the applied pressure extends close to the contact edge. On separation, the contact area remains the same, regardless of the magnitude of the applied pressure. However, the stress state and displacement are proportional to the applied load. During the unloading process, the contact area decreases followed by a continuous variation of slip/stick boundaries.

In chapter 6, a two-dimensional mechanical lap joint was subjected to a constant normal load causing it to jump to a particular configuration. It was shown that the application of cyclic bulk loading has a substantial effect on the stick/slip geometry and the interfacial tractions. The contact width smoothly decreases in size upon the application of tensile bulk tension and a higher amount of energy is dissipated for the tension case. However, the contact size increases when the lap joints are under compressive bulk load. The results also show that the energy dissipation decreases as the coefficient of friction at the contact interface increases.

In Chapter 7, an axisymmetric receding contact between a circular elastic disc against an elastically similar half-space has been studied. It was found that the disc separates if the area where pressure is acting upon is not sufficiently large. The separation points remain unchanged as the normal load monotonically increases. Upon removal of the applied load, the contact area decreases in size and the evolution of the stick and slip zones shows a similar pattern to that which occurred in the plane receding contact. When the torsion is applied, the contact area decreases and the stick/slip transition shifts inward towards the centre of the disc. This is due to the slip zone lengthening. The direction of the resultant slip changes towards the tangential directions. It will be perpendicular to the radial direction when the torsion approaches its spinning limit. The results are the same if the sign of the torsion is reversed and the only difference is the reverse in sign of the resultant slip direction.

8.2 Future work

There are several areas which merit further exploration prompted by this work. These include the following:

1. Optimisation problem

One of the important quantities that can be optimized for design against fretting fatigue is the contact geometry. It can be optimized to minimize the possibility of fretting fatigue.

2. Degree of coupling

The degree of coupling is an important parameter in shakedown analysis of frictional elastic systems. Therefore it would be useful if I can quantify the degree of coupling of the systems. A starting point would be to look at different elastic mismatch of the problems and compute the reduced stiffness matrices as discussed in chapter 3. Then quantify the coupling term of the reduced stiffness matrix using the norm. I can then carry out the shakedown analysis the method as discussed in chapter 4 and investigate how a different degree of coupling affects the results.

3. Multiple bolt arrays

Examining how the order in which the bolts are tightened could lead to a different interfacial response of a contact. For example, a symmetrical arrangement where three bolts are placed closely together. Consider the centre bolt is tightened first followed by the outer bolts. Second, the outer bolts are tightened first and the centre bolted.

4. Lower loading limit of shakedown

The upper limit of shakedown of continuous coupled systems was investigated in chapter 4. There exists another limit of shakedown whereby below this load factor will always shake down. One way of solving this is to consider the constraint equations of the contact nodes. This would require an efficient method of solving the problem as the computational cost will increase significantly as the number of nodes is increased. For a system of N nodes the total number of simultaneous equations is $2^{N-1}N$.

5. Shakedown of receding contact

As discussed in chapter 5, one of the characteristics of receding contact is that it snaps to a particular configuration upon infinitesimal of the applied normal load and the separation point remains fixed. It would be useful to extend the method developed in chapter 4 to analyse this class of problems. For example, consider the plane receding contact problem in chapter 5 when the normal load is cycled between some maximum and minimum values.

Appendix A: Calibration for Asymptote K_N for Rounded Edge Contact

The contact pressure for a radiused semi-infinite flat and rounded punch characterised by the edge radius R, can be written as [112]:

$$p(x) = \frac{3K_N}{4\sqrt{a_{round}^3}}\left[2\sqrt{x a_{round}} + [x - a_{round}]\ln\left|\frac{\sqrt{a_{round}} - \sqrt{x}}{\sqrt{a_{round}} + \sqrt{x}}\right|\right], \tag{A.1}$$

where a_{round} is the radiused portion of the contact and can be found from [113], $E^* = \frac{E}{\left[2(1-\nu^2)\right]}$ for elastically similar materials, and K_N can be defined

$$K_N = \frac{-2E^*\sqrt{a_{round}^3}}{3\pi R}. \tag{A.2}$$

If $\frac{t}{a_{round}} \gg 1$, the pressure varies in the forum $p(t) = \frac{K_N}{\sqrt{t}}$. If the observation point is very close to the edge of the contact, $0 < \frac{t}{a_{round}} \ll 1$, the pressure varies in the form:

$$p(t) = \frac{3K_N\sqrt{t}}{a_{round}}. \tag{A.3}$$

Appendix B: Extracting Mtx file

Detailed instructions on how to construct the model and obtain the .mtx file are provided below.

B.1 Creation and Material Properties

(a) Start the ABAQUS/CAE viewport by doubling click on the ABAQUS icon to create a new model database.

(b) In the model tree, right click on Parts and select create. In the 'create part' window select 2D planar, Deformable, shell and specify the approximated size of the model(e.g. 10).

(c) You should now be in the sketch window, define the origin to be (0,0) by click on the 'sketcher options' and click on origin. Enter (0,0) in the x-y coordinate window.

(d) Sketch an arbitrary rectangle in ABAQUS CAE. Click on the 'create straight line icon' and adjust the dimensions of the rectangle to the required values. Then click done

(e) In the model tree, right click 'Material' → click create material. In the edit material window, click mechanical → click elasticity → click elastic → specify the values of Young Modulus, E and poison ratio, v.

(f) Right click 'section assignment' in the model tree → click create → select the relevant section in the ABAQUS viewport → click done. In the Edit Section Assignment window, click on the icon to create the section → click solid section and homogeneous.

(g) In the Assembly, right click on instance → click 'Create' → select the relevant Part name → click ok.

(h) Go the 'Mesh' section, click on the contact boundary, and specify the number of elements (e.g. 10) and a grading ratio.

(i) Click on each of the remaining boundaries and choose the number of elements and the grading ratio (or uniform).

This procedure ensures that the nodes on the contact boundary are numbered sequentially, but they will generally be in the middle of the nodal list. Figure 3.12 shows a simple mesh generated by this procedure. Notice that the nodes on the lower (contact) boundary are numbered sequentially between 1 on the left and 21 on the right. Similarly, the nodes on the top surface (externally loaded) are numbered between 22 on the left and 42 on the right. These numbers can also be identified by examining the list of nodes and elements in the input files (See editing input files subsection).

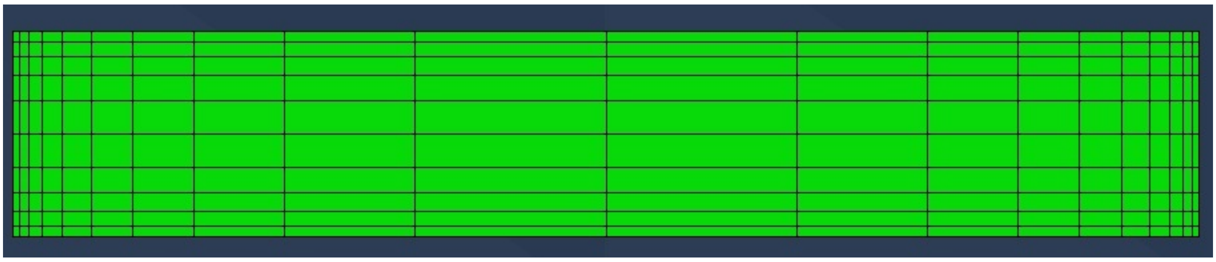

Figure B.1 – A simple mesh of an elastic rectangular body

B.2 Create the ABAQUS input files

(j) Once the mesh is created, click on 'Step' → click 'Create' → Type the step name as S2 → click 'Continue' and click 'Ok'. This will generate additional text in the input file related to a possible first loading step on the structure. However, I do not need to activate such a loading step.

(k) In the model tree, right click on the job icon at the bottom left hand corner → click 'Create' → Click 'Continue' and click 'Ok'. Now right click on the job name you just created and click on 'write input command'. The input file will be copied to the directory that you specify. For the mesh shown in Figure B.1, the beginning of this file will appear as

```
*Heading
** Job name : One Model name : Model-1
** Generated by : Abaqus / CAE 6.10 - EF1
*Preprint, echo = NO, model = NO, history = NO, contact = NO
** PARTS
*Part, name = Part-1
*Node
*Element, type = CPS4R
1     0         0
2     0.019     0
3     0.042     0
4     0.066     0
...............
21    0         1
22    0.019     1
23    0.042     1
34    0.066     1
...............
** ASSEMBLY
..............
** MATERIALS
..............
** STEP
..............
*Step, name = S2
*Static
1., 1., 1e-05, 1.
** OUTPUT REQUESTS
.............
```

Sometimes the above procedure will cause the contact nodes to be numbered sequentially, but not necessarily starting with unity. In either case, I need to identify the node number for the first contact node N_1 and the last contact node N_2 defined such that $N1 < N_2$. In addition, the first and last externally loaded nodes N_3, N_4 need to be identified. In the above case, $N_1 = 1$, $N_2 = 21$, $N_3 = 22$ and $N_4 = 42$.

B.3 Edit the ABAQUS input files

(l) I then insert the commands

```
*STEP, name = S1
*MATRIX GENERATE, STIFFNESS
*END  STEP
```

This command should be inserted just before the step S2.The input file in the step module should now look like

```
*STEP:S1
*STEP, name = S1
*MATRIX GENERATE ,STIFFNESS
*END STEP
**STEP:S2
*Step, name = S2
*Static
1., 1., 1e-05, 1.
```

Note that the command in part (l) has been tested in ABAQUS version 9, 10-1, 10-2. However, if you use ABAQUS version 6.11 then it will only export the .sim file. There is an extra command line needed to convert .sim file to.mtx file.

```
*STEP
*MATRIX GENERATE ,STIFFNESS
*MATRIX GENERATE,STIFFNESS
*END STEP
```

(m) You can now submit a job to obtain .mtx files. (See submission of ABAQUS input file subsection)

B.4 Submission of ABAQUS input file

After editing the input file by inserting the command (See *edit ABAQUS input file* subappendix). I then run the job in ABAQUS which will create a file with extension .mtx.

There are two way of submitting ABAQUS input files. Before submitting ABAQUS input files the users should check if the corresponding input files are located in the working directory. You can specify the location of the working directory by clicking file on the top left of the ABAQUS/CAE viewport and select the 'Set Work Directory' option. The working directory is where all the output files will be stored. You can now submit the job by using one of the following commands.

a) Run the job using the command line. Run an ABAQUS by typing the following command line in the ABAQUS command editor.

abaqus job=jobname.inp (e.g. if job name is matrix then the command is abaqus job= matrix.inp)

b) Run the job using CAE

Running from ABAQUS/CAE using Job → click 'Create' → 'Select' input file in the source icon → select your input file → click 'Continue'. After doing one of the two methods the .mtx will be located in the working directory you specified.

Appendix C: Global Stiffness Matrix

The .mtx file can be converted to global stiffness matrix using MATLAB. The .mtx file exported from ABAQUS is in sparse format. Only the non-zero components in the bottom left triangle are exported and these each appear as a comma-separated set of five numbers (i, p, j, q, s) representing respectively

(1) the row node i,

(2) the degree of freedom for the row node p,

(3) the column node j,

(4) the degree of freedom for the column node q,

(5) the matrix entry s

For a two degree of freedom problem $p, q \in \{1, 2\}$ and $i, j \in \{1, NT\}$ where N_T is the total number of nodes. To avoid excessive computing time and possible excessive memory requirements, it is important to perform the static reduction process also in sparse matrix format, but the MATLAB sparse format distinguishes elements but not degrees of freedom and hence uses sets of three comma separated numbers in the format (k, l, s) where $k, l \in \{1, 2NT\}$. The conversion is accomplished

$$k = 2(i-1) + p$$

$$l = 2(j-1) + q$$

The following MATLAB code converts the ABAQUS .mtx file to the global stiffness matrix. The users have to specify two inputs which are .mtx file and the total number of nodes (NT).

% Import .mtx file from ABAQUS (Input 1)

% Read ASCII - delimited file of numerical data into matrix

$S = dlmread(\,filename)$

% Extract row array dimensions N for the number of iteration k

$[N, M] = size(S)$

% NT = Total number of nodes (Input 2)

$NT = S(end, 1)$

% Make sparse matrix for global stiffness matrix

$K = sparse(2*NT, 2*NT);$

% To convert the sparse form matrix to global stiffness matrix.

$i = 2\left(S(:,1) - 1\right) + S(:,2);$

$j = 2\left(S(:,3) - 1\right) + S(:,4);$

$s = S(:,5);$

$s = [s; s];$

$[ij, loc] = unique([i \quad j; j \quad i], \ 'rows');$

$K = accumarray(ij, s(loc), [], @\max, [])$

Appendix D: Evolutionary Algorithm

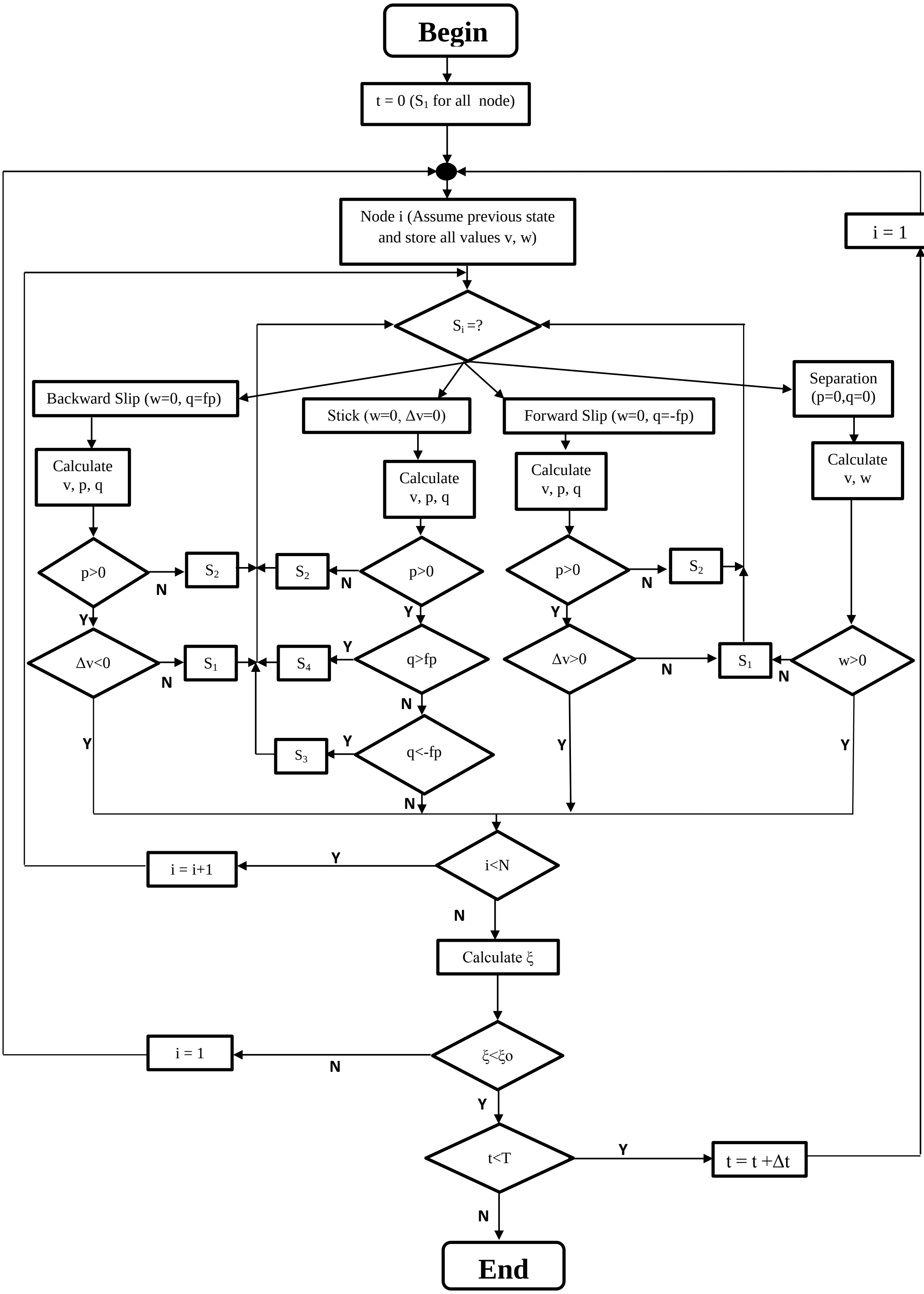

References

1. Coulomb, C.A., *Theorie des machines simples, en ayant regard au frottement de leurs parties, et a la roideur des cordages.* meM. Math. Phys. Acad. Sci, Paris, 1785: p. 161-342.
2. Hertz, H., *On the contact of elastic solids.* J. Reine Angew. Math., 1882. **92**: p. 156-171.
3. Boussinesq, J., *Application des potentiels a 1 etude de 1' equilibre et du mouvement des solides elastiques.* Gauthier-Villars, Paris, 1885: p. 508.
4. Cerruti, V., *Acc. Lincei.* Mem. fis. mat., Roma, 1882.
5. A., F., *Sur la repartition des pressions dans un solide rectangulaire charge transversalement* Comptes Rendus Mecanique, Paris, 1892. **114**: p. 1465.
6. Timoshenko, P. and J.N. Goodie, *Thoery of elasticity*, ed. n. edn. 1951, New York: McGraw Hill.
7. Gladwell, G.M.L., *Contact Problems in the Classical Thoery of Elasticity.* 1980: Sijhoff and Noordhoff, Alphen aan den Rijn.
8. Johnson, K.L., *Contact Mechanics* 1985: Cambridge University Press, Cambridge.
9. Cattaneo, C., *Sul conttatto di due corpi elastici: distribuzione locale degli storzi. Pend.d'Acad naz.dei Lincei.* Pend.d'Acad naz.dei Lincei, 1938. **27**(Series 6): p. p. 342, 434,474.
10. Mindlin, R.D., *Compliance of Elastic Bodies in Contact.* Journal of Applied Mechanics-Transactions of the Asme, 1949. **16**(3): p. 259-268.
11. Mindlin, R.D. and H. Deresiewicz, *Elastic Spheres in Contact under Varying Oblique Forces.* Journal of Applied Mechanics-Transactions of the Asme, 1953. **20**(3): p. 327-344.
12. Jager, J., *A new principle in contact mechanics.* Journal of Tribology, 1998. **120**: p. 677-684.
13. Ciavarella, M., *The generalized Cattaneo partial slip plane contact problem. I - Theory.* International Journal of Solids and Structures, 1998. **35**(18): p. 2349-2362.
14. Nowell, D. and D.A. Hills, *Mechanics of fretting fatigue tests.* International Journal of Mechanical Sciences, 1987. **29**(5): p. 355-365.
15. Williams, M.L., *Stress Singularities Resulting from Various Boundary Conditions in Angular Corners of Plates in Extension.* Journal of Applied Mechanics-Transactions of the Asme, 1952. **19**(4): p. 526-528.
16. Bogy, D.B., *Edge-bonded dissimilar orthogonal elastic wedges under normal and shear loading.* Journal of Applied Mechanics, 1968. **35**: p. 460-466.
17. Dundurs, J., *Discussion of edge-bonded dissimilar orthogonal elastic wedges under normal and shear loading.* Journal of Applied Mechanics, 1969. **36**(650-652).
18. Bogy, D.B., *Two edge-bounded elastic wedges of different materials and wedge angles under surface tractions* ASME Journal of Applied Mechanics, 1971. **38**(377-386).
19. Gdoutos, E.E. and P.S. Theocaris, *Stress concentration at the apex of a plane indenter acting on an elastic half-plane.* Journal of Applied Mechanics, 1975. **42**: p. 688-692.
20. Comninou, M., *Stress singularity at a sharp edge in contact problems with friction.* Journal of Applied Mathematics and Physics, 1976. **27**: p. 493-499.
21. Spence, D.A., *An eigenvalue problem for elastic contact with finite friction.* Proceedings of the Cambridge Philosophical Society, 1973. **73**(249-268).

22. Spence, D.A., *The hertz contact problem with finite friction.* Journal of Elasticity, 1975. **5**: p. 297-319.
23. Eden, E.M., W.N. Rose, and F.L. Cunningham, *The edurance of metals.* Proc. I Mech E, 1911. **4**: p. 139.
24. Tomlinson, G.A., *The Rusting of Steel Surfaces in Contact.* Proceedings of the Royal Society of London. Series A, Containing Papers of a Mathematical and Physical Character, 1927. **115**(771): p. 472-483.
25. Warlow-Davies, E.J., *Fretting Corrosion and Fatigue Strength: Brief Results of Preliminary Experiments.* Proceedings of the Institution of Mechanical Engineers, 1941. **146**(1): p. 32-38.
26. McDowell, J.R., *Fretting corrosion tendencies and several combinations of materials.* Symposium on Fretting Corrosion, 1953. **STP 144**(ASTM, Philadelphia): p. 24-39.
27. Fenner, A.J. and J.E. Field, Rev. Metallurgie, 1958. **55**(No. 57): p. 1.
28. Fenner, A.J. and J.E. Field, *A study of the onset of fatigue damage due to fretting.* Proc. NE Coast Institute of Engineers and Shipbuilders, 1960. **76**: p. 183.
29. Nishioka, K., S. Nishimura, and K. Hirakawa, *Fundamental investigation of fretting fatigue - part 1. On the relative slip amplitude of press-fitted assemblies, Bull.* ASME, 1968. **11**: p. 437-445.
30. Nishioka, K. and K. Hirakawa, *Fundamental investigation of fretting fatigue-part2 Bull.* JSME, 1969a. **12**(50): p. 180-187.
31. Nishioka, K. and K. Hirakawa, *Fundamental investigation of fretting fatigue-part3. Bull.* JSME, 1969b. **12**(51): p. 397-407.
32. Nishioka, K. and K. Hirakawa, *Fundamental investigation of fretting fatigue.* JSME, 1969c. **12**(52): p. 408-414.
33. Nishioka, K. and K. Hirakawa, *Fundamental investigation of fretting fatigue-part5. Bull.* JSME, 1969d. **12**(52): p. 692-697.
34. Nishioka, K. and K. Hirakawa, *Fundamental investigation of fretting fatigue - part 6. Bull.* JSME, 1972. **15**(80): p. 135-144.
35. Milestone, W.D. and J.T. Janeczko, *Friction between steel surfaces during fretting.* Wear, 1971. **18**(1): p. 29-40.
36. Endo, K., H. Goto, and T. Fukunaga, *Frictional force in fretting fatigue, Bull.* JSME, 1974. **17**(n108): p. 647-654.
37. Hoeppner, D.W. and G.L. Goss, *A fretting fatigue damage threshold concept* Wear, 1974. **27**: p. 61.
38. Endo, K. and H. Goto, *Initiation and propagation of fretting fatigue cracks.* Wear, 1976. **38**: p. 311-324.
39. Alic, J. and A. Kantimathi, *Fretting Fatigue, With Reference to Aircraft Structures.* SAE Technical Paper 790612, 1979.
40. Bramhall, J., *Studies in Fretting Fatigue*, 1973, University of Oxford.
41. Nowell, D., *An Analysis of Fretting Fatigue*, 1988, University of Oxford.
42. Waterhouse, R.B., *Fretting Fatigue*. 1981: Applied Science Publishers, London.
43. Bannantine, J.A., J.J. Comer, and J.L. Handrock, *Fundamentals of Metal Fatigue Analysis*. 1990: Prentice Hall.
44. Hills, D.A. and D. Nowell, *Mechanics of Fretting Fatigue*. 1994: Kluwer Acadamic Publishers.
45. Filon, L.N.G., *On an Approximate Solution for the Bending of a Beam of Rectangular Cross-Section under any System of Load, with Special Reference to Points of Concentrated or Discontinuous Loading.* Philosophical Transactions of the Royal Society of London. Series A, Containing Papers of a Mathematical or Physical

Character, 1903. **201**(ArticleType: research-article / Full publication date: 1903 / Copyright © 1903 The Royal Society): p. 63-155.
46. Coker, E.G. and L.N.G. Filon, *Treatise on photo-elasticity*. 1957: Cambridge University Press.
47. Dundurs, J. and M. Stippes, *Role of Elastic Constants in Certain Contact Problems.* Journal of Applied Mechanics, 1970. **37**(4): p. 965-970.
48. Tsai, K.C., J. Dundurs, and L.M. Keer, *Elastic Layer Pressed against a Half Space.* Journal of Applied Mechanics-Transactions of the Asme, 1974. **41**(3): p. 703-707.
49. Dundurs, J. *Properties of elastics bodies in contact*. in *Modelling and Simulation, Proceedings of the Annual Pitssburgh Conference*. 1975.
50. Ahn, Y.J. and J.R. Barber, *Response of frictional receding contact problems to cyclic loading.* International Journal of Mechanical Sciences, 2008. **50**(10-11): p. 1519-1525.
51. Comninou, M. and J.R. Barber, *Frictional slip between a layer and a substrate due to a periodic tangential surface force.* International Journal of Solids and Structures, 1983. **19**(6): p. 533-539.
52. Bree, J., *Elastic-plastic behaviour of thin tubes subjected to internal pressure and intermittent high-heat fluxes with application to fast-nuclear-reactor fuel elements.* Journal of Strain Analysis for Engineering Design, 1967. **2**(3): p. 226-238.
53. Churchman, C.M., A.M. Korsunsky, and D.A. Hills, *The application of plasticity principles to friction.* Journal of Strain Analysis for Engineering Design, 2006. **41**(4): p. 323-328.
54. Saez, R., et al., *Frictional shakedown in a complete contact.* Journal of Strain Analysis for Engineering Design, 2003. **38**(4): p. 329-338.
55. Melan, E., *Zur plastizitat des raumlichen kontinuums.* Ing. Arch., 2011. **9**: p. 116-126.
56. Klarbring, A., M. Ciavarella, and J.R. Barber, *Shakedown in elastic contact problems with Coulomb friction.* International Journal of Solids and Structures, 2007. **44**(25-26): p. 8355-8365.
57. Barber, J.R., A. Klarbring, and M. Ciavarella, *Shakedown in frictional contact problems for the continuum.* Comptes Rendus Mecanique, 2008. **336**(1-2): p. 34-41.
58. Ahn, Y.J., E. Bertocchi, and J.R. Barber, *Shakedown of coupled two-dimensional discrete frictional systems.* Journal of the Mechanics and Physics of Solids, 2008. **56**(12): p. 3433-3440.
59. Ruiz, C., P.H.B. Boddington, and K.C. Chen, *An investigation of fatigue and fretting in a dovetail joint.* Experimental Mechanics, 1984. **24**(3): p. 208-217.
60. O'Connor, J.J. and K.L. Johnson, *The role of surface asperities in transmitting tangential forces between metals.* Wear, 1963. **6**(2): p. 118-139.
61. Khadem, R. and J.J. Oconnor, *Axial Compression of an Elastic Circular Cylinder in Contact with 2 Identical Elastic Half Spaces.* International Journal of Engineering Science, 1969. **7**(8): p. 785-&.
62. O'Connor, J.J., *The role of elastic stress analysis in the intrepretation of Fretting Fatigue Failures*, in *Fretting Fatigue*, R.B. Waterhouse, Editor. 1981, Applied Science, London. p. pp.23--66.
63. Cattaneo, C., *Sul contatto di due corpi elastici: Atti Accad. naz. Lincei Rc. Ser.* 1938. **6, .27**: p. pp.342--348, 434--436, 474--478
64. Nowell, D., D. Dini, and D.A. Hills, *Recent developments in the understanding of fretting fatigue.* Engineering Fracture Mechanics, 2006. **73**(2): p. 207-222.
65. Dini, D., *Studies in Fretting Fatigue with particular applicatio to almost complete contacts.*, 2003, University of Oxford.

66. Dini, D. and D.A. Hills, *A method based on asymptotics for the refined solution of almost complete partial slip contact problems.* European Journal of Mechanics a-Solids, 2003. **22**(6): p. 851-859.
67. Dini, D. and D.A. Hills, *Bounded asymptotic solutions for incomplete contacts in partial slip.* International Journal of Solids and Structures, 2004. **41**(24-25): p. 7049-7062.
68. Muskhelishvili, N.I., *Some basic problems of mathematical theory of elasticity*. 1975: Noordhoff Layden.
69. Szolwinski, M.P. and T.N. Farris, *Observation, analysis and prediction of fretting fatigue in 2024-T351 aluminum alloy.* Wear, 1998. **221**(1): p. 24-36.
70. Murthy, H., G. Mseis, and T.N. Farris, *Life estimation of Ti-6Al-4V specimens subjected to fretting fatigue and effect of surface treatments.* Tribology International, 2009. **42**(9): p. 1304-1315.
71. Gean, M.C. and T.N. Farris, *Elevated temperature fretting fatigue of Ti-17 with surface treatments.* Tribology International, 2009. **42**(9): p. 1340-1345.
72. Murthy, H., G. Gao, and T.N. Farris, *Fretting fatigue of single crystal nickel at 600 degrees C.* Tribology International, 2006. **39**(10): p. 1227-1240.
73. Lykins, C.D., S. Mall, and V. Jain, *An evaluation of parameters for predicting fretting fatigue crack initiation.* International Journal of Fatigue, 2000. **22**(8): p. 703-716.
74. Lykins, C.D., *An investigation of fretting fatigue crack initiation behavior of the titanium alloy Ti-- 6Al--4V.*, 1999, University of Dayton.
75. Morrissey, R.J. and P.J. Golden, *Fatigue strength of a single crystal in the gigacycle regime.* International Journal of Fatigue, 2007. **29**(9-11): p. 2079-2084.
76. Shyam, A., et al., *Fatigue-crack-propagation thresholds in a nickel-base superalloy at high frequencies and temperatures.* Metallurgical and Materials Transactions a-Physical Metallurgy and Materials Science, 2002. **33**(7): p. 1949-1962.
77. Wöhler, A., *Über die Festigkeitsversuche mit Eisen und Stahl.* Zeitschrift für Bauwesen, 1870. **20**: p. 73-106.
78. Kitagawa, H. and S. Takahashi. *Applicability of fracture mechanics to very small cracks or the cracks in the early stage.* in *Proceedings of the Second International Conference on Mechanical Behavior of Materials*. 1976. Metals Park, OH, USA.
79. Araujo, J.A. and D. Nowell, *Analysis of pad size effects in fretting fatigue using short crack arrest methodologies.* International Journal of Fatigue, 1999. **21**(9): p. 947-956.
80. Dini, D., D. Nowell, and I.N. Dyson, *The use of notch and short crack approaches to fretting fatigue threshold prediction: Theory and experimental validation.* Tribology International, 2006. **39**(10): p. 1158-1165.
81. Fouvry, S., et al., *Prediction of fretting crack propagation based on a short crack methodology.* Engineering Fracture Mechanics, 2008. **75**(6): p. 1605-1622.
82. Nowell, D. and D.A. Hills, *Open cracks at or near free edges.* The Journal of Strain Analysis for Engineering Design, 1987. **22**(3): p. 177-185.
83. Hills, D.A., et al., *Solution of crack problems: the distributed dislocation technique*. 1996: Kluwer Acadamic Publishers.
84. Otsuka, A., K. Mori, and T. Miyata, *The condition of fatigue crack growth in mixed mode condition.* Engineering Fracture Mechanics, 1975. **7**(3): p. 429-432,IN15-IN18,433-439.
85. Otsuka, A., K. Tohgo, and H. Matsuyama, *Fatigue crack initiation and growth under mixed mode loading in aluminum alloys 2017-T3 and 7075-T6.* Engineering Fracture Mechanics, 1987. **28**(5-6): p. 721-732.

86. Dini, D., A. Sackfield, and D.A. Hills, *Comprehensive bounded asymptotic solutions for incomplete contacts in partial slip.* Journal of the Mechanics and Physics of Solids, 2005. **53**(2): p. 437-454.
87. Fouvry, S., et al., *Application of an energy wear approach to quantify fretting contact durability: Introduction of a wear energy capacity concept.* Tribology International, 2007. **40**(10-12): p. 1725-1726.
88. Nowell, D. and D. Dini, *Stress gradient effects in fretting fatigue.* Tribology International, 2003. **36**(2): p. 71-78.
89. Araujo, J.A. and D. Nowell, *The effect of rapidly varying contact stress fields on fretting fatigue.* International Journal of Fatigue, 2002. **24**(7): p. 763-775.
90. Navarro, C., S. Munoz, and J. Dominguez, *On the use of multiaxial fatigue criteria for fretting fatigue life assessment.* International Journal of Fatigue, 2008. **30**(1): p. 32-44.
91. Ding, J., et al., *Simple parameters to predict effect of surface damage on fretting fatigue.* International Journal of Fatigue, 2011. **33**(3): p. 332-342.
92. Korsunsky, A.M., et al., *Comparative assessment of dissipated energy and other fatigue criteria.* International Journal of Fatigue, 2007. **29**(9-11): p. 1990-1995.
93. Weinzapfel, N., F. Sadeghi, and V. Bakolas, *An approach for modeling material grain structure in investigations of Hertzian subsurface stresses and rolling contact fatigue.* Journal of Tribology, 2010. **132**(4).
94. Goh, C.H., D.L. McDowell, and R.W. Neu, *Plasticity in polycrystalline fretting fatigue contacts.* Journal of the Mechanics and Physics of Solids, 2006. **54**(2): p. 340-367.
95. Zhang, M., D.L. McDowell, and R.W. Neu, *Microstructure sensitivity of fretting fatigue based on computational crystal plasticity.* Tribology International, 2009. **42**(9): p. 1286-1296.
96. Atkinson, K.E., *An introduction to numerical analysis,* ed. n. edition. 1989.
97. Antoni, N. and Q.S. Nguyen, *Shakedown theorems in Contact Mechanics.* Comptes Rendus - Mecanique, 2008. **336**(4): p. 341-346.
98. Melan, E., *Theorie statisch unbestimmter systeme aus ideal-plastichem baustoff.* sitzungsber.d.akad.d.wiss.Wein, 1963. **2A(145)**: p. pp.195--218.
99. Earles, S.W.E., *Theoretical Estimation of the Frictional Energy Dissipation in a Simple Lap Joint.* Journal of Mechanical Engineering Science, 1966. **8**(2): p. 207-214.
100. Ciavarella, M., et al., *Reduced dependence on loading parameters in almost conforming contacts.* International Journal of Mechanical Sciences, 2006. **48**(9): p. 917-925.
101. Hibbitt and K. &Sorensen, *ABAQUS Theory Manual, Version 6.10*. 2011: Simulia INC.
102. Puri, G.M., *Python Script for ABAQUS*. 2012.
103. Mindlin, R.D., et al., *Effects of an osciallating tangential force on the contact surface of elastic spheres.* Proc.1st US National Congress of Applied Mechanics, 1952: p. pp.203--208.
104. Karuppanan, S. and D.A. Hills, *Frictional complete contacts between elastically similar bodies subject to normal and shear load.* International Journal of Solids and Structures, 2008. **45**(17): p. 4662-4675.
105. Dini, D. and D.A. Hills, *Unsymmetrical shear loading and its influence on the frictional shakedown of incomplete contacts.* Proceedings of the Institution of Mechanical Engineers, Part C: Journal of Mechanical Engineering Science, 2004. **218**(5): p. 469-475.

106. Gaul, L., J. Roseira, and J. Becker, *Structural damping with friction beams.* Shock and Vibration, 2008. **15**(3-4): p. 291-298.
107. Petrov, E.P. and D.J. Ewins, *Effects of damping and varying. contact area at blade-disk joints in forced response analysis of bladed disk assemblies.* Journal of Turbomachinery-Transactions of the Asme, 2006. **128**(2): p. 403-410.
108. Dowell, D.J. and S.Cherry. *On passive and semi-active friction damping for seismic repsonse control of structures*. in *Eleventh World Conference on Earthquake Engineering*. 1996.
109. Eriten, M., A.A. Polycarpou, and L.A. Bergman, *Development of a Lap Joint Fretting Apparatus.* Experimental Mechanics, 2011. **51**(8): p. 1405-1419.
110. Thaitirarot, A., D.A. Hills, and D. Dini. *Plane receding contact* in *Proceeding of the 9th Tribo UK Conference in Tribology*. 2012. National Centre for Advanced Tribology, UK.
111. Hills, D.A., D. Nowell, and A. Sackfield, *Mechanics of Elastic Contacts*. 1993: Butterworth-Heineman Ltd.
112. Mugadu, A., et al., *The application of asymptotic solutions to characterising the process zone in almost complete frictional contacts.* International Journal of Solids and Structures, 2004. **41**(2): p. 385-397.
113. Ciavarella, M., D.A. Hills, and G. Monno, *The influence of rounded edges on indentation by a flat punch.* Proceedings of the Institution of Mechanical Engineers, Part C: Journal of Mechanical Engineering Science, 1998. **212**(4): p. 319-327.